Measuring the momentum distribution of a lattice gas at the single-atom level

Hugo Cayla

université PARIS-SACLAY

INSTITUT d'OPTIQUE GRADUATE SCHOOL ParisTech

NNT : 2018SACLO005

Thèse de doctorat

Measuring the momentum distribution of a lattice gas at the single-atom level

Thèse de doctorat de l'Université Paris-Saclay
préparée à l'Institut d'Optique Graduate School

Ecole doctorale n°572 Ondes et Matière (EDOM)
Spécialité de doctorat : Physique

Thèse présentée et soutenue à Palaiseau, le 09/11/2018, par

HUGO CAYLA

Composition du Jury :

Frédéric Chevy Ecole Normale Supérieure, Laboratoire Kastler Brossel	Rapporteur
Bruno Laburthe-Tolra Université Paris 13, Laboratoire de Physique des Lasers	Rapporteur
Karyn Le Hur Ecole Polytechnique, Centre de Physique Théorique	Présidente du jury
Tommaso Roscilde Ecole Normale Supérieure de Lyon, Laboratoire de Physique	Examinateur
Christoph Westbrook Institut d'Optique Graduate School, Laboratoire Charles Fabry	Directeur de thèse
David Clément Institut d'Optique Graduate School, Laboratoire Charles Fabry	Co-directeur de thèse

à David Lynch
Cinéaste superfluide et supraconducteur.

Remerciements

La rédaction de la version finale de ce manuscrit vient clore près de 4 ans de travail au laboratoire Charles Fabry, et près de 7 ans passés à l'Institut d'Optique, c'est-à-dire un bon quart de ma vie. Dans les quelques lignes qui suivent, j'aimerais remercier un grand nombre de personnes, que j'ai eu le plaisir de côtoyer pendant toutes ces années.

Je voudrais commencer par remercier David Clément, qui a été mon encadrant de thèse, et qui m'a fait confiance dès mes premiers pas maladroits dans la salle de manip. David possède un dynamisme, un enthousiasme et un esprit d'équipe qui ont été des moteurs essentiels pour mener à bien ce projet de recherche. Sa compréhension intuitive des phénomènes physiques et son exigence bienveillante m'ont beaucoup inspiré et m'ont considérablement aidé à aiguiser mon esprit scientifique. Merci à lui!

J'ai passé l'essentiel de ces trois années à travailler avec Marco Mancini et Cécile Carcy. Merci à Marco pour tous les bons moments passés, à débattre de géopolitique ou de sujets plus grivois, et à écouter du rock et du funk en alignant des miroirs. A presto, amico! Merci à Cécile pour sa bonne humeur, son énergie, sa force de travail et ses attentions, en espérant ne pas l'avoir trop choquée avec mes goûts musicaux et mon délabrement vestimentaire. Je lui souhaite bonne chance pour la suite (et fin) de son périple de thésarde. Je n'oublie pas les anciens : Rockson Chang et Quentin Bouton, qui m'ont beaucoup appris; ni le petit nouveau : Antoine Ténart, qui sera j'en suis sûr parfaitement capable de poursuivre l'aventure de l'Hélium sur réseau. Merci également à la manip, pour ses condensats et les beaux résultats qu'elle nous a donnés. Je lui pardonne ses avaries.

Notre équipe évolue au sein du groupe Optique Atomique (futur groupe Gaz Quantique). Je tiens à remercier son fondateur, Alain Aspect, qui malgré sa réputation internationale a toujours du temps à accorder à la jeune génération. Merci pour ses précieux conseils et ses nombreuses anecdotes. Merci également à Chris Westbrook qui a suivi avec intérêt mes travaux de thèse, et avec qui j'ai eu beaucoup de conversations stimulantes sur les questions de corrélations et de galettes à micro-canaux. Merci à tous les autres permanents du groupe, Denis Boiron, Marc Cheneau, Thomas Bourdel, Isabelle Bouchoule et Vincent Josse, qui contribuent tous à la bonne ambiance et à l'esprit d'entraide qui règne au sous-sol. Qui dit sous-sol dit groupe Optique Quantique, et je remercie l'ensemble de ses membres, particulièrement Antoine Browaeys pour son soutien. Merci aux nombreux thésards et post-docs du laboratoire pour le serrage de coude collectif, et les soirées passées à Paris, à Berlin, à Arkose ou aux Houches. Merci à Aisling, Vincent D, Pierre, Maxime, Amaudric, Maximilian, Anaïs, Steven, Giuseppe, Julien, Guillaume, Muktar, Clémence, Baptiste, Ziyad, Adrien, Mauro, Aliénor, Sylvain, Martin, Vincent L, Ludo, Eric et Léonard. J'espère n'oublier personne...

Je remercie également les différents enseignants avec qui j'ai collaboré pendant mes deux années de monitorat : Fabienne Bernard, Lionel Jacubowiez, Thierry Avignon, Cé-

dric Lejeune, Julien Villemejane, Nicolas Dubreuil, Henri Benisty et Yvan Sortais. En vrac, j'aimerais aussi remercier Patrick Georges, notre directeur de labo, pour sa gentillesse envers les thésards, Sébastien de Rossi, Emilie Sakat et Florence Nogrette avec qui il est toujours agréable d'échanger, ainsi que les différents services communs grâce auxquels nous fonctionnons au quotidien.

J'ai eu la chance de pouvoir faire de la vidéo en toute liberté au sein du laboratoire. Je remercie chaleureusement Christian Beurthe et Sophie Coumar de l'atelier d'optique pour m'avoir laissé découvrir et filmer leur beau métier. Merci à Ilias et Laure pour notre tournage au labo, et à Mattéo, qui s'est bousillé les bras à la perche. Je remercie également le LabEx PALM d'avoir accepté de financer notre websérie sur la recherche (MANIP), Gaëlle Lucas-Leclin pour son aide précieuse et son engagement dans la réalisation de ces vidéos, et mon frère Georges pour les superbes morceaux qu'il a composé à cette occasion. Et bien sûr je remercie Karen Perronet, David Clément (à nouveau), Thierry Chanelière et Elizabeth Boer-Duchemin pour avoir joué le jeu en acceptant de se confier à la caméra.

Enfin, hors du labo, je souhaiterais remercier mes proches pour leur soutien durant ce marathon qu'est la thèse. Merci aux amis, les Mathieu, Simon, Thomas, Jerem'. Merci à la famille, ma mère, mes frères, Etienne et tous ceux qui sont venus à ma soutenance. Et comme souvent, mon dernier mot va à Laure. Merci pour tout, tout.

Contents

Introduction

In 1924, L. de Broglie took the next step of M. Planck's and A. Einstein's hypothesis on quanta, and postulated that every particles of matter, like electrons or atoms, can also behave like waves [1]. This idea of a wave-particle "duality" was confirmed in 1928, with the first experiment of electronic diffraction by J. Davisson and L. Germer [2] at Bell Labs. According to de Broglie, a particle of mass m and velocity v is also described by a wave of wavelength λ. Those quantities are linked through the Planck constant h with the relation :

$$\lambda = h/mv. \tag{1}$$

For a thermodynamic ensemble of particles at temperature T, we can define the statistical average of λ, known as the thermal de Broglie wavelength :

$$\lambda_{dB} = \frac{h}{\sqrt{2\pi m k_B T}}, \tag{2}$$

where k_B is the Boltzmann constant. The notion of thermal wavelength connects to the quantum or classical nature of the system. If the density of the ensemble n is such that $\lambda_{dB}^3 n \ll 1$, then the system behaves classically, because the matter-waves do not overlap, and the particles see each other as individual objects. On the other hand, when $\lambda_{dB}^3 n \simeq 1$, the wave nature of the particles has to be taken into account, and the ensemble behaves as a quantum system.

Challenges of many-body quantum physics

In a copper wire, the atomic density is $\simeq 1.4 \times 10^5 \text{mol.m}^{-3}$, and since copper has one free electron per atom, the electronic density available for conduction is $\simeq 10^{29} \text{m}^{-3}$. This, combined to the light mass of the electrons (9×10^{-31} kg), leads to $\lambda_{dB}^3 n \gg 1$ at room temperature. So even something as common as the charges inside a copper wire behaves like a quantum ensemble. In 1929, F. Bloch calculated the wave functions of an electron inside a periodic potential, today known as the Bloch waves [3], establishing the first quantum theory of solids. Periodic potential are well adapted to describe the crystal-like structures of the ions inside metals, and for the simple case of non-interacting electrons in a sinusoidal potential, the Schrödinger equation can be solved (see section 4.1). Things become much richer and more complicated when electron-electron interactions, or electron-ion interactions are taken into account : there is no simple solution anymore, and the existing numerical methods are rapidly overwhelmed by the dimensionality of the Hilbert space, which grows exponentially with the number of particles in the system.

Solid-state physics gives emblematic examples of many-body quantum states, where the interactions between the particles give birth to fascinating physical phenomena, like superconductivity or spontaneous magnetization in metals [4], but emerging phenomena such as superfluidity or pairing mechanism can be found in all sorts of many-body systems : liquid Helium [5], neutron stars [6], atomic nucleus [7], etc. In all cases, couplings between the particles make those systems extremely difficult to study, both experimentally and theoretically, even if the microscopic

ingredients describing each quantum object are well understood. On the contrary, some macroscopic observations simply lack of microscopic models, like high temperature superconductivity, considered one of the biggest mystery of solid-state physics.

Cold atoms experiments : a suitable platform to study many-body systems

In this context, cold atoms experiments constitute a very interesting platform to study many-body systems. Since the end of the 20th century, physicists are able to cool down, manipulate, and probe atomic ensembles of thousands of individual objects [8]. The development of laser-cooling and trapping techniques have allowed to reach quantum degeneracy in diluted vapors ($\lambda_{dB}^3 n > 1$) [9], and to engineer various geometry of potentials to trap the atoms. Among them, the crystal-like structure of optical lattices enable the investigation of analogous condensed-matter models in a controllable way [10].

More recently, the use of Feshbach resonance to tune the interactions between the particles [11], and the development of new detection schemes able to probe individual atoms [12, 13] considerably increased the versatility of cold atoms experiments. Controling the interactions permits to explore a wide range of many-body regimes, from weakly interacting to strongly correlated systems [14], while single-atom-probing allows to investigate quantum correlations between the particles [15], giving new insights on the many-body wave function. But most of this new methods are probing individual positions or spins, while detection techniques sensitive to individual momenta are rare.

The momentum : a key quantity to explore many-body quantum physics

The particle-wave duality lies in the de Broglie hypothesis, which connects the momentum $p = mv$ of the particle to its wave vector $k = 2\pi/\lambda$. Indeed, equation (1) can be re-written

$$\hbar k = mv \tag{3}$$

Momentum and position are linked by the Heisenberg inequality, making p a complementary variable to describe many-body systems. In particular, it has been widely used to investigate the emergence of coherence in atomic vapors, through the estimation of the condensed fraction in time-of-flight measurements [16, 17]. Inversely, all excitations have a momentum signature given by the dispersion relation, making momentum space very useful to probe the temperature [18], the interactions strength [19], or the collective excitations [20] for instance. We can also mention some pairing mechanisms, like the celebrated BCS pairing [21], or the quantum depletion [22], only observable in momentum.

In cold atoms experiments, there are mainly two ways to probe the momentum distribution: Bragg spectroscopy, and Time-of-Flight (ToF) imaging. Bragg spectroscopy is a stimulated 2-photons process giving access the dynamic structure factor of a system, and constitutes an indirect measurement of the momentum distribution. On the other hand, ToF imaging probes the atomic density after an expansion time. The spatial distribution of the cloud can be mapped to the momentum distribution under two conditions : (a) the expansion time has to be long enough for the cloud to enter the Far-Field Regime (FFR), equivalent to the Fraunhofer diffraction in optics [23, 22, 24], and (b) the interactions between the particles have to be negligible during the expansion, to avoid distortions of the distribution.

Long time of flight and electronic detection, a new approach to investigate many-body systems

ToF imaging has been widely used with optical probes to measure the momentum distribution of lattice gases [25, 26, 16, 17, 27], but the short expansion time allowed by standard absorption imaging were proven insufficient to enter the FFR [23, 22, 24], where the mapping between the positions and the momenta is accurate. Indeed, with realistic experimental parameters, the FFR is reached in several hundred of milliseconds, making the cloud too diluted for absorption imaging. The aim of the Lattice Gases experiment at Institut d'Optique is to circumvent the limitations of standard imaging, by probing lattice clouds by electronic means. Directed by David Clément of the Optique Atomique group, this team started its activity in 2011 with the building of a new Helium machine. At the beginning of 2015, they obtained their first Bose-Einstein condensates of metastable Helium He*, and I joined the effort shortly after, first as an intern, and later as a PhD student. My first task was to help installing and developing the Micro Channel Plates (MCP) detector, that probes the He* cloud after a long ToF of 325ms. He* possesses an internal energy of 20eV, high enough to extract an electron from a metallic surface. This one-electron signal is then amplified by the MCP, and turned into a detectable electronic shower. The use of a delay-line anode at the output of the amplification allows to reconstruct the 3D positions of millions of individual particles per second.

This detection scheme has two main advantages : its efficiency at very low densities, allowing measurements in the FFR, and its single-atom sensitivity. Put together, those assets constitute a way to probe the momentum of individual particles if one manage to suppress the interactions during the expansion. This is made possible by optical lattices, as we shall discuss in this thesis. The ToF properties of the 3D lattice are indeed essential to our approach : after turning off the trap, the initial expansion is driven by the ground state energy of the single-site trapping potential, much bigger than the interaction energy in general. Hence, under certain conditions [23, 28], the interactions during the ToF can be neglected, giving access to the in-situ momentum distribution in the FFR. Demonstrating this last assertion was the main goal of this work.

This manuscript

The manuscript is organized in five chapters. In the first chapter, we describe the experimental apparatus, its different cooling stages and the detection process, with an emphasis on the MCP detector operation and performances. The second chapter extends the first one, and describes the "software" part of the detection process by detailing the methods used to reconstruct the 3D positions of the detected particles. We also present an algorithm computing second order correlation functions from the 3D distribution, and we test it on different systems (Bose-Einstein condensate, lattice gas, thermal distribution).

The third chapter deals with the measurement of the asymptotic momentum distribution of a Bose-Einstein condensate released from an harmonic trap, and the observation of k^{-4} decaying structures in the tail of the distribution. This decay is not captured by mean-field theory, and its interpretation is discussed.

The last two chapters are dedicated to the 3D lattice gas. In chapter four, we demonstrate the access to the FFR of expansion, and the mapping between the atomic position and momentum is established by comparison with numerical Quantum Monte-Carlo (QMC) simulations, the temperature being the sole adjustable parameter. Finally, in chapter five, we exploit our ability to probe the momentum distribution to build a precise thermometry method, which allows us to

explore the superfluid to normal-gas transition. We use the single-particle, 3D distribution of the gas to measure the condensed fraction and the second-order correlations across the transition.

Chapter 1

Description of the experimental apparatus

In order to obtain a quantum degenerate gas, we need to raise both n and λ_{dB} to reach quantum degeneracy. This is done through a series of cooling (lowering T) and compression (raising n) techniques, including but not limited to : cryogeny, laser cooling, evaporative cooling, magnetic trapping, optical trapping, etc. Those techniques, as well as the equally important detection techniques, are performed under vacuum, within the experimental apparatus that constitutes a cold atom experiment.

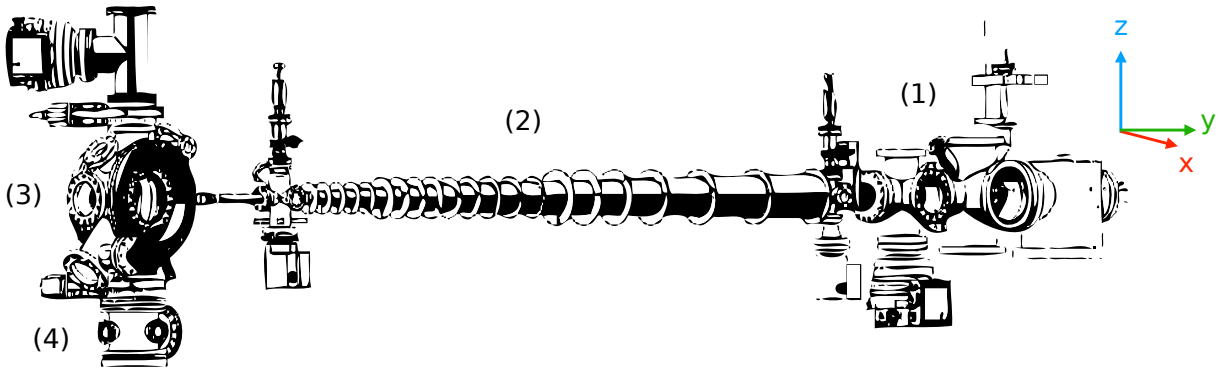

Figure 1.1: Sketch of the vacuum system. From right to left : (1) source chamber, (2) Zeeman slower, (3) science chamber, (4) MCP chamber.

This chapter presents our experiment, working with quantum gases of metastable Helium. In this peculiar high energetic state, Helium-4 can be detected electronically at the single-atom level, which constitutes the heart of our approach to perform original measurements on many-body quantum systems. The chapter is divided in two sections. The first section focuses on the cooling and trapping steps of the experimental cycle. Most of these steps have already been described in previous thesis (see [29] for a full description of the source and the Doppler cooling, and [30] to learn more about the sub-Doppler stage and the hybrid trap). In this manuscript, we briefly recall the physical principles behind these techniques, and report the current performances obtained in terms of atom number and temperature. An important part of this thesis has been dedicated to the installation, the development, and the characterization of the Micro-Channel Plate (MCP) electronic detector. The second section gives a detailed description of the full detection chain,

from the MCP itself to the electronics that transform the signal into computable data.

1.1 Cooling, trapping and condensation of metastable Helium 4

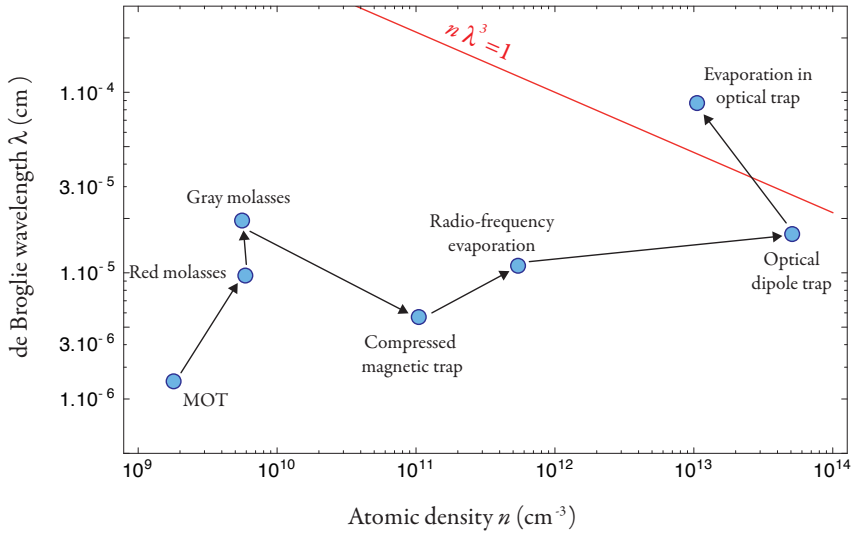

Figure 1.2: Phase-space density path along the different cooling and trapping stages.

We start from a pure gas of ground state bosonic Helium-4 (^{4}He) at room temperature. A DC discharge transfer a fraction of the atoms in the metastable state, and we laser-cool the gas down to Doppler and sub-Doppler temperatures, leading to an increase of λ_{dB} and n. The cloud is then spin-polarized and loaded inside a magnetic quadrupole trap, that is adiabatically compressed in order to raise furthermore the density. After a Radio-Frequency (RF) evaporation stage, we transfer the gas from the magnetic trap into a crossed optical dipole trap, where we obtain a Bose-Einstein Condensate (BEC) with a second stage of evaporative cooling. This elementary sample can then be transferred into an optical lattice by adiabatically decreasing the dipole trap amplitude while ramping the lattice laser power. The overall cooling and trapping sequence takes less than 10s, ultimately limited by the evaporative cooling stages. In spite of this, the sequence is rather short compared to similar experiments, which is very important for a setup aiming at measuring the 3D distribution of very diluted cloud over thousands of experimental runs.

Before going into details, let us define the referential (x, y, z) of the apparatus. The gravity axis is taken as the z-axis, which points towards the roof of the lab. The Zeeman slower defines the y-axis, which is directed from the science chamber to the source chamber (opposite to the atomic jet, see figure 1.1). Finally, the x-axis completes the orthogonal basis.

1.1.1 Production of metastable Helium and laser-cooling stages

Metastable Helium

The first excited state of Helium, 2^3S, is special for many reasons :

- First of all, it has a long lifetime, which is the reason why it is called "metastable". Usually, radiative decay limits the lifetime of excited states to the order of the nanosecond, while

the metastable Helium state, noted He*, has a lifetime of 8000s, exceeding by far the 10s duration of our experimental cycle. It is actually the atomic state with the longest lifetime known today [31].

- Helium is a noble gas, meaning that its ground state 1^1S_0 is extremely stable, and one needs to furnish a lot of energy to excite it. For this reason, the metastable state is 20eV above the ground state. With this high internal energy, He* can extract an electron from a metallic surface, which gives the possibility to detect it by electronic means.

- Finally, He* is close to optical transitions, since $2^3S \rightarrow 2^3P$ can be addressed with a 1083nm laser, yielding the possibility to laser cool He*. The first BEC of bosonic ^{4}He* was obtained simultaneously at Institut d'Optique and LKB in 2001 [32, 33], while the first degenerate Fermi gas of ^{3}He* was obtained at the Amsterdam LaserLab in 2006 [34].

The main difficulty with the cooling of He* arises from the Penning losses [35], which is an inelastic collision process where two metastable atoms are lost by redistributing their internal energy. The reaction is :

$$\mathrm{He}^* + \mathrm{He}^* \rightarrow \mathrm{He} + \mathrm{He}^+ + \mathrm{e}^-. \tag{1.1}$$

In particular, Penning collisions strongly limit the atomic density during the molasses phases, since they are enhanced by the presence of light (light-assisted Penning collisions [36]) and the presence of spin mixtures [37]. To circumvent those effects, the usual technique is to work with a spin-polarized gas in a magnetic trap [32, 38, 39, 40] to cross the Bose-Einstein condensation transition. Our approach is slightly different, as we use a hybrid magnetic/optical trap to enhance the stability and the rapidity of the cooling cycle [41] (see section 1.1.2).

The source

The first step is to transfer a fraction of the bosonic ^{4}He atoms coming from a pressurized bottle into the metastable 2^3S_1 state. The 20eV energy difference between the ground state 1^1S_0 and 2^3S_1 prevents us from addressing the transition optically. Instead, we excite the gas through a plasma discharge [42].

The plasma is generated in a DC discharge between a needle brought to high voltage (typically -3kV) and a grounded skimmer, which makes the junction between the source chamber and the molasses chamber, where the atomic beam is optically filtered and collimated. A sketch of the source is shown in figure 1.3 (a). The needle is inserted in a glass tube, inside which the Helium flows. The glass tube is glued to a Boron-Nitride (BN) cylinder, pierced with a small hole to let the plasma jet goes through. The BN is itself inlaid inside a copper piece, which is cooled down by liquid nitrogen, allowing the plasma to be cold enough, so the metastable atoms can be efficiently captured by the transverse molasses and the Zeeman's slower beam. As for the BN, it is a ceramic with the good thermal and electrical properties to ensure both the cryogeny of the plasma and the electrical insulation between the needle and the grounded copper.

During this thesis, we have used two materials for the needle : aluminum and tungsten. The latter gave bad results, since it was ejecting black metallic dust during the discharge, which were obstructing the BN hole. The aluminum needle, on the other hand, does not seem to eject matter the same way, but still consume itself over time, probably because of oxidation. When the plasma operates every day, the needle has a typical lifetime of several months, and has to be replaced periodically. Figure 1.3 (c) is a picture of a consumed needle, too damaged to allow the plasma to work, and a brand new needle, ready to replace it.

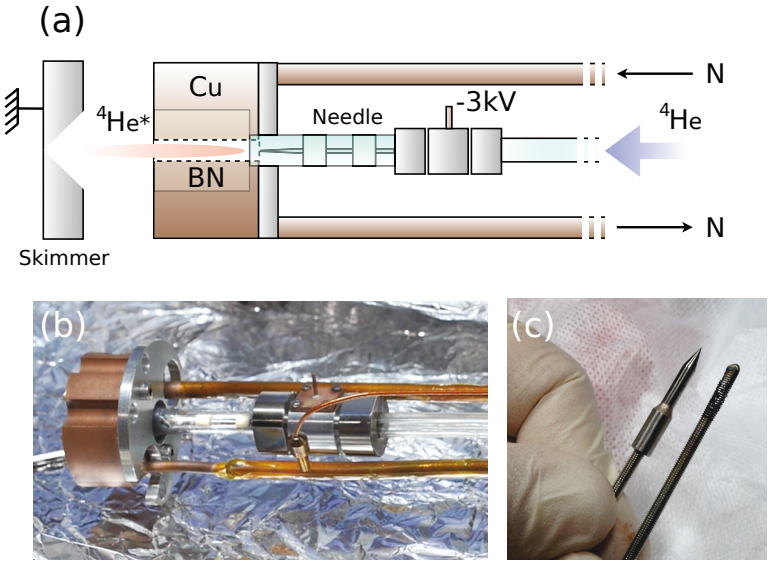

Figure 1.3: The source system. (a) From right to left : ^{4}He flows through a plastic pipe before entering a glass tube, where a DC discharge between a needle at -3kV and a grounded skimmer produces a Helium plasma containing some metastable atoms ^{4}He*. The plasma is cooled down to $\sim$ 200K by liquid nitrogen, circulating inside a copper piece. (b) Photograph of the piece, ready to be put back under vacuum. (c) New aluminum needle (left), that will replace the consumed one (right).

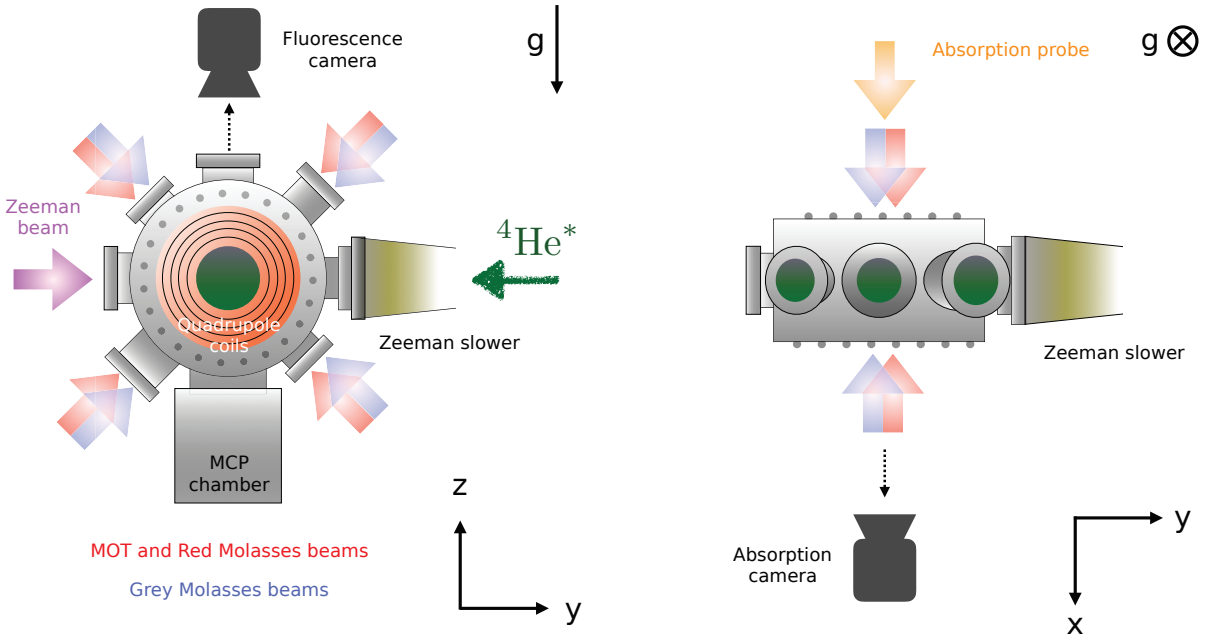

Figure 1.4: Scheme of some beams trajectories around the science chamber, used in the MOT loading and molasses cooling stages. We have also represented the position of the two cameras used for the absorption and fluorescence imaging, as well as the direction of the absorption probe beam. We use the MOT beams on resonance for the fluorescence probe.

The pressure in the source chamber is set by the flux of Helium, controlled with a valve at the output of the pressurized bottle. We typically work at 10^{-5}mBar. The ratio between this pressure and the pressure inside the transverse molasses chamber (after the skimmer) can vary with the different configurations of distances needle/BN, and needle/skimmer since it changes the shape of the atomic jet. This ratio is usually between 50 and 10, so that the pressure in the molasses chamber is between 2×10^{-7}mBar and 10^{-6}mBar. The current of the plasma is typically 10mA (with small fluctuations over time) for -3kV applied between the needle and the skimmer. The rate of production of metastable atoms is very low : one is created every 10^4 atoms.

Laser cooling and fluorescence imaging

There exists two main classes of laser-cooling mechanisms : Doppler cooling, and sub-Doppler cooling. The first one is based on momentum exchanges between a two-level atom and a near-resonant light. The second class actually contains various techniques based on the multi-level spectra of "real-life" atomic species. It allows to reach much lower temperatures than the Doppler cooling, but the associated capture velocity being small, it requires the presence of some Doppler mechanisms as well. Both types of mechanisms are implemented on the experiment, and will be briefly discussed. A more detailed introduction to the laser cooling theories can be found here [8].

We use two different lasers to cool down, image, and optically pump the atoms. Both lasers operate close to 1083nm in order to couple the metastable state 2^3S_1 to one of the 2^3P states, of natural line-width $\Gamma = 2\pi \times 1.6$MHz. The transverse molasses, Zeeman slower, Doppler-cooling,

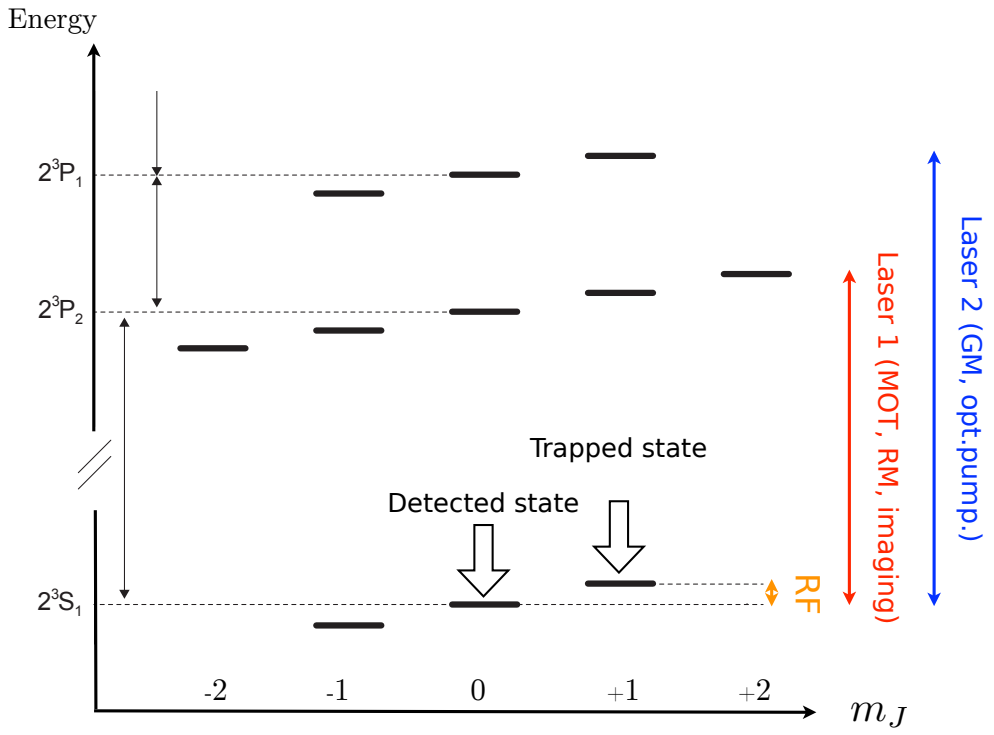

Figure 1.5: ^{4}He atomic levels used for the laser cooling. The MOT and red molasses stage are realized with the $2^3S_1 \rightarrow 2^3P_2$ transition, and the grey molasses are performed with a blue detuned light working on the $2^3S_1 \rightarrow 2^3P_1$ transition. The atoms are optically pumped in the $m_J = +1$ state for the quadrupole and optical trap phases. To get rid of stray magnetic fields during the time of flight, and to control the flux of particle reaching the MCP detector, a fraction of the expanded cloud is transferred into the non-magnetic state, $m_J = 0$, with a RF pulse at the beginning of the expansion.

and imaging light are derived from a mono-mode fibered laser from NKT Photonics and amplified via an Ytterbium doped fibered amplifier from Keopsys. The output light has a power of 2W, a bandwidth of 50kHz, addressing the $2^3S_1 \rightarrow 2^3P_2$ transition. The second laser, used both for sub-Doppler cooling and spin polarization of the gas, is a homemade cavity diode, amplified with an Ytterbium Manlight amplifier. It delivers a power of 500mW, with a linewidth of $\sim$ 5MHz, and it works on the $2^3S_1 \rightarrow 2^3P_1$ transition. Both lasers are locked in frequency to a saturated absorption spectroscopy signal, obtained through a Helium cell. A fraction of the atoms inside the cell is transferred to the metastable state thanks a high voltage circuit generating a plasma [43].

The Zeeman slower After the source, the metastable atoms are separated from the rest of the gas and collimated by transverse molasses light. The jet then enters a Zeeman slower with an average velocity of 1.2km.s^{-1}. The Zeeman slower was first demonstrated by W. D. Phillips in 1982 [44], who used it to slow down an atomic jet of Sodium. Nowadays, it is the first cooling step of many cold atoms experiments. It is made of a tube, with vacuum in the inner part, where the atomic vapor propagates, and a coil wrapped around the outer part.

The principle is to shine a resonant beam onto the atomic jet flowing inside the tube, with a wave vector opposite to the velocity of the cloud, to slow it down by radiative pressure. This mechanism is based on the absorption by an atom of a photon from the laser mode $\vec{k}_{ab}$, followed by a spontaneous emission in a random mode $\vec{k}_{sp}$, so that the momentum exchanged between the atom and the light is :

$$\Delta\vec{p} = \hbar\vec{k}_{ab} + \hbar\vec{k}_{sp}. \tag{1.2}$$

By energy conservation, we have $||\vec{k}_{ab}|| = ||\vec{k}_{sp}||$, but $\vec{k}_{ab}$ is always pointing along the laser, while $\vec{k}_{sp}$ has a random direction, with an isotropic probability distribution. Hence, $\langle\hbar\vec{k}_{sp}\rangle = \vec{0}$, and the average momentum exchange is :

$$\langle\Delta\vec{p}\rangle = \langle\hbar\vec{k}_{ab}\rangle + \langle\hbar\vec{k}_{sp}\rangle = \hbar\vec{k}_{ab}. \tag{1.3}$$

Since the atom movement is opposed to $\vec{k}_{ab}$, a large number of absorption/spontaneous emission cycles reduces its velocity. This process is efficient only if the atom remains resonant with the light while its velocity decays, which is made difficult because of the Doppler shift. The idea of the Zeeman slower is to compensate the Doppler shift with a Zeeman effect: the coil around the outer part is wrapped in such a way that the magnetic field applied inside the tube follows the velocity decay. The light mass of Helium implies the use of a long Zeeman slower of two meters, at the end of which the velocity of our gas is reduced to 50m.s^{-1}. This is slow enough to be trapped by the 3D Magneto-Optical Trap (MOT) inside the science chamber.

Magneto-Optical trap In order to reach the quantum degeneracy, cooling the gas is not enough and confining potentials are also needed to raise the atomic density. The first techniques demonstrating the possibility to trap neutral atoms emerged in the mid 80s, and were using the spin [45] or the electric dipole [46] of the atoms to confine them in the local minima of a magnetic or an optical trap. As we shall see, the MOT, first obtained by S. Chu at Bell's lab in 1987 [47], is based on a more subtle effect, allowing the radiative pressure to trap and cool the atoms in the same time.

A 3D MOT is made of 3 pairs of red-detuned counter-propagating beams, crossing along the three direction of space, and a magnetic quadruple whose center coincides with the crossing

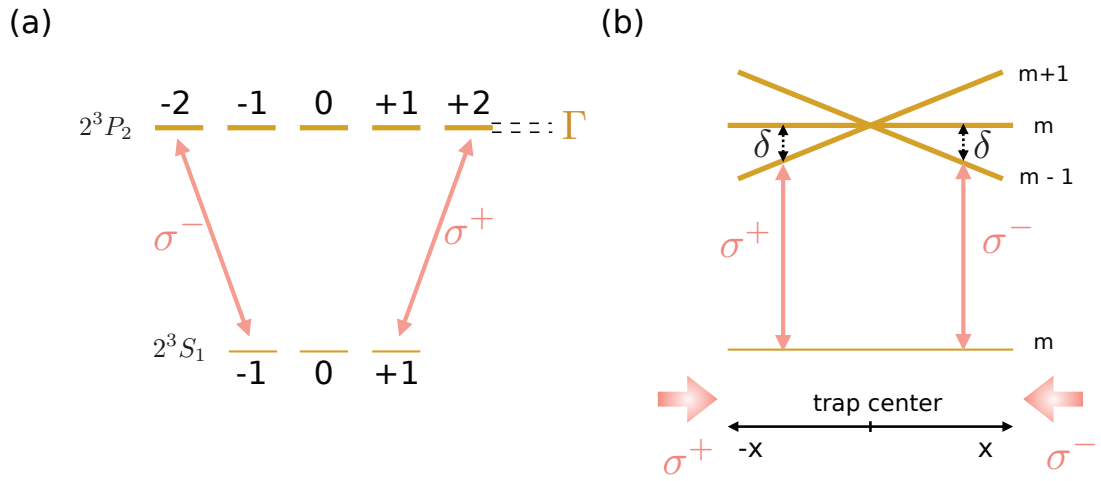

Figure 1.6: Scheme of the Magneto Optical Trap principle. (a) Relevant sub-level of the $2^3S_1 \rightarrow 2^3P_2$ transition addressed by counter propagating red-detuned beams with circular polarization. (b) One dimensional version of the trapping mechanism of the MOT. A magnetic gradient linearly shifts the hyperfine energy levels, so that an atom moving away from the trap center sees a resonant light, and is pushed back by radiative pressure. This constitutes a trapping effect, in addition to the Doppler cooling mechanism.

point of the beams. An atom at the center of the cloud with zero velocity is weakly affected by the off-resonant light. But if it acquires a velocity and moves away from the center, two things happen. On the one hand, the Zeeman shift due to the local magnetic gradient brings the atom on resonance, and the radiative pressure pushes it back, which constitutes a trapping mechanism (see figure 1.6). On the other hand, the Doppler effect also brings the atom closer to resonance along the beam whose wave vector is opposed to the velocity, leading to a momentum exchange with the light, and ultimately, to a decay of the atom velocity along that direction. This is a rough description of the Doppler cooling mechanism. It is indeed a cooling technique, since the atoms with a non-zero velocity are more submitted to the radiative force.

In practice, the beams of our MOT are red-detuned by $\delta = -37\,\Gamma$ with a total intensity of $50\,\mathrm{I}_{sat}$, with $\mathrm{I}_{sat} = 0.16\mathrm{mW.cm}^{-2}$. The quadrupole is produced by a pair of coils centered on the x-axis, and working in anti-Helmoltz configuration. The resulting magnetic gradient at the center of the trap is about $25\mathrm{G.cm}^{-1}$. A large detuning to load the MOT has two main advantages : (a) it ensures a large volume of capture, which makes the loading of the trap more efficient, and (b) it limits the losses due to light-assisted penning collisions, which depend both on density and detuning [36, 35]. After 1s of loading, the temperature of the cloud is typically 1mK, with 2×10^9 atoms loaded inside. We then compress the cloud to raise the density, by changing the detuning to $-7.5\,\Gamma$ in 30ms while reducing the power to $0.28\,\mathrm{I}_{sat}$ to keep the rate of light-assisted penning collision low.

Red molasses The magnetic field of the MOT is then switched off, and the detuning is reduced, so that the Doppler cooling becomes the main mechanism of the light-atom interaction. The resulting cold vapor is what we call an optical molasses. Red-detuned molasses were historically obtained before the MOT [48], which can be seen as a trapped molasses. The Doppler theory of laser cooling predicts a minimum temperature achievable, known as the Doppler limit [8] : for

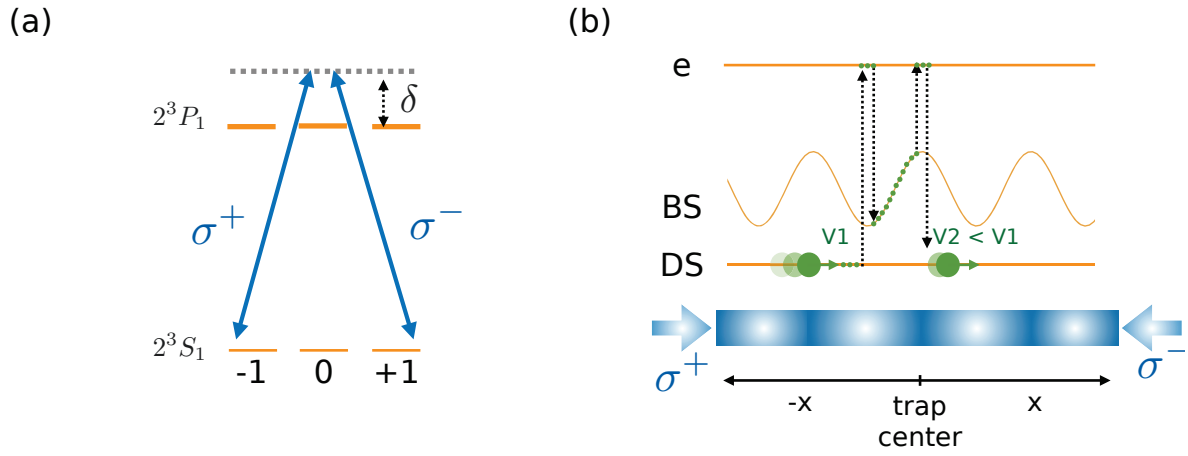

Figure 1.7: Scheme of the grey molasses principle. (a) Lambda structure obtained from the $2^3S_1 \rightarrow 2^3P_1$ transition addressed by counter propagating blue-detuned beams with circular polarization. (b) One dimensional version of the grey molasses cooling mechanism, where a lattice potential is formed by the contra-propagating beams interference. An atom in the dark state with a velocity v_1 can couple to the bright state, preferentially in the "valley" of the lattice potential. It then reduces its velocity by "climbing a hill" of potential, before being preferentially transferred back to the dark state from the "top of the hill". His final velocity v_2 is smaller that v_1, so that its coupling to the bright state is reduced.

a small saturation parameter (low laser intensity), and a detuning of $\delta = \Gamma/2$, one can reach $T_D = \hbar\Gamma/2k_B$. For ^{4}He*, $T_D = 38.4\mu$K, a temperature we have experimentally demonstrated [49]. The downside is that the constraint on the low laser intensity ($I \ll I_{sat}$) leads to an important loss in atom number, which dramatically decreases the density. Hence, we choose different parameters ($0.28\,I_{sat}$, ramping the detuning from $-9\,\Gamma$ to $-1.25\,\Gamma$) to obtain a cloud of 2×10^9 atoms at 80μK in 5ms. The temperature, although not minimal, is low enough to proceed with sub-Doppler cooling.

Sub-Doppler cooling in grey molasses The first molasses in the 80s were actually much colder than the temperature expected from the Doppler limit [18, 50]. Those red-detuned molasses, obtained with alkali-metal atoms, are characterized by a complex multilevel ground state, giving birth to a new class of mechanism, today known as sub-Doppler cooling [51]. Interestingly, in red molasses of ^{4}He*, those process are highly inefficient since their capture velocity is below the recoil velocity [49]. It is however possible to reach sub-Doppler temperatures by working with the so-called "grey" molasses.

The grey molasses were first investigated in the 90s with Cesium [52, 53, 54], and have recently came back in fashion, with the good cooling performances obtained with Lithium and Potassium [55, 56, 57], opening the way to all-optical cooling schemes. It is a sub-Doppler technique based on a lambda configuration (two ground states $|g_1\rangle$ and $|g_2\rangle$, and one excited state $|e\rangle$). In such systems, one can create a quantum superposition of $|g_1\rangle$ and $|g_2\rangle$ to obtain a Dark State $|\mathrm{DS}\rangle$, i.e. a state uncoupled to the light, which is loaded inside a blue detuned lattice. The orthogonal state to $|\mathrm{DS}\rangle$ is the Bright State $|\mathrm{BS}\rangle$, which is coupled to the light, so that its energy is modulated by the lattice intensity because of the dipolar force (see section 1.1.2).

If the velocity of the atom is zero, then $|DS\rangle$ is an Eigen-vector of the Hamiltonian, meaning that an atom in $|DS\rangle$ remains in this state. On the other hand, for an atom with a non-zero velocity, there is a coupling between $|DS\rangle$ and $|BS\rangle$, which is maximum in the minima of the potential, and thus the atom will be more probably transferred to $|BS\rangle$ in the "valley" of the optical lattice. On the opposite, the probability to go back in $|DS\rangle$, through a transfer to $|e\rangle$, is higher in the maximum of the potential. The atom then falls back into $|DS\rangle$ with a reduced velocity because it "climbed a hill" of potential (see figure 1.7 (b)). This velocity reduction makes another coupling to $|BS\rangle$ less likely, leading to an accumulation of atoms in $|DS\rangle$.

We use circularly polarized beams, together with the $2^3S_1 \rightarrow 2^3P_1$ transition to create the lambda structure (the $0 \rightarrow 0$ transition being forbidden), like shown in figure 1.7 (a). The frequency is blue detuned by $\delta = +10\,\Gamma$, and the power is set to $28\,I_{sat}$. After 5ms, the cloud is composed of about 1.5 to 2×10^9 atoms at $\sim 20\mu$K.

Fluorescence imaging Both the temperature and the atom number are evaluated by analyzing the time of flight profiles of the atomic distribution. Indeed, once released from its trap, the cloud falls freely and converts its thermal energy into kinetic energy along the direction i via the relation $mv_i^2 = k_BT$. To obtain those profiles, we shine a resonant light onto the atoms through the MOT fibers, and we measure the fluorescence of the sample with an InGaAs camera whose optical axis is along the z-axis (gravity). The InGaAs is well adapted to detect the 1083nm infra-red light (80% quantum efficiency), but this technology is limited in terms of pixel matrix compared to the CCD camera (256×320 pixels of $30\mu m^2$ in our case). We estimate the resolution in the image plane to be 125μm. On figure 1.8 we present a typical set of fluorescence images of a grey molasses cloud, expanding during the time of flight.

1.1.2 Evaporative cooling and Bose-Einstein condensation

An apparatus aiming at measuring 3D distributions and two-body correlations must have a short experimental sequence and a good stability over a large number of cycles. Good performances, both in terms of rapidity and stability, have been demonstrated with ^{87}Rb in a hybrid scheme combining a magnetic quadrupole trap and a red-detuned optical dipole trap [58]. Magnetic traps ensure a large capture volume, and they are used in other ^{4}He experiments as the final trap to reach Bose-Einstein condensation [32, 38, 39, 40]. The lifetime in a quadrupole trap is severely restricted by Majorana losses occurring at the center, where the magnetic field is zero [59]. To prevent this effect, one has to use a so called "clover leaf" field, which removes the local zero of the field, but increases the instability of the trap since this configuration is very sensitive to small current fluctuations. In that regard, a hybrid approach where Bose-Einstein condensation is reached in the dipole trap has two main advantages : it does not require a "clover leaf" structure (better stability) and it benefits from the rapid evaporation offered by optical trap (shorter cycle).

Magnetic trap

The first step before loading the quadrupole trap is to spin polarize the gas in the $m_J = +1$ state with optical pumping. To do so, we generate a magnetic bias along the gravity (z-axis) with a pair of coils in Helmoltz configuration, in order to define a quantization axis. We then shine a σ^+ beam on the $2^3S_1 \rightarrow 2^3P_1$ transition to pump the atoms in the $m_J = +1$ state of 2^3S_1. We apply the magnetic quadrupole, using the same anti-Helmoltz coils than for the MOT stage, with an initial gradient of ~ 5 G.cm^{-1}. The energy of the $m_J = +1$ state follows the magnetic field variations because of the Zeeman effect, resulting in a trapping potential :

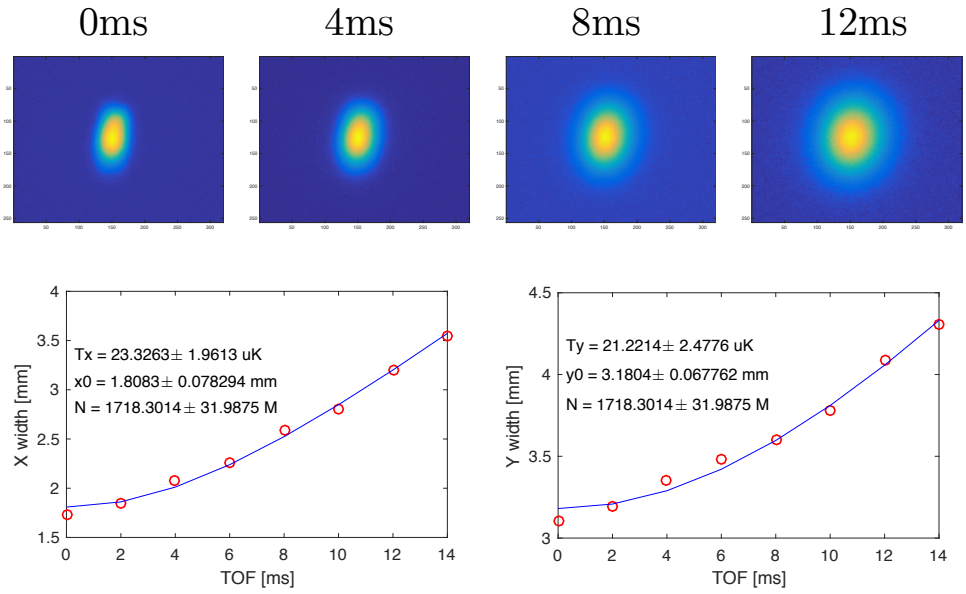

Figure 1.8: Florescence imaging of expanding grey molasses clouds, at different times of flight. The atom number can be calculated by measuring the amount of emitted light, and the temperature can be extracted from the evolution of the cloud size during expansion.

$$V_M(x,y,z) = g\mu_b B\sqrt{x^2 + \frac{y^2}{4} + \frac{z^2}{4}}, \tag{1.4}$$

with g the Landé factor, μ_B the Bohr magneton and B the amplitude of the field. The Penning collision rate in a spin polarized gas is 4 orders of magnitudes lower than for an unpolarized ensemble [60], so n is not strongly limited by the inelastic collisions anymore. We thus compress the gas by squeezing the trap, ramping the gradient to 35 G.cm^{-1}, which increases the density by a factor of 5.

We can further improve the quantity $\lambda_{dB}^3 n$ by performing an evaporative cooling. The idea is to remove the most energetic atoms from the trap, and let the rest of the cloud thermalize at a lower temperature. Since the most energetic particles will tend to expand more in trap, they will experience a higher Zeeman shift between the hyperfine level of the 2^3S_1 state. So, by applying an RF field, we can couple atoms to the non-trapped sate ($m_J = 0$) or the anti-trapped state ($m_J = -1$) in a way which is selective in energy. The RF signal is generated by the computer, and amplified through a 70W Prana amplifier before being wired to an antenna that generates the field. In practice, we ramp the RF frequency between 40MHz and 4MHz in 3s (thermalization process takes time inside a quadrupole, because the atomic trajectories are very complex). We typically reach between 50×10^6 and 150×10^6 atoms at $\sim 70\mu$K, depending on the molasses stage, and the optimization of the RF transfer. 50×10^6 is the minimum to obtain a BEC, while 150×10^6 is a comfortable number to ensure stability.

Loading of the crossed trap and evaporative cooling

The Optical Dipole Trap (ODT) is composed of 2 far red-detuned beams at 1550nm, generated by an IPG Photonics fibered laser, and stabilized in intensity through PID circuits. The two beams are labelled ODT1 and ODT2, the first being recycled after the science chamber to obtain the second. They are respectively characterized by a waist of 133μm and 63μm, and a maximal power of 18W for ODT1. They cross in the (x,y) plane, with a 40° angle (see figure 1.11), and their frequencies are shifted by 40MHz in order to avoid light interference effects inside the trap. The trapping potential effect is created by a coupling between the electric field $\vec{E}$ and the atomic dipole moment $\vec{D} = \alpha\vec{E}$, where α is the polarizability of the atoms :

$$V_D(x,y,z) = -\frac{1}{2}\langle \vec{D}\vec{E} \rangle = -\frac{1}{2}Re(\alpha)I(x,y,z). \tag{1.5}$$

The potential is therefore proportional to the light intensity, and in the case of a red detuning, the atoms are attracted by the maxima of $I(x,y,z)$, so they tend to accumulate at the center of the crossed trap. In this situation, the gaussian shape of the beams generates a potential that may be approximated by a harmonic trap if the cloud is much smaller than the waist, which is the case for the BEC.

About 6×10^6 atoms are loaded from the quadrupole, by switching on ODT1 and ODT2 at full power during 500ms, while ramping down the magnetic field. Superimposing the center of the two traps will not maximize the loading, because of the Majorana losses [59] at the center of the quadrupole, and slightly offsetting the two centers gives better results [30]. This delicate setting can hopefully be fine-tuned with magnetic biases along the three directions of space, able to modify the position of the magnetic zero in a controllable way. The ODT is very narrow compared to the magnetic trap, and the simple fact of loading it increases the density by 2 orders of magnitude, while lowering the temperature by a factor of 2.

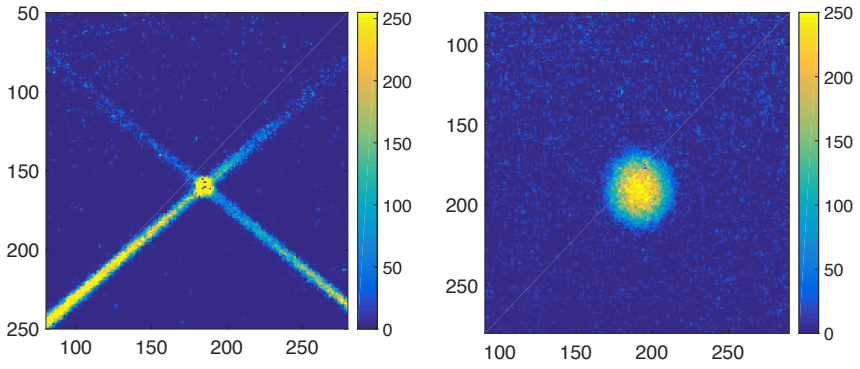

Figure 1.9: Example of absorption imaging pictures. Left : thermal cloud trapped in the ODT. Right : BEC after an expansion of 10ms. The axes are in unit of the camera pixel.

When the ODT is fully loaded, we ramp-down the power of the beams in 400ms to progressively open the trap, allowing the most energetic particles to escape, which constitutes a new evaporative sequence. We rapidly cross the Bose-Einstein condensation [41], ending up with typically 5×10^5 atoms (measured by absorption imaging, see the next paragraph) and a temperature of the order of the chemical potential (measured by the MCP, see chapter 3). The typical trapping frequencies we obtain at the end of the evaporation are $(\omega_x, \omega_y, \omega_z) \sim 2\pi \times (90, 420, 440)$ Hz. A brief theoretical description of the Bose-Einstein condensation phenomenon is done in chapter 3.

Absorption imaging

The resolution of the fluorescence imaging is too low to properly image the cloud loaded inside the ODT, or the expanding BEC. Hence, we use a second scheme, based on absorption imaging [61]. A probe beam with a weak intensity ($I_{sat}/5$) is partially absorbed by the atoms, and is imaged onto a second InGaAs camera. The density of the cloud is accessed with the quantity of absorbed light , while the size and shape of the expanding distribution is obtained with the cloud's shadow. Due to geometric constraint, the probe beam is not parallel to any axis on which we can produce a clean, uniform magnetic field. The polarization of the light (ideally σ^+) is thus not well defined on the atoms, and we reach the optimal imaging condition by switching off all magnetic bias.

The resolution in the image plane is 12μm, which is not enough to properly resolve the gas in situ (the Thomas-Fermi radius in the imaging plane is about 15μm) but is sufficient to resolve the condensate after a short time of flight. The atom number N is calibrated with a measure of the Thomas-Femi radius after an expansion time t, which in the limits of $t \gg \omega_{\mathrm{odt}}$ increases linearly in time, with a velocity scaling as $N^{1/5}$ [62]. This calibration is confirmed by a measurement of the condensation temperature, $T_c \propto N^{1/3}$ (see equation 3.5).

Lifetime of the condensate

We monitor the atom number in the condensate as a function of the holding time inside the crossed trap to measure its lifetime. The pressure in the science chamber being very low (less than 10^{-10}mBar) and the laser very far-detuned (about 500nm away from the resonance), the elastic collisions with the background and the photon scattering are not limiting compared to

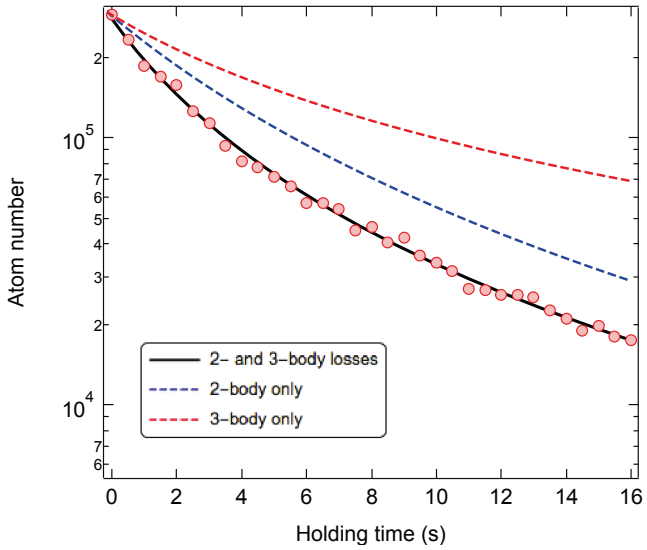

Figure 1.10: Atom number in the condensate (measured by absorption imaging) as a function of the holding time inside the optical dipole trap. The decay is well fitted by a 2-body and 3-body inelastic collision dynamic. The overall lifetime of the sample inside the trap is of the order of 5s.

2 and 3-body Penning losses. In this case, the time evolution of the atom number inside the condensate is driven by :

$$\frac{dN}{dt} = -k_2\langle n^2\rangle - k_3\langle n^3\rangle \tag{1.6}$$

where k_2 and k_3 are respectively the 2 and 3 body loss rate, and $\langle ...\rangle$ indicates an average of the density over the condensate profile, that can be solved analytically for the Thomas-Fermi regime [63].

Figure 1.10 shows a plot of the atom number in the condensate as a function of the holding time in the ODT. The curve is well fitted by the numerical solution of equation 1.6. The k_2 and k_3 coefficient are free parameters of the fit, and the obtained values $k_2 = 1.6 \times 10^{-14}$ cm^3.s^{-1} and $k_3 = 0.7 \times 10^{-27}$ cm^6.s^{-1} are compatible with those expected for a 1-1 spin polarized mixture, $k_2 = 2 \times 10^{-14}$ cm^3.s^{-1} and $k_3 \simeq 1 \times 10^{-27} cm^6.s^{-1}$ [37].

1.1.3 The 3D optical lattice

General description

Optical lattices were developed in the early 2000s, and have been intensively used in the cold atom community since then [10], finding applications in quantum information, or allowing to investigate condensed-matter problems with a new experimental perspective. An optical lattice is a periodic dipole trap, created by the interference of counter-propagating beams, which creates a crystal-like structure for neutral atoms. During the thesis, we have developed and installed a 3D optical lattice in our science chamber, leading to the first lattice gas of metastable Helium [64]. The potential resulting from the interferences of the three pairs of counter-propagating beams of wavelength λ_L can be written :

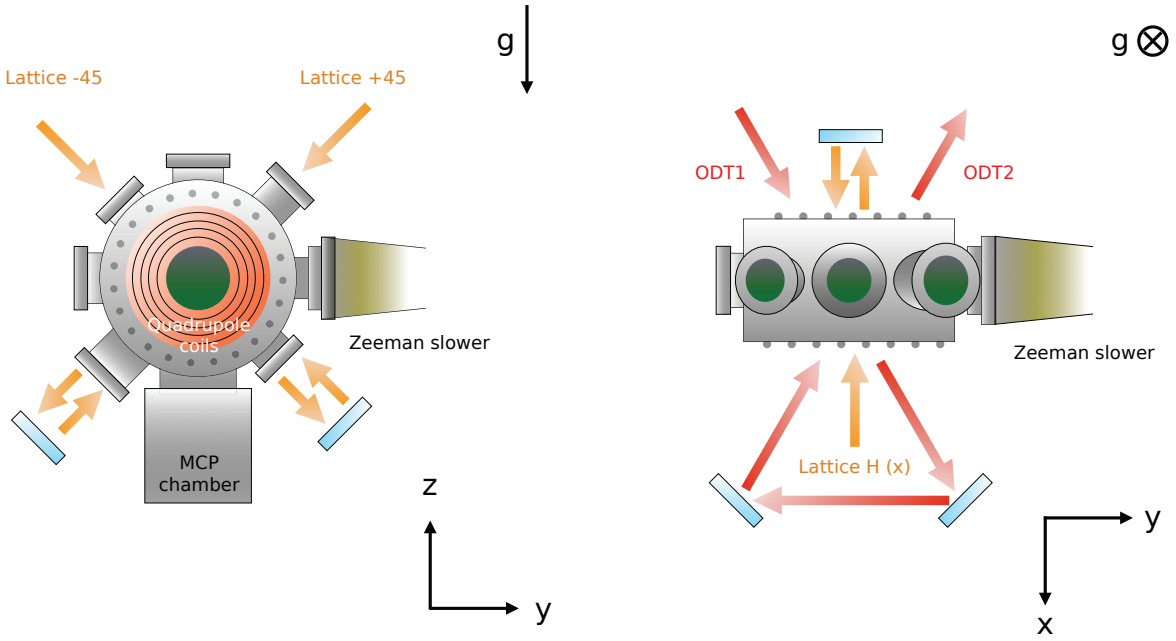

Figure 1.11: Scheme of the ODT and 3D lattice beams trajectories around the science chamber. The ODT is made of two beams, ODT1 and ODT2, which cross with a 40°angle. The lattice is made of 3 retro-reflected beams crossing orthogonally along the 3 directions of space. The interference between one beam and its retro-reflection creates a sinusoidal interference pattern.

$$V_L(x,u,v) = V_0\left(\sin^2\left(\frac{k_a}{2}x\right) + \sin^2\left(\frac{k_a}{2}u\right) + \sin^2\left(\frac{k_a}{2}v\right)\right) + V_{ext}(x,u,v). \tag{1.7}$$

For technical reasons, the Eigen-axis of the lattice are defined by the basis (x,u,v) which is obtained by a 45° rotation of the (x,y,z) basis around the x-axis (figure 1.11). The quantity $k_a = \frac{2\pi}{a}$ is the momentum scale associated to the lattice, and $a = \lambda_l/2$ is the lattice spacing. $V_{ext}(x,u,v)$ comes from the gaussian profile of the beams, and can be treated as being a 3D harmonic potential, the atoms being localized at the bottom of the trap. Consequently, the frequencies of this external potential depend on the beams' waists and power. Finally, the depth V_0 is proportional to the light intensity. It is a key quantity for the physics we want to investigate, and has to be calibrated as precisely as possible (see section 4.2.2).

Practical implementation

We use a mono-mode fibered laser from Keopsys operating at $\lambda_l = 1550$nm to generate the lattice potential. Its maximal output power is supposed to be around 15W (12W in practice, after one year of use). The main beam is split in 3 sub-beams which are shifted in frequency (70, -80 and +80MHz) before being brought onto the apparatus through 3 photonic-crystal fibers. The beams are focused at the center of the science chamber, and they cross orthogonally along the three directions of space. At the output of the science chamber, each beam is focused on a mirror and retro-reflected back in such way that the first passage and the reflection are superimposed. The resulting standing wave creates a sinusoidal intensity pattern with an external confinement, i.e. an optical lattice. The ultra-narrow linewidth of the laser (around 40kHz) is a crucial asset to ensure the coherence over the 1m of the full retro-reflexion path. The 3 beams are independently

stabilized in intensity to ensure a good control on the lattice depth and avoid heating due to intensity noise.

Two sizes of waist have been used during this thesis : the work described in chapter 4 and chapter 5 have been conducted with waists of $(223, 208, 204)\mu$m (uncertainty 10%). Being limited in laser power for technical reasons, we later decided to reduce the waists to $(141, 151, 155)\mu$m in order to reach the high lattice depth required to investigate interesting regimes, like Mott insulators or 1D systems. The loading of the cloud inside the lattice is done with adiabatic exponential ramps, while the ODT is switched off the same way. An adiabatic transfer will ensure that the atoms remain in the lowest energy mode of the trap, meaning the fundamental Bloch band of the lattice.

1.2 The Micro-Channel Plate detector

When transferred in the metastable state, Helium atoms can be detected individually by electronic methods, which constitute an amazing asset to study particle-particle correlations in a many-body quantum system. For this reason, the detection chain is one of the most important aspect of our experiment. MCP detectors are exotic creatures in a cold atom lab, but are widely used in many fields of high energy physics (particle accelerator [65], mass spectrometry [66], atomic physics [67], ...), and military technologies (night vision). When coupled to delay line anodes, this great tool can reconstruct the 3D distribution of millions of particles per second, if the read-out electronics (discriminator and digital convertor) are fast-enough. The main drawbacks are its low detection efficiency (about 25% for ^{4}He*) and the high resistivity of the micro-channels preventing a fast reloading of the charges and making the detector very sensitive to local flux saturation [68, 69, 70].

1.2.1 The plates

General description and characteristics

The plates are metal-coated thin discs, pierced by millions of tubes, generally of 10 to 30 micrometers diameter. When polarized, each of those micro-channels acts as a discharge amplifier, and when a metastable Helium atom (or a particle with sufficiently high internal energy) falls into one of them, it can extract a first electron, which in turn can extract secondary electrons and trigger an electronic cascade. The micro-channels are also tilted of a few degrees, so that it is impossible for a particle to fall through the plate without touching the wall of one channel. During this thesis, we have used 3 models of MCP, two from Hamamatsu (that we call MCP H1 and H2) and one from Burle industries (MCP B), all of them having a diameter of about 8cm. We actually use pairs of MCP, in a z-stack configuration (see figure 1.12) to increase the gain, which is of the order of 10^4 per plate. When mounted like this, one has to be very careful that the orientation of the micro-channels is reversed to ensure the continuity of the electronic shower.

The characteristics of the different plates we used are summarized in table 2.2. Part of the observations discussed in chapter 3 have been conducted with MCP H1. The measurement presented in chapter 4 and 5 were obtained with MCP B. Later, we were interested to test MCP H2 because of its high open area ratio (ratio between the surface covered by the micro-channels and the total surface of the plate), which should provide a higher quantum efficiency (see section 1.2.4).

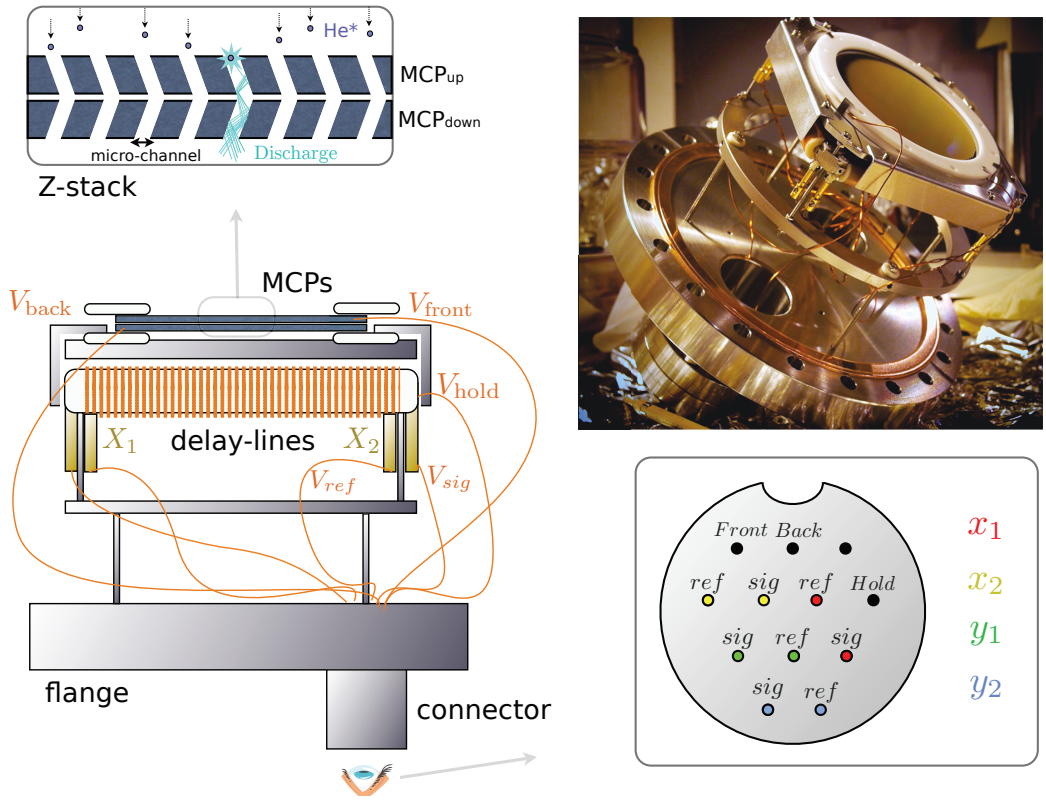

Figure 1.12: Sketch of the detector. From top to bottom : the pair of MCPs is mounted in Z-stack configuration, and is held by white ceramic pieces. A metastable atom falling on a micro-channel will trigger an electronic discharge that excites the 2 orthogonal delay lines braided beneath the stack. The wires coming from the flange are used both for supplying the different parts of the detector, and collecting the signal from the lines. We also draw the different connections, as they appear when looked from beneath the flange.

Table 1.1: MCP comparison

	Hamamatsu 1 (H1)	Burle (B)	Hamamatsu 2 (H2)
micro-channel diameter (μm)	~12	~25	~12
center to center spacing (μm)	< 15	~32	< 15
micro-channel angle (°)	20 ±1	8 ±1	20 ±1
open area ratio (%)	70	45	90
gain (@1.2 kV)	8.10^3	$> 10^4$	10^4
material	inconel	nichrome	inconel

Polarization

The total stack is typically polarized between -2kV and -2.4kV, with a homemade high voltage power supply. The difference of potential between the top and the bottom has to be negative, to accelerate the electrons towards the delay lines. The best option is to ground the top of the stack, and set the bottom of the stack to a positive voltage. The alternative option, which is to apply a negative voltage at the top of the stack can damage the MCP. Indeed, the MOT produces a large quantity of positive ions due to light-assisted Penning collisions, which are strongly attracted by the -2kV of the top MCP surface, 50cm below, resulting in a high velocity beam of He^+ rushing to the surface of the plate. This effect actually costs us our first pair of MCP (H1) ...

Degassing

Once put under vacuum, the plates tends to degas for a long time, because of particles accumulated inside the micro-channels during the manufacturing process [71]. The standard baking techniques were not very efficient in our case, since keeping the plates at 100°C for a few days was not enough to obtain the extremely low vacuum needed ($< 10^{-10}$mBar). We found the so called "burn-in" cleaning to be the most efficient method. It consists in continuously sending a homogenous flux of particles onto the MCP surface (He^* or UV photons in our case), while supplying the stack with higher and higher voltages. The repeated discharge of the micro-channel tends to empty them from their residual impurities.

1.2.2 The delay lines

Beneath the stack, two orthogonal Roentdek delay lines are braided around a holding board (at potential V_{hold}), one along the x direction, and the other one along the y direction. Each line is actually a waveguide, so that an electronic shower coming from the plate hitting the delay lines generates 4 pulses : 2 counter-propagating pulses along the line x, and 2 counter-propagating pulses along the line y, like shown in figure 1.13.

The pulses start from the impact point x_{imp} (y_{imp}), then move towards each extremity of the line, at position $-\frac{L_x}{2}$ and $\frac{L_x}{2}$, ($-\frac{L_y}{2}$ and $\frac{L_y}{2}$) . If one records the arrival times $(t_{x_1}, t_{x_2}, t_{y_1}, t_{y_2})$ of the pulses, the position of the impact in the plane is given by :

$$x_{imp} = \frac{1}{2}(t_{x_1} - t_{x_2})v_x \tag{1.8}$$

$$y_{imp} = \frac{1}{2}(t_{y_1} - t_{y_2})v_y, \tag{1.9}$$

where $v_{x/y}$ is the velocity of the pulse along the direction x/y. Note that in order to cover the full surface, the delay line coding for the x direction is wrapped in loops around the x axis, so that we have $L_x = L_{dl}/N_{loops}$ and $v_x = v_{dl}/N_{loops}$, where L_{dl} and v_{dl} respectively stand for the full length of the line, and the velocity of the pulses inside (the same goes for the y direction). With the measurement of the arrival times, one can also recover the impact time t_{imp} :

$$t_{imp} = t_{x_1} + t_{x_2} - \frac{L_x}{v_x} = t_{y_1} + t_{y_2} - \frac{L_y}{v_y}. \tag{1.10}$$

This last equation, providing that we know the velocity of the atom along gravity v_g, gives access to the vertical dimension $z = v_g \times t_{imp}$. So by precisely recording the times $(t_{x_1}, t_{x_2}, t_{y_1}, t_{y_2})$, of the pulses exiting the delay lines, we can reconstruct the 3D distribution of the particles reaching the plates. We also see the appearance of a new important quantity : $\frac{L_x}{v_x}$ (or $\frac{L_y}{v_y}$), which is the time it takes for a pulse to run through the entire delay line x (or y). In the following, we will

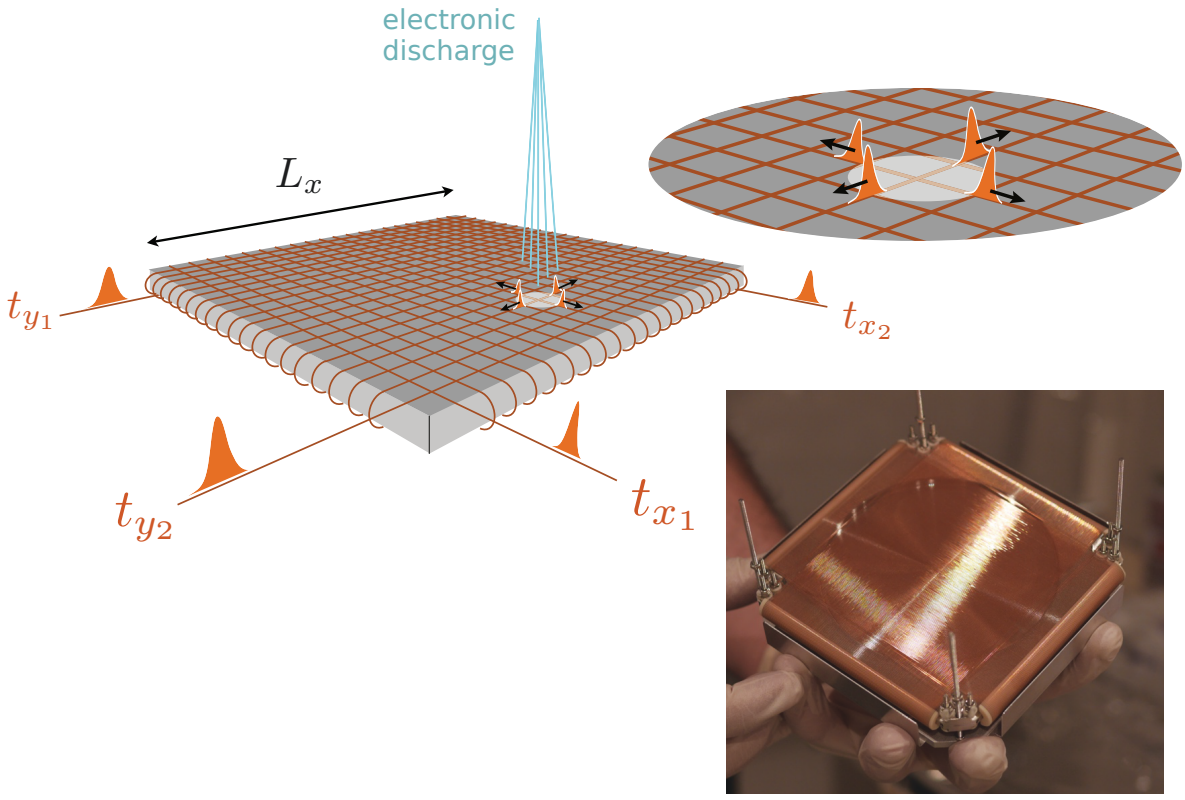

Figure 1.13: The 2 orthogonal delay lines (x and y) are looped around a holding board beneath the MCP. When the lines are excited by an electronic discharge, 2 pairs of counter propagating pulses (one for each line) are generated, and run throughout the lines of transverse length L_x and L_y. Recording the arrival time of the pulses at each extremity of the delay lines gives access the x and y coordinates of the impact point, as well as the impact time.

note $t_{dl} = \frac{L_x}{v_x} = \frac{L_y}{v_y}$, assuming that the delay lines along x and y are identical. In our case, $t_{dl} \simeq 100$ns.

To be a bit more precise, the waveguide of each line is composed of two wires, separated by half a millimeter : a reference wire (at potential V_{ref}) and a signal wire (at potential V_{sig}) The counter-propagating pulses are defined by a negative difference of potential between ref and sig (the amplitude strongly depends on the plates' polarization), and so the way the lines are supplied does play a role in the efficiency of the detection. We have set the voltages according to Roentdek recommendations for neutral particles [72] : if we note V_{back} to potential of the lower face of second MCP, then $V_{\text{back}} \leq V_{\text{hold}} \leq V_{\text{back}} + 250\text{V}$, $V_{\text{ref}} = V_{\text{back}} + 250\text{V}$ and $V_{\text{sig}} = V_{\text{back}} + 300\text{V}$. The other characteristics of the lines are also given by Roentdek :

- $v_{x/y} = 1 \times 10^6 \text{m.s}^{-1}$
- $N_{loops} = 100$
- $L_{dl} = 20\text{m}$
- $L_{x/y} = 10\text{cm}$

1.2.3 Electronic chain

The electronic chain is made of two parts (plus a pre-amplification stage) : a Constant Fraction Discriminator (CFD) and a Time to Digital Converter (TDC). The role of the discriminator is to convert the pulses from the delay line into a NIM signal (logical 0 -1V). The NIM signal has a sharp raising edge, and is then fed to the Time to Digital Converter in order to be transformed into an arrival time.

The Constant Fraction Discriminator

The discriminator is the key component of the detection chain, because the amount of precision at which it pinpoints the arrival time of the pulses will determine the spatial resolution of the detector. In practice the pulses exiting the lines do not have the same amplitude, because all the electronic discharges from the MCP do not couple to the line with the same efficiency. The main difficulty in that case, is to have a discrimination stage which is not sensitive to the amplitude of the pulses. A simple raising edge discriminator will trigger as soon as the signal cross a certain threshold, and so the time associated to the pulses will strongly depend on its amplitude : a high amplitude signal would be detected sooner that a low amplitude signal, even if their arrival times are identical. A CFD on the other hand, is sensitive to a fixed fraction of the raising pulse, and therefore corresponds to our needs.

The CFD directly operates at the output of the delay lines. Since there are two lines, each of them having two extremities, there is a total of 4 outputs to treat (x_1, x_2, y_1, y_2), each of them has its own discriminator than can be set independently. To illustrate the principle, let's consider one analog pulse A_{in} in one of the output. The pulse is pre-amplified with an adjustable gain, before being fed to the discriminator. It is then split into two identical analog pulses A_1 and A_2. A "bimodal pulse" A_b is then generated by the electronic operation

$$A_b(t) = A_1(t) - A_2(t - \tau) \times f_c, \tag{1.11}$$

where $f_c \in [0, 1]$ is the so-called constant fraction, and τ is a delay. The signal A_b has a zero-point crossing which is used as a reference time to trigger the NIM signal. Overall, we have tested two types of CFD, one from Surface-Concept and one from Roentdek. The latter is easier

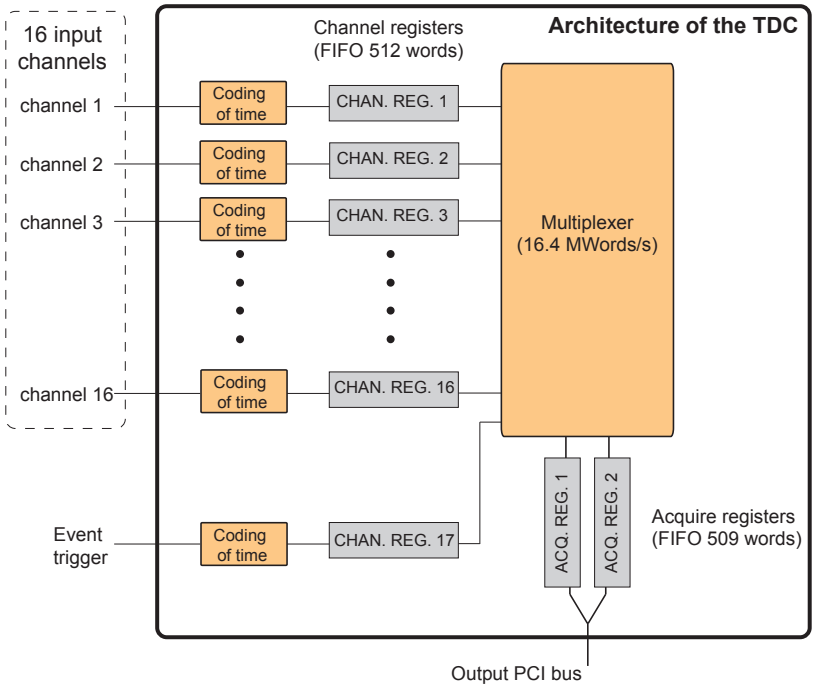

Figure 1.14: Sketch of the Time to Digital Converter architecture. The words coming from the 4 channels are stored into "Channel Registers" FIFO buffers, and are loaded into "Acquisition Registers" by a 16.4MHz multiplexer. The registers are then emptied through the PCI bus.

to program and gives us better results in terms of electronic noise. A detailed description of this CFD settings can be found in the appendix.

The Time to Digital Converter

We use a FPGA-based TDC developed by R. Sellem and D. Heurteau at the LUMAT (Orsay). The elementary coding step is $t_0 = 120ps$, and the resolution is measured at $0.52(2)t_0$ [73]. The arrival times are encoded into a 32bits word. The 26 first bits are the "small clock", and allow to continuously code time with step of t_0 over a cycle of $t_0 \times 2^{26} \simeq 8$ms. The small clock is then re-set to 0, and the value of the 27^{th} bit is flipped. One has to "keep track" of the value of this 27^{th} bit in order to count the numbers of digit flip N_{flip}. The total time of the "big clock" is then :

$$t = t_0 \times 2^{26} \times N_{\text{flip}} + \text{small clock}. \tag{1.12}$$

The last 4 bits are used to code the input channel. The TDC can work with up to 16 channels, but we will be using only 4 (x_1, x_2, y_1, y_2). After being converted, the words are stored into FIFO buffers called channel registers before being distributed into two acquisition registers by a multiplexer working at 16.4MHz, limiting the maximum flux per channel to 16.4 / 4 = 4.1MHz. The acquisition registers are then emptied inside the computer RAM via the PCI bus. All the registers (channel and acquisition) have a maximum capacity of 509 words. Figure 1.14 is a scheme of the overall architecture.

1.2.4 Performances of the detector

Quantum efficiency

The quantum efficiency is one of the main draw-back of the MCP when used with He*, especially when one looks for N-body correlations. It has been measured to be 9% by [74], and $25\% \pm 15\%$ in [75]. This value is related to the surface coverage of the micro-channels (typically 50%), and to the probability of exciting an electronic shower.

To evaluate the quantum efficiency of our detector, we compare the atom number of a cloud detected by absorption, with the atom number of the same cloud detected onto the plate. This measurement, conceptually rather simple, raises many technical difficulties. First of all, there are not many suitable clouds on which we can perform the comparison. It has to be cold enough to fall entirely onto the MCP, characterized by a radius $R_{\mathrm{MCP}} = 4$cm situated 50cm below the science chamber. For the center of mass of the cloud, this leads to a time of flight of about $t_{\mathrm{tof}} = 300$ms. So if we note σ_v the RMS of the cloud's velocity distribution (assuming spherical symmetry), we need to have :

$$\sigma_v \times t_{\mathrm{tof}} < R_{\mathrm{MCP}} \Rightarrow T < \frac{mR^2}{k_B t_{\mathrm{tof}}^2}. \tag{1.13}$$

With Helium's light mass, we obtain $T < 8\mu$K. The only clouds cold enough to reach this condition are the ones we can produce in the ODT during the final evaporation stage. At this stage, we have only a few million atoms left, so the only way to properly detect them by absorption imaging is to reach a high optical density, i.e. to Bose-condense the gas. That raises an other issue : the local saturation of the MCP. Empirically, the condensates are so dense that they make the plates saturate as soon as there are more than a few hundred atoms inside. On the other hand, the absorption imaging can not accurately image condensates with less than a few thousand of atoms. To solve this issue, we use a RF Rabi-oscillation at the beginning of the expansion to transfer a fraction of the atom from the $m_J = +1$ state to the non-magnetic $m_J = 0$ state, and we remove the remaining $m_J = +1$ atoms by applying a magnetic gradient. This procedure allows us to produce a regular BEC of 10^5 atoms, and send only a controlled fraction of it onto the MCP. The weakness of this calibration being that it relies on two other calibrations : the atom number detected by absorption imaging, and the Rabi frequency.

The method to calibrate the absorption imaging was briefly described in section 1.1.2. As for the Rabi frequency Ω_R, we can calibrate it by monitoring the 3-level Rabi oscillation as a function of the RF duration t_{rf}, either with fluorescence imaging or with the MCP. After separating the populations of the 3 hyperfine states with a magnetic bias, it is possible to measure those populations by fluorescence, and to monitor their oscillation dynamic. In 1.15, we see that the oscillations of the $m_J = 0$ population is not very "clean". This is due to the high number of Penning collisions inside the cloud [76]. On the other hand, only the evolution of the $m_J = 0$ population can be measure with the MCP. To avoid saturation effects, we detune the RF frequency with respect to the resonance. Figure 1.15 show the calibrations we performed with those various techniques.

The quantum efficiency we extract for MCP B (which was used for the experiment described in chapter 4 and 5) is 25(5)%, compatible with the efficiency of [75]. We are also interested in measuring the efficiency of a new generation of plates from Hamamatsu (MCP H2), whose micro-channels opening have been engineered in a beveled way, so that the open ratio area is almost twice bigger than the one of MCP B. We measure a quantum efficiency of $\sim 33\%$.

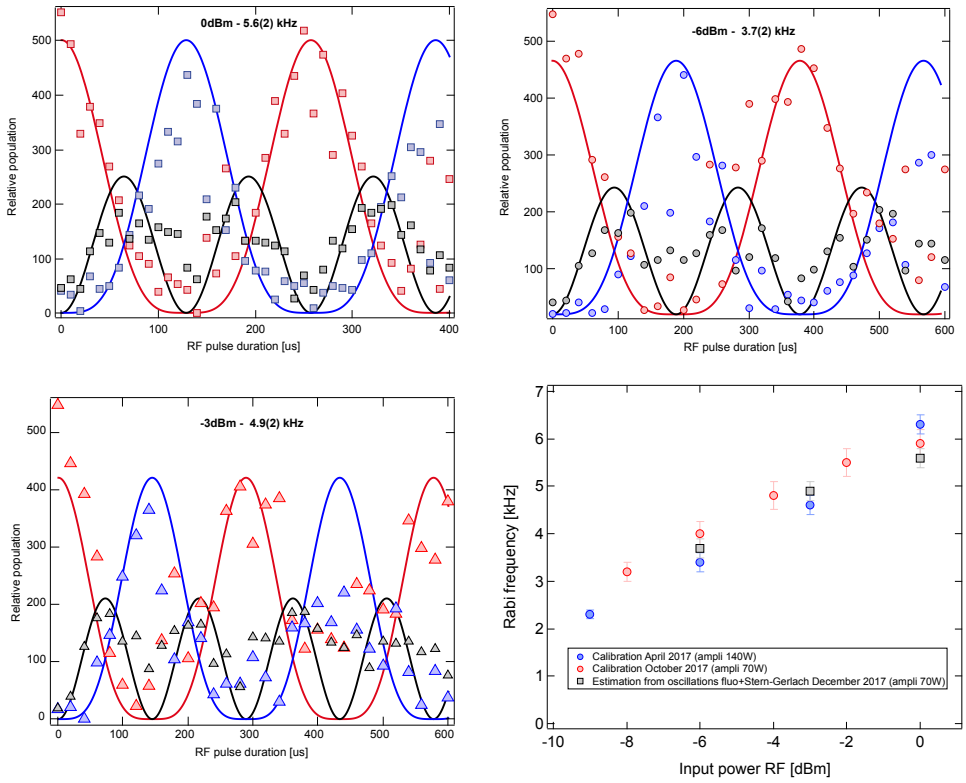

Figure 1.15: Calibration of the RF Rabi-frequency for different RF powers. The first 3 panels show the measured population in the hyperfine states of 2^3S_1. These populations are separated by a magnetic bias, and measured by fluorescence imaging. The solid lines are fits of the Rabi oscillations for this 3-level system. The extracted Rabi frequencies correspond to the grey squares of the calibration curve (bottom right panel). The other data point corresponds to calibrations performed with the MCP.

Gain map

The gain is inhomogeneous over the surface of the detector for many reasons : dust on the plates, local defects, mechanical stress, irregularity in the delay lines, etc. This calls for a characterization of the gain in the experimental conditions. We produce gain maps by imaging spatially large cloud distribution to ensure a homogeneous flux onto the plate. We usually image the atoms out-coupled from the quadrupole trap during the RF stage. Those atoms have a very large velocity distribution, both because of the high temperature of the cloud and because some of them are $m_J = -1$ atoms repelled from the trap in a random direction. The other advantage is that this distribution produces a rather low count rate onto the plate ($< 10^6$ particles.s^{-1}) which is convenient to avoid local saturation or TDC's buffer overflow. In figure 1.16, we compare the gain maps of different MCP pairs. The Hamamatsu H1 gain profile exhibits a hole at the center. This is the result of our bad initial choice of polarization sign of the plates : -2KV voltage at the top of the stack. The hundreds of millions of ions generated per second inside the MOT were therefore accelerated at about 10^{11}m.s^{-2} toward the MCP, leading to an accelerated aging of the micro-channels situated right under the MOT. On the other plate, the gain over the surfaces is rather homogeneous, apart from rapidly varying patterns that we identify as the delay line, because of its period (0.5mm) and the fact of being identical with all the MCPs we tested. This structure is smooth enough to be corrected by simply dividing the acquired data by the gain map, like shown in figure 1.16 (c).

Resolution along the three directions

In-plane resolution As shown in equations 1.8 and 1.9, the in-plane position of the atoms reaching the detector are calculated with the arrival times of the pulses exciting the delay lines. Consequently, the elementary coding step t_0 of the TDC also defines an in-plane pixel :

$$x_0 = \frac{1}{2} t_0 v_x \tag{1.14}$$

$$y_0 = \frac{1}{2} t_0 v_y \tag{1.15}$$

With the Roentdek values [72], the elementary pixel is $x_0 = y_0 = 60\mu$m, defining a lower bound for the in-plane resolution σ_x and σ_y. Of course, the electronic chain has a certain noise that will induce dispersion in the measure of the time, and consequently worsen the spatial resolution. If we assume that all the channels have the same time dispersion σ_t, and that the noise is statistically independent between the 4 channels, then following equation 1.8 we have :

$$\sigma_x = \frac{1}{2}\sqrt{\sigma_{t_{x1}}^2 + \sigma_{t_{x2}}^2}\, v_x = \frac{\sigma_t}{\sqrt{2}} v_x. \tag{1.16}$$

Hence, within those hypothesis, evaluating σ_t yields the in-plane resolution. We now define the quantity D as :

$$D = t_{x1} + t_{x2} - (t_{y1} + t_{y2}). \tag{1.17}$$

According to equation 1.10, we should have $\langle D \rangle = \frac{L_x}{v_x} - \frac{L_y}{v_y} = t_{dl} - t_{dl} = 0$ (where $\langle . \rangle$ is a statistical average over many runs). In practice, the length difference between the delay lines and the dispersion of the pulses during the propagation leads to a non zero value of $\langle D \rangle$ everywhere. However, this value only depends on the delay lines, and can be directly measured since it is calculated from the arrival times. Similarly to the gain map, we reconstruct the $\langle D \rangle$ map, which has a characteristic hyperboloid distribution (see figure 1.17). The next step is to notice that :

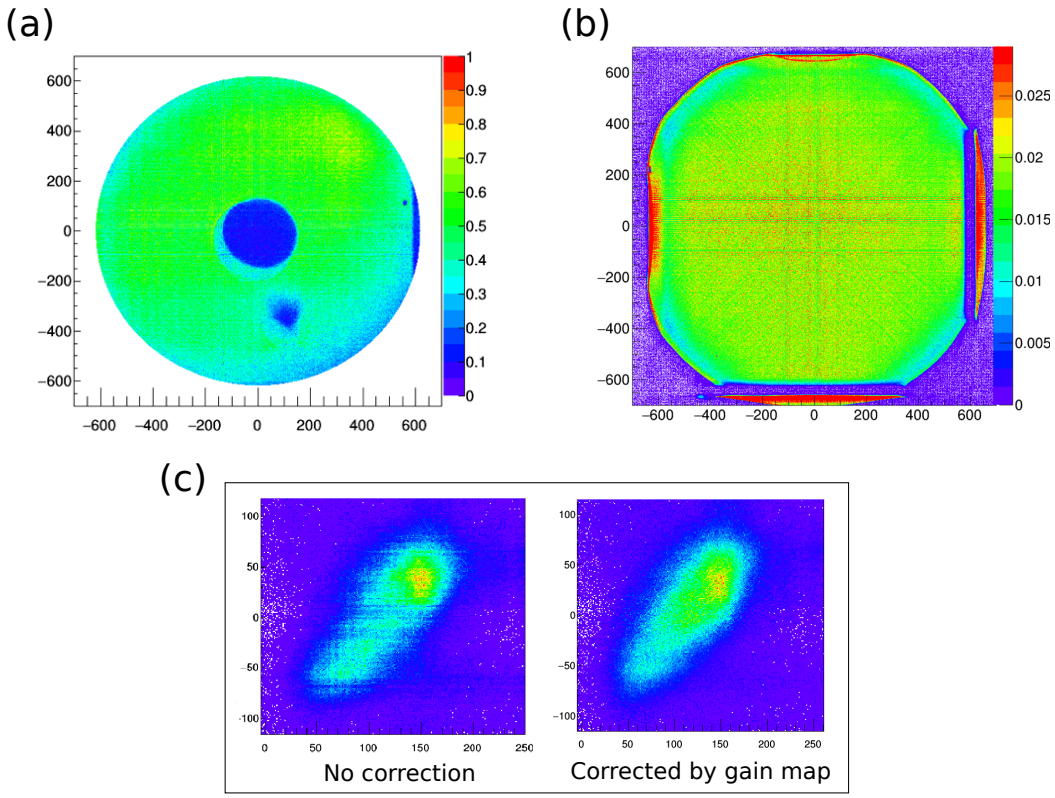

Figure 1.16: (a) Gain map of the MCP H1. The horizontal and vertical axis are in units of the coding step x_0 and y_0 (see text). The damages caused by the ions produced during the MOT stage is clearly visible at the center (see text). (b) Gain map of MCP B. The gain is rather homogeneous, with rapidly oscillating structure corresponding to the delay lines. (c) Example of a cloud detected on the MCP, with and without the correction of the gain map.

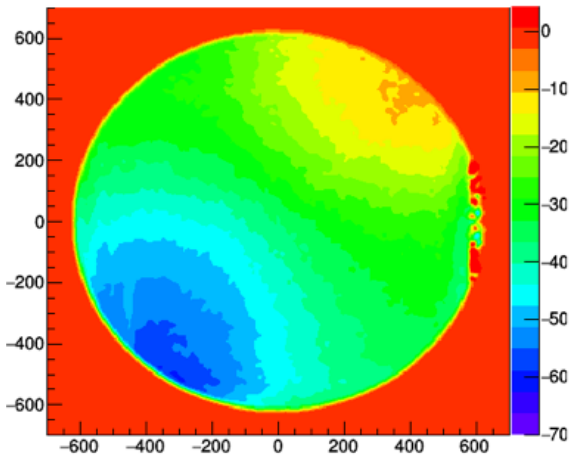

Figure 1.17: Maps of the $\langle D \rangle$ quantity over the plate. All the axis are in units of the coding step x_0 (horizontal) and y_0 (vertical) and t_0 (colors). We see the presence of a gradient coming from a length-difference of between the delay lines.

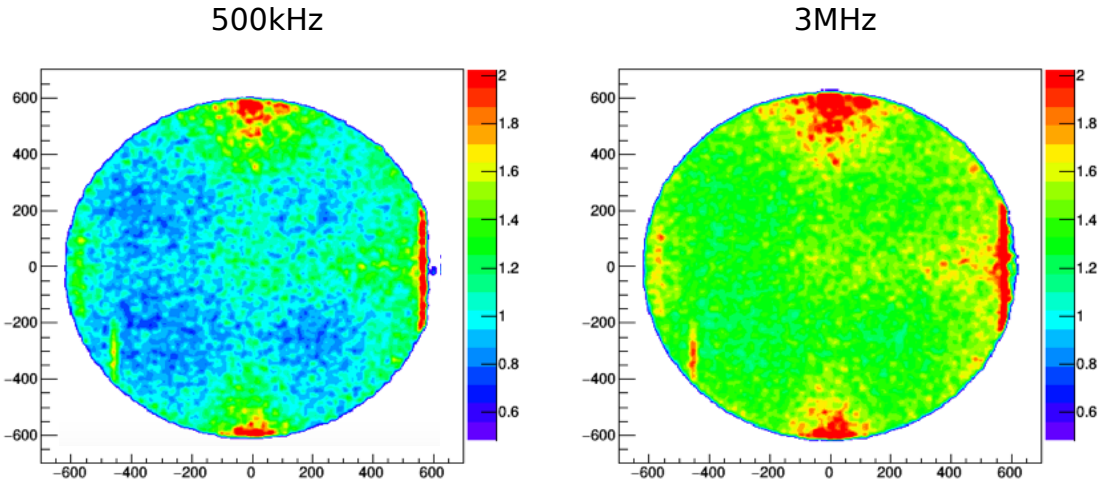

Figure 1.18: Map of the local resolution ($\frac{\sigma_D}{2\sqrt{2}}$) on the MCP B for 2 different flux of particles. The units are in elementary coding steps : for instance, a value of 1.2 corresponds to a local resolution of 1.2 pixel x_0 (y_0). We see that the flux worsen the resolution.

$$\sigma_D = \sqrt{\sigma_{t_{x1}}^2 + \sigma_{t_{x2}}^2 + \sigma_{t_{y1}}^2 + \sigma_{t_{y2}}^2} = 2\sigma_t. \tag{1.18}$$

Finally, by combining equation 1.16 and 1.18 we obtain :

$$\sigma_{x/y} = \frac{\sigma_D}{2\sqrt{2}} v_{x/y} \tag{1.19}$$

So by computing a third kind of map, the σ_D map, we can evaluate the local in-plane resolution anywhere in the plate. Figure 1.18 shows the maps of the local in-plane resolution for the MCP B, obtained with 2 different incoming fluxes of particles. We observe a worsening of the resolution with the flux.

Finally, we want to validate this method by comparing the resolution extracted with σ_D to a direct measurement of the resolution. We have imaged a flux of photons coming from a UV lamp onto MCP H1. A Cu-Alloy sheet with a honeycomb pattern of about 1mm periodicity has been mounted just above the plate, in order to evaluate the point spread function of the detector. As shown in figure 1.19, the extracted value of the resolution is coherent with the variation of σ_D as a function of the flux (more details about this experiment can be found in [73]). Note that this comparison relies on two different definitions of the resolution. The quantity σ_D is connected to the precision at which one can reconstruct the in-plane position of a particle, while the resolution measured with the point spread function is an "optical" resolution, i.e. the ability of the system to separate two point-like objects. At best, we can say that a measure of σ_D gives an evaluation of the in-plane resolution, but does not constitute a direct measurement.

Vertical resolution We can apply the same reasoning and notice that t_0 also defines a time pixel for the vertical axis. To roughly convert it in spatial resolution, we can use the velocity V_{CM} of the center of mass of the cloud, i.e. the vertical velocity acquired by an atom initially at rest and falling onto the detector, 50cm below. We have $V_{CM} \simeq 3\text{m.s}^{-1}$, and so $z_0 = V_{CM} \times t_0$ is of the order of half a nanometer. Since the σ_t width that we evaluate experimentally is a few t_0, the resolution along the vertical axis that we evaluate with this method is orders of magnitude

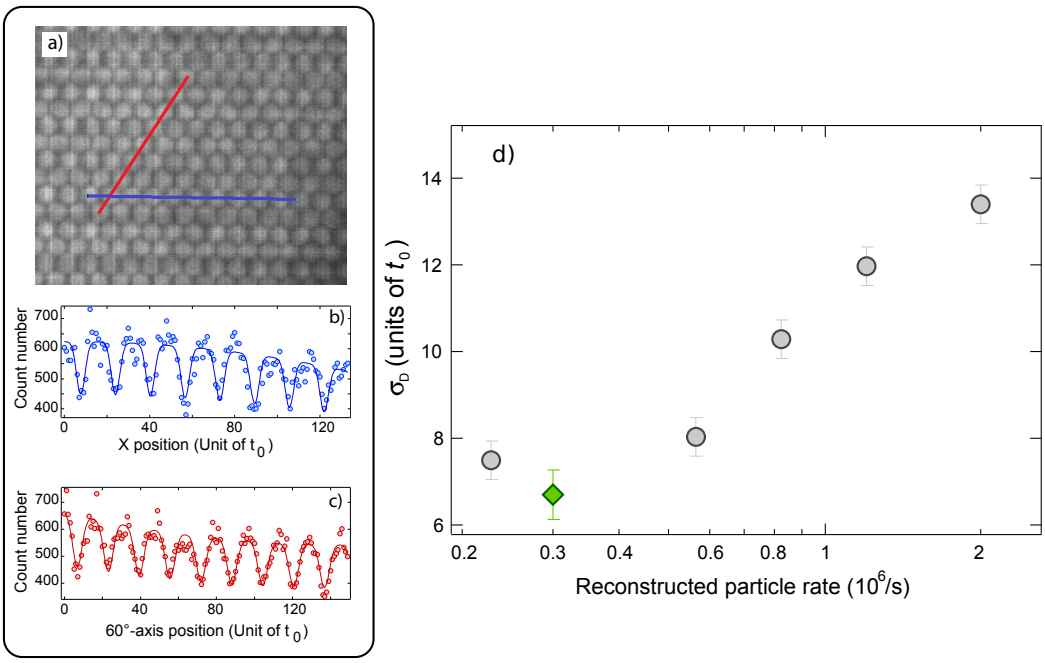

Figure 1.19: a) Measurement of the resolution of the detector by imaging UV photons through a a metallic sheet with a honeycomb pattern. The point-spread function is extracted along the x axis (b) and an axis at 60°(c). d) Average value of σ_D over the plate for the different flux (grey dots), compared to the resolution obtained with the point-spread function (green diamond).

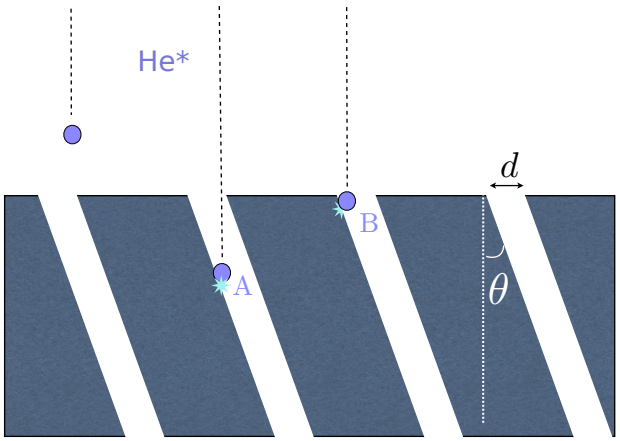

Figure 1.20: The angle of the micro-channel limits the vertical resolution, Atoms A and B are detected in the same time, even if they are vertically separated by $d/tan(\theta)$.

better than the in-plane resolution. This is of course too good to be true. Figure 1.20 illustrates how the vertical resolution is limited by a geometrical constraint given by the angle θ of the micro-channels : the atoms A and B are touching the wall of the micro-channel of diameter d at the same time, and thus they will be detected simultaneously, even though they are separated by a distance of :

$$\sigma_z = \frac{d}{tan(\theta)}. \tag{1.20}$$

Equation 1.20 sets a limit to the best vertical resolution one can theoretically access. From the value of table 2.2, we deduce a vertical resolution of 177μm for MCP B, and 32μm for MCP H1 and H2, equivalent to the in-plane resolution. This being said, to our knowledge there exists no experimental work which has formally demonstrated this limitation, because of the difficulty to produce a very narrow temporal signal with a source of massive particles. In our case, the narrowest structure that we can create (the diffraction peaks described in chapter 4 and 5) are of the order of the mm scale in the MCP plane, and do not permit to see a clear difference of resolution between the z axis and the x/y axis. All we can say is that we resolve well those narrow structures along the 3 directions of space. On the other hand, the measurements of second-order correlation functions suggest that the vertical resolution is actually better than this theoretical limit based on the channel angle (see section 2.3.2). Note that there exist a test of the temporal resolution conducted with a UV mode-locked picosecond laser [77]. However, the extreme velocity of the photons compared to the atoms does not permit to conclude how the resolution is impacted by a finite penetration of the particle inside the micro-channels. For instance, the 177μm penetration depth of MCP B corresponds to a sub-picosecond time for particles traveling at the speed of light, which is below any TDC resolution.

Different saturation regime

There are 3 main saturation effects that can occur with the detector. A first one is the local saturation of the MCP, linked to the reloading time of the micro-channels. It is a physical constraint that can vary from one MCP to the other. The second type of saturation is a global effect and comes from the electronics. Indeed, the multiplexor of the TDC works at 4.1MHz for the 4 channels, which defines an upper bound of the total flux of particles that our detection chain can handle. Finally, there is a "software saturation" of the algorithm that reconstructs the 3D position of the atoms from the list of arrival times. As detailed in section 2.1, the algorithm has a limited capacity to temporally distinguish the signals coming from different atoms. In this chapter, we only describe the two types of "hardware saturation".

Local saturation of the plate The local saturation of the MCP is a well-known, yet not completely understood phenomenon linked to the charge reloading after a detection event [68, 69, 70]. The very narrow pore of the micro-channel leads to a slow reloading time, and saturation effects can appear at count rates of the order of a few channel^{-1}.s^{-1} [68]. Furthermore, the electronic discharge generated by a detection event creates a very localized variation of the electric field, which tends to affect the reloading of the neighboring sites as well [70]. The overall impact of the saturation thus strongly depends on the type of MCP, its polarization, or the size of the area submitted to particle flux, and need to be estimated experimentally. With this in mind, we have imaged a series of condensates onto the plates, with more and more atoms transferred in the $m_J = 0$ state (the only one detected, the atoms in $m_J = +/-1$ being repelled by a magnetic kick), and we investigate the difference between the measured flux and the expected one. The results, summed up in figure 1.21, show a deviation from the linear regime around a flux of 2×10^5atoms.cm^{-2}.s^{-1}, and a saturation flux of 4×10^5atoms.cm^{-2}.s^{-1}. Those numbers

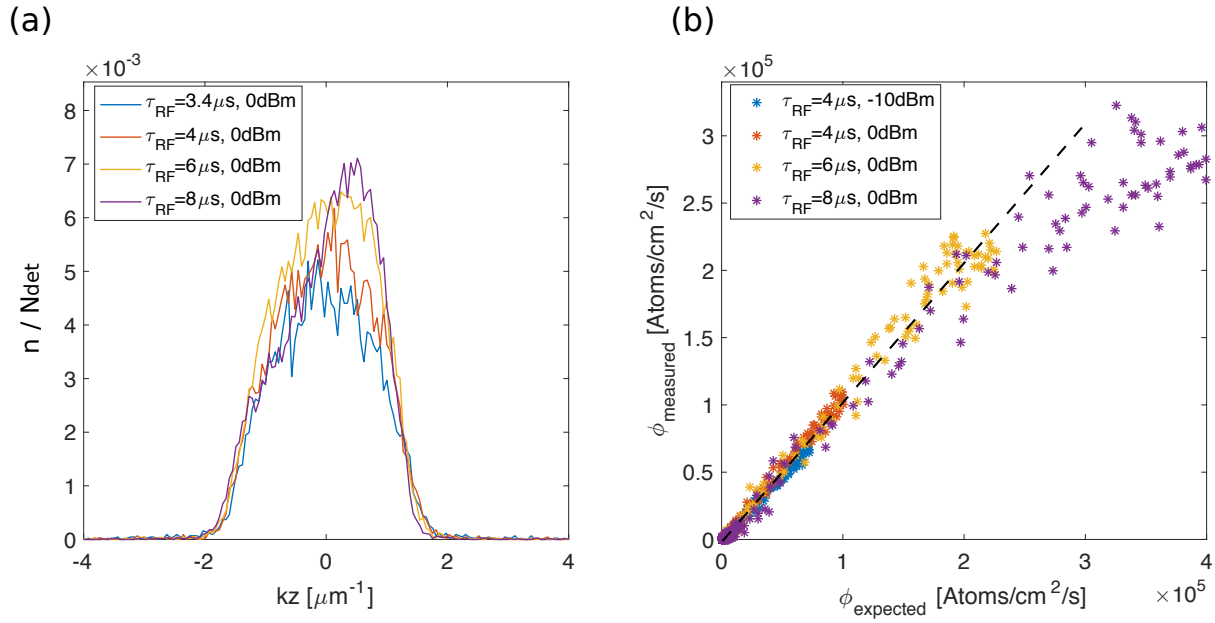

Figure 1.21: Study of the MCP saturation. Condensed clouds are sent onto the detector with different fluxes. The flux is regulated by the duration and the amplitude of the RF pulse (τ_{RF}), which transfers the atoms in the detectable state $m_J = 0$. (a) 1D density profiles of the BEC obtained with narrow cut along the z-axis. The profiles are normalized by the total number of atoms detected onto the plate $\mathrm{N_{det}}$. We clearly see that the saturation tends to distort the profiles which becomes asymmetric at high flux (purple profile). (b) Ratio between the measured flux and the expected flux on various points of the density profiles.The expected flux is an extrapolation, based on the RF transfer parameters, of the low flux data. We clearly see a deviation from the linear response around of flux of $\sim 2 \times 10^5 \mathrm{atoms.cm^{-2}.s^{-1}}$.

are of the same order than other measurements previously reported with metastable Helium (see for instance [78]). We notice that, in addition to a decay of the overall number of detected atoms, the saturation tends to deform the distribution with a characteristic asymmetry. This deformation appears for fluxes slightly above the linear response limit, and therefore constitutes an excellent way to identify the local saturation "by eye".

Global saturation of the TDC To estimate the impact of the TDC's multiplexer limitation, we have imaged very broad distributions of particles (in this case, UV photons), homogeneously distributed onto the plates, in order to get rid of any effect of local saturation. We then measured the reconstruction efficiency η for different fluxes of photons. η is defined as the ratio between the number of reconstructed particles, corresponding to the identification of a quadruplet $(t_{x_1}, t_{x_2}, t_{y_1}, t_{y_2})$, and the average number of electronic pulses detected in the channels (x_1, x_2, y_1, y_2). A reconstruction efficiency close to 1 is both a sign of low noise in the channels (the electronic pulses detected are coming from real particle event, and not from electronic noise) and a sign that the electronics are not missing any pulse (if a pulse is missed from one of the channel (x_1, x_2, y_1, y_2), the other 3 pulses will not lead to any reconstruction, and η will decrease). A good setting of the CFD thresholds is crucial to avoid missing pulse and to reach a low level of noise. In figure 1.22, we have plotted η as a function of the incoming particle flux, characterized by a high number of counts per channel. We observe a clear decay of the

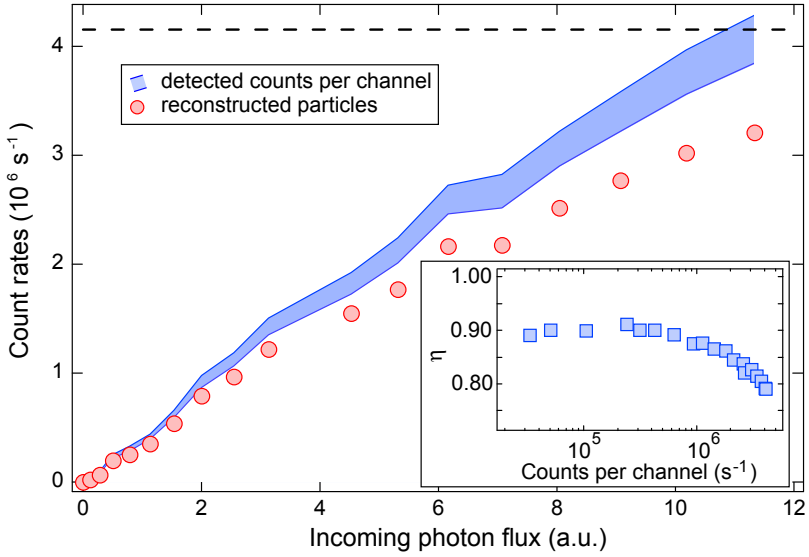

Figure 1.22: Reconstructed particles as a function of the counts rate. The reconstruction efficiency η decreases when the flux becomes of the order of a few MHz.

reconstruction efficiency as we approach the operation rate of the multiplexer. In this regime, the TDC misses some channel counts due to the limited size of the channel registers and the finite speed as which the multiplexer empties them.

Chapter 2

Reconstruction and correlations of individual particles in three dimensions

Over the past decade, new observation methods have emerged to probe individual degrees of freedom in quantum systems. The most famous of this new observation techniques is probably the quantum gas microscope [12], allowing single-site and single-particle optical probing in lattice systems. Measuring the position [79], the spin [80], or the phase [81] of individual particles leads to a deeper understanding of the wave function, with the calculation of correlation functions. In that regard, the second-order correlation function $g^{(2)}$ (2-body or or 2-point intensity correlations) is a key quantity allowing to probe fundamental properties of the system, like the nature of the ground state [80, 82], the coherence properties [83, 84], the presence of pairing mechanisms [26], the hidden periodicity [85] or even the quantum statistics [86]. Our single-atom detection process enables the possibility to characterize strongly correlated quantum states through its correlation functions in momentum space.

We have presented the MCP detector and described its performances in terms of resolution and acquisition rate. The first section of the present chapter focuses on the "software" part of the detection process, by describing the algorithm used to reconstruct the 3D coordinates of the detected atoms from the raw data. The second section describes the calculation and normalization method for the second-order correlation functions. The most basic example of second-order correlations present in bosonic systems is the local density correlations, the so-called "bunching". In the third section, we investigate the bosonic bunching of various systems in order to test the algorithm.

2.1 Reconstruction algorithm

2.1.1 Identification of time quadruplets and calculation of 3D coordinates

As explained in 1.2.1, an atom detected by the MCP produces a quadruplet of pulses, and the arrival times of those pulses at the extremity of the delay-lines $(t_{x_1}, t_{x_2}, t_{y_1}, t_{y_2})$ contains all the information about the 2D position (x, y) and impact time t of the particle via equation 1.8, 1.9 and 1.10. So in order to reconstruct the list of all the atom's position and impact time $\mathcal{L} = \{x^a, y^a, t^a\}_a$ (where a is the index of the atom) one needs to identify first the list of quadruplets $\mathcal{L}_4 = \{t^a_{x_1}, t^a_{x_2}, t^a_{y_1}, t^a_{y_2}\}_a$. The list of 32 bits words that we obtain at the output of the TDC actually corresponds to 4 lists $\{t^i_{x_1}\}_i, \{t^j_{x_2}\}_j, \{t^k_{y_1}\}_k, \{t^l_{y_2}\}_l$, and the main goal of the reconstruction algorithm is to deduce $\mathcal{L}_4$ out of those 4 lists. To do so, we are helped by two properties of the quadruplets :

Property 1 *Let $\mathcal{Q}$ be a quadruplet of arrival times. If $\mathcal{Q} \in \mathcal{L}_4$, then $\forall (t_1, t_2) \in \mathcal{Q}$ we have :*

$$|t_1 - t_2| \leq max\left(\frac{L_x}{v_x}, \frac{L_y}{v_y}\right) = t_{dl}, \tag{2.1}$$

Property 1 expresses the fact that the pulses generated by a same detection event will all arrive at the end of the delay-line within a certain time window, by definition equal to t_{dl}.

Property 2 *Let $\mathcal{Q} = (t_{x_1}, t_{x_2}, t_{y_1}, t_{y_2})$ be a quadruplet of arrival times. If $\mathcal{Q} \in \mathcal{L}_4$, then, according to equation 1.17 we have :*

$$D_{\mathcal{Q}} = t_{x_1} + t_{x_2} - (t_{y_1} + t_{y_2}) \simeq \langle D(x,y) \rangle, \tag{2.2}$$

where $\langle D(x,y) \rangle$ is the average value of the D quantity at position $(x,y) = \left(\frac{v_x}{2}(t_{x_1} - t_{x_2}), \frac{v_y}{2}(t_{y_1} - t_{y_2})\right)$

We have developed an algorithm based on those 2 properties, illustrated by figure 2.1. It takes as an input the 4 lists of the TDC $\{t^i_{x_1}\}_i, \{t^j_{x_2}\}_j, \{t^k_{y_1}\}_k, \{t^l_{y_2}\}_l$ and outputs the list $\mathcal{L}$ of impact times and in-plane positions. The algorithm follows a procedure that we can summarize as follow :

- For each time $t^i_{x_1}$, we try to find the corresponding $t^i_{x_2}, t^i_{y_1}$ and $t^i_{y_2}$. We start by making a list $L^i_{\mathcal{Q}}$ of all the possible quadruplet $\{t^i_{x_1}, t^j_{x_2}, t^k_{y_1}, t^l_{y_2}\}_{j,k,l}$ which are inside a time window t_{dl} (property 1).
- If there is more than one quadruplet in the list $L^i_{\mathcal{Q}}$, we chose the one whose $D_{\mathcal{Q}}$ quantity minimize $|D_{\mathcal{Q}} - \langle D(x,y) \rangle|$ (property 2).
- We then calculate the quantities x^i, y^i and t^i from the quadruplet using equations 1.8, 1.9 and 1.10, and add (x^i, y^i, t^i) to the list $\mathcal{L}$.
- Finally we remove the quadruplet from the 4 lists of the TDC $\{t^i_{x_1}\}_i, \{t^j_{x_2}\}_j, \{t^k_{y_1}\}_k, \{t^l_{y_2}\}_l$.

We are interested in the calculation of the distribution of $\{\vec{k}\}$, where $\hbar\vec{k} = m\vec{v}$, is the momentum. The 3D coordinates of an atom velocity (v_x, v_y, v_z) can be deduced from the set (x, y, t), providing that we know the coordinates of the origin, i.e. the in-plane position and impact time of an atom with $\vec{v} = \vec{0}$. In our experiment, the symmetries of the different traps are such that it coincides with the center of mass of the cloud, meaning that $\vec{v}_{\text{cm}} = \vec{0}$. In practice, it is not always easy to estimate this center of mass from a single experimental cycle, because of the local saturation of the MCP at high flux, or the small number of atoms at low flux. Once we have determined $(x_{\text{cm}}, y_{\text{cm}}, t_{\text{cm}})$, we can retrieve all the 3D velocities with :

$$v_x = \frac{1}{t}(x - x_{\text{cm}}) \tag{2.3}$$

$$v_y = \frac{1}{t}(y - y_{\text{cm}}) \tag{2.4}$$

$$v_z = \frac{g}{2t}(t^2 - t^2_{\text{cm}}) \tag{2.5}$$

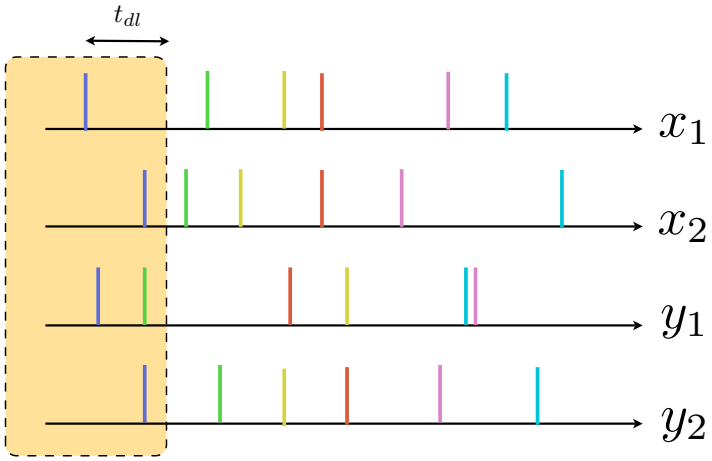

Figure 2.1: Sketch of the 4 lists of arrival times given by the TDC. Each color corresponds to an atom. The goal of the algorithm is precisely to realize this coloring, i.e. to identify the quadruplets corresponding to an atom. To do so, we start from the first arrival time of the x_1 list, and identify all the possible quadruplets contained within a time window t_{dl}. In this example, there are 2 possibilities : (blue, blue, blue, blue) and (bleu, blue, green, blue). To identify the good one, we compare their D quantities (see text).

2.1.2 Performances and storage

Complexity

In terms of computational complexity, the algorithm executes a number of elementary operations whose upper bound scales as $N_{x_1} \times n_{x_2} \times n_{y_1} \times n_{y_2}$, where N_{x_1} is the number of counts in channel x_1, and $n_{...}$ is the average number of counts per unit of t_{dl} detected on the other channels. For a fixed acquisition time, if we assume well balanced channels (CFD's thresholds correctly set) and high reconstruction efficiency (no saturation of the TDC), the complexity is bounded above by N^4 , where N is the number of detected particles.

The algorithm is coded in C++ with the ROOT framework. ROOT is a computational environment developed at CERN, and provides a broad set of functionality to handle, display and store massive dataset. It is well adapted to our experiment, since a typical dataset is composed of several hundred experimental runs, each one corresponding to the detection of a cloud with up to several thousands atoms. The machine-oriented, low complexity architecture of C++, coupled to the good performance of our calculation computer provides an appreciable rapidity of execution. To give an idea, it takes about 1.2s to reconstruct 250ms of acquisition with a flux of 3×10^5 atoms.s^{-1}.

Software saturation

The 2 properties used to identify the quadruplet are not error-proof. Some wrong quadruplet identifications can occur when the flux becomes high enough, in particular when too many quadruplets satisfy the property 1. We thus have a "software saturation", which is easily identifiable because of a characteristic "cross" pattern (see figure 2.2). To understand this distribution,

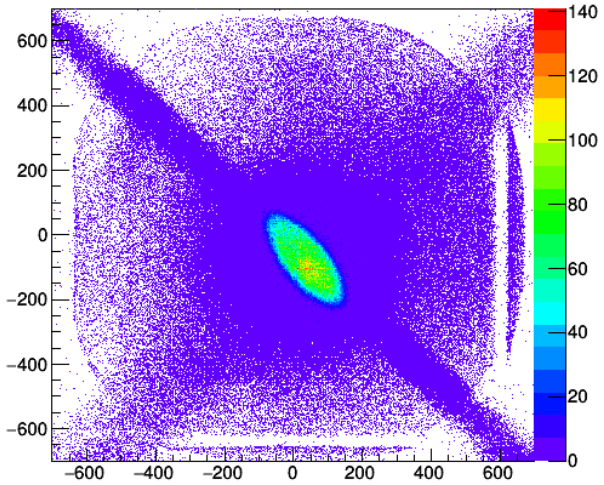

Figure 2.2: Time-integrated distribution of a BEC falling onto the MCP, obtained by averaging ∼ 500 experimental realizations. A 45°cross in the low density region corresponding to a "software saturation" is clearly visible.

we can follow a simple reasoning.

Let's consider one pixel of the MCP at the position X and Y, and two atoms falling on that pixel at time t^A and t^B. In that case, the four channels give us 8 times : $t^A_{x1}, t^A_{x2}, t^A_{y1}, t^A_{y2}, t^B_{x1}, t^B_{x2}, t^B_{y1}, t^B_{y2}$, and 6 possibles ways to combine them:

- $(t^A_{x1}, t^A_{x2}, t^A_{y1}, t^A_{y2})$ and $(t^B_{x1}, t^B_{x2}, t^B_{y1}, t^B_{y2})$ the 'good' combination that reconstruct correctly the atoms' position.
- $(t^A_{x1}, t^A_{x2}, t^B_{y1}, t^A_{y2})$ and $(t^B_{x1}, t^B_{x2}, t^A_{y1}, t^B_{y2})$
- $(t^A_{x1}, t^A_{x2}, t^A_{y1}, t^B_{y2})$ and $(t^B_{x1}, t^B_{x2}, t^B_{y1}, t^A_{y2})$
- $(t^B_{x1}, t^A_{x2}, t^A_{y1}, t^A_{y2})$ and $(t^A_{x1}, t^B_{x2}, t^B_{y1}, t^B_{y2})$
- $(t^A_{x1}, t^B_{x2}, t^A_{y1}, t^A_{y2})$ and $(t^B_{x1}, t^A_{x2}, t^B_{y1}, t^B_{y2})$
- $(t^A_{x1}, t^B_{x2}, t^B_{y1}, t^A_{y2})$ and $(t^B_{x1}, t^A_{x2}, t^A_{y1}, t^B_{y2})$
- $(t^A_{x1}, t^B_{x2}, t^A_{y1}, t^B_{y2})$ and $(t^B_{x1}, t^A_{x2}, t^B_{y1}, t^A_{y2})$

Now let's assume we have a high particle rate, so that $t^A - t^B$ is so small that all those combinations verify the first condition of the algorithm : $t_{x1} - t_{x2} \leq t_{dl}$ AND $t_{y1} - t_{y2} \leq t_{dl}$. The only thing that can discriminate the good quadruplets from the bad ones is the 2nd condition of the algorithm : the good quadruplet is the one that minimize the D value $(t_{x1} + t_{x2} - t_{y1} - t_{y2})$. The problem is that if we assume the MCP to be ideal (D = 0 for every "good" quadruplet) we find that the first combination (the good one) leads to D = 0 as expected, but also the two last ones. For example the last combination gives :

$D_1 = t^A_{x1} + t^B_{x2} - t^A_{y1} - t^B_{y2} = (t^A + \frac{L_{dl}}{v_{dl}} + \frac{X}{vx}) + (t^B + \frac{L_{dl}}{v_{dl}} - \frac{X}{vx}) - (t^A + \frac{L_{dl}}{v_{dl}} + \frac{Y}{vx}) - (t^B + \frac{L_{dl}}{v_{dl}} - \frac{Y}{vx}) = t^A + t^B - t^A - t^B = 0$

and

$D_2 = t^B_{x1} + t^A_{x2} - t^B_{y1} - A_{y2} = t^B + t^A - t^B - t^A = 0$

So with an ideal MCP, the reconstruction of the position of those two atoms, falling almost simultaneously on the same pixel will be given by one of those 3 combinations (the 1st one and the two last ones) with equiprobability. In other words, the good position has 1/3 chance to be "chosen". Now if we calculate the positions obtained by those 2 wrong combinations, we find :

- $X1 = \frac{t^A_{x1} - t^B_{x2}}{2} = X + \frac{t^A - t^B}{2v_x}$ $\quad Y1 = \frac{t^B_{y1} - t^A_{y2}}{2} = Y + \frac{t^B - t^A}{2v_x}$ $\quad T1 = \frac{t^A + t^B}{2}$

  and

  $X2 = \frac{t^B_{x1} - t^A_{x2}}{2} = X + \frac{t^B - t^A}{2v_x}$ $\quad Y2 = \frac{t^A_{y1} - t^B_{y2}}{2} = Y + \frac{t^A - t^B}{2v_x}$ $\quad T2 = \frac{t^A + t^B}{2}$

- $X1 = \frac{t^A_{x1} - t^B_{x2}}{2} = X + \frac{t^A - t^B}{2v_x}$ $\quad Y1 = \frac{t^A_{y1} - t^B_{y2}}{2} = Y + \frac{t^A - t^B}{2v_x}$ $\quad T1 = \frac{t^A + t^B}{2}$

  and

  $X2 = \frac{t^B_{x1} - t^A_{x2}}{2} = X + \frac{t^B - t^A}{2v_x}$ $\quad Y2 = \frac{t^B_{y1} - t^A_{y2}}{2} = Y + \frac{t^B - t^A}{2v_x}$ $\quad T2 = \frac{t^A + t^B}{2}$

So the "wrong" reconstruction will populate a 45 degree cross centered on the (X,Y) pixel, even with an ideal MCP. This effect starts to be visible when the probability of having more than two atoms falling nearby within a time window t_{dl} is not negligible, which typically happens when condensates of a few hundreds atoms hit the plate.

Storage

For each experimental run, the list of velocities can be stored, as well as other details (the lists $\mathcal{L}$ and $\mathcal{L}_4$, the distribution of D, ...) in ROOT file format, which is very handy to manipulate directly with ROOT. To give an idea, a TDC file which contains the list of all the 32 bits words of an experimental run of 10^5 atoms is 2 Mb of size. The corresponding ROOT file, storing the full reconstruction ($\mathcal{L}$, $\mathcal{L}_4$, histograms of the 2D in-plane distribution, of the average D distribution, ...) is 9Mb of size. As a comparison, exporting the sole list $\mathcal{L}$ in standard .txt format generates a file of 9Mb as well.

2.2 Calculation of two-body correlations

2.2.1 The integrated $g^{(2)}$

We want to compute the 6D-normalized second order correlation function :

$$g^{(2)}(\vec{k}, \vec{k'}) = \frac{\langle n(\vec{k}) n(\vec{k'}) \rangle}{\langle n(\vec{k}) \rangle \langle n(\vec{k'}) \rangle}, \tag{2.6}$$

and more precisely, the diagonal $g^{(2)}(\vec{k}, \vec{k})$ (bunching) and anti-diagonal $g^{(2)}(\vec{k}, -\vec{k})$ (pairing). In order to increase the signal-to-noise ratio and to plot this 6D quantity in an intelligible way, we need to "compact" the informations. A first step is to consider the quantities integrated over all the $\vec{k}$:

$$g_{\pm}^{(2)}(\delta\vec{k}) = \frac{\int_{\vec{k}}\langle n(\vec{k})n(\pm\vec{k}+\delta\vec{k})\rangle \,\mathrm{d}\vec{k}}{\int_{\vec{k}}\langle n(\vec{k})\rangle\langle n(\pm\vec{k}+\delta\vec{k})\rangle \,\mathrm{d}\vec{k}}. \tag{2.7}$$

Where $g_{+}^{(2)}$ and $g_{-}^{(2)}$ are 3D-functions. Before performing further integration, let's stress the fact that the different spatial axis are not equivalent in general. For instance, our ODT is anisotropic (see 1.1.2), and so the trapped cloud does not have the same size along the 3 directions of space. Consequently, the variations of the k-correlations will not have the same size along k_x, k_y and k_z. The other system described in this manuscript, the 3D lattice, does not even have a spherical symmetry. To put it in a nutshell, we need to integrate the $g^{(2)}$ function, in a way that does not mix the informations between independent spatial axes. We choose to use a similar method than [83], and calculate a set of 6 1D-functions $\{g_{\pm}^{(2)}(\delta k_i)\}_{i=x,y,z}$, where each function $g_{\pm}^{(2)}(\delta k_i)$ is plotted along the i-axis, and is doubly integrated, firstly over the transverse plane $\Delta k_{\perp}$ (orthogonal to i) and then over all the $\vec{k}$. So we have :

$$g_{\pm}^{(2)}(\delta k_i) = \frac{\int_{\vec{k}}\int_{\Delta k_{\perp}}\langle n(\vec{k})n(\pm\vec{k}+k_{\perp}+\delta k_i)\rangle \,\mathrm{d}\vec{k}\,\mathrm{d}k_{\perp}}{\int_{\vec{k}}\int_{\Delta k_{\perp}}\langle n(\vec{k})\rangle\langle n(\pm\vec{k}+k_{\perp}+\delta k_i)\rangle \,\mathrm{d}\vec{k}\,\mathrm{d}k_{\perp}}. \tag{2.8}$$

2.2.2 Description of the algorithm

The $g_{\pm}^{(2)}$ are based on expecting values $\langle . \rangle$ of observables, and are thus defined for a sufficiently high amount of experimental run. One run corresponds to the production of the gas of interest, and its detection with the MCP. It provides a distribution of 3D k-coordinates that we note D_r for the r^{th} run. We start by describing how to compute the numerator of the $g_{\pm}^{(2)}$ functions, and discuss the normalization procedure (the denominator) in a second time.

The numerator

Let's focus on the numerator of $g_{+}^{(2)}$ along z (the other functions work the same way). The idea of the algorithm is to fill a histogram $\mathcal{H}_r$ for each distribution D_r. $\mathcal{H}_r(\delta k_z)$ is an average of all the histograms $H_a(\delta k_z)$, where a is the index of the atoms in D_r. $H_a(\delta k_z)$ is the number of atoms inside a tube of section $2\Delta k_{\perp}$ centered onto a, and whose k_z coordinate is separated from a by δk_z (see figure 2.3).

Here is a pseudo-code version of the algorithm running on each distribution D_r :

Begin
  for each atom a in D_r :
    for each atom $b \neq a$ in D_r :
      if $|x_a - x_b| \leq \Delta k_{\perp}$ **and** $|y_a - y_b| \leq \Delta k_{\perp}$:
        $\delta k_z = |k_{z_a} - k_{z_b}|$
        $H_a(\delta k_z) = H_a(\delta k_z) + 1$
  $\mathcal{H}_r = \frac{\sum_a H_a}{N_r}$ (average over all the atoms, N_r being the number of atoms in D_r)
End

By definition, the average of $\mathcal{H}_r$ over all the distributions is equal to the numerator of $g_{+}^{(2)}$ along z, since :

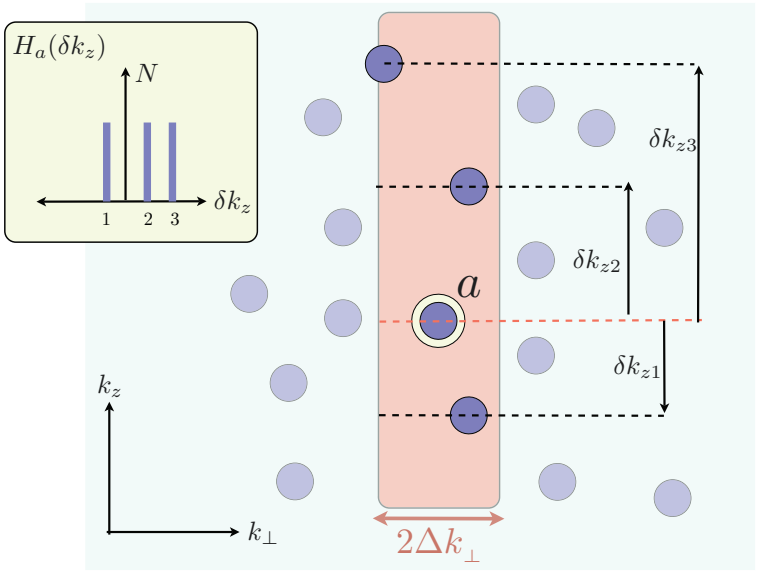

Figure 2.3: To calculate the $g_+^{(2)}$ function along z, we make an average over all the atoms a of the histogram H_a. $H_a(\delta k_z)$ is the number of atoms inside a tube of section $2\Delta k_\perp$ centered onto a, and whose k_z coordinate is separated from a by δk_z. In this example, there are 3 atoms that contribute to the histogram H_a, at positions 1, 2 and 3.

$$\langle \mathcal{H}_r(\delta k_z)\rangle_r = \langle \int\!\!\int_{\Delta k_\perp} n(\vec{k})n(\vec{k}+k_\perp+\delta k_z)\,\mathrm{d}\vec{k}\,\mathrm{d}k_\perp\rangle_r = \int\!\!\int_{\Delta k_\perp} \langle n(\vec{k})n(\vec{k}+k_\perp+\delta k_z)\rangle_r\,\mathrm{d}\vec{k}\,\mathrm{d}k_\perp. \quad (2.9)$$

Normalization : the sum method

To calculate the denominator, we need to integrate the quantity $\langle n(\vec{k})\rangle\langle n(\vec{k}+\delta k_z)\rangle$ over all $\vec{k}$. Since it is very time and memory consuming to store $n(\vec{k})$ for each cloud, we do not compute the denominator directly, and use a "sum method". It consists in creating a distribution $D_{av} = \sum_{r\in R} D_r/N_R = \langle D_r\rangle_{r\in R}$ which is an average over a subset R of N_R experimental clouds. If R is a representative sample (meaning if N_R is large enough), then the momentum distribution $n_{av}(\vec{k})$ given by D_{av} is close to the statistical average $\langle n(\vec{k})\rangle$. In particular, all correlations between the atoms have been washed away. So by applying the algorithm of the previous paragraph to the distribution D_{av}, the histogram $\mathcal{H}_{av}$ at the output will be equal to the denominator of $g_+^{(2)}$, since :

$$\mathcal{H}_{av}(\delta k_z) = \int\!\!\int_{\Delta k_\perp} n_{av}(\vec{k})n_{av}(\vec{k}+k_\perp+\delta k_i)\,\mathrm{d}\vec{k}\,\mathrm{d}k_\perp = \int\!\!\int_{\Delta k_\perp} \langle n(\vec{k})\rangle\langle n(\vec{k}+k_\perp+\delta k_i)\rangle\,\mathrm{d}\vec{k}\,\mathrm{d}k_\perp. \quad (2.10)$$

Figure 2.4 shows an example of the normalization procedure applied to a thermal lattice gas.

Results and Performances

The advantage of this method is to perform the statistical average over a quantity which is already integrated, thus it is very weakly consuming in terms of computer RAM. The algorithm stores only the $\mathcal{H}_r$ quantity, which are 1D histograms. Storing the value of $n(\vec{k})$ for all $\vec{k}$ would

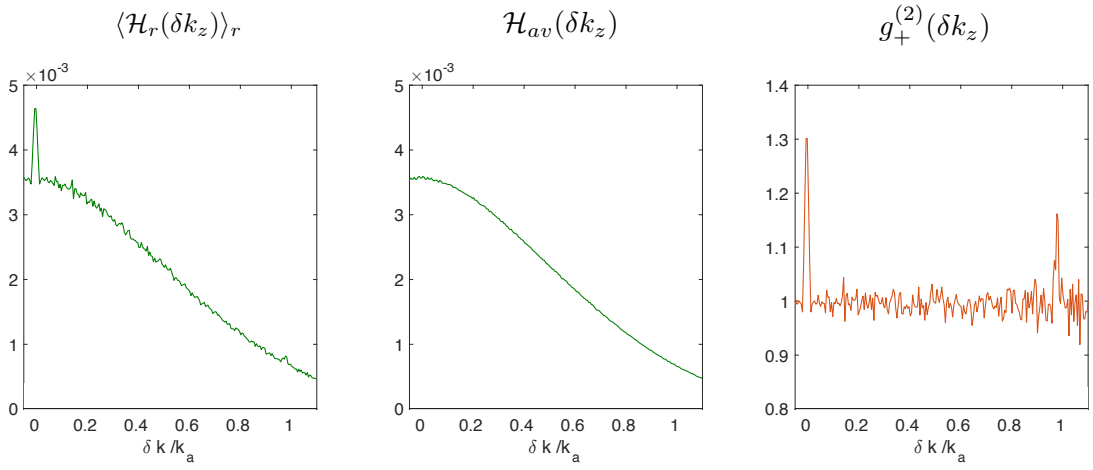

Figure 2.4: Example of a $g_+^{(2)}(\delta k)$ calculation obtained with a thermal gas of 40×10^3 atoms released from the optical lattice. The dataset corresponds to $\sim$ 3000 experimental realizations, with $\sim$ 2500 detected particles per shot (the detection includes : (1) the RF transfer to the detectable state, (2) the quantum efficiency of the MCP and (3) the reconstruction efficiency of the algorithm). The numerator (left) is the average over all the detected atoms and over all the dataset of $\mathcal{H}_r(\delta k)$, calculated along the gravity axis with a transverse integration of $\Delta k_\perp = 12 \times 10^{-3}\, k_a$ (in unit of the lattice momentum scale). The denominator (center) corresponds to an histogram $\mathcal{H}_r(\delta k)$ averaged over all the atoms of a single ensemble, composed of the sum of $\sim$ 300 experimental realizations. The result of the division of those two distributions is the $g_+^{(2)}(\delta k)$ function (right), and show a correlation peak at $\delta k = 0$, and $\delta k = k_a$, coming from the periodic structure of the lattice (see section 2.3.2).

raise the need in memory resources to the power of 3 (for the 3 directions of space). Looping over all the atoms, rather than over all the $\vec{k}$-modes is also very time saving because for our very dilute gas, most of the $\vec{k}$-modes are empty. If we note $\mathcal{N}$ the number of experimental run, and N_r, the average number of atoms per run, the computational complexity of the numerator calculation scales as $\mathcal{N} \times N_r^2$ since we perform a double loop over the atoms. For the same reason, the denominator calculation complexity scales as $N_{av}^2 = N_R^2 \times N_r^2$. For the subset R to be representative, we usually take $N_R = \mathcal{N}/10$, so that the total complexity of the $g_\pm^{(2)}$ calculations scales as $\mathcal{N}^2 \times N_r^2$. The main limitation of this method is its sensitivity to shot to shot fluctuation of the cloud. Indeed, only a few percent of variation in the size of the cloud (due to temperature or atom number fluctuations for instance) is enough to distort the normalized function. To be a bit more quantitative, we have run the algorithm on simulated dataset: an uncorrelated, random distribution of atomic positions. The $g_\pm^{(2)}$ functions of such a distribution should be completely flat and equal to 1 for all δk_i. The simulation can include controlled shot-to-shot fluctuation of the cloud size, and the impact of this fluctuation is shown in figure 2.5. We see that only 10% fluctuation of the cloud's size is enough to produce a visible quadratic background.

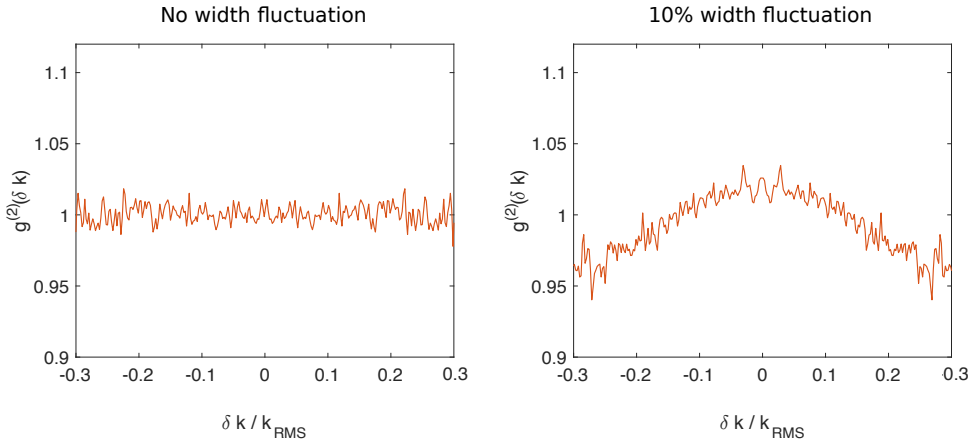

Figure 2.5: Calculation of $g_+^{(2)}(\delta k)$ on a simulated datasets. The simulation is made of 100 realizations of a gaussian distribution of 500 uncorrelated atoms (flat $g^{(2)}$) and of width $k_{\mathrm{RMS}} = 6\mu\mathrm{m}^{-1}$. On the left panel, the width of the distribution is fixed, and only the position of the particles is random. On the right panel, the width of the cloud has a random shot to shot fluctuation, of $0.6\mu\mathrm{m}^{-1}$ on average. We see that this 10% fluctuation is enough to create a visible curvature on the uncorrelated, supposedly flat $g^{(2)}$ signal.

2.3 Example of a $g^{(2)}$ measurement : the bosonic bunching

Bunching arises in all bosonic systems, as soon as there are fluctuations in the populations of the modes. It results from multi-particles interferences coupled to the intrinsic bosonic constraint of symmetrization under particle exchange. It can be described as the tendency of bosons to occupy the same quantum state, meaning that the joint probability of measuring two bosons in the same mode is higher than the product of the individual probabilities. Therefore, a bunching behavior can not be demonstrated by measuring only the average population of a quantum state, one need also to access its second-order fluctuations.

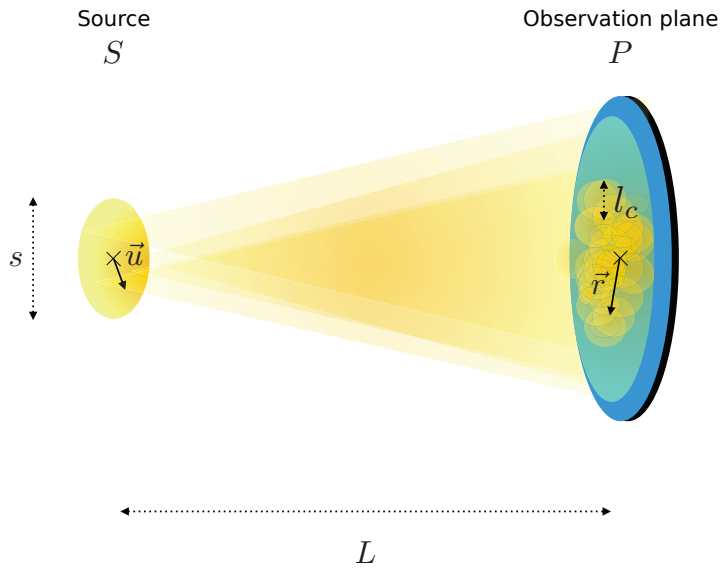

Figure 2.6: Illustration of the HBT effect with classical light : a fully incoherent monochromatic source S of size s produces intensity correlation patterns of size $l_c \propto s^{-1}$ on an observation plane P situated at a distant L, far away from S.

The Hanbury-Brown and Twiss (HBT) effect is one of the most famous manifestation of bosonic bunching. Originally conducted for astronomical purposes in 1956 [87, 88], the HBT experiment raised the debate about the interpretation of the bunching for photons, and it took some time to construct a convincing explanation in terms of quantum particle interference [89]. Since then, HBT-like measurements have been performed on a variety of systems, including atomic ensembles [83, 90, 84]. In this section, we test the algorithm by measuring second-order functions in momentum space for different configurations of trapped clouds. To fix the idea, let us start by a brief description of the HBT effect with classical light.

2.3.1 The Hanbury-Brown and Twiss effect

Generalities

The HBT experiment with classical light is based on the Electromagnetism effect described by the Van Cittert-Zernike theorem [91] : the intensity fluctuations of a radiation emitted by a spatially incoherent source situated far away from the observation plane, are correlated over a distance (or a time) inversely proportional to the size of the source. This is, for instance, the origin of the speckle diffraction pattern, easily observable when a laser is transmitted or reflected by a granular medium.

Let us consider an observation plane P illuminated by a spatially incoherent source S, at a distance L from P (figure 2.6). To simplify the discussion, we assume S to be monochromatic, of wavelength λ. The amplitude A of the field at a point $\vec{r}$ of the plane P is a function of the amplitudes a of all the source points $\vec{u}$, and within the Fraunhofer approximation ($L \gg \lambda, |\vec{r}|, |\vec{u}|$), it can be written :

$$A(\vec{r}) \propto \int_S a(\vec{u}) e^{\frac{i\pi}{\lambda L}|\vec{r}-\vec{u}|^2} \, d\vec{u} \tag{2.11}$$

We define the second order correlation function in amplitude between A_1 and A_2 at position $\vec{r}_1$ and $\vec{r}_2$ of P as :

$$G^{(2)}(\vec{r}_1, \vec{r}_2) = \langle A_1^* A_1 A_2 A_2^* \rangle \tag{2.12}$$

S is spatially incoherent, meaning that the amplitude $a(\vec{u})$ has a random initial phase, uniformly distributed between 0 and 2π. If the probability distribution of this phase is sufficiently broad and homogeneous (meaning that many modes of the field are populated, which is the case for a thermal light) the probability distribution of $A(\vec{r})$ is a gaussian, as a consequence of the central limit theorem [91]. In this case, equation 2.12 can be re-written :

$$G^{(2)}(\vec{r}_1, \vec{r}_2) = \langle I_1 \rangle \langle I_2 \rangle + \langle A_1^* A_2 \rangle \langle A_2^* A_1 \rangle , \tag{2.13}$$

where $I_1 = A_1^* A_1$. The cross terms correspond to $G^{(1)}(\vec{r}_1, \vec{r}_2)$, the first order correlation function of the spatial amplitude in P. From equation 2.11 we have :

$$G^{(1)}(\vec{r}_1, \vec{r}_2) = \langle A_1^* A_2 \rangle \propto \int\int_S \langle a^*(\vec{u}) a(\vec{v}) \rangle \, e^{-\frac{i\pi}{\lambda L}(|\vec{r}_1 - \vec{u}|^2 - |\vec{r}_2 - \vec{v}|^2)} \, d\vec{u} \; d\vec{v} , \tag{2.14}$$

which involves the first order correlation function of the source's spatial amplitude $\langle a^*(\vec{u}) a(\vec{v}) \rangle$. If we suppose that S is perfectly incoherent, we can write $\langle a^*(\vec{u}) a(\vec{v}) \rangle = I(\vec{u}) \delta(\vec{u} - \vec{v})$, and so :

$$G^{(1)}(\vec{r}_1, \vec{r}_2) \propto \int\int_S I(\vec{u}) e^{-\frac{2i\pi}{\lambda L}(\vec{r}_1 - \vec{r}_2)\vec{u}} \, d\vec{u} \; d\vec{v} . \tag{2.15}$$

Hence, $G^{(1)}(\vec{r}_1, \vec{r}_2)$ is given by the Fourier-transform of the intensity distribution of the source. Consequently, for a homogeneous intensity distribution, $G^{(1)}(\vec{r}_1, \vec{r}_2)$ decays on a "correlation" length scale of $l_c = |\vec{r}_1 - \vec{r}_2| \sim \lambda L / 2\pi s$, where s is the size of S. Finally, we can write the normalized second order correlation function :

$$g^{(2)}(\vec{r}_1, \vec{r}_2) = \frac{\langle I_1 I_2 \rangle}{\langle I_1 \rangle \langle I_2 \rangle} = 1 + \frac{|G^{(1)}(\vec{r}_1, \vec{r}_2)|^2}{\langle I_1 \rangle \langle I_2 \rangle} = 1 + |g^{(1)}(\vec{r}_1, \vec{r}_2)|^2 . \tag{2.16}$$

$g^{(2)}(\vec{r}_1, \vec{r}_2)$ is equal to 2 when $\vec{r}_1 \simeq \vec{r}_2$, and to 1 when $|\vec{r}_1 - \vec{r}_2| > \lambda L / s$

In their famous experiment [88], Hanbury-Brown and Twiss used two telescopes to measure the two-point intensity correlation of the light emitted by Sirius, and extracted the apparent angular size of of the star (6.8ms of arc) with a precision of 10%.

Bunching with cold atoms

Bunching effect is not limited to photons, and can be found in other systems, like a thermal gas of bosonic atoms. The first experiment demonstrating the presence of bunching with neutral atoms was conducted by M. Yasuda and F. Shimizu ([92]), using a beam of metastable ^{20}Ne atoms extracted from a magnetic trap, and detected by a golden mirror.

In 2005, different groups performed HBT-like experiments with various cold atom systems. Öttl et al. [93] observed a flat $g^{(2)}$ signal with an atom laser, as it is expected for a coherent source [89, 94]. The atoms were extracted from a BEC contained in a magnetic trap (using an RF radiation transferring the atoms to an untapped state) and detected through a high-finesse cavity using light. The authors demonstrated that adding noise to the RF field induces mode-fluctuations in the atomic beam, "destroying" the coherence and leading to the emergence of bunching. Schellekens et al. [83] also compared the correlations of a coherent and non-coherent gas, by measuring the $g^{(2)}$ function of a BEC and a thermal cloud of metastable Helium. It was

the first experiment to use MCP to measure second order correlations in a cold-atom gas, and their results are compatible with the ideal (non-interacting) case (see 2.3.2). Finally, Fölling et al. [85] measured bunching with a third type of system : a Mott insulator, which is an incoherent lattice gas. Contrary to the two previously cited experiments using atom-counting techniques, Fölling et al. measured the density correlation of an expanding cloud distribution with absorption imaging. The limited resolution of this technique usually does not allow to observe bunching, because the local correlation signal is hidden by the autocorrelation of the cloud when the resolution is bigger than the correlation length. However, in the lattice, the spatial symmetry induces a periodicity in the bunching signal, enabling the possibility to observe "higher-order" bunching peaks outside of the autocorrelation peak.

More recently, Perrin et al. [84] have measured HBT correlations across the Bose-Einstein transition, using a light-sheet to probe density slices of an the expanding ^{87}Rb cloud at the single-atom level. They observed a rapid decay of the bosonic bunching below the critical temperature T_c. A similar study of the $g^{(2)}$ variations across the transition is presented at the end of this manuscript.

2.3.2 Measurement of bosonic bunching with our setup

The measured quantity

In our setup, the observation plane is the MCP detector, and we use the momentum coordinate system : $\vec{k} = m\vec{v}/\hbar$, where $\vec{v}$ is the velocity of the atoms obtained from equations 2.3, 2.4 and 2.5. With those notations, the bosonic bunching leads to a peak centered on $g^{(2)}(\delta k = 0)$. In first approximation, we can model this peak by a gaussian :

$$g^{(2)}(\delta\vec{k}) = 1 + \prod_{i=x,y,z} \exp\left(\frac{-\delta k_i^2}{l_{c_i}^2}\right), \tag{2.17}$$

with l_{c_i}, the second-order momentum correlation length along direction i. For a non-interacting thermal gas of temperature T, released from an harmonic trap of frequency $\omega_{x,y,z}$, the value of l_{c_i} can be linked to the in-trap coherence length $l_i^{(t)}$ (first-order spatial correlation length) through the relation [94] :

$$l_{c_i} = \frac{m\omega_i}{\hbar} l_i^{(t)}. \tag{2.18}$$

The value of the coherence length can also be calculated : $l_i^{(t)} = \hbar/\sqrt{mk_BT} = \lambda_{dB}/\sqrt{2\pi}$, and since the RMS size of the trapped cloud is $s_i = \sqrt{k_B/m\omega_i^2}$, we have :

$$l_{c_i} = 1/s_i. \tag{2.19}$$

which is analogous to the "bosonic" HBT effect : the second-order correlation length after expansion is proportional to the inverse of the source size.

Effect of the finite resolution and integration

If we now take into account the finite resolution of the detector along the 3 axis $(\sigma_x, \sigma_y, \sigma_z)$, the "effective" correlation width that we measure is :

$$w_i = \sqrt{l_{c_i}^2 + (2\sigma_i)^2}. \tag{2.20}$$

The factor of 2 in front of the resolution comes from the fact that : (a) σ_i is defined as a RMS, while l_{c_i} is defined as a $1/e$ width (factor $\sqrt{2}$) and (b) σ_i is the 1-particle resolution, while l_{c_i} is a distance between 2 particles, so we need to consider the 2-particle resolution (another factor $\sqrt{2}$).

We can now write the expression of the measured correlation signal, which takes the form ([94], [78]) :

$$g^{(2)}(\delta\vec{k}) = 1 + h \prod_{i=x,y,z} \exp\left(\frac{-\delta k_i^2}{w_i^2}\right), \tag{2.21}$$

where $h = \prod_i \frac{l_{c_i}}{w_i}$ is the bunching amplitude. We see that when σ_i is of the order of l_{c_i}, the bunching signal is broadened, and the amplitude is reduced.

We also need to take into account the effect of the transverse integration $\Delta k_\perp$ described in section 2.2.2. In practice, to increase the correlation signal, we often have $\Delta k_\perp > l_{c_i}$, which further reduces the bunching amplitude. For the calculation, let assume that we compute the function $g^{(2)}(\delta k_z)$ along axis z, by integrating the signal over $\pm\Delta k_\perp$ along x and y, we thus have :

$$\begin{aligned} g^{(2)}(\delta k_z) &= \frac{1}{(2\Delta k_\perp)^2} \iint_{-\Delta k_\perp}^{\Delta k_\perp} 1 + h \prod_{i=x,y,z} \exp\left(\frac{-\delta k_i^2}{w_i^2}\right) dxdy \\ &= 1 + h\frac{\pi w_x w_y}{(2\Delta k_\perp)^2} \exp\left(\frac{-\delta k_z^2}{w_z^2}\right) \operatorname{erf}\left(\frac{\Delta k_\perp}{w_x}\right) \operatorname{erf}\left(\frac{\Delta k_\perp}{w_y}\right), \end{aligned} \tag{2.22}$$

with $\operatorname{erf}(x) = \frac{2}{\sqrt{\pi}} \int_0^x \exp(-y^2)dy$, the error function.

Results

We have measured second-order correlations in momentum space for the following systems :

- A BEC, which is a spatially coherent source where no bunching is expected.
- A thermal cloud ($T > T_c$) released from the ODT, which constitute a spatially incoherent, anisotropic source. As mentioned before, the momentum bunching in such a system is compatible with the non-interacting case, meaning that the interactions between the Helium atoms are weak enough for the cloud to behave like an ideal source of bosons. The anharmonicity of the trap should lead to an anharmonicity of the bunching peak (equation 2.19).
- A thermal cloud released from the lattice (incoherent isotropic source with periodic bunching).

All those measurements have been performed with MCP B.

Thermal lattice gas Contrary to the ODT, the external trapping potential of the 3D lattice constitutes a quasi-isotropic trap (see section 1.1.3). Even if it is unclear how HBT remains valid for the strongly interacting lattice gas (see chapter 5), it is reasonable to think that this isotropy of the trap will lead to a rather isotropic shape for the bunching peak in momentum, which will help us to evaluate the resolution of the detector along the 3 spatial axis. We compute

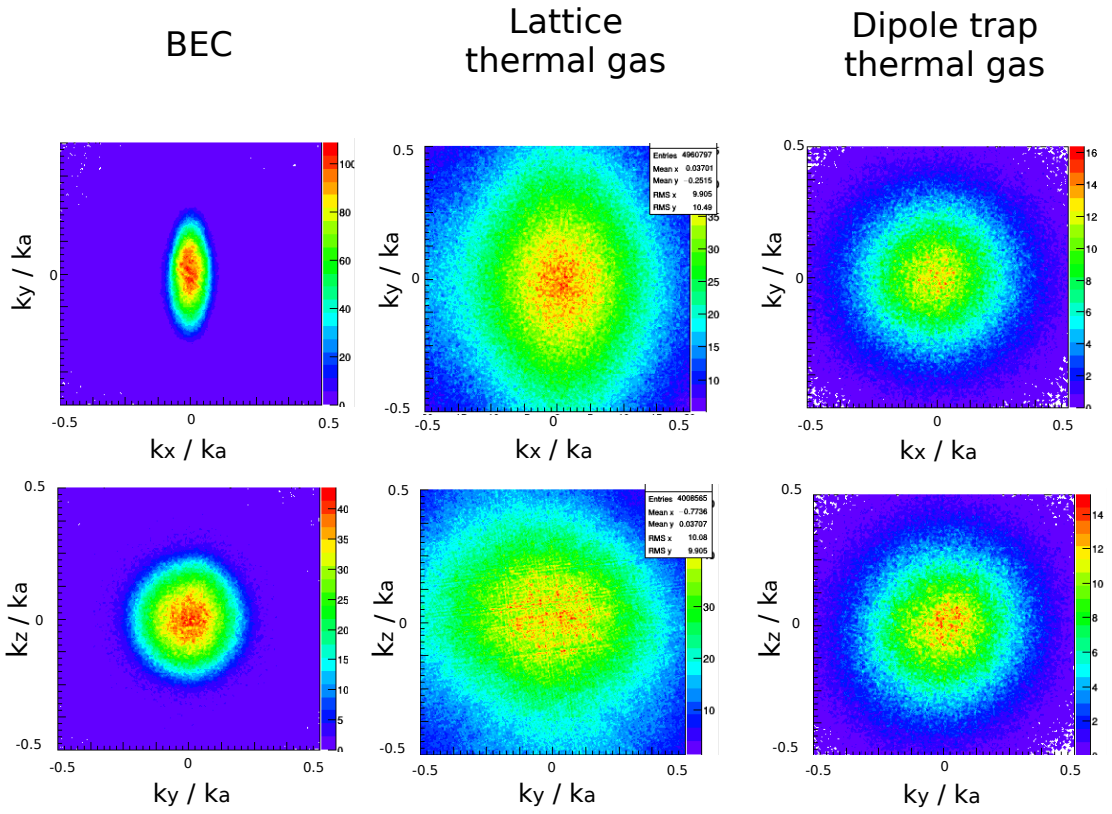

Figure 2.7: Different systems to test the algorithm : a Bose-Einstein condensate, a thermal gas released from the lattice, and a thermal gas released from the dipole trap. The 2D pictures are plotted along the science chamber axis, and are obtained by integrating the 3D density distribution along the transverse direction (the 2D plot (k_x, k_y) is obtain by integrating the full distribution along the axis k_z etc.

the $g^{(2)}$ function of a thermal cloud of about 40×10^3 atoms released from the lattice with $V_0 \simeq 9.6E_r$, corresponding to the following trapping frequencies along the lattice eigen-axes : $(308, 295, 298)$Hz, estimated from the oscillations of a BEC inside the trap formed by the first passage (no retro-reflections) of the 3 lattice beams. Let's recall that one of the lattice beam is aligned along the x direction of the science chamber, and the two other beams are crossing with a 45° angle in the transverse plane (y, z), so that the correlations along y and z are not calculated along the lattice axes (figure 1.11). The temperature of the cloud, evaluated with our thermometry method (see chapter 5) is about 40% above the critical temperature, ensuring the absence of condensed fraction. The dataset corresponds to $\sim$ 3000 experimental realizations, with $\sim$ 2500 detected particles per shot.

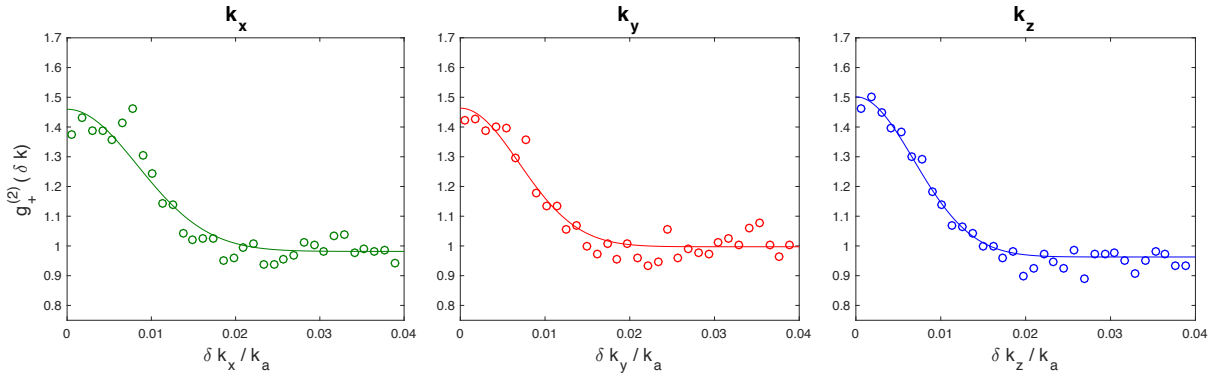

Figure 2.8: Local second-order correlation function $g_+^{(2)}(\delta k)$ in the thermal lattice gas. The correlations are calculated along the 3 axis (x, y, z), with a transverse integration $\Delta k_\perp = 0.0072\, k_a$. The solid line in each panel is a gaussian fit $b + a\exp(-\delta k^2/w^2)$ used to extract the effective bunching amplitude a, the effective correlation width w, and the baseline b.

Figure 2.8 shows the result of the algorithm calculation along the 3 axis, for $\Delta k_\perp = 7.2 \times 10^{-3} k_a$ (in unit of the lattice wave vector, defined in section 1.1.3). We clearly see the presence of a peak at $\delta k = 0$ in all directions, which is the signature of a 3D bunching. With a gaussian fit, we extract the parameters of this correlation peak along the 3 directions and we find :

Table 2.1: Parameters of the correlation peak in the thermal lattice gas

	x	y	z (gravity)
Bunching amplitude	0.48 ± 0.03	0.47 ± 0.03	0.54 ± 0.025
Bunching width (unit of k_a)	$11.8 \pm 0.8 \times 10^{-3}$	$9.8 \pm 0.7 \times 10^{-3}$	$9.6 \pm 0.5 \times 10^{-3}$
Baseline	0.98 $\pm$0.05	1 $\pm$ 0.05	0.96 $\pm$ 0.01

As explained in the previous section, the interesting quantity of the bunching peak lies in its correlation width l_{c_i}, which is linked to the measured width w_i and the resolution σ_i through

equation 2.20. In particular, when l_{c_i} is of the order of σ_i, one has to know precisely the resolution to be quantitative about the correlation width. Unfortunately, this is not an easy task with our detector : as we saw in section 1.2.4, the in-plane resolution of the MCP depends on the flux of particle reaching the plates, and it has not been directly measured for all flux regimes. We can roughly estimate it through the measurement of $\sigma_D/2\sqrt{2}$ (equation 1.19), which is close to the TDC limit for this dataset, i.e. $\sigma_x \sim \sigma_y \sim 1.4 \times 10^{-3}\, k_a$ (60μm in real-space unit). On the other hand, the vertical resolution has never been estimated experimentally. If we use the geometrical limitation given by the micro-channels angle (equation 1.20) as a definition of the vertical resolution, we find $\sigma_z \sim 4.2\times10^{-3}\, k_a$, which leads to two inconsistencies. Firstly, it would result in a very anisotropic bunching $(l_{c_x}, l_{c_y}, l_{c_z}) = (11.5, 9.4, 5)\times10^{-3}\, k_a$ difficult to justify; and secondly, equation 2.22 would give an effective bunching amplitude of 0.4 along the gravity axis, slightly off compared to the measured 0.54 ± 0.025. We shall then change our analysis strategy.

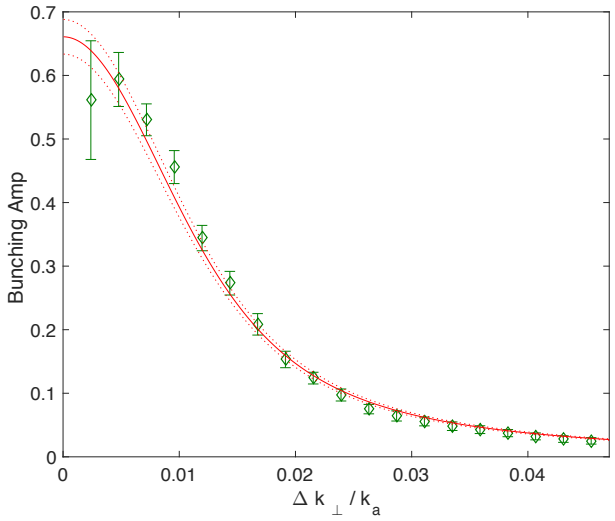

Figure 2.9: Effective bunching amplitude of the thermal lattice gas, as a function of the transverse integration $\Delta k_\perp$. The solid line is a fit based on equation 2.22 to extract the resolution $\sigma_x \simeq \sigma_y \simeq \sigma_z$. To perform the fit, we use the effective correlation width $w_{x,y,z}$ extracted from figure 2.8, and we assume that the real bunching amplitude is 1, so that $g^{(2)}(\delta k = 0) = 2$. From the fit, we obtain $\sigma_{x,y,z} = 2.5 \pm 0.1 \times 10^{-3}\, k_a$.

Considering the symmetry of the lattice trap, it is plausible that the correlation length is identical along direction y and z (both calculated at 45° of the lattice axis), and slightly different along the direction x (calculated along the lattice axis). It is also reasonable to assume that the in-plane resolution is identical along x and y, because the signal is treated by the same electronic chain. In the following, we thus postulate $l_{c_y} = l_{c_z}$, and $\sigma_x = \sigma_y$, and since $w_y \simeq w_z$, we also have $\sigma_y \simeq \sigma_z$. So by posing $\sigma_{x,y,z} = 2.45 \times 10^{-3}\, k_a$, the bunching amplitude calculated from equation 2.22 becomes compatible with the measured amplitude, and it leads to $(l_{c_x}, l_{c_y}, l_{c_z}) = (10.6, 8.3, 8.1)10^{-3}\, k_a$. To be a bit more precise and to further test equation 2.22, we run the algorithm for several transverse integrations $\delta k_\perp$, and fit the variation of the bunching amplitude to extract the resolution. The results are shown in figure 2.9, and confirm that equation 2.22 describes well the decay of the bunching amplitude with $\Delta k_\perp$. The fit gives $\sigma_{x,y,z} = 2.5 \pm 0.1 \times 10^{-3}\, k_a$.

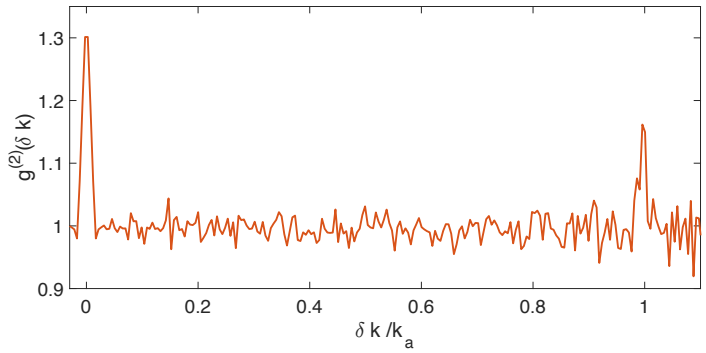

Figure 2.10: Function $g_+^{(2)}(\delta k)$ calculated along the lattice axis, with $\Delta k_\perp = 12 \times 10^{-3}\, k_a$. In addition to the local bunching, a correlation signal is visible at $\delta k = k_a$, illustrating the periodic bunching expected from the lattice structure.

Finally, in figure 2.10, we have plotted the function $g_+^{(2)}(\delta k)$ along the lattice axis, calculated with $\Delta k_\perp = 12 \times 10^{-3}\, k_a$ over a larger δk domain to investigate the k_a periodicity of the correlation signal, expected for a thermal gas inside a lattice [22]. The signal indeed exhibits two correlation peaks, at $\delta k = 0$ and $\delta k = k_a$, the latter being about half the height of the first one. An explanation of this difference can arise from the difficulty to precisely identify the vector $\vec{k}_a$ along which we plot the profile. Empirically, a mistake of a few degrees in the determination of the lattice axis is enough to make the secondary peak collapses.

ODT thermal gas We now investigate the bunching in a thermal cloud of about 3×10^5 atoms released from the anisotropic ODT. The trapping frequencies along the science chamber axis are the following, up to a 10% uncertainty, : $(118, 361, 418)$Hz. The $g^{(2)}$ calculation is computed for $\Delta k_\perp = 12\times10^{-3}\,k_a$, on a dataset of ~ 500 realizations with 1500 atoms detected per shot. The result is shown in figure 2.11.

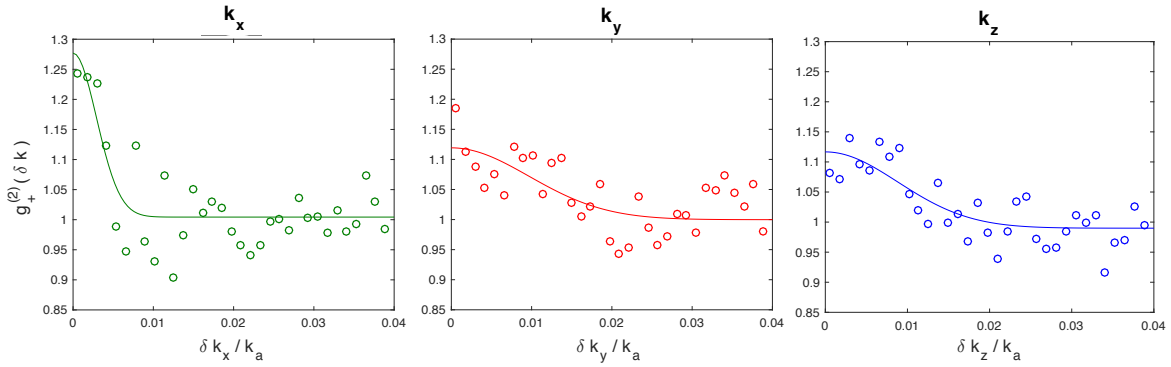

Figure 2.11: Local second-order correlation function $g_+^{(2)}(\delta k)$ in the ODT thermal gas. The correlations are calculated along the 3 axis (x, y, z), with a transverse integration $\Delta k_\perp = 0.012\,k_a$. The solid line in each panel is a gaussian fit $b + a\exp(-\delta k^2/w^2)$ used to extract the effective bunching amplitude a, the effective correlation width w, and the baseline b.

The temperature T of the gas can be directly extracted with a bose fit from the momentum profile (see figure 2.12) and we find $T = 320\pm30$nK. The RMS size s_i of the trapped cloud along direction i can be deduced from an energetic argument :

$$\frac{1}{2}m\omega_i^2 s_i^2 = \frac{1}{2}k_B T \quad \Rightarrow \quad s_i = \sqrt{\frac{k_B T}{m\omega_i^2}}, \tag{2.23}$$

leading to $(s_x, s_y, s_z) \simeq (35, 11.4, 9.8)\,\mu$m. One can wonder if this system is well described by an HBT treatment, since at this temperature, we do not have $\lambda_{dB} \ll s_i$, in other words, the correlation length of the source is not very small compared to the size of the system. For the thermal cloud inside the ODT, $\lambda_{dB} = 1.5\mu$m at $T = 320$nK, while the size of the system along the less confining direction (x) is 36μm (factor of 20). It is thus incorrect to treat the first-order correlation function of the source as a delta function (equation 2.14 to equation 2.15). Furthermore, the central limit theorem used to justify a gaussian distribution of the atomic density in the observation plane is not valid close to the transition, where the Bose statistic leads to an occupation of a finite number of low energy modes. That being said, a full calculation of the two-body correlations in an expanding, ideal Bose gas taking into account the Bose-Einstein statistic have been performed in [94]. The authors show that even at the critical temperature, the $g^{(2)}$ function calculated over the entire cloud corresponds to the "HBT limit", which justifies the use of s_i^{-1} to evaluate l_{c_i}.

We thus find : $(l_{c_x}, l_{c_y}, l_{c_z}) = (s_x^{-1}, s_y^{-1}, s_z^{-1}) = (3.5, 11, 12.6)\times10^{-3}\,k_a$ with a 12% uncertainty. Using the resolution obtained previously $\sigma_{x,y,z} \simeq 2.5\times10^{-3}\,k_a$ (the flux of detected particles is similar than the lattice gas one, so the in-plane resolution should be close), we deduce the expected effective width $(w_x, w_y, w_z) \simeq (6\pm1,\ 12\pm2,\ 14\pm3)\times10^{-3}\,k_a$, compatible with the

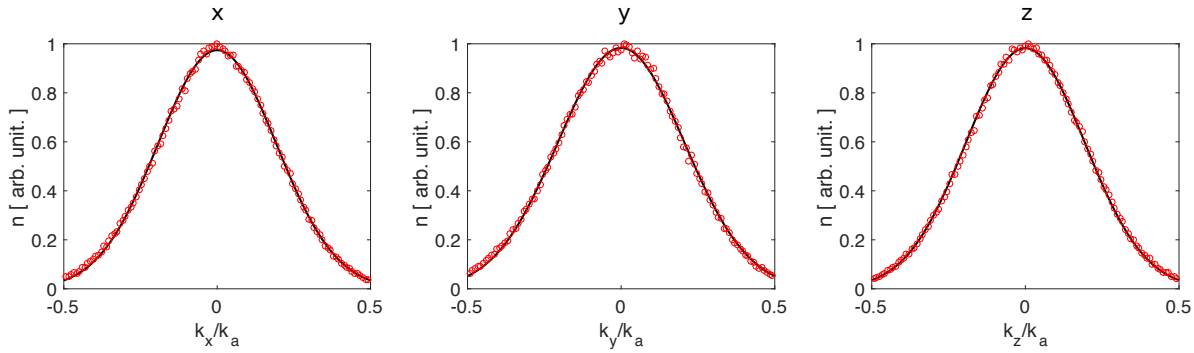

Figure 2.12: 1D plot of the thermal cloud released from the ODT obtained by integrating the distribution along the transverse directions (red dots). Fitting this distribution with a Bose function (black line) allows us to extract the temperature of the cloud at $T = 320$nK.

Table 2.2: Parameters of the correlation peak in the ODT thermal gas

	x	y	z (gravity)
Bunching amplitude	0.27 ± 0.05	0.12 ± 0.03	0.127 ± 0.03
Bunching width (unit of k_a)	$4.1 \pm 0.9 \times 10^{-3}$	$13.6 \pm 4 \times 10^{-3}$	$12.6 \pm 3 \times 10^{-3}$
Baseline	1 ± 0.01	1 ± 0.01	0.99 ± 0.005

value extracted from the gaussian fit (see table 2.2). Finally, by taking into account the transverse integration ($\Delta k_\perp = 12 \times 10^{-3}\, k_a$), we can calculate the expected width and amplitude of the 3D bunching from equation 2.22, and we find (0.3 ± 0.05, 0.17 ± 0.03, 0.16 ± 0.03), also compatible with the measured amplitude within error-bars. It is interesting to notice that, even though the equipartition of the thermal energy leads to a spherical momentum distribution, the anisotropy of the trap is still "coded" in the cloud through its two-particles correlation function.

BEC Finally, we compute the $g^{(2)}$ of a BEC of about 2×10^5 atoms released from the ODT. As expected, the correlation signal is flat along the 3 axis (figure 3.11), because of the spatial coherence of the cloud. The high number of atoms, even with a low RF transfer, ensures a good signal-to-noise ratio.

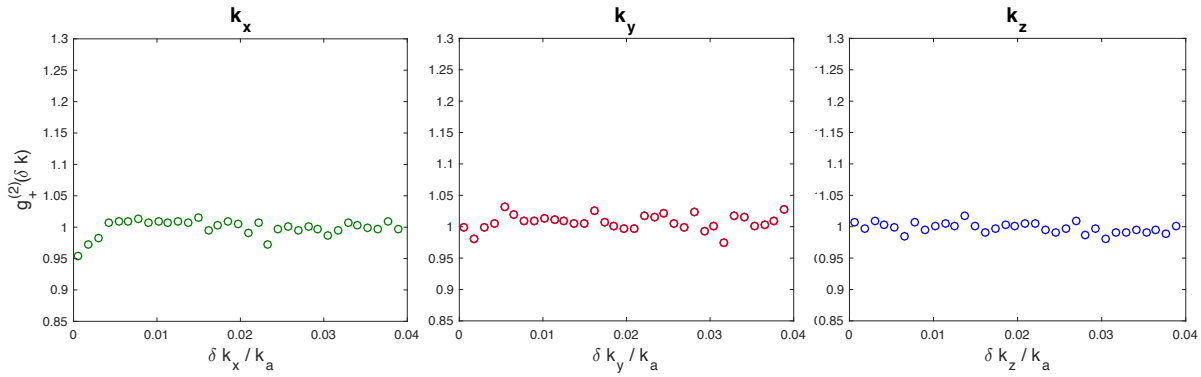

Figure 2.13: Local second-order correlation function $g_+^{(2)}(\delta k)$ in the BEC. The correlations are calculated along the 3 axis (x, y, z), with a transverse integration $\Delta k_\perp = 0.012\, k_a$.

Chapter 3

Investigating the asymptotic momentum distribution of a Bose-Einstein condensate

The first system we wish to study is the Bose-Einstein Condensate (BEC) in a harmonic trap. Predicted by A. Einstein in the mid 1920s, it is defined as a macroscopic occupancy of the lowest energy level of a thermodynamic ensemble. The BEC was first seen as a theoretical curiosity emerging form the low temperature behavior of the Bose-Einstein statistics, but in 1937, the discovery by P. L. Kapitza [95] and J. F. Allen [5] of superfluidity in liquid ^{4}He constituted the first experimental observation of this phenomenon, as F. London made the link between the superfluid transition and the Bose-Einstein condensation [96]. In the 1980s, with the rapid development of laser cooling techniques, the possibility to observe a gaseous BEC became real, and the first condensates were obtained in 1995 at JILA by E. Cornell and C. Wieman with ^{87}Rb [9] and at MIT by W. Ketterle with ^{23}Na [97]. Those discoveries paved the way for a new generation of cold atom experiments, where the coherence properties of this new state of matter are used to study quantum physics in a new way.

A BEC in a harmonic trap is a conceptually very simple object. At $T \simeq 0$, it can be described as a gas where almost all the atoms occupy the 1-particle ground state of the trap. However, it possesses a richness of many-body phenomenon to explore, from in-trap collective excitations [98, 99], to contact interactions [100, 101], or expansion dynamic [102, 103]. In our setup, where the scattering length can not be tuned to zero, the release of the mean-field energy during the free-fall distorts the cloud [104], preventing us to access the in-trap momentum distribution from a Time of Flight (ToF) measurement. Yet, we can still hope to observe signatures of many-body manifestations in the asymptotic momentum distribution.

The first section briefly recalls some generalities about trapped BEC, and defines key quantities that will be used throughout the manuscript (chemical potential, critical temperature, condensed fraction, ...). The second section describes the experiment we conducted at the beginning of this thesis, and the observation of a power-law k^{-4} decay in the asymptotic momentum distribution of the expanding BEC. This first series of measurements led to a publication in 2016 [105], where this power-law tail is interpreted as a signature of the quantum depletion (see also [30]). This initial interpretation, and its controversies, are discussed. In the last section, we present a series of recent measurement giving new insights on the origin of this signal.

3.1 The trapped Bose-Einstein condensate

3.1.1 Quantum statistics and condensation of ideal bosons

Einstein and Bose

In one of his famous (or rather legendary) articles of 1905 [106], A. Einstein postulates the existence of light's quanta to explain the photoelectric effect. Twenty years later, S. Bose inferred the mathematic formula governing the statistics of an ensemble of indistinguishable photons, recovering Planck's law [107]. Shortly after, Einstein generalized the concept for an ideal gas of massive particles, providing the first quantum theory of an ideal gas [108]. The Bose-Einstein distribution thus replaces the Maxwell-Boltzmann distribution at low temperature, by taking into account the indistinguishability of the microscopic particles. For a gas of Bosons at temperature T, the average number of particles $\langle n_k \rangle$ per mode k can be written :

$$\langle n_k \rangle = \frac{1}{e^{(\epsilon_k - \mu)/k_B T} - 1}, \tag{3.1}$$

where ϵ_k is the energy of the mode k, k_B is the Boltzmann constant, and μ is the chemical potential, that fixes the number of particles. By studying the behavior of this distribution at low T, Einstein predicted that below a certain critical temperature T_c, a macroscopic portion of the atoms will "condensate" in the lowest energy mode available [108].

Condensation in a harmonic trap

Let's consider an ensemble of N non-interacting particles of mass m confined in a 3D harmonic potential of frequency $(\omega_x, \omega_y, \omega_z)$. In such a trap, the energy levels are well known [109], and can be written

$$\epsilon_{n_x,n_y,n_z} = \hbar\omega_x n_x + \hbar\omega_y n_y + \hbar\omega_z n_z + \epsilon_0, \tag{3.2}$$

with $\epsilon_0 = \frac{\hbar}{2}(\omega_x + \omega_y + \omega_z)$, the ground state energy of the harmonic trap, sometimes referred to as the "zero-point" energy. We note N_0 the number of atoms in the ground state, and N_{exc} the number of atoms in the excited states. From the Bose-Einstein distribution, it can be shown that N_{exc} can be written :

$$N_{exc} = \left(\frac{k_B T}{\hbar\varpi}\right)^3 \sum_{n>0} \frac{Z^n}{n^3}, \tag{3.3}$$

where we have defined the fugacity $Z = e^{(\mu-\epsilon_0)/k_B T}$, and $\varpi = (\omega_x\omega_y\omega_z)^{1/3}$. The sum in this last expression can be expressed as a polylogarithm function $g_3(Z)$, bounded above by $\zeta(3)$, where ζ is the Riemann function. It means that for a given T, the population in the excited states has an upper bound :

$$N_{exc} \leq \left(\frac{k_B T}{\hbar\varpi}\right)^3 \zeta(3). \tag{3.4}$$

Consequently, the population of the excited states can be saturated, and any new particle added to the system will automatically populate the lowest energy mode. If we now fix the number of particles, but make the temperature vary, N_{exc} will saturate as soon as $N = \left(\frac{k_B T}{\hbar\varpi}\right)^3 \zeta(3)$, leading to an expression for the critical temperature :

$$T_c = \frac{\hbar\varpi}{k_B}\left(\frac{N}{\zeta(3)}\right)^{1/3}. \tag{3.5}$$

Below T_c, the maximum value of N_{exc} is smaller than N, and since $N_0 = N - N_{exc}$, the lower the temperature, the higher N_0. This mechanism can lead to an arbitrary large occupancy of the ground state, which is precisely the phenomenon known as the Bose-Einstein condensation. This accumulation of particles in a single microscopic state results in a phase coherence over the entire system. By analogy with the laser, the BEC can be seen as a coherent source of matter-wave.

Another useful quantity to define is the condensed fraction :

$$f_c = \frac{N_0}{N} = 1 - \left(\frac{T}{T_c}\right)^{1/3} \tag{3.6}$$

For our experimental parameters, T_c is of the order of 700nK, and the coldest temperatures we can achieve are of the order of $\mu/k_B = 200$nK, leading to $f_c \simeq 98\%$. The thermally excited fraction is called the "thermal depletion" of the condensate.

3.1.2 The mean-field approximation

Two-body contact interactions

Up to now, we have neglected the interactions between the particles. In the following, we consider only the 2-body interactions, which can be described by scattering theory [110]. For our very low temperatures, the only relevant process is the s-wave scattering, characterized by the scattering length a_s, that is positive for repulsive interactions. Within this approximation, the potential for contact interactions can be written :

$$V_{int}(\vec{r}_i - \vec{r}_j) = \frac{4\pi\hbar^2 a_s}{m}\delta(\vec{r}_i - \vec{r}_j) = g\delta(\vec{r}_i - \vec{r}_j) \tag{3.7}$$

For a $m_J = +1$ spin-polarized gas in the 2^3S_1 state of ^{4}He*, $a_s = 7.5\text{nm} \simeq 142a_0$, where a_0 is he Bohr radius.

The Gross-Pitaevskii equation

We can now write the complete hamiltonian of the system :

$$H = \sum_i \left[\frac{\vec{p_i}^2}{2m} + V_{trap}(\vec{r}_i)\right] + \sum_{i\neq j} V_{int}(\vec{r}_i - \vec{r}_j). \tag{3.8}$$

To solve this equation analytically, we use the so-called mean-field approximation. The idea is to get rid of the mathematical difficulties raised by the 2-body interactions, by considering that all the particles "feel" the same mean-field, given by the average of the interaction potentials with all the other particles of the gas. Hence, the ground state becomes a product of 1-particle states $|\psi\rangle = |\phi\rangle \otimes |\phi\rangle \otimes ... \otimes |\phi\rangle$. We then use the variational principle, minimizing $\langle\psi| H |\psi\rangle - \mu \langle\psi|\psi\rangle$, which leads to the Gross-Pitaevskii (GP) equation [111, 112] for the 1-particle state:

$$\mu\phi(\vec{r}) = -\frac{(\hbar\vec{\nabla})^2}{2m}\phi(\vec{r}) + V_{trap}(\vec{r})\phi(\vec{r}) + Ng|\phi(\vec{r})|^2\phi(\vec{r}), \tag{3.9}$$

where the non-linear term $Ng|\phi(\vec{r})|^2\phi(\vec{r})$ corresponds to the mean-field potential.

For a non-interacting gas in a harmonic trap, the shape of the ground state's wave function is given by the (gaussian) ground state of the harmonic oscillator, but the presence of the mean-field potential modifies this shape. Like most of the experiments involving trapped BEC, our

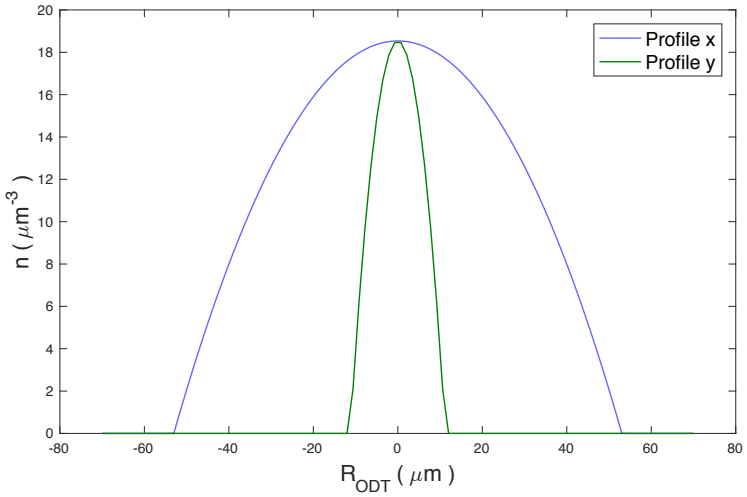

Figure 3.1: Thomas-Fermi prediction for the in-situ density profile of a Bose-Einstein condensate with our experimental parameters (2×10^5 atoms, see section 3.2.1). The distribution is plotted along two axis : x (89Hz trapping frequency), and y (419Hz trapping frequency).

system is well described by the Thomas-Fermi approximation[110], where the mean-field energy is large enough so we can neglect the kinetic term. The GP equation thus gives :

$$\phi(\vec{r}) = \sqrt{\frac{\mu - V_{trap}(\vec{r})}{g}} e^{i\theta(\vec{r})}, \tag{3.10}$$

where the phase $\theta(\vec{r})$ has to be homogeneous to minimize the energy. We finally obtain the in-trap density profile $n(\vec{r}) = |\phi(\vec{r})|^2$, known as the Thomas-Fermi profile :

$$n(\vec{r}) = \frac{\mu}{g}\left[1 - \sum_{i=x,y,z}\left(\frac{r_i}{R_i}\right)^2\right], \tag{3.11}$$

where $R_i = \sqrt{\frac{2\mu}{m\omega_i^2}}$ is the Thomas-Fermi radius. Figure 3.1 shows a plot of $n(\vec{r})$ obtained by using equation 3.11 with our experimental parameters.

Finally, it is useful to introduce the healing length, which represents a beyond mean-field correction to the Thomas-Fermi profile [110] :

$$\xi = \frac{\hbar}{\sqrt{2m\mu}}. \tag{3.12}$$

Indeed, ξ is the minimum length-scale over which $n(\vec{r})$ can vary. In other words, if the trap potential varies on distance shorter than ξ, the density will not be able to follow, and the profile will be smoothened. In the mean-field work-frame, $2\pi/\xi$ also defines the largest momentum component of the BEC.

Free-fall expansion

When released from the trap, the mean-field energy converts into kinetic energy, and thus plays a role in the expansion of the cloud. Using the time-dependant GP equation in the Thomas-Fermi regime, one can show that the density profile remains parabolic throughout the expansion [104], but the exact solution has to be calculated numerically. It is however possible to infer the asymptotic root-mean-square velocity v_∞ of the atoms released from an isotropic trap, with an energy conservation relation [110] :

$$v_\infty^2 = \frac{\hbar^2}{m^2 R(0)^2} + \frac{gN}{3\sqrt{2\pi^3} m R(0)^3}, \tag{3.13}$$

where $R(0)$ is the Thomas-Fermi radius at the beginning of the expansion. It clearly shows the effect of the trap on the expansion : the tighter the trap, the smaller $R(0)$, and so the bigger v_∞. Even if equation 3.13 is calculated for an isotropic trap, the physical intuition remains valid for various geometries : squeezing the atoms along one direction will raise the amount of mean-field energy released in that direction, changing the aspect-ratio of the cloud. For instance, our cigar-shaped Optical Dipole Trap (ODT) gives "birth" to a pancake-shaped cloud at large ToF.

3.1.3 Beyond mean-field : the Bogoliubov approach

Introduction

Because of its high condensed fraction, the weakly interacting BEC at finite temperature is well described by the Bogoliubov approach [113], that takes into account the interactions beyond the mean-field approximation. To describe this theory, we need to introduce the second-quantization formalism, that will also be useful in the next chapter. For simplification, we consider a homogeneous system of volume V instead of the harmonic trap.

Let a_k and $a_k^\dagger$ be the annihilation and creation operators of momentum $\hbar k$. Applying a_k (resp. $a_k^\dagger$) to the wave function of the gas destroys (resp. creates) a particle with momentum $\hbar k$. We have the usual commutation relations :

$$[a_i, a_j] = 0, \tag{3.14}$$

$$[a_i, a_j^\dagger] = \delta_{i,j}. \tag{3.15}$$

With those notations, the Hamiltonian takes the form :

$$H = \sum_k \frac{\hbar^2 k^2}{2m} a_k^\dagger a_k + \frac{g}{2V} \sum_{k_1,k_2,l} a_{k_1-l}^\dagger a_{k_2+l}^\dagger a_{k_1} a_{k_2}, \tag{3.16}$$

where l stands for the momentum conservation during the interaction process.

Bogoliubov transformation

If $f_c \simeq 1$, most of the atoms are in the $k = 0$ state, and the collisions will mainly occur between condensed atoms, or between a condensed atom and an atom in a higher k-mode, but rarely between two $k \neq 0$ atoms. The Bogoliubov approximation consists in keeping only the second order terms in $k \neq 0$ in the expression of H, and replacing a_0 and $a_0^\dagger$ by $\sqrt{N_0}$. The hamiltonian can then be split in two parts : a part containing only the $\sqrt{N_0}$ terms, taking the form of the mean-field Hamiltonian (GP), and a part beyond the mean-field description containing all the $k \neq 0$ operators, that can be written :

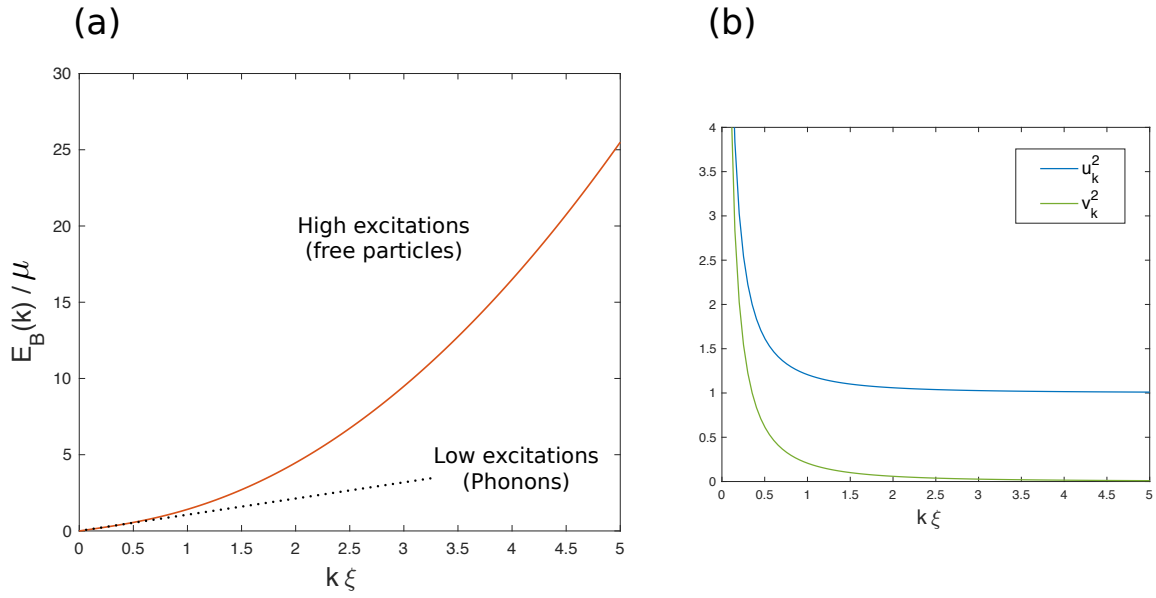

Figure 3.2: (a) Energy spectrum of Bogoliubov excitations, plotted as a function of $k\xi$. The low-k behavior is linear (phonon-like excitations), while the high-k is quadratic (free-particles excitations). (b) Square of the Bogoliubov coefficients, u_k^2 and v_k^2. Both coefficients diverge at $k = 0$.

$$H_B = \sum_{k\neq 0} \left(\frac{\hbar^2 k^2}{2m} + gn \right) a_k^\dagger a_k + \frac{gn}{2} \sum_{k\neq 0} (a_k^\dagger a_{-k}^\dagger + a_k a_{-k}), \tag{3.17}$$

where we have made the approximation $N_0/V = n$. By essence, H_B contains all the informations about the collective excitations of the BEC (at least to the second order in a_k). We therefore switch to the basis of the "quasi-particles" elementary excitations $(b_k^\dagger, b_k)$, defined by :

$$b_k^\dagger = u_k a_k^\dagger + v_k a_{-k}, \tag{3.18}$$

with u_k and v_k, the Bogoliubov coefficients. In this basis, H_B takes the simple form :

$$H_B = \sum_{k\neq 0} E_B(k) b_k^\dagger b_k, \tag{3.19}$$

which is the expression of a non-interacting gas of quasi-particles. The energy spectrum of those quasi-particles is :

$$E_B(k) = \sqrt{\frac{\hbar^2 k^2}{2m} \left(\frac{\hbar^2 k^2}{2m} + 2gn \right)}. \tag{3.20}$$

Like shown in figure 3.2 (a), $E_B(k)$ possesses a phononic linear part for low excitations ($k \ll \frac{1}{\xi}$), and a free particle quadratic part for high excitations ($k \gg \frac{1}{\xi}$). Figure 3.2 (b) shows a plot of the square of the Bogoliubov coefficients u_k^2 and v_k^2, that can be easily expressed from the quasi-particles energy-spectrum :

$$u_k^2 = \frac{\hbar^2 k^2/2m + gn + E_B(k)}{2E_B(k)}, \tag{3.21}$$

$$v_k^2 = \frac{\hbar^2 k^2/2m + gn - E_B(k)}{2E_B(k)}, \tag{3.22}$$

Quantum depletion

Now let us calculate the number of atoms in the excited states N_{exc}, also referred as the depleted atoms. We start from $N_{exc} = \sum_k \langle a_k^\dagger a_k \rangle$, and we apply the Bogoliubov transformation, leading to :

$$N_{exc} = \sum_{k\neq 0} (u_k^2 + v_k^2) \langle b_k^\dagger b_k \rangle + \sum_{k\neq 0} v_k^2. \tag{3.23}$$

The left term of the sum corresponds to the already mentioned thermal depletion. The average number of quasi-particles $\langle b_k^\dagger b_k \rangle$ is given by the Bose-Einstein distribution, and a gas at $T = 0$ (no excitations) corresponds to a vacuum of quasi-particles, i.e. $\langle b_k^\dagger b_k \rangle = 0$. However, even at $T = 0$, we have $N_{exc} \neq 0$, because the right term of the sum does not vanish. This term corresponds to the atoms leaving the condensate due to the interactions, as it is energetically favorable to maintain a small fraction of atoms in the excited state to lower the total energy. This population is called the quantum depletion.

3.2 Observation of a k^{-4} decay in the asymptotic momentum distribution of a BEC

In this section, we present the 2016 results published in Physical Review Letters [105], where the investigation of the asymptotic momentum distribution of an expanding BEC leads to the observation of a k^{-4} decay in the high momentum regions. More details on this study can also be found here [30].

3.2.1 Experimental sequence and momentum profiles

Preparation and detection of the condensate

We start by loading a spin polarized $m_J = +1$ BEC of about 2×10^5 atoms in our ODT. The following trapping frequencies are used for this experiment : $(\omega_x, \omega_y, \omega_z) = 2\pi \times (89, 419, 438)$Hz. We can apply or not a controlled heating sequence. In that case, the lattice beams are adiabatically turned ON in 30ms and superimposed to the ODT, we then heat-up the gas by applying non-adiabatic lattice pulses of 500μs. After that, the cloud is kept 100ms in the lattice for thermalization, before being adiabatically loaded back inside the ODT.

The gas is finally released by rapidly ($\sim 2\mu$s) switching off the trap. To regulate the flux of atoms reaching the detector, we apply a Radio-Frequency (RF) sweep after 2ms of expansion in order to transfer a fraction of the atoms to the non-magnetic $m_J = 0$ state. The detuning between the magnetic sub-levels is set to 10MHz with a magnetic bias, and we span the RF frequency by 1MHz around the resonance. The sweep is performed in 1ms, during which the RF power is kept constant, the value depending on the fraction of atoms we want to transfer. Right after this RF sequence, we apply a magnetic gradient in order to remove all the atoms that are

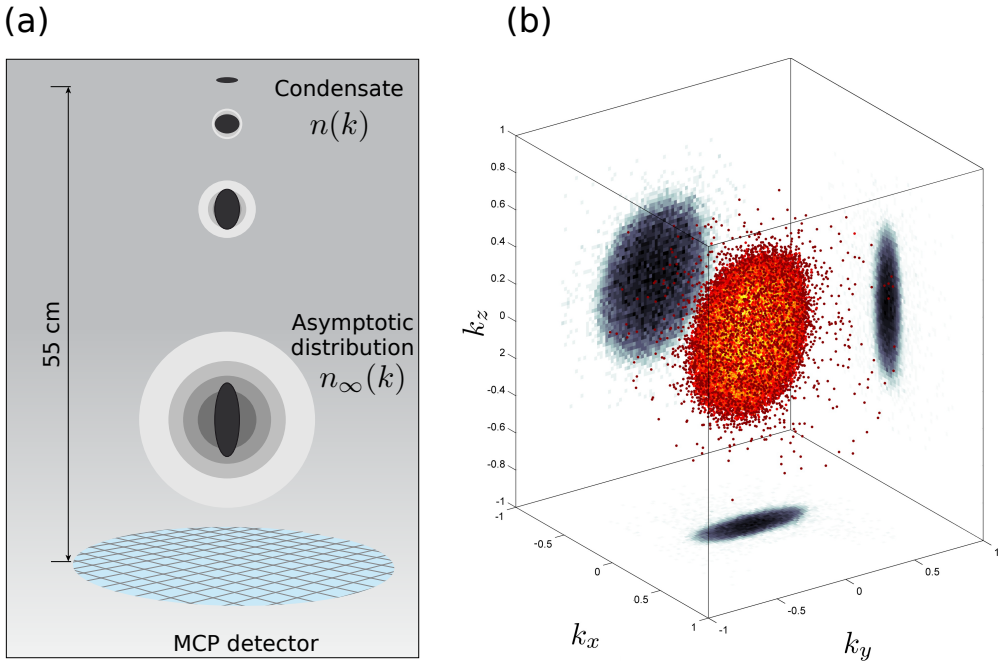

Figure 3.3: (a) The cloud expands from the cigar-shaped trap and inverts its aspect ratio due to the mean-field potential, while depleted atoms escape the trap with a spherical symmetry. When the cloud is very diluted, the expansion becomes ballistic and the distribution can be mapped to the asymptotic momentum distribution $n_\infty(\vec{k})$ that we detect onto the MCP. (b) Reconstruction of $n_\infty(\vec{k})$ obtained by averaging a few hundred of experimental cycles.

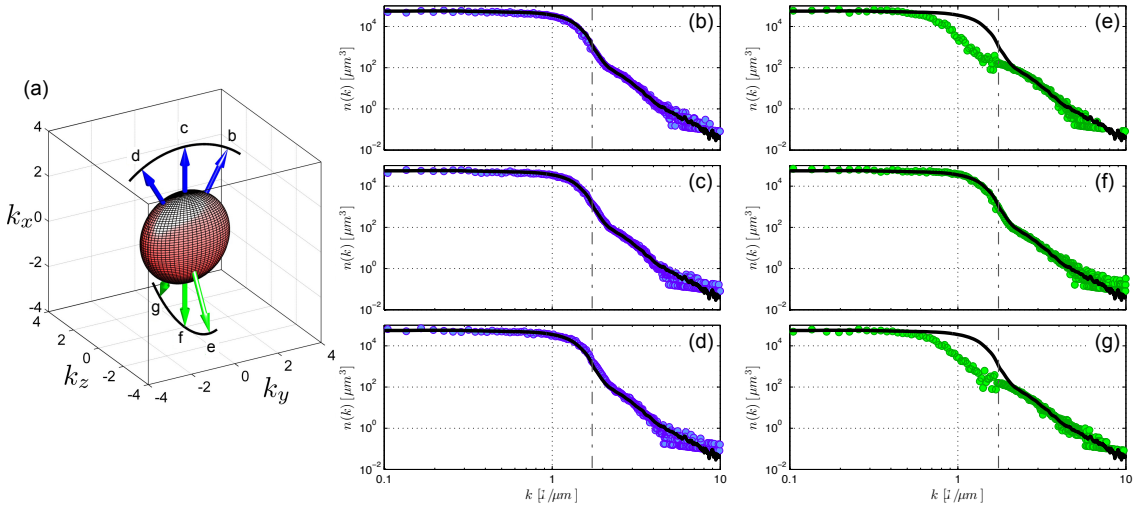

Figure 3.4: Log-log scale plots of the 1D momentum profiles obtained from counting the number of atoms inside narrow tubes oriented along various directions. The vertical dashed-dotted line indicates the separation between the central dense distribution (the BEC), and the surrounding low density distribution (excited particles above the BEC). The blue dotted lines correspond to the profiles calculated along the radial direction (b), (c) and (d). The green dotted lines correspond to the profiles calculated along the transverse direction direction (e), (f) and (g). The solid black line is an average of the three radial profiles, and highlight both the anisotropy of the BEC distribution and the isotropy of the diluted distribution beyond the BEC.

not in the non-magnetic state before they can reach the detector. Like explained below, this flux regulation allows us to circumvent the saturation effect, and explore a large range of densities.

The MCPs are located 55cm below the trap, leading to a mean ToF of 325ms. The velocity $\vec{v}$ of the detected atoms are reconstructed using equations 2.3, 2.4, 2.5. We define the momentum $\vec{k} = m\vec{v}/\hbar$ (expressed in μm^{-1}), and the asymptotic distribution detected onto the MCP is noted $n_\infty(\vec{k})$. Figure 3.3 presents an example of such a distribution obtained with the detector. We observe an anisotropic dense central region corresponding to the condensate, and a diluted, isotropic distribution around. The "pancake" shape of the condensate is a consequence of the mean-field potential.

Extraction of the 1D density profiles

We generate 1D density profiles from the 3D distribution by counting the number of particles inside narrow tubes, centered onto the BEC's center-of-mass. Those tubes are oriented along various directions in order to study the isotropy of the distribution. In figure 3.4, we see that the low density region around the BEC seem to have a spherical symmetry, because the 1D profiles decay similarly along all the six directions. On the contrary, the condensate's distribution is anisotropic because of the release of the mean-field energy.

For all the directions, we have used two different sizes for the tubes. In the high density regions (between 0 and $2\mu\text{m}^{-1}$) the transverse size of the tubes is $\pm 0.1\mu\text{m}^{-1}$, while in the low density regions (beyond $2\mu\text{m}^{-1}$), the transverse size is $\pm 0.8\mu\text{m}^{-1}$. For those measurements it was not possible to perform a spherical integration, because the MCP H1 is damaged in the central region (see figure 1.16).

To increase the density dynamic of the detected distributions, we merge data with a high-flux of particles falling onto the detector (typically 45% of the initial distribution transferred to the detectable state by RF coupling), and data with a low-flux of particles (typically 15% of RF transfer). Indeed, at high-flux, the denser region of the distribution (the core of the BEC) saturates the MCP, while at low-flux, the signal in the diluted halo is too low, and it would require much more experimental runs to extract the average profile. With this merging technique, we manage to reconstruct a density profile over more than 5 decades (figure 3.5), with typically half-a day of data-taking.

3.2.2 Observation of a k^{-4} decay : effect of temperature and density

Asymptotic momentum distribution

First, let's insist on the fact that the observed distribution $n_\infty(\vec{k})$ can not be directly associated to the in-situ momentum distribution $n(\vec{k})$. Indeed, the mean-field energy ($\sim \mu$) released at the beginning of the ToF dominates the typical kinetic energy given by the momentum distribution ($\sim \hbar^2 \omega_{\rm odt}^2/\mu$). For our system, within the mean-field approximation, $\mu/h \simeq 4$kHz, while $\omega_{\rm odt}/2\pi = 438$Hz for the most confining direction, so that $\mu \gg \hbar\omega_{\rm odt}$. Our observable is rather the asymptotic momentum distribution, i.e., the momentum distribution of the expanding cloud when the density has dropped sufficiently for the expansion to become ballistic.

Longitudinal momentum profile

We focus on the 1D momentum-profile along the radial direction of the condensate, because the angular symmetry allows to integrate the distribution over a larger volume (i.e. over more tubes). The radial distribution of $n_\infty(\vec{k})$ obtained with this integration is plotted on figure 3.5. We observe 3 momentum-regions. The first region (**I**) is the one associated to the condensate, while the two other regions (**II** and **III**) are situated outside of the condensate, in the low density part of the distribution. Figure 3.6 presents the simulations performed by C. Qu of the 3D mean-field expansion, obtained with the GP equation at $T = 0$. It shows that region **I** has the expected width due to the release of the mean-field energy, and that region **II** and **III** are not predicted by the zero-temperature mean-field theory.

The second region (**II**) is well adjusted by a polylogarithm $g_{3/2}$ function (see equation 3.24), corresponding to the Bose distribution integrated over the harmonic trap [114]. We interpret it as the signature of the thermal depletion due to a non-zero temperature in the system. It corresponds to the thermal excitations of the condensate, and thus its population grows with the temperature. This interpretation is validated by the fact that the population of this region raises as we increase the temperature of the gas (see below). The last region (**III**) has a k^{-4} scaling over one decade. The physical interpretation of this last contribution will be discussed thoroughly in the following.

Effect of the temperature

To confirm the nature of region (**II**), we raise the temperature T of the gas with the controlled heating sequence. Figure 3.7 shows 1D radial profiles obtained for different T. We clearly see that region **II** is more and more populated as we increase T, and still compatible with a thermal distribution. Region **III** keeps roughly the same amplitude and scaling for all the temperatures, so it does not seem to be related to the thermal excitations of the gas. The fit function we use to extract the parameters describing region (**II**) and (**III**) is :

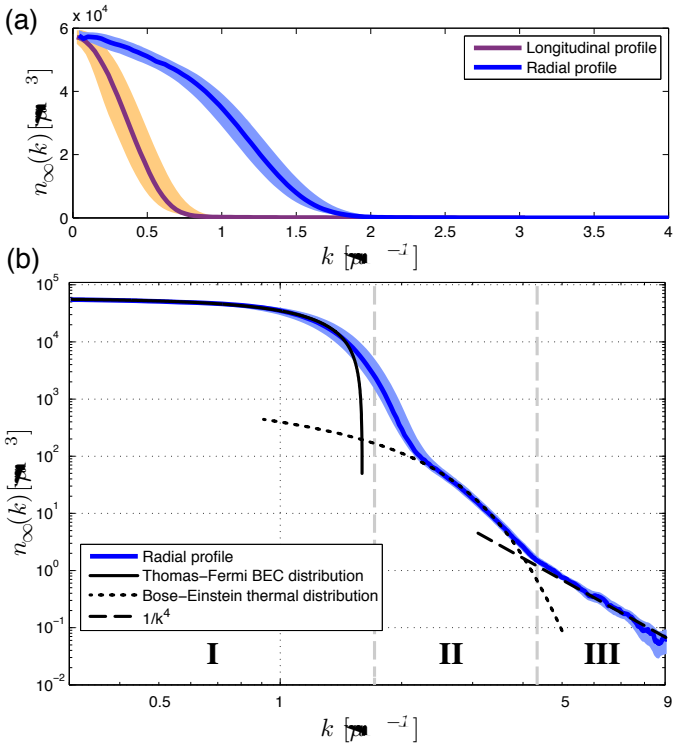

Figure 3.5: (a) Linear plot of the momentum profiles along the radial (blue) and longitudinal (purple) directions. The solid lines are a smoothed average of the data, while the shaded area indicates the standard deviation. (b) Log-log scale plot of the radial profile. We distinguish 3 parts. Region **I** is associated to the condensate, and the solid black line show the mean-field scaling solution in the Thomas-Fermi approximation. Region **II** is associated to the thermal depletion, and the dotted line is a non interacting Bose fit. We can extract the temperature of the gas from this fit, which in this case is $T = 0.22\,T_c$. Finally, region **III** has a polynomial decay over a decade, compatible with a k^{-4} power law (dashed-line).

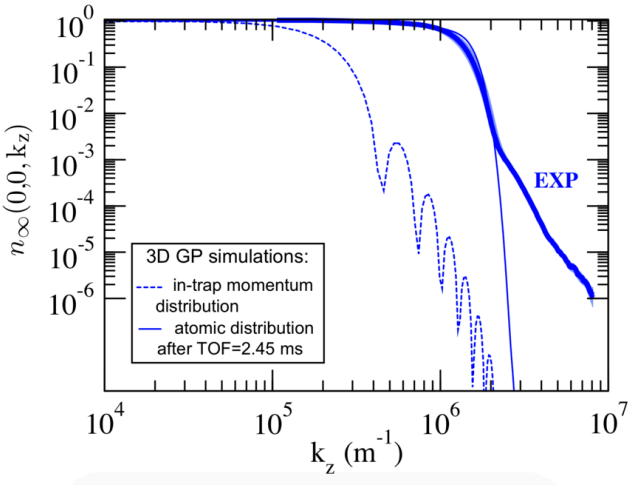

Figure 3.6: Comparison between the experimental radial profile, and the mean-field simulation of the expansion dynamics of a BEC at $T = 0$ with our experimental parameters. The central density has been normalized to one for both the numerics and the data. The simulation is based on the GP equation, beyond the Thomas-Fermi approximation, and we see that asymptotic solution does not reproduce the observed low density tails.

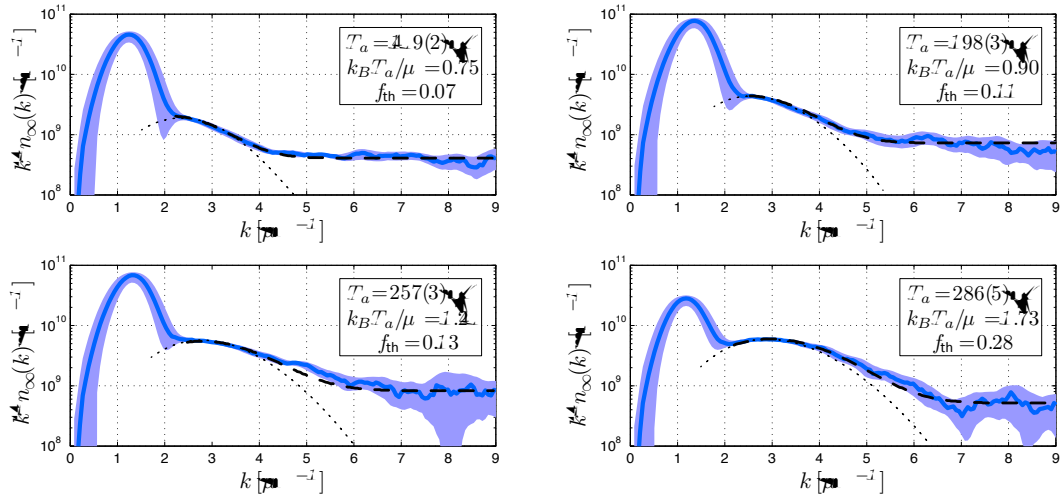

Figure 3.7: Semi-log plot of the $k^4 n_\infty(k)$ distribution along the radial axis for various temperature, the solid blue lines are a smoothed average of the data, while the shaded area indicates the standard deviation. The dashed-line is a fit using equation 3.24, while the dotted line is a fit of the thermal part only. For each panel, we indicate the extracted temperature, the ratio $k_B T/\mu$, and the thermal fraction $f_{th} = N_{th}/N$.

$$n_{\text{fit}}(k) = \frac{N_{th} g_{3/2}[exp(-k^2\lambda_{dB}^2/4\pi)]}{1.202(2\pi/\lambda_{dB})^3} + \frac{\mathcal{A}}{(2\pi)^3 k^4}, \tag{3.24}$$

with N_{th} the number of thermally depleted atoms, λ_{dB}, the thermal de Broglie wavelength, and $\frac{\mathcal{A}}{(2\pi)^3}$, the amplitude of the k^{-4} tail. Note that N_{th} and λ_{dB} are independent parameters of the fit, but those two physical quantities are connected through equation 3.6. For each temperatures, we have checked that the extracted values of $f_{th} = N_{th}/N$ and T were indeed following the expected behavior (see chapter 4 of [30]).

Effect of the density

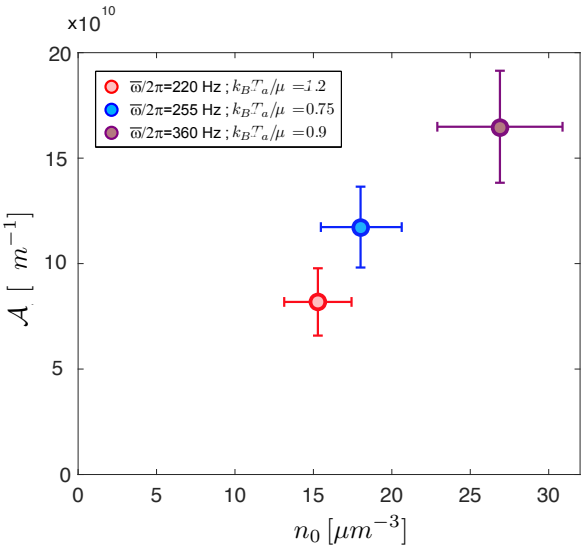

Figure 3.8: Amplitude $\mathcal{A}_\infty = lim_{\to\infty}(2\pi)^3 k^4 n_\infty(k)$ plotted as a function of the central density n_0.

We can also vary the density of the cloud by changing the trapping frequencies $(\omega_x, \omega_y, \omega_z)$, directly linked to the ODT's laser Intensity. We observe an increase of the tail's amplitude in region **III** as we raise the density (figure 3.9), suggesting that this feature is linked to the interactions between the particles.

3.2.3 Initial interpretation : the quantum depletion

Quantum depletion and Tan's contact

The spherical symmetry of regions **II** and **III** suggests that those distributions are not affected by the mean-field energy during the ToF, and we assume they can be related to original momentum features of the trapped gas. Another way to say this is to notice that those regions extend beyond $k = 2\pi/\xi$, meaning that the initial kinetic energy of those atoms is higher than the highest kinetic energy provided by the mean-field potential, so their expansion is mainly due to their initial velocity.

A k^{-4} decay of the momentum distribution is expected for a gas described by 2-body contact interactions. This power-law comes from the Fourier transform of the 1-body density matrix

[115]. It has been directly observed in fermionic systems [116], and probed in bosonic system with spectroscopy methods [19]. The amplitude of this decay, the so called Tan's contact, has the amazing property of being connected to various macroscopic thermodynamic quantities of the system (free energy F, volume V , pressure P ...) through universal relations [117, 118]. In particular, the contact C is the thermodynamic conjugate of the inverse scattering length through the equation of state of the gas :

$$dF = -SdT - PdV + \mu dN + Cd\frac{1}{a_s} \tag{3.25}$$

This k^{-4} decay is also predicted by Bogoliubov, since the v_k^2 momentum distribution of the quantum depletion (equation 3.23) scales as k^{-4} for high k (equation 3.22), and its amplitude corresponds to Tan's contact. The total momentum distribution of an interacting BEC at finite temperature is therefore composed of :

- the condensate itself, whose in-situ momentum distribution is a narrow peak around $k = 0$, and whose asymptotic distribution is enlarged by the mean-field potential.

- the thermal depletion, whose distribution is a Bose function (or rather a polylogarithm function in the case of a trapped system).

- the quantum depletion of the atoms populating higher k-modes because of 2-body interactions. At high k, its momentum distribution decays as k^{-4}.

At this level where both the BEC and the thermal depletion are identified, it is tempting to relate the observed k^{-4} tail of $n_\infty(k)$ to the quantum depletion. Beyond the simple match in scaling and symmetry, the tail's amplitude seems rather insensitive to a change of temperature (figure 3.7), while it increases with the density (figure 3.8). To compare this variations with the theory, we evaluate the amplitude of the contact C for our trapped system, using the local density approximation (valid for inhomogeneous system of size s, if $k \gg s^{-1}$). We find :

$$C = (2\pi)^3 \lim_{k\to+\infty} k^4 \times n(k) = (2\pi)^3 \lim_{k\to+\infty} k^4 \times \frac{\hbar^3}{(2\pi\hbar)^3} \int |v_k(\vec{r})|^2 d\vec{r} \simeq \frac{64\pi^2}{7} a_s^2 n_0 N_0 \text{ [105]}. \tag{3.26}$$

Hence C/N_0 varies linearly with the central density n_0, and we thus re-plot the data of figure 3.9 as a function of $\mathcal{A}/N_0$ (figure 3.9). The result is compatible with a linear scaling, but the slope is higher than the theory by a factor of ~ 6.4, which challenges our interpretation.

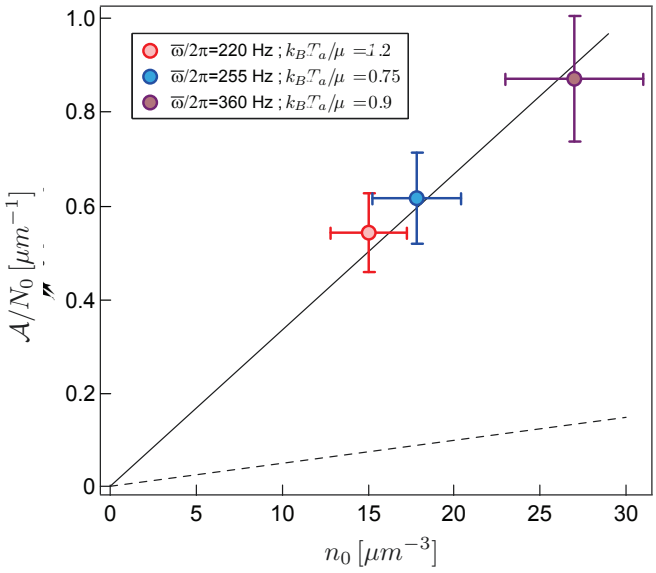

Figure 3.9: Amplitude $\mathcal{A} = lim_{\to\infty}(2\pi)^3 k^4 n_\infty(k)$ per condensed particle N_0, plotted as a function of the central density n_0. The dashed line is the Bogoliubov prediction in the local density approximation. The solid line is the Bogoliubov prediction times 6.4.

Time dependence of the contact in an expanding atomic system

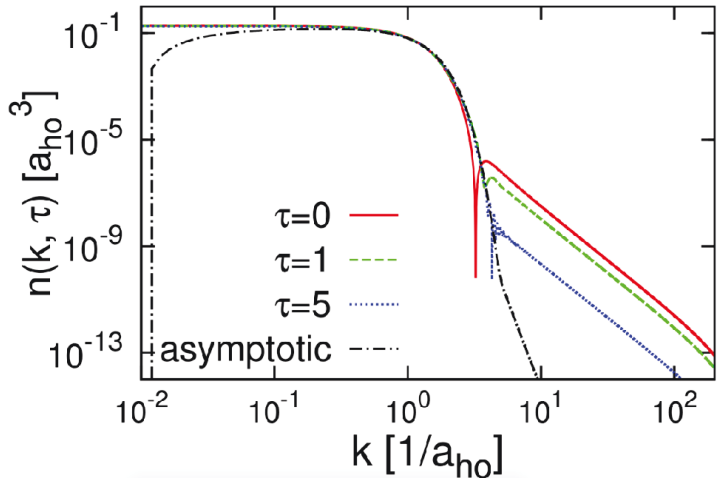

Figure 3.10: Log-log scale plot of the momentum distribution of an expanding system of two interacting particles (scattering length a), released from a harmonic trap (frequency ω and length $a_{\rm ho}$). The different plots represent different expansion times, in unit of the dimensionless parameter $\tau = \omega\, t$. We see a progressive decay of the amplitude of the k^{-4} tail, that vanishes at large time.

We have collaborated with C. QU, L. Pitaevskii and A. Stringari to better understand the dynamic of the momentum distribution during the first instants of the ToF, when the cloud

density is still high, and the interactions between the atoms still play a role. In [103], they have investigated the evolution of the momentum distribution of various expanding systems at $T = 0$. Analytic results on the trapped unitary Fermi gas suggest that the high k component associated to the contact interactions should vanish on a timescale of $1/\omega$, where ω is the trapping frequency. They also used Monte-Carlo simulations on a simple two-particles model, and show that the asymptotic momentum distribution do not exhibit k^{-4} tails either, even though the in-trap momentum distribution possesses such features (see figure 3.10). Those conclusions have a rather simple physical interpretation : during the expansion, the high-k components of the gas ($k \gg \mu$) follow adiabatically the decay of the condensate density, resulting in an adiabatic decay of the value of the contact, in a timescale of $1/\omega$. In other words, in absence of a non-adiabatic process that would disturb the dynamic of the expansion (quickly turning off the interactions for instance), one should not expect to see a k^{-4} decay in the asymptotic momentum distribution.

3.3 New measurements : the role of the $m_J = 0$ atoms

The results discussed in this section shine some new lights on the 2016 measurements, especially due to the observation of a non zero in-trap population of atoms in the $m_J = 0$ state (the trapped BEC being mainly a spin-polarized $m_J = +1$ gas). Those results are very preliminary, and we are still investigating those questions in order to produce a more detailed study in the future.

3.3.1 New setup and experimental sequence

We have conducted a series of new measurements with some updates on the apparatus :

- First, the MCP have been lifted up by 10 cm, reducing the ToF by 10%. We observe similar profiles with this new configuration, supporting the idea that what we measure is an asymptotic distribution, and not a transient shape.
- We also use a different pair of MCP (MCP B, with no hole in the middle), enabling us to perform broader integrations, and to confirm the spherical symmetry of the distribution in the tails.
- The broader integration volume allows to calculate $g^{(2)}$ functions. The results are shown in figure 3.11. The absence of correlations in region **I**, and the observation of bunching in region **II** and **III** further confirm that the tails of the distribution do not belong to the condensate [83]. We stress the fact that this bunching signal is mainly given by region **II**, as region **III** alone is too diluted to provide enough correlation statistics.
- We changed the RF transfer stage, by performing a Rabi oscillation rather than a sweep. It helps us to better control the amount of atoms transferred in the detectable state. We also investigate the impact of the instant of the transfer, by shining the RF at different time after the release of the cloud : at the very begining of the expansion ($\sim 2\mu$s after the opening of the trap), while the cloud is still very dense (in our case, $1/\omega \sim 300\mu$s), and after 10ms, when the cloud is very diluted, and the expansion is ballistic. We do not observe any difference on the asymptotic profiles.

3.3.2 Presence of an in-trap spin mixture

We eventually realized that a small fraction (less than 1%) of the atoms present in the ODT were actually in the $m_J = 0$ state. To measure this population, we simply let the cloud expand in the

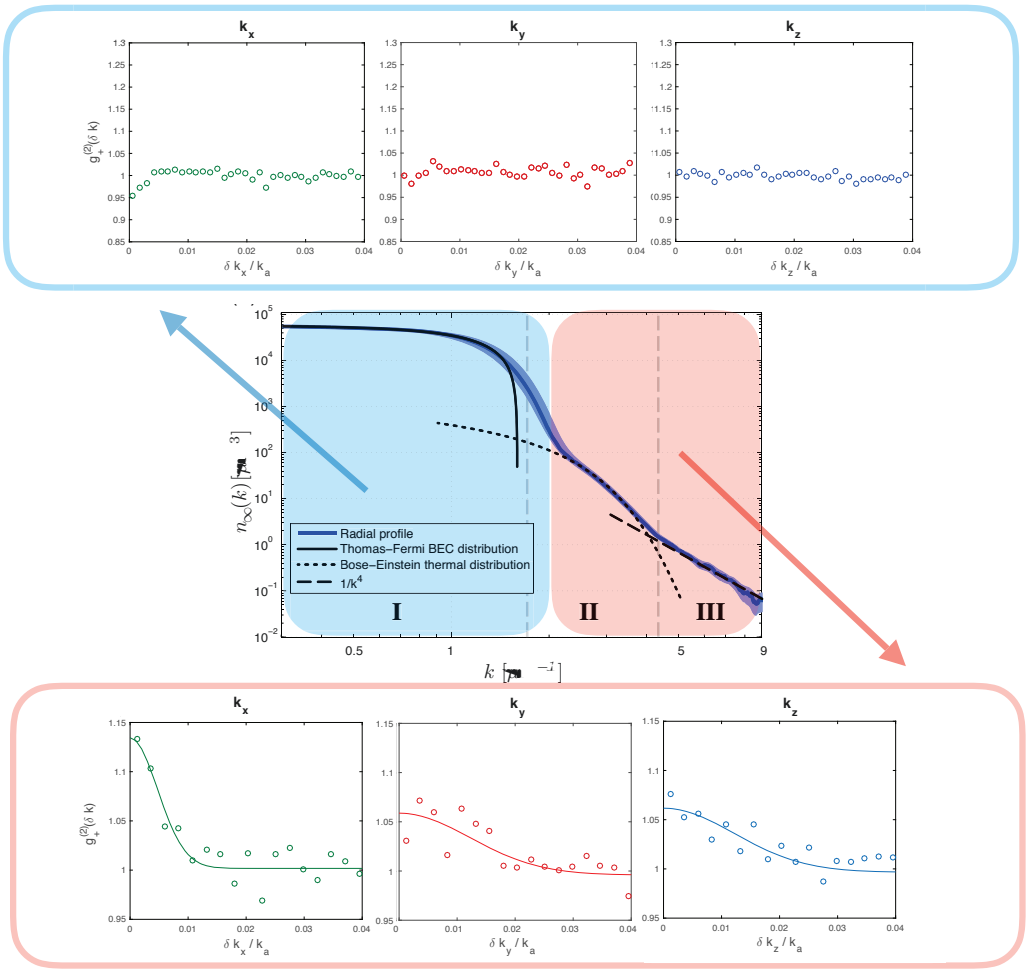

Figure 3.11: Local second order correlation functions calculated in the different momentum regions. The atoms in regions **II** and **III** exhibit a clear bunching signature, confirming that they do not belong to the condensate. Note that due to the density difference between region **II** and **III**, the correlation signal is dominated by the atoms of region **II**. The asymmetry of the bunching peak and amplitude is due to the asymmetry of the trap (see chapter 2).

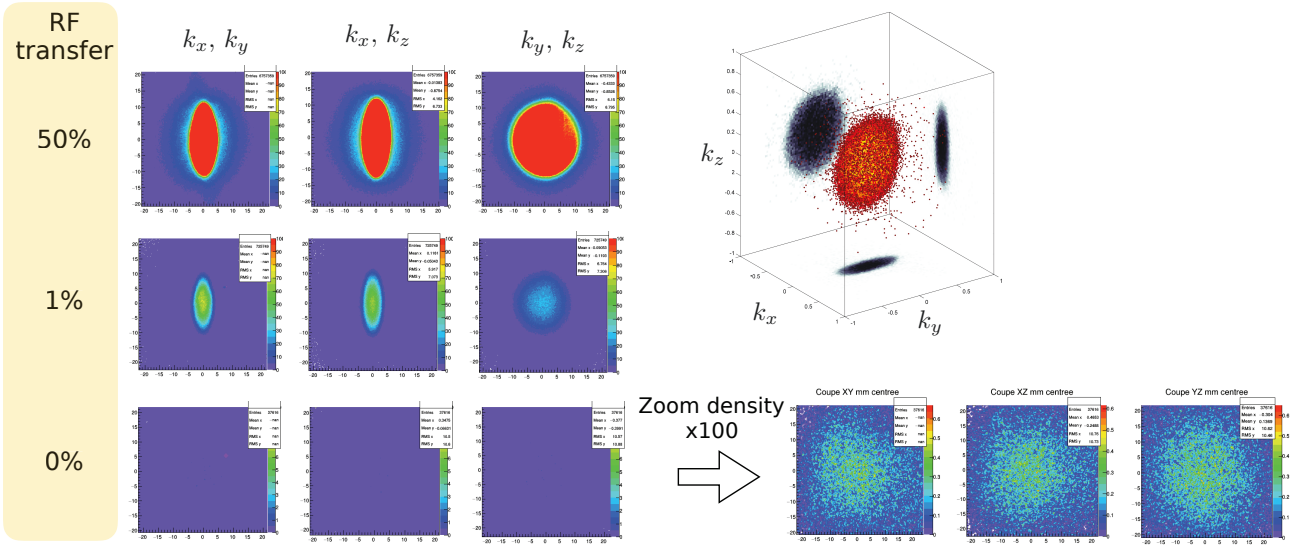

Figure 3.12: 2D projections of $n_\infty(k)$ obtained by integrating the density along the orthogonal axis (the (k_x, k_y) projection is obtained by integrating the density along k_z, etc.). The projections are shown for different RF transfer, corresponding to the amount of $m_J = +1$ atoms transferred to the detected state $m_J = 0$. Even in absence of RF transfer (0%), a diluted cloud of atoms is detected, indicating that an in-trap population of atoms is in the $m_J = 0$ state.

presence of a magnetic gradient, without making any RF transfer, so the only atoms reaching the plate are the one insensitive to magnetic fields. Like we see on figure 3.12, the observed distribution is rather isotropic and very diluted, with no visible condensed fraction. We did not notice it with the 2016 setup, because most of the distribution was falling in the "hole" of the MCP detector (the central defect of MCP H1, see figure 1.16). Furthermore, this distribution is way too diluted to be observed by absorption imaging.

Origin and lifetime

Having $m_J = 0$ atoms in the ODT is unexpected, because it is loaded from the quadrupole trap, that contains only $m_J = +1$ atoms. However, it is possible that spin-flips occur during the transfer, since it requires an opening of the quadrupole and a displacement of the cloud. This can lead to non-trivial, and magnetically "non-adiabatic" trajectories (Majorana spin-flip effect [59]). There also exists a possible in-trap creation process [37], where two +1 atoms collide and flip their spin. We have ruled out this last hypothesis by making a similar experimental cycle, but with a spin polarized $m_J = -1$ BEC, where such spin-relaxation mechanism are not energetically favorable, and we observed the same amount of atoms in $m_J = 0$.

In the absence of an in-trap creation mechanism, the population in $m_J = 0$ should rapidly decay due to the penning collisions. The 0-0 penning collision rate is very high ($k_2^0 = 7.6 \times$

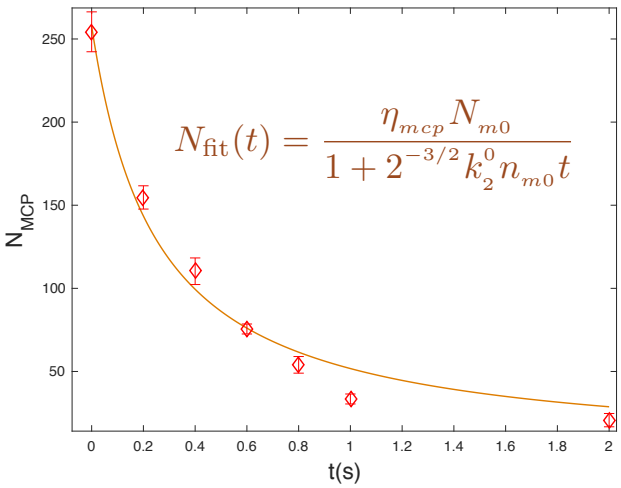

Figure 3.13: Number of $m_J = 0$ atoms detected onto the MCP in absence of RF transfer, as a function of the holding time after evaporation. Assuming that the lifetime is limited by 2-body 0-0 Penning collisions, and that the in situ distribution of the cloud is gaussian, the extracted central density n_{m0} is $16 \pm 2 \times 10^{15}\mathrm{m}^{-3}$. MCP B were used for those measurements, so that we have assume $\eta_{\mathrm{mcp}} = 25\%$ (see chapter 1)

$10^{-10}\,\mathrm{cm}^3\,\mathrm{s}^{-1}$ [119]), 4-orders of magnitude higher than the 1-1 rate. After the evaporation, we have measured the decay of the $m_J = 0$ population to extract the in-trap density (figure 3.13). By assuming a gaussian distribution, the initial central density extracted from the fit is $16 \times 10^{15}\mathrm{m}^{-3}$, not far from the expected $8 \times 10^{15}\mathrm{m}^{-3}$ for a thermal distribution at equilibrium with the BEC (measured at $\sim$ 300nK for those parameters). So the very low density of $m_J = 0$ atoms allows the coud to survive a few seconds in the ODT.

Asymptotic momentum distribution

The most peculiar aspect of those "parasites" atoms in $m_J = 0$ is their asymptotic momentum distribution $n_\infty(k)$. The cloud has a spherical symmetry, and its radial distribution is not compatible with a Bose function (see figure 3.14). In particular, at large k, the distribution scales as k^{-4}, and we thus wonder if this cloud is responsible for the k^{-4} decay observed in 2016. In a regular experimental cycle, the atoms reaching the plates are always in $m_J = 0$, the BEC distribution observed on the detector being transferred in $m_J = 0$ from the $m_J = +1$ state with a RF pulse. The same pulse also transfers a part of the parasite atoms in $m_J = \pm 1$, while the rest of the cloud remains in $m_J = 0$, and is thus detected. Hence, the total distribution measured on the detector is a mixture of the two clouds, and it is not straightforward to know which is which.

Separation of the spin components One solution is to separate the two distributions in ToF. It actually raises several technical difficulties with our current setup. Differentiating the two clouds' high k components requires to separate them by large distances. Figure 3.15 shows a measurement in which we have separated the two distributions by the maximum distance allowed by the MCP detector ($\sim 4\mu m^{-1}$). To do so, a magnetic gradient is applied at the beginning

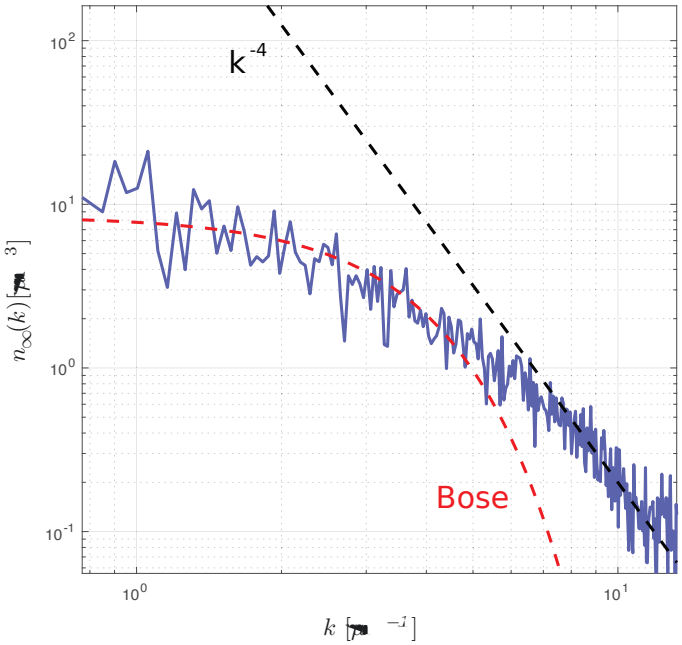

Figure 3.14: Log-log scale plot of the $n_\infty(k)$ distribution of the $m_J = 0$ population present in the trap. The high-k density decays with a k^{-4} tail.

of the expansion to push the $m_J = +1$ BEC away from the $m_J = 0$ parasite cloud, before performing the usual RF transfer. We see that this separation is not enough to prevent the high k components of the "parasite" cloud to mix with the high k component of the BEC. In principle, we could separate them a lot more along the gravity axis, where we are not limited by the finite size of the detector. This would require the installation of gradient coils along the z direction of our science chamber.

Removing the $m_J = 0$ population We could also think of extinguishing the "parasite" atoms with a well chosen Rabi pulse, transferring all the atoms initially in $m_J = 0$ to a non detected state. This is not straightforward either, because the magnetic bias used to define the quantization axis has a gradient-like inhomogeneity of 0.2 G.cm^{-1}, that tends to separate the center of the two in-trap populations, making the RF resonance different for the BEC and the $m_J = 0$ cloud. We instead perform an optical pumping stage, similar to the one described in section 1.1.2, reducing the in-trap population of $m_J = 0$ atoms by a factor of $\sim$10. After the expansion, the amplitude of the k^{-4} wings on the $n_\infty(k)$ distribution is strongly reduced as shown in figure 3.16, and does not follow the linear behavior of figure 3.9 anymore.

Removing the in-trap condensate It is also interesting to observe the $n_\infty(k)$ popluation in absence of an in-trap BEC. We completely remove the $m_J = +1$ BEC from the ODT, by lowering the trapping frequencies and applying a magnetic gradient. The $m_J = 0$ atoms are not effected by the gradient, and therefore remain trapped. In figure 3.17, we compare the $n_\infty(k)$ distribution of the "parasite" cloud, with and without the presence of the BEC in the ODT. We see that the k^{-4} decay is not present in the second case, suggesting that this polynomial decay arises from an interplay between the two spin components.

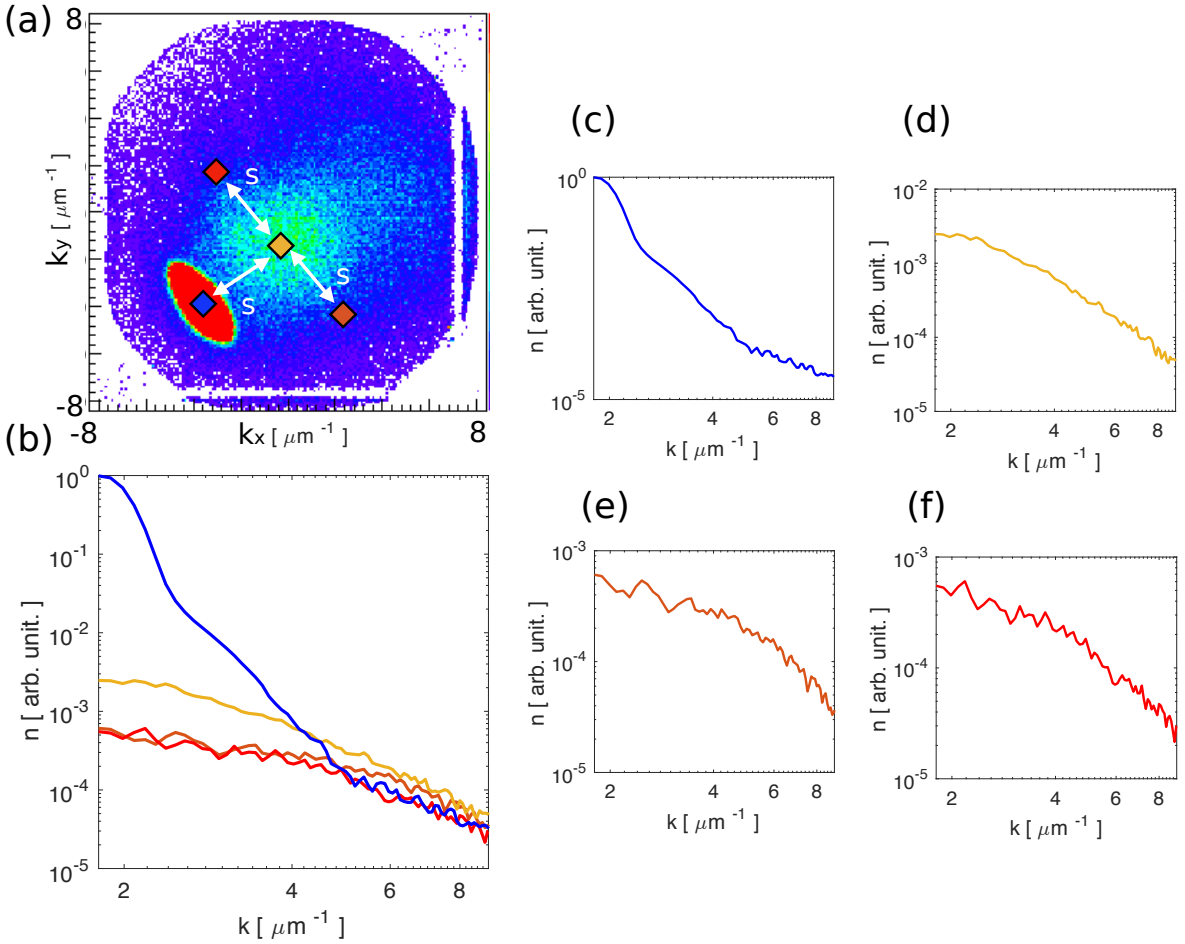

Figure 3.15: (a) Detection of the BEC (dense, anisotropic cloud in the bottom-left of the detector) situated at a distance s from the "parasite" cloud (diluted, isotropic distribution centered on the detector). The two clouds have been separated by a magnetic gradient applied at the beginning of the expansion. Various density profiles ((c), (d), (e), (f)) are plotted along the gravity axis (z, orthogonal the detector) with an angular integration of $\sim 10°$. Those density profiles are centered on : (c) the BEC (d) the "parasite" cloud, (e) and (f) two other regions at a distance s from the parasite cloud. We see that all the high k components of the different profiles seem rather identical (b), suggesting that the BEC and the "parasite" cloud are not well enough spatially separated to distinguish their respective high momentum distributions.

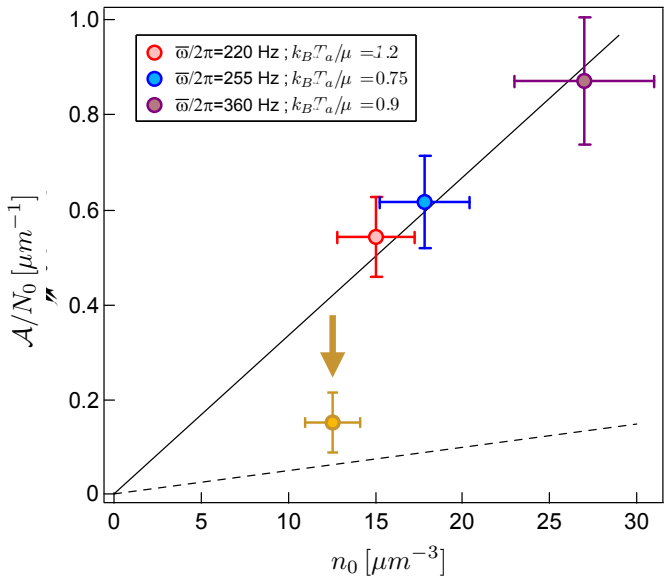

Figure 3.16: Same plot as figure 3.9 with a new experimental point (yellow), obtained after applying an optical pumping stage on the trapped cloud, reducing the in-trap population in the $m_J = 0$ state by a factor of ~ 10.

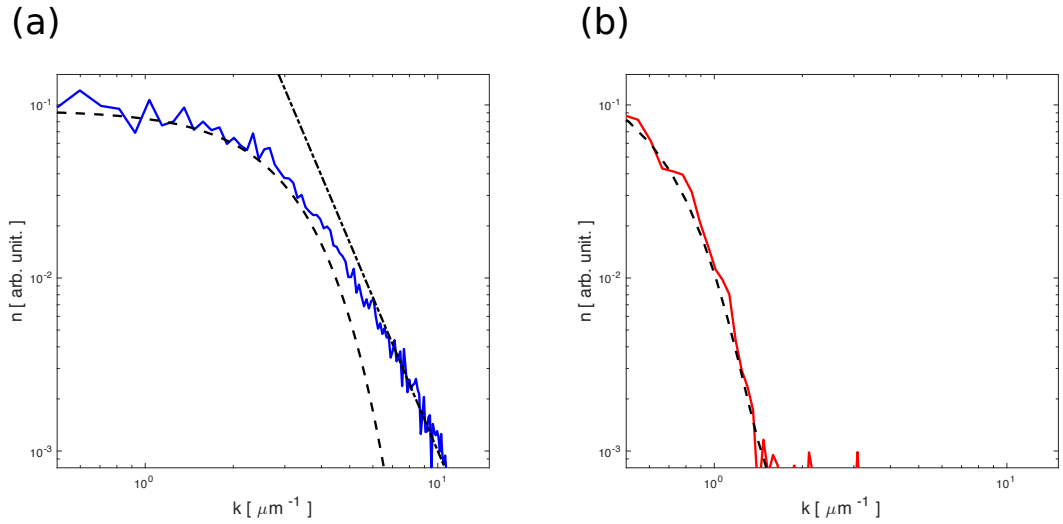

Figure 3.17: Log-log scale plot of the $n_\infty(k)$ distribution of the $m_J = 0$ population present in the trap, (a) in presence, and (b) in absence of the $m_J = +1$ BEC. The dashed lines are Bose fits, and the dashed-dotted line is a k^{-4} decay.

Conclusion

Although very preliminary, those recent observations strongly suggest that the k^{-4} decay observed in the asymptotic momentum distribution of the expanding $m_J = +1$ BEC is due to the presence of a small in-trap population of $m_J = 0$ atoms. This raises a list of questions to address in the future, namely :

- What is the nature of the coupling between the two spin components, and how does it give birth to such high-amplitude k^{-4} tails? Is it an in-trap mechanism or an effect due to the release of the gas?
- Is there a k^{-4} decay in the asymptotic momentum distribution of the population initially in $m_J = +1$, or is the observed tail due to the $m_J = 0$ atoms only?
- How does this k^{-4} decay survives the expansion? Is there a non-adiabatic process involved when the trap is turned off?

Chapter 4

Measuring the momentum distribution of a lattice gas at the single-atom level

Quantum gases loaded into optical lattices, or "lattice gases", offer the opportunity to study, in a controllable way, simple condensed matter models of interacting particles, like the Bose-Hubbard model or the Ising model [10]. In 2002, the observation by Greiner et al. [25] of the superfluid to Mott insulator phase transition with ultra-cold Rubidium atoms loaded in an optical lattice constituted a major breakthrough, and opened the era of the investigation of quantum phase diagrams with optical lattices.

Many lattice gas experiments rely on Time-of-Flight (ToF) optical imaging to measure the momentum distribution of the system [25, 26, 16, 17, 27]. The main limitation of optical probe is their inefficiency at long ToF, due to the rapid decay of the atomic density during the expansion. For typical experimental parameters, those short ToF are not sufficient to access the Far-Field Regime (FFR) of expansion, where the spatial distribution of the gas can be mapped to the momentum distribution [23, 22, 24]. Furthermore, in 3D systems, the finite resolution and the column integrated density of optical measurements strongly limit the ability to unambiguously identify the appearance of a coherent fraction [23, 120, 121]. This chapter describes how the MCP detector circumvent those limitations, by achieving a 3D atom-per-atom detection of a lattice gas in the FFR.

The first section recalls some generalities of lattice physics, and introduces the Bose-Hubbard model. The ToF expansion of atoms released from the lattice is also discussed, and the criterion for entering the FFR is established. In the second section, we describe the experimental sequence and prove that the FFR is reached, with a measurement of the "sharpness" of the atomic interference pattern. In the last section, we compare the measured distributions with theoretical in-trap momentum distributions, calculated by ab-initio quantum Monte-Carlo (QMC) methods.

4.1 Quantum gas in optical lattice : equilibrium properties and expansion

4.1.1 The Bose-Hubbard model

In the following, we present the basic theoretical tools necessary to describe interacting quantum particles inside a sinusoidal potential. This first part (until the derivation of the Bose-Hubbard Hamiltonian) is strongly inspired by [122].

Generalities

Like discussed in section 1.1.3, once loaded inside the 3D optical lattice, the potential felt by the atoms is given by equation 1.7. In this paragraph, we first consider non-interacting particles. The hamiltonian of the system is thus :

$$H = \frac{P_x^2}{2m} + \frac{P_y^2}{2m} + \frac{P_z^2}{2m} + V_0 \left(\sin^2\left(\frac{k_a}{2}x\right) + \sin^2\left(\frac{k_a}{2}y\right) + \sin^2\left(\frac{k_a}{2}z\right)\right) + V_{ext}(x,y,z). \quad (4.1)$$

We see that H is completely separable along the 3 directions of space. To simplify the discussion, let us consider a homogeneous ($V_{ext} = 0$) system along one direction only :

$$H_1 = \frac{P_x^2}{2m} + V_0 \sin^2\left(\frac{k_a}{2}x\right). \quad (4.2)$$

The natural spatial and momentum scale of the problem are a and k_a. We also define the recoil energy of the lattice, that is the energy acquired by an atom absorbing a photon at $\lambda_l =$ 1550nm:

$$E_r = \frac{\hbar^2}{8ma^2} \quad (4.3)$$

Because of the spatial periodicity of the hamiltonian (period a), we can apply the Bloch theorem [3] to deduce the form of the Eigen functions of H_1 :

$$\psi_{n,q}(x) = e^{iqx} u_{n,q}(x) \quad n \in \mathbb{N}, \;\; q \in \mathbb{R} \quad (4.4)$$

The function $\psi_{n,q}$ are called the Bloch waves (see figure 4.2), and $\hbar q$ is the quasi-impulsion, with q defined modulo k_a. As for the $u_{n,q}$ functions, they have a spatial periodicity of a and verify :

$$\left[\frac{(P_x + \hbar q)^2}{2m} + V_0 \sin^2\left(\frac{k_a}{2}x\right)\right] u_{n,q}(x) = E_n(q) u_{n,q}(x). \quad (4.5)$$

The Eigen energies $E_n(q)$ define a band structure, n being the index of the band. They verify $E_n(q) < E_{n+1}(q)\ \forall(q,n)$ (no inter-band crossing) and $E_n(q + k_a) = E_n(q)\ \forall(n,q)$ (periodicity of k_a) so that we can restrict ourselves to the interval $\left[-\frac{k_a}{2}, \frac{k_a}{2}\right]$ called the first Brillouin zone. With the approximations we have done so far (no interactions and homogeneous system), the energy $E_n(q)$ and the functions $u_{n,q}$ can be easily calculated numerically. In figure 4.1, we plot the first 4 energy bands for $V_0 = 0, 5, 10$ and $15E_r$. We can see that raising the lattice depth has two main effects on the band structure : decreasing the bands' width, and increasing the energy gap between the bands.

We can also introduce the Wannier functions [123], defined from the Bloch waves by :

$$w_{n,j}(x) = \sqrt{\frac{a}{2\pi}} \int_{\mathrm{BZ}} \psi_{n,q}(x) e^{-ijqa} \, \mathrm{d}q \quad j \in \mathbb{N}, \quad (4.6)$$

where BZ designates an integration over the first Brillouin zone. With equation 4.6, we have built a basis indexed over the lattice sites j instead of the quasi-impulsion q, leading to a simple physical interpretation for the Wannier basis : $w_{n,j}$ is the wave function of a particle localized at the j-th site of the lattice. Note that contrary to the Bloch waves, the Wannier functions are not Eigenstates of the Hamiltonian, so that a particle initially localized inside a lattice site can "jump" from one site to another over time, by tunneling through the potential barrier.

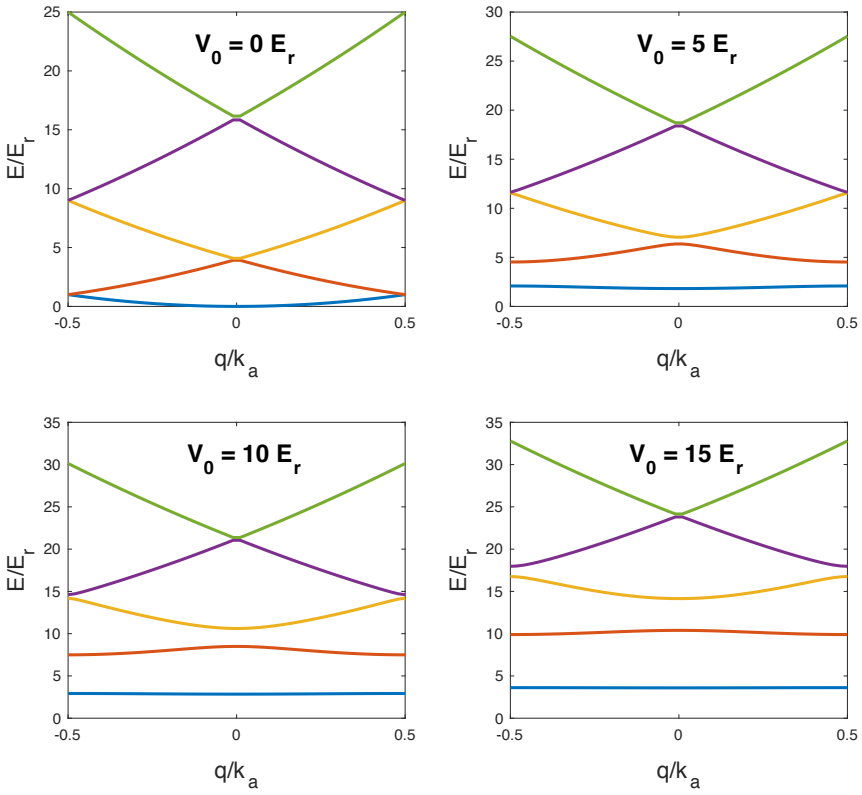

Figure 4.1: First five energy bands for various values of the lattice depth V_0. Note the opening of a gap between the first bands as the depth increases.

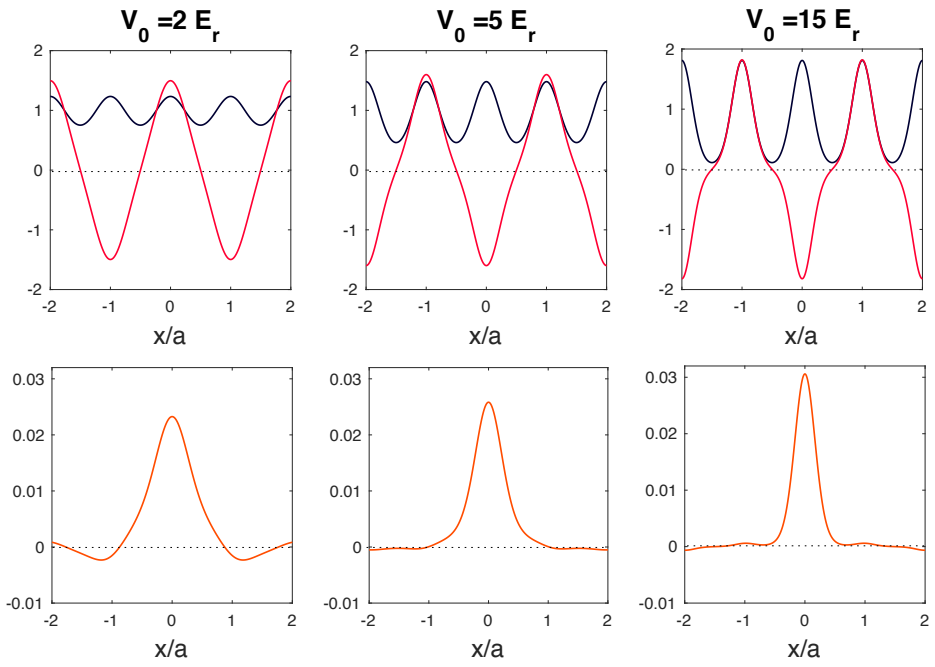

Figure 4.2: Top : Real part of the Bloch waves of the fundamental band ($n = 0$) for different lattice depths. The blue curve corresponds to the quasi-momentum $q = 0$, while the red curve corresponds to $q = k_a/2$. Bottom : Real part of the Wannier function of the fundamental band.

To characterize this important effect, let us introduce the second-quantization notations. The operator $b_{n,q}$ (resp. $b^\dagger_{n,q}$) annihilates (resp. creates) a particle in the n-th energy band, with a quasi-momentum $\hbar q$. Similarly, the operator $a_{n,j}$ (resp. $a^\dagger_{n,j}$) annihilates (resp. creates) a particle in the n-th energy band, in the lattice site j. In second-quantization, the hamiltonian can be re-written :

$$H_1 = \sum_n \int_{\mathrm{BZ}} E_n(q) b^\dagger_{n,q} b_{n,q} \, \mathrm{d}q. \tag{4.7}$$

We can also invert relation 4.6 to obtain :

$$b_{n,q} = \sqrt{\frac{a}{2\pi}} \sum_j a_{n,j} e^{ijqa} \tag{4.8}$$

which combined to equation 4.7 gives :

$$H_1 = \sum_n \sum_{j,j'} J_n(j-j') a^\dagger_{n,j'} a_{n,j}, \tag{4.9}$$

where we have defined the tunnel coupling $J_n(j-j') = \frac{a}{2\pi} \int e^{i(j-j')qa} E_n(q) \, \mathrm{d}q$ between the site j and j'.

$J_n(j-j')$ decrease with $|j-j'|$ and with V_0, so that in the tight-binding approximation (deep lattice), only the tunneling amplitude between neighboring sites is not negligible.

Bose-Hubbard Hamiltonian

So far, we have considered non-interacting particles, and we now introduce an interaction term H_{int} to our Hamiltonian. Just like in chapter 3, we will see that the interactions play a fundamental role in the equilibrium properties of the system. In the lattice, the 2-body contact interactions take the form :

$$H_{int} = \frac{g}{2} \int \phi^\dagger(x)\phi^\dagger(x)\phi(x)\phi(x)\ \mathrm{d}x, \tag{4.10}$$

where $\phi(x)$ ($\phi^\dagger(x)$) is the bosonic field operator that annihilates (creates) a particle at position x. And since we have :

$$\phi(x) = \sum_n \sum_j w_{n,j}(x) a_{n,j}, \tag{4.11}$$

equation 4.10 becomes :

$$H_{int} = \frac{g}{2} \sum_{n_1,j_1} \sum_{n_2,j_2} \sum_{n_3,j_3} \sum_{n_4,j_4} a^\dagger_{n_4,j_4} a^\dagger_{n_3,j_3} a_{n_2,j_2} a_{n_1,j_1} \int w^*_{n_4,j_4} w^*_{n_3,j_3} w_{n_2,j_2} w_{n_1,j_1}\ \mathrm{d}x. \tag{4.12}$$

Let us introduce further approximations. For a BEC, we can make the reasonable hypothesis that all the atoms occupy only the lowest energy band, in a narrow region around $q = 0$. Furthermore, the interaction energy is too low to induce coupling to higher energy bands, since $\mu \ll V_0$. In the following, we thus consider only the fundamental band $n = 0$, dropping the index n from the notations. We can also notice that the scattering length a_s is 2 orders of magnitude lower than the lattice spacing a (7.5nm compared to 775nm) so only the interactions between the atoms in the same lattice site need to be taken into account. Those two approximations considerably simplify equation 4.12, since there is no sum over n anymore, and only one sum over j. By introducing the number of atoms in site j, $n_j = a^\dagger_j a_j$, and the on-site interaction energy $U = g \int |w_{0,0}(x)|^4\, \mathrm{d}x$, we obtain :

$$H_{int} = \frac{U}{2} \sum_j n_j(n_j - 1) \tag{4.13}$$

With the additional tight-bidding approximation, and the notation $J = J_0(1)$, we can now write the complete hamiltonian in the Bose-Hubbard (BH) form :

$$H_{BH} = -J \sum_j (a^\dagger_j a_{j+1} + a^\dagger_{j+1} a_j) + \frac{U}{2} \sum_j n_j(n_j - 1) \tag{4.14}$$

Within this framework, illustrated by figure 4.3, the nature of the homogeneous ground state is driven by two quantities : U and J, both of them depending on the lattice amplitude. In particular, the ratio U/J varies rapidly with V_0. If we restrict the discussion to the case of integer filling (M lattice sites and $N \propto M$ particles), then the ground state $|\Psi_0\rangle$ is exactly known for the 2 extreme cases :

- $U/J \to 0$ $|\Psi_0\rangle = \frac{1}{\sqrt{N!}} (b^\dagger_{q=0})^N |0\rangle$. The system is Superfluid (SF), with a condensed fraction of ~ 1. The atoms are delocalized, leading to a phase coherence over the entire system.
- $U/J \to \infty$ $|\Psi_0\rangle = \frac{1}{\sqrt{N!}} \prod_j a^\dagger_j |0\rangle$. The atoms are localized on the lattice sites, and the high interaction energy prevents them from tunneling to an already occupied site. The system is in the so-called Mott Insulator (MI) regime : an insulator phase caused by the interactions. The coherence is lost and the condensed fraction is 0.

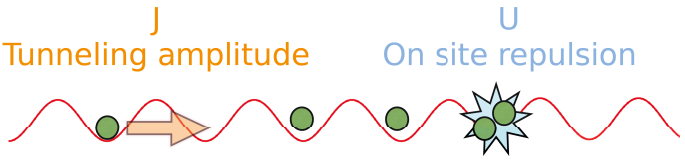

Figure 4.3: Illustration of the Bose-Hubbard model. The physic of the homogeneous system depends on two quantities : the tunneling amplitude between neighboring sites J, and the on-site interaction energy U.

For intermediate values of U/J, finite temperature, and/or inhomogeneous (trapped) system, there is no analytical solution for the Hamiltonian, but it can still be exactly solved numerically with QMC calculations. Let us however mention the existence of various approximations giving good predictions for certain regimes, at $T \simeq 0$:

- For $U/J \ll 1$ in a regime of shallow lattice, where most of the atoms are condensed, and only a small fraction populates the higher q modes, we can apply the Bogoliubov treatment (see chapter 3), by setting $b_0 = b_0^\dagger = \sqrt{N}$, and keeping only the terms quadratic in b_q and $b_q^\dagger$ ($q \neq 0$). We can then deduce the excitation spectrum and the Eigenstates of the system [124, 125], with the Bogoliubov transformation.

- For $U/J > (U/J)_C$, where most of the atoms are localized in the lattice sites, there subsist some tunneling that can couple the ground state $|\Psi_0\rangle$ (perfect MI) to the first excited state $|\Psi_1\rangle = \frac{1}{\sqrt{N}} \sum_j (a_j^\dagger a_{j+1} + a_{j+1}^\dagger a_j)$. The system is still insulating, but the appearance of delocalized particle-hole excitations establish a short-distance phase coherence.

- Another approach consists in treating each lattice site independently, thus writing the hamiltonian in the decoupled form : $H_{dec} = \sum_j H_j$ [126]. The idea is to make the approximation $a_j^\dagger a_k \simeq a_j^\dagger \langle a_k \rangle + \langle a_j \rangle^* a_k$, neglecting all correlations between lattice sites, except for the coherent coupling $\alpha = \langle a_j \rangle$ (which is the same for all j). By essence, this approximation is not adapted to describe spatial correlations in the lattice, but it can handle both Fock states (localized atoms) and coherent states (delocalized atoms). Therefore, the decoupled ground state coincides with both SF phase and MI phase for the asymptotic values of U/J, and can capture some accurate behaviors in-between. We will use this approach several times in the following.

The SF to MI transition is a second-order quantum phase transition occurring at $T = 0$, and for a critical value $(U/J)_C$ depending on the filling factor. At finite T, there is no transition, but only a crossover. Below $(U/J)_C$, the SF to normal gas (NG) transition at T_c is equivalent to the Bose-Einstein condensation. The critical temperature T_c decreases with the ratio U/J, and goes to 0 at $(U/J)_C$. On the other hand, there is no MI to NG transition, just a crossover. Figure 4.4 is a sketch of the BH phase diagram along the axis U/J and T.

For inhomogeneous systems, the spatial variations of the chemical potential modify this simple picture, since both the filling factor and the density become position-dependent. For the SF to MI transition, it leads to the famous wedding-cake structure [124], where both SF and MI phases coexist inside the trap. The case of the SF to NG transition in a inhomogeneous system is discussed in the next chapter.

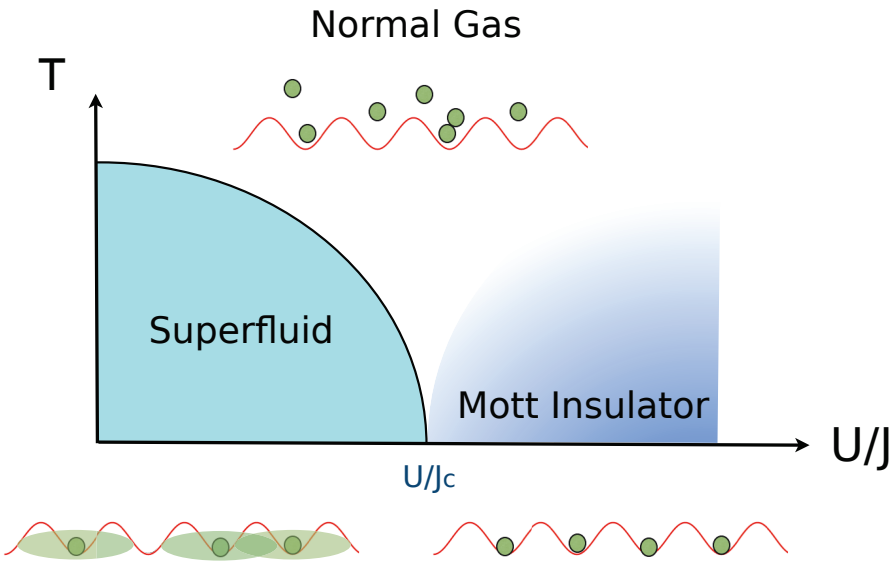

Figure 4.4: Sketch of the phase diagram of the Bose-Hubbard hamiltonian for a homogeneous system with unity (or commensurate) filling. A system prepared in the superfluid state can undergoes two phase-transitions : the usual transition to normal gas at $T = T_c(U/J)$, and an interaction-induced quantum phase transition to the Mott insulator state at $(U/J)_c$ and $T = 0$. In both cases, the superfluid fraction goes to zero. On the other hand, the Mott insulator to normal gas transition is a smooth crossover.

4.1.2 Expansion from the lattice

Non-interacting case

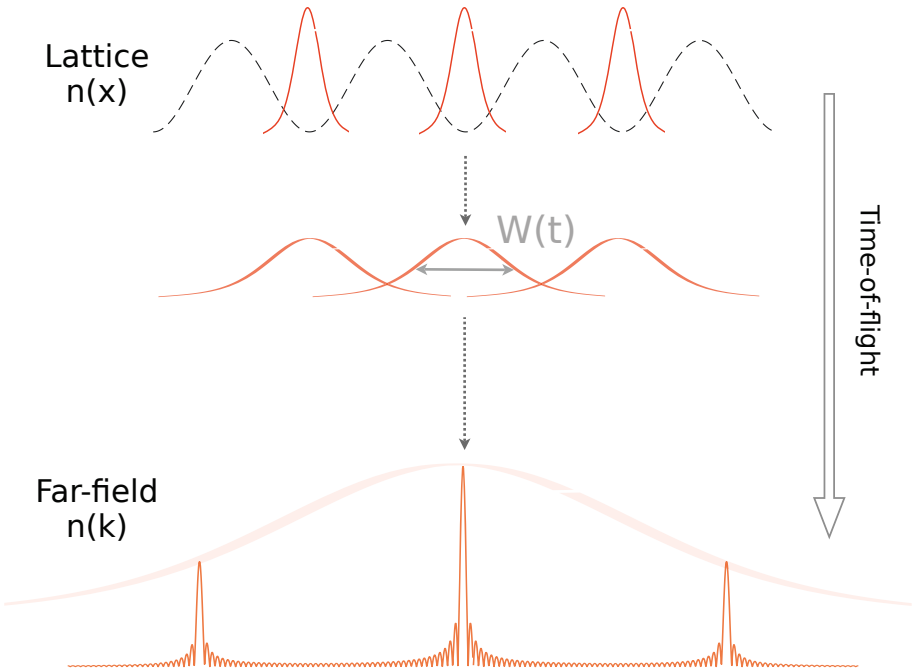

Figure 4.5: After switching off the lattice trap, the cloud expands freely while falling under the effect of gravity. The width $W(t)$ of the Wannier function shortly enters a regime where it increases linearly with time. The interference between the overlapping wave packets fully develop in the far-field regime, and the spatial distribution can be mapped to the momentum distribution.

In the non-interacting case, after abruptly removing the lattice potential, the cloud expands freely until a point where it enters the FFR of expansion, where the density distribution gives access to the in-trap momentum distribution. An analogy can be made with an optical wave diffracted by a given transmission pattern $T(x, y)$. In the Fraunhofer diffraction regime, far from the (x, y) plane, the intensity distribution of the field is directly proportional to the Fourrier transform of $T(x, y)$.

We will now describe this expansion, and derive the conditions to enter the FFR. We do not make any assumption about the lattice filling, and suppose that our system is homogeneous, well described by the BH Hamiltonian, and contains N atoms, initially distributed along M lattice sites. The calculations are still performed along one direction of space for simplification, and the size of the system along this direction is noted $L = Ma$. At any moment t of the free-fall, equation 4.11 can be re-written :

$$\phi(x,t) = \sum_j w_j(x,t) a_{n,j}, \tag{4.15}$$

where we have introduced the expanding version of the Wannier functions $w_j(x,t) = w_0(x - ja, t)$.

Like in [22], we can approximate it by the ground state of a harmonic oscillator of length a_0 :

$$w_0(x-ja,0) \simeq \frac{e^{-(x-ja)^2/(2a_0^2)}}{\pi^{1/4}\sqrt{a_0}} \tag{4.16}$$

$$w_0(x-ja,t) \simeq \frac{1}{\pi^{1/4}\sqrt{W(t)}} exp\left[\frac{-(x-ja)^2}{2W^2(t)}\right] exp\left[i\frac{-(x-ja)^2}{2W^2(t)}\frac{\hbar t}{ma_0^2}\right], \tag{4.17}$$

where $W(t) = a_0\sqrt{1+(\hbar t/ma_0^2)^2}$ is the width of the expanding Wannier function, that can be approximated by $W(t) \simeq \hbar t/ma_0$ after a very short time of expansion, even at low lattice amplitude. In the case of Helium, for $V_0 = 3E_r$, the width $W(t)$ is multiplied by 100 after 300μs of free-fall. In the envelop of $w_0(x-ja,t)$, we can thus rapidly neglect the dependency in ja : $ja \leq L \ll W(t)$, so

$$exp\left[\frac{-(x-ja)^2}{2W^2(t)}\right] \simeq exp\left[\frac{-x^2}{2W^2(t)}\right] exp\left[\frac{-x\times ja}{W^2(t)}\right], \tag{4.18}$$

and $x \times ja/W^2(t)$ can also be neglected if we restrict ourselves to a region where $x \ll W(t)^2/Ma$, which is always true in practice.

As for the phase term of $w_0(x-ja,t)$, we need to wait a much longer time in order to get rid of the quadratic dependence of ja (equivalent to the fresnel phase in optics). Indeed, $\frac{(x-ja)^2}{2W^2(t)}\frac{\hbar t}{ma_0^2} \simeq \frac{(x-ja)^2}{2a_0W(t)}$, and so we need $\frac{(ja)^2}{2a_0W(t)} \ll 1\ \forall j$, which can be re-written

$$t > t_{ff} = mL^2/2\hbar \tag{4.19}$$

defining the condition to enter the FFR [23, 22]. When $t \simeq t_{ff}$, the accuracy of the mapping between the spatial distribution of the (non interacting) cloud and the momentum distribution is already at the percent-level. For a gas of rubidium with a phase coherence over $M = 50$ lattice sites, $t_{ff} \simeq 400$ms, very far from the usual optical imaging conditions. For Helium, much lighter than rubidium, the same conditions give $t_{ff} \simeq 60$ms. With such a time of flight, the density of the cloud has dropped by ~ 12 orders of magnitude, even for low lattice amplitude, making it very difficult to image optically. The electronic detection offered by the MCP, however, allows to image very diluted clouds because of its single-particle sensitivity. The detector is located 50cm below the science-chamber, leading to an average time-of-flight of $\sim$300ms (ToF of the center of mass), that satisfies the far-field condition for most of the cases.

In the FFR, the expansion is ballistic, and we can define the momentum $\hbar k$ from the position x by :

$$\hbar k = mx/t \tag{4.20}$$

the expanding Wannier function can finally be approximated by :

$$w_j(k) \simeq A(k)e^{-ikaj} \tag{4.21}$$

$$A(k) \propto exp\left[-k^2a_0^2/2\right] e^{i\omega t}, \tag{4.22}$$

where $\omega = \hbar k^2/2m$. We can also use equation 4.6 to retrieve the form of the Bloch waves in the FFR :

$$\psi_q(k) \simeq \frac{1}{\sqrt{M}} A(k) \frac{\sin\left(Ma(k-q)/2\right)}{\sin\left(a(k-q)/2\right)}, \tag{4.23}$$

directly connected to the Fourrier transform of $\psi_q(x)$ in the trap, so that the quantity $n(k) = \langle \phi^\dagger(k)\phi(k) \rangle$ is indeed equal to the initial momentum distribution of the gas. Figure 4.5 shows the evolution of the cloud's spatial distribution during the ToF, as it gets closer and closer to the momentum distribution.

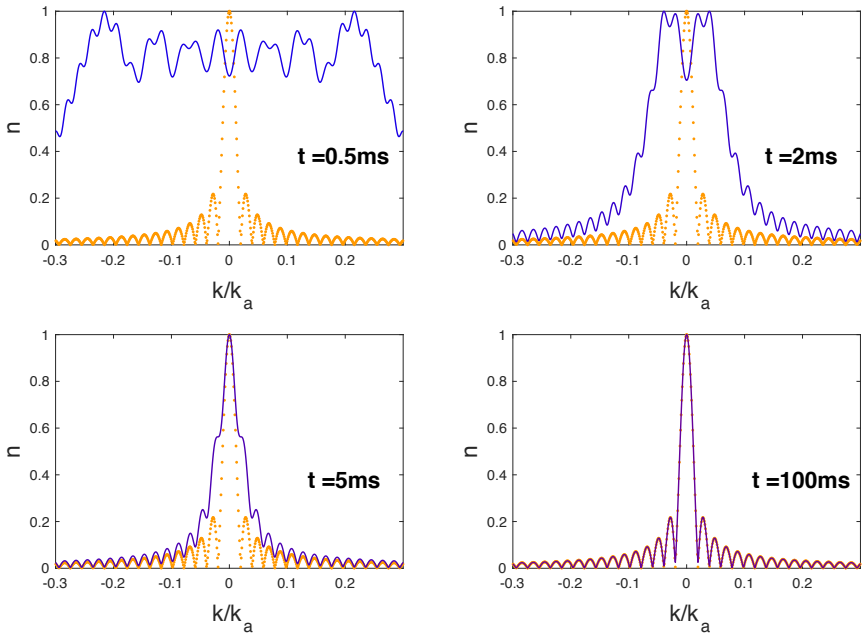

Figure 4.6: Modulus of the expanding superfluid wave packet (solid line) for various ToF, compared to the in-trap momentum distribution (orange-dotted line). For time longer than t_{FF} ($\simeq$ 50ms in this example) the spatial distribution of the wave packet matches the initial momentum distribution. Note that the horizontal axis changes for the different ToF, because of the definition of k 4.20.

The role of the interactions

How does the conclusion of the previous section hold for our interacting, trapped system? Describing the impact of the interactions on the expanding lattice gas is notoriously difficult. Contrary to the case of the trapped BEC, the physics of the first instants of the ToF can not be captured by a mean field calculation, because the lattice structure adds the timescale $1/\omega_{site}$ of the single site's expansion, which dominates all the other energy scales. Indeed, we easily enter a regime where $\hbar\omega_{site} \gg \mu$, meaning that the initial expansion is driven by the zero-point energy of the lattice sites, rather than the mean field released energy. When the expanding Wannier functions start to overlap ($W(t) \sim a$), the density is divided by a factor of $(a/a_0)^3$, very high in general. Therefore, we do not expect the mean field energy to play a significant role at this level as well [23].

There exists little theoretical work describing the effect of the interactions beyond the mean field approximation. In [127], the authors performed a 1D model on a small system (10 atoms

expanding from 10 lattice sites). The calculations, based on the truncated Wigner function, show that interactions during the expansion reduce the contrast of the diffraction peaks by almost a factor of 2. Of course, one expects this effect to be much less dramatic in 3D. In [28] the authors have used a site-decoupled approach to calculate (for any dimension) the impact of the on-site interactions just after the lattice potential is switched off. Their conclusion, similar to [23], is that the on-site interactions tend to enlarge the width of the expanding Wannier function, and create a dephasing between the center and the edge of the trap, which in both cases reduce the contrast of the diffraction peaks. However, with our small scattering length (much smaller that the separation between two lattice sites) having a lattice filling close to unity is enough to make those effects negligible.

In conclusion, the expansion of a 3D lattice gas with $\hbar\omega_{site} \gg \mu$, and with a filling factor close to 1 at the center of the trap should be ballistic with a very good approximation, and so the atomic distribution in the FFR is expected to be close to the in-trap momentum distribution of the gas.

- In this regime, the expansion energy during the ToF is dominated by the zero point energy of the lattice site, so one expects that the mean field energy does not play a role during the expansion.
- The unitary filling assures a sufficiently homogeneous distribution of the interaction energy among the sites, leading to a uniform phase evolution of the wave packets expanding from each site, and therefore no additional interference effect that would disturb the distribution during the ToF.

Now, we need to test these physical arguments experimentally, which is the object of the next sections.

4.2 Entering the far field regime of an expanding lattice gas

4.2.1 Choice of the system and experimental sequence

We choose to take our measurements with $U/J = 10$, far enough from the MI transition ($(U/J)_c \sim 30$) for the system to be fully coherent, but also sufficiently high to have a strongly interacting gas. Indeed, with a site-decoupled approach based on the Gutzwiller ansatz [126], we can show that those parameters lead to a depleted fraction of 15%, 2 orders of magnitude higher than for the trapped BEC. It corresponds to a lattice depth $V_0 \simeq 9.6E_r$ and a measured external trapping frequency of $\omega_{\text{ext}} = 2\pi(308, 295, 298)$Hz along the science chamber axis. This leads to $M \simeq 50$ lattice sites, that we load with a BEC of about 4×10^4 atoms in order to be close to the unity filling at the trap center. The interest of working with a coherent lattice gas comes from the presence of the diffraction peaks. They constitute narrow structures in momentum density, a good way to confirm that the FFR is reached, and that our resolution is good enough to image k structures of the order of $\sim 1/L$.

We perform the adiabatic loading by ramping up the 3 lattice beams with an exponential ramp of duration 100ms, and characteristic time 20ms. In the meantime, the ODT is ramped down with a 80ms ramp of characteristic time 20ms. We can check the adiabaticity of the loading by applying a time-reverted version of the sequence, unloading the atoms back in the ODT from the lattice, and verifying that we see no loss of atoms nor visible thermal fraction. We usually hold the gas several dozen of ms, depending on wether or not we chose to apply

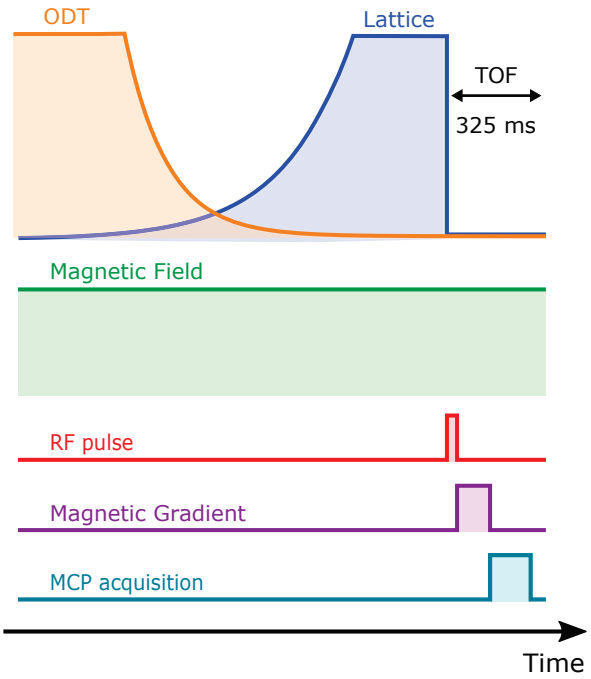

Figure 4.7: Scheme of the experimental cycle. The atoms are loaded in the lattice (blue) from the ODT (orange). After a holding time, the lattice is cut and the gas expands freely. During the time-of-flight, a fraction of the atoms is transferred into the $m_J = 0$ state with an RF pulse (red), and the rest is pushed away by a magnetic gradient (violet). A homogeneous magnetic field (green) ensures a fixed energy difference between the spin levels. Finally, the atoms in $m_J = 0$ are detected on the MCP detector (cyan) after a time of flight of 325ms.

a heating sequence to raise the temperature of the sample. The heating sequence is done by quickly modulating the lattice amplitude of one arm with square pulses of 500μs duration, the number and the amplitude of those pulses depend on the amount of energy we want to deposit in the system.

Finally, the lattice is abruptly switched off and the cloud expands freely. We then image the distribution, either with the absorption probe after a short ToF (0ms to 20ms), or with the MCP detector after a ToF of 325ms. In that case, a controllable fraction of the atoms is transferred in the detected $m_j = 0$ with a RF Rabi oscillation just after switching off the trap. We then remove the other atoms with a magnetic kick. The fraction we chose to transfer depends on the density of the studied sample (typically between 1% and 50%), the aim being to maximize the signal while trying to avoid saturation effect of the MCP (like in chapter 3). The entire cycle is summarized in figure 4.7.

4.2.2 Calibration of the lattice depth

We calibrate the lattice depth V_0 with 2 methods : Kapitza Dirac oscillations, and parametric heating. These techniques are based on different physical phenomena, and possess their pros and cons.

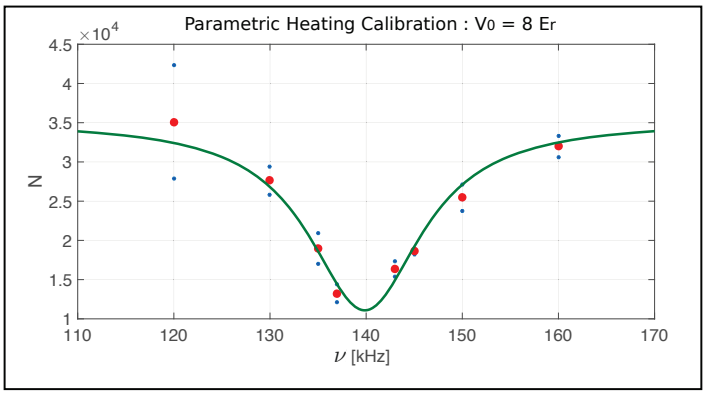

Figure 4.8: Parametric heating calibration. Atom number in an expanding lattice cloud measured by absorption, after a sinusoidal modulation of frequency ν of the lattice amplitude. The lattice depth is fully characterized by the central frequency of the dip.

Parametric heating

By modulating the lattice amplitude V_0 with a frequency ν, we create two sidebands $\pm h\nu$ in the laser spectrum, that can transfer an energy $2h\nu$ to the atoms via a resonant 2-photon process. This is a way to measure V_0 by probing the energy difference between the fundamental band of the lattice (populated by the atoms) and the second excited band. Indeed, the amplitude modulation is an even-parity process [128] that can couple only wave function of the same parity, so there is no transfer between the ground band and the first excited band at quasi-momentum $q = 0$.

Figure 4.8 shows the atom number N measured by absorption, plotted as a function of the modulation frequency of the lattice. A transition to the second excited bands will create a loss of atoms, so this measurement can directly be seen as a resonance curve, the dip in atom number indicating an inter-band transition. The advantage of this technique is to directly perform the calibration inside the lattice, contrary to Kapitza Dirac pulses (see below), applied either in the ODT or in free space.

Kapitza Dirac

Instead of loading the atoms inside the optical lattice, we apply a short pulse of lattice light to the BEC for a duration τ (typically a few dozen of μs). The Kapitza Dirac approximation can be applied if $\tau \ll \frac{1}{\omega_{\text{site}}}$ where ω_{site} is the trapping frequency of one lattice site (approximated by local harmonic potential). In this regime, the population of atoms that acquires a momentum $\pm\hbar k_a$ oscillates with τ. The amplitude and the frequency of the oscillation of the diffracted population (that can be directly probed by a time of flight imaging with the absorption scheme) is fully characterized by the lattice depth. The main advantage of this technique is to give a unambiguous experimental signal to work on when aligning the lattice (for instance : maximizing the population in the diffracted peak for a small value of τ).

Figure 4.9 presents an example of such a Kapitza Dirac oscillations, and the corresponding analysis. There are two major drawbacks with this technique. First : it is difficult to control and measure the amplitude of a light pulse on the microsecond timescale, making the uncertainty of

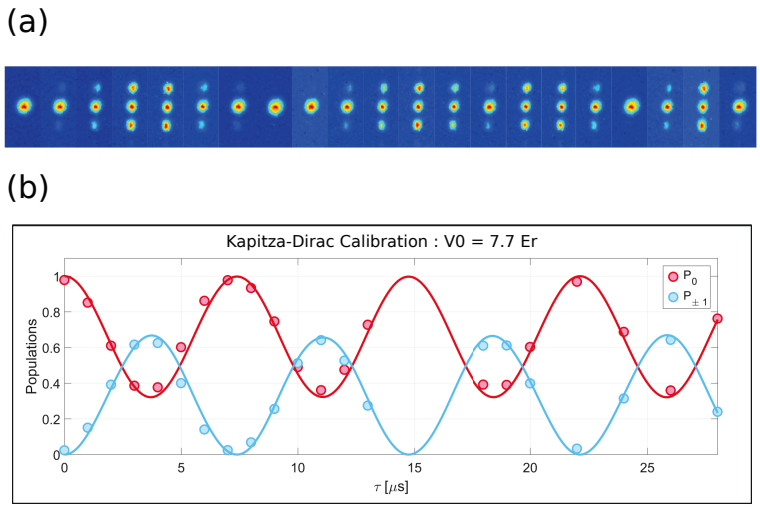

Figure 4.9: a) Absorption imaging pictures of an expanding BEC after a lattice pulses of various time. In the Kapitza-Dirac regime, the population in the diffracted peaks oscillates with the applied time of the pulse. b) The lattice depth is fully characterized by the amplitude and period of the oscillations.

the calibration difficult to evaluate. Second : this calibration is not directly performed in the lattice trap, so it might not reflect fully the experimental conditions.

3D band mapping

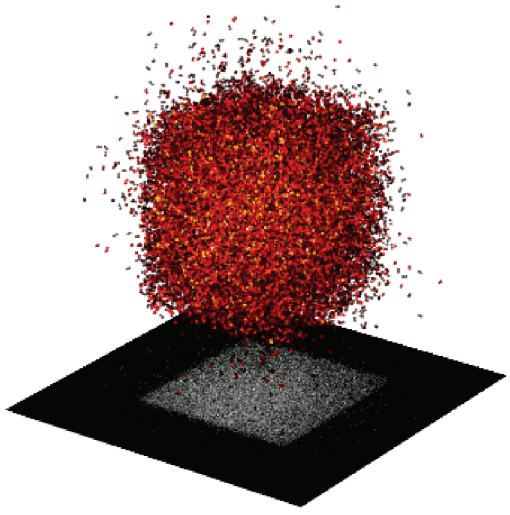

Figure 4.10: 3D band mapping. After an heating sequence, the lattice trap is adiabatically opened by an exponential ramp of 100ms. The cloud expands freely and falls on the MCP detector. The cube-shape of edge k_a of the distribution indicates that the energy distribution spreads over the entire Brillouin-zone. The very small fraction of atoms outside of the cube shows that most of the gas populates the first energy band.

The aim of the heating sequence is to vary T in order to explore the phase diagram of the BH model. For this model to remain valid, one has to make sure that the heating pulses do not induce transition to higher energy bands. We use the band mapping technique [129] that consists in opening slowly the trap to adiabatically map the Bloch waves to the plane waves of the free particle basis. If we note E_x the energy of the an atom along the x lattice, then the band mapping will project this atom on the free particle state of momentum $\hbar k_x = \sqrt{\frac{E_x}{2m}}$. If the atoms are inside the fundamental band, their energy along one of the lattice arm is limited to E_r, and so the resulting $\vec{k}$ distribution is contained inside a cube centered on $\vec{0}$ and with an edge of k_a. On the other hand, observing atoms outside of this cube means that the population in the excited band is not zero. Figure 4.10 shows a distribution of atoms detected on the MCP, obtained with the band mapping technique. The temperature of the gas is high enough to populate entirely the first Brillouin zone, but the inter-band energy gap ($\simeq 6E_r$ for $V_0 = 10E_r$) strongly limits the transitions to higher energy bands. Note that in this case, about 1% of the atoms are outside of the cube.

4.2.3 Measurement of the "sharpness" of the diffraction pattern

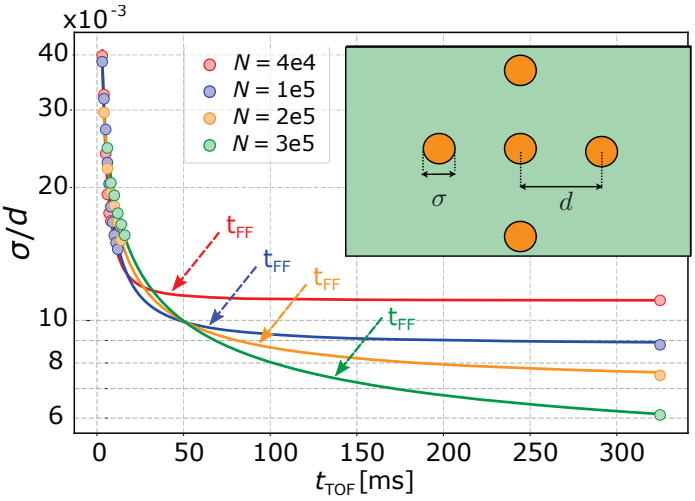

Figure 4.11: Evolution of the ratio σ/d during the time of flight. The small time ($t_{\mathrm{TOF}} <$ 20ms) measurements are performed with absorption imaging, the long time measurement ($t_{\mathrm{TOF}} \simeq$ 325ms) is detected on the MCP. The solid curves are plotted to guide the eyes.

As stated before, a Helium gas coherent over 50 lattice sites ($L = 50a$) will enter the FFR in about 50ms. Therefore, the average 325ms of ToF necessary to reach the MCP guarantee that this condition is fulfilled. However, we would like to confirm equation 4.19 experimentally. In the FFR, the distance d between the diffraction peaks is given by k_a, and the width σ of each peak is Fourrier-limited, meaning that $\sigma \simeq 2\pi/L$, and so $\sigma/d \simeq a/L$ is constant over time. In the early stage of the expansion, all the momenta are not "fully developed" yet. The low momenta develop first, so the effect of the short expansion time is mainly to broaden the peaks (see figure 4.6), and thus $\sigma/d > a/L$. As we get closer to the FFR, the peaks get narrower and σ/d tends to its asymptotic value. In figure 4.11, we have plotted the ratio σ/d measured at small ToF

(absorption imaging) and long ToF (MCP detection). The evolution of the ratio is compatible with the expected behavior, saturating at a asymptotic value. We have checked that for bigger system size (larger N), the initial ToF dynamics is slower (it takes more time to enter the FFR), and the final value of the ratio, inversely proportional to L, is lower.

4.3 Experimental results and comparison with the Bose-Hubbard model

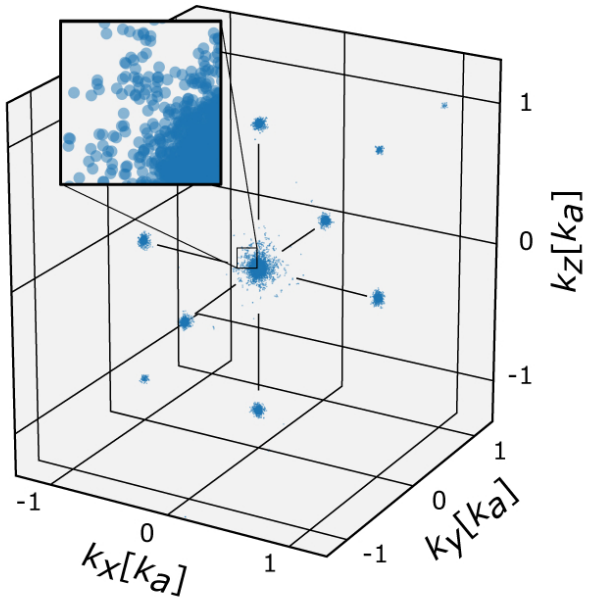

Figure 4.12: Example of a dataset obtained by reconstructing the 3D distribution of hundreds of clouds falling onto the MCP. Each dot corresponds to a single detected atom.

We will now focus on the asymptotic momentum distribution $n_\infty(\vec{k})$ of the lattice gas detected on the MCP. Like in chapter 3, we define $\vec{k} = m\vec{v}/\hbar$, with $\vec{v}$ calculated form the detector signals using equations 2.3, 2.4, 2.5. Contrary to the case of the trapped BEC, there is no angular symmetry in the lattice ToF distribution, so we need to accumulate much more data to look for low densities. In this section, we present the comparison between $n_\infty(\vec{k})$ and ab initio QMC calculation of the in-trap momentum distribution, obtained with the BH model for the parameters measured in the experiment.

4.3.1 Extraction of 1D profiles and comparison with Quantum Monte Carlo

1D cut in the 3D distribution

A typical dataset, like the one shown in figure 4.12, is composed of 500 to 1000 experimental runs. Each run corresponds to the detection by the MCP of 100 to 3000 particles, depending on the RF transfer we choose to apply. As mentioned before, the amount of atoms we transfer in the detectable state depends on the density of the sample. For a temperature higher than T_c, the condensed fraction is zero, and the average density in momentum space is low, because

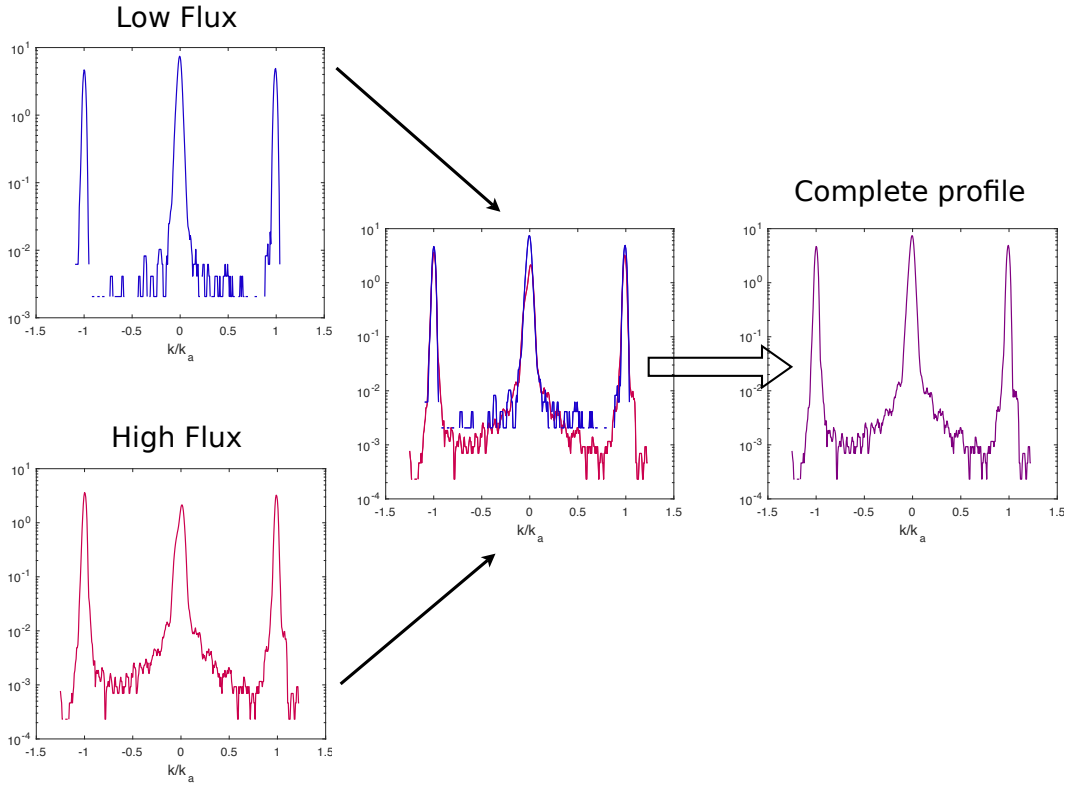

Figure 4.13: Semi-logarithmic plot of a 1D profile $n_\infty(k,0,0)$, obtained by combining high-flux and low-flux profiles extracted from the 3D measurement. We see that the low-flux data do not allow to image the low-density region of the distribution, while the high-density data exhibit visible saturation effect on the diffraction peaks (asymmetry). Combining the two allows us to reach a high-dynamic range in density ($\sim$ 4 decades).

the distribution is spread over all the first Brillouin zone (width $\propto 1/a$). We therefore need to transfer a high fraction of the cloud in $m_J = 0$ (up to 50%) to raise the signal-to-noise ratio.

For a temperature below T_c, the momentum distribution of the cloud is composed of two regions, corresponding to the condensed fraction (width $\propto 1/L$) and the depleted fraction (width $\propto 1/a$). Since $(L/a)^3 \gg 1$, the density ratio between the 2 regions is high : up to 4 orders of magnitude. To image the full density range, we use the same technique than for the BEC (see chapter 3) and take 2 datasets, with low and high RF transfer. We then combine the two to obtain the full distribution.

We extract 1D density profiles from the 3D distribution by calculating the histogram $n_\infty(k,0,0)$ of the number of atoms inside boxes centered on $\vec{k} = (k,0,0)$, and of size $(\Delta k, 3\Delta k, 3\Delta k)$, where $\Delta k = k_a/160$. We recall that the resolution of the detector is of the order of $2 \times 10^{-3}\, k_a$, i.e. $k_a/500$. Figure 4.13 presents a typical 1D profile extracted from our 3D distribution, obtained by merging high-flux and low-flux data.

Comparison with quantum Monte-Carlo calculation

As mentioned before, the equilibrium properties of the BH hamiltonian for trapped system at finite temperature can be exactly calculated with the QMC "worm algorithm". Such simulations

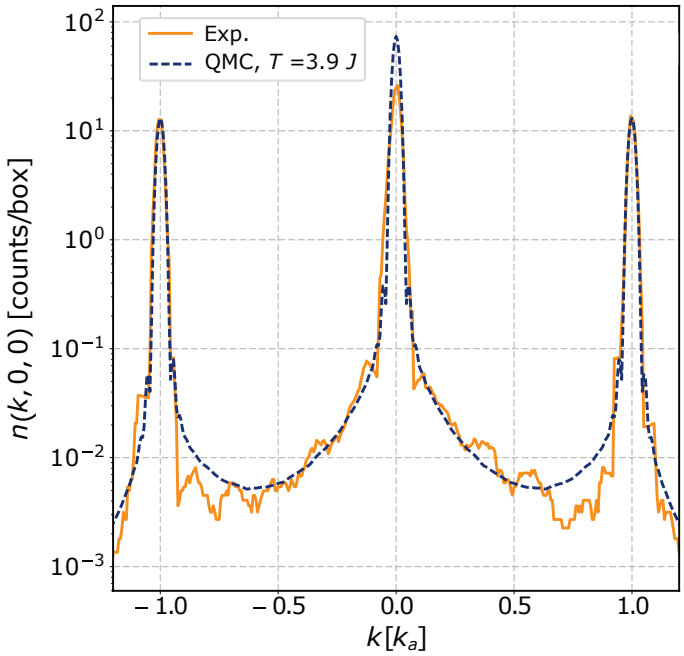

Figure 4.14: Comparison between the complete 1D profile $n_\infty(k, 0, 0)$, and $n(k, 0, 0)$ extracted from the QMC simulation, calculated for our experimental parameters ($U/J = 10$, ...) and $T = 3.9J$.

have been performed by G. Carleo on the ETH Zurich cluster with our experimental parameters, that are :

- N, measured with absorption imaging (about 15% fluctuations).
- a, given by the laser wavelength.
- V_0, calibrated by Kapitza-Dirac oscillations and parametric heating (about 10% uncertainty).
- V_{ext}, obtained by measuring the oscillations of the center of mass of the cloud in the trapped formed by the first passage of the lattice beams (about 10% uncertainty).
- m, the mass of ^{4}He.

The only quantity we do not measure independently is the temperature, and it is left as a "free" parameter. The QMC calculations, that have been performed for various T, gives us a theoretical momentum distribution $n(\vec{k})$ that we can compare to $n_\infty(\vec{k})$. To take into account the efficiency of the detection process, we rescale the experimental data by matching the height of the diffraction peaks to the one of the QMC calculation. Figure 4.14 shows the comparison between one of our experimental datasets, and a QMC profile at $T = 3.9J$. We see a good agreement over more than 3 orders of magnitude in density, except for the central region. As explained in the next section, we attribute this mismatch to the local saturation of the detector.

Apart from this, the excellent match found in the width of the side peaks further confirm that we have reached the FFR, because the high momenta corresponding to the narrowest features of

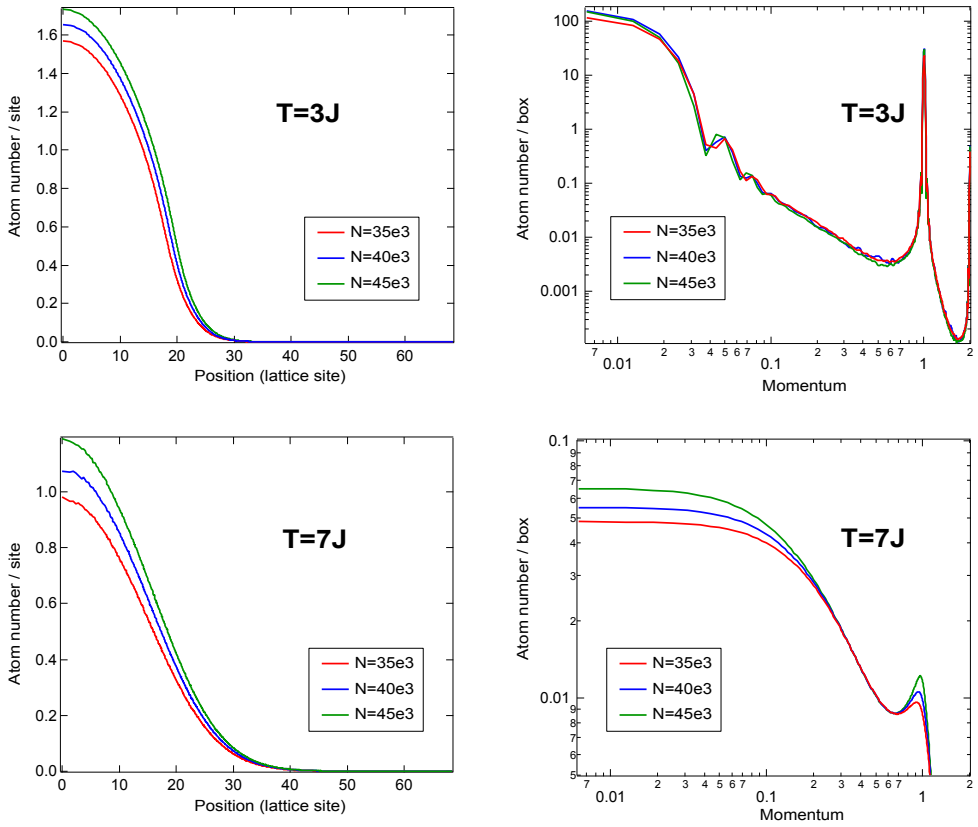

Figure 4.15: QMC calculations with our experimental parameters, for $T = 3J$, and $T = 7J$. Left : in-trap density profiles in linear scale. Right : momentum density profiles in log-log scale. The different curves in each panel correspond to different N, to take into account the 15% variations of atom number on our experiment.

the diffraction pattern are fully developed. It also confirms that the resolution of the detector is good enough to image structures smaller than $k_a/10$, which is coherent with the resolutions established in chapters 1 and 2. Finally, even though our main source of uncertainty is the atom number N ($\sim 15\%$ fluctuations), figure 4.15 shows that this fluctuation actually has a very small impact on the QMC profiles $n(\vec{k})$ at this temperature.

4.3.2 Investigating the saturation of the central peak

Evidence of saturation

Due to the narrow width of the diffraction peaks, we reach the regime of local saturation of the MCP as soon as there are a few dozen atoms populating the peaks. To be a bit more quantitative, we can use the reference value measured in section 1.2.4. The peak can be approximated by a sphere of radius $k_a/12$, corresponding to the excitation of an area of 10mm^2 of the MCP, during 1ms. The non-linear regime of $2 \times 10^5 \text{atoms.cm}^{-2}.\text{s}^{-1}$ is then reached for 20 atoms only. This is the case for the central peak, even for our "low-flux" dataset (see figure 4.16), but not for the first-order diffraction peaks, lower in density by a factor of 5 due to the Wannier envelop.

To confirm the presence of saturation, we investigate the evolution of the 1D profiles distri-

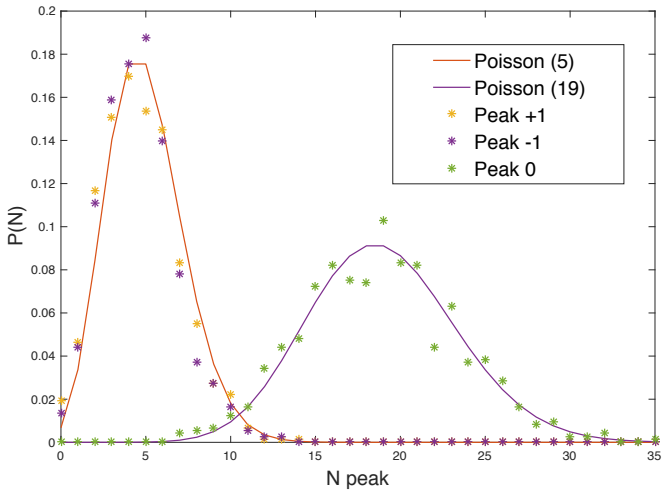

Figure 4.16: Statistic of the number of atoms detected in the different peaks for the low-flux data (less than 1% of the atoms transferred in the detectable state). The distribution is compatible with a Poissonian law.

bution, as we change the transverse integration $\mathcal{I}$ of the boxes. To do so, we generate a series of histograms $n_\infty(k,0,0)_\mathcal{I}$ of the number of atoms inside boxes centered on $\vec{k}=(k,0,0)$, and of size $(\Delta k,\mathcal{I},\mathcal{I})$. Since the saturation increases with the density, we expect the small transverse integration profiles to be more sensitive to this effect, because they probe the high-density core of the peaks. In figure 4.17, we plot the evolution of different peak amplitudes A_p as a function of $\mathcal{I}$ (from $3\Delta k$ to $90\Delta k$). To compare this evolution with a non-saturated case, we have divided the $A_p(\mathcal{I})$ curves by $A_{p_2}(\mathcal{I})$, where p_2 is the second-order diffraction peak of the high-flux dataset, that we assume not saturated. Each curve is then normalized to its asymptotic value, in order to compare the variations only. The plot reveals that all the peaks above a certain threshold (20 atoms detected per shot) exhibit a density depression at the peak's core. This translates in a fast decay of $A_p(\mathcal{I})/A_{p_2}(\mathcal{I})$ at low $\mathcal{I}$, and constitutes a signature of the MCP saturation.

Circumventing the saturation effect

One way to get rid of the saturation effect would be to lower even more the flux, by reducing the amount of transferred atoms to values lower than 1%. This is very time-consuming since it implies to accumulate much more data to reconstruct a complete profile. Another way is to take advantage of the symmetry of the momentum distribution. In figure 4.18, we show a plot of the density $n_\infty(k,0,\pm k_a)$ along the first and second order diffraction peaks, all below the saturation thresholds. We compare this profile to the QMC calculation $n(k,0,0)$, the height of the central peak of those two distributions being normalized to 1 to get rid of the multiplying factor coming from the decay of the Wannier envelope. The very good agreement we obtain further confirm that, apart from the central peak, the diffraction pattern matches well the one expected from the BH Hamiltonian.

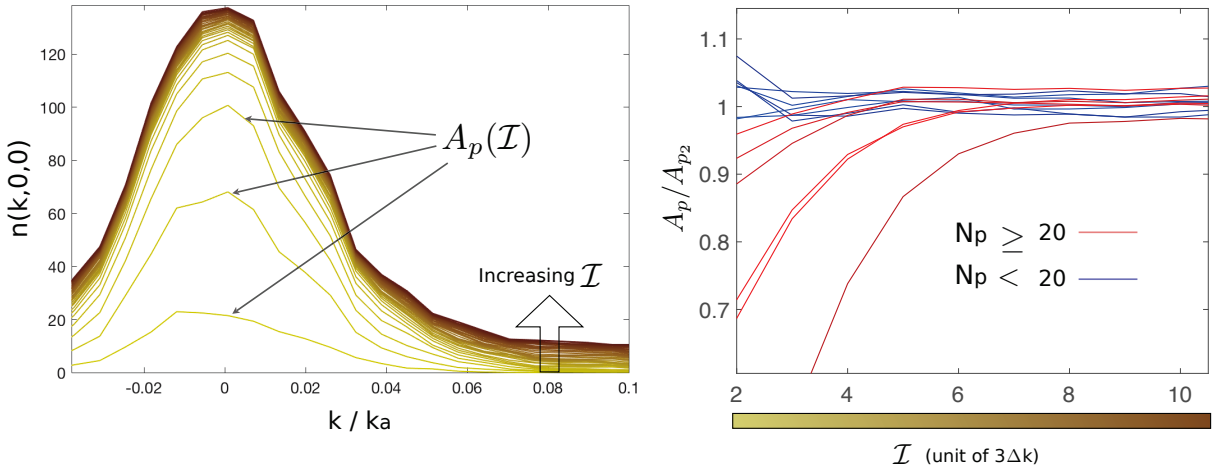

Figure 4.17: Left : n(k,0,0) 1D profile as we increase the transverse integration $\mathcal{I}$. We are interested in the evolution of the peak's amplitude $A_p(\mathcal{I})$. Right : normalized plots $A_p(\mathcal{I})/A_{p_2}(\mathcal{I})$ for various peaks (0-order, 1st-order and 2nd-order diffraction peaks). The plots in shades of red correspond to peaks whose densities are close or above the saturation threshold (20 atoms / shot). On the other hand, the plots in shades of blue are below this threshold.

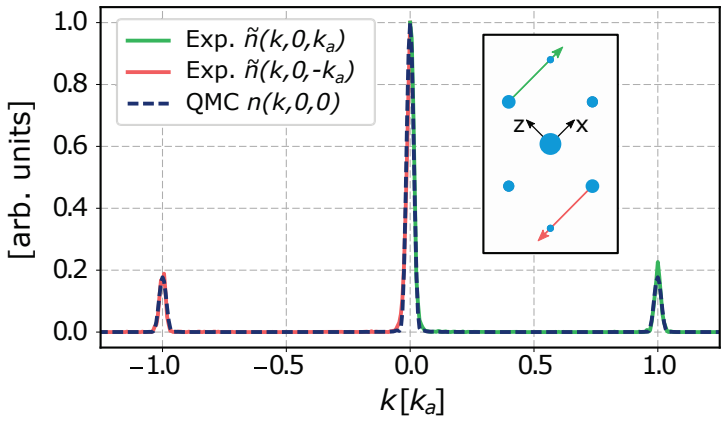

Figure 4.18: Comparison between the 1D profile $n_\infty(k, 0, \pm k_a)$, and $n(k, 0, 0)$ extracted from the QMC simulation. We are interested in the ratio between the main peak and the side peaks, that are all below the saturation regime of the detector. The comparison is done by normalizing the height of the first-order peak (central peak of this distribution) to 1.

4.3.3 Conclusions

The comparison with the QMC calculations confirms that the ballistic approximation for a lattice SF close to unity filling is good over several orders of magnitude. It allows us to benchmark our technique by measuring the momentum distribution of a 3D lattice gas of 4×10^5 bosons, loaded inside 50^3 lattice sites. The fact that this measurement is performed in the FFR with single-particle sensitivity gives us access to the microscopic population of the modes, an asset we will exploit in the next chapter.

Chapter 5

Momentum distribution across the superfluid to normal gas transition

In the previous chapter, we have compared the 3D distribution $n_\infty(\vec{k})$ of an expanding lattice gas in the Far-Field Regime (FFR), with the in-trap momentum distribution $n(\vec{k})$ predicted by the Bose-Hubbard (BH) Hamiltonian. The latter has been calculated using a QMC approach with our experimental parameters, except for the temperature, which is not measured in the experiment. Having the temperature as an adjustable parameter of the simulation can be seen as an asset, since it allows to perform a precise thermometry of the system, and therefore to explore the BH phase diagram at finite temperature. This is the object of the present chapter.

The first section describes how we construct a "thermometer curve" from the QMC simulations, through a simple density ratio in momentum space. In the second section, we present a direct measurement of the condensed fraction f_c, using the 3D distribution to separate the condensate's peak from the excited modes. By combining this measurement to the thermometry method, we can plot f_c as a function of the temperature T across the Superfluid (SF) to Normal Gas (NG) transition, and extract the critical temperature. The last section is dedicated to the measurement of the second order correlations across the transition. We again exploit the three dimensional aspect of the data to investigate the evolution of the correlations in the excited modes only, preventing the signal to be flattened by the emergence of the condensate.

5.1 Thermometry in the 3D lattice

5.1.1 Temperature in optical lattices : state of the art

A quantity difficult to access

Cold atoms experiments generally offer a better control over the microscopic quantities than over the macroscopic ones, like the temperature. Indeed, by construction, ultra-cold gases are isolated from the rest of the world, and in absence of coupling to any kind of reservoir, there exists no button to set the temperature of the system. In the case of lattice gases, it can also be very hard to evaluate the temperature experimentally. For inhomogeneous (trapped) system, a couple of methods based on the local density approximation use the in-situ density fluctuations to extract the temperature of a lattice gas [130, 131]. Alternatively, the RMS width of the trapped system can be used [132]. Those techniques require an high resolution imaging of the in-trap density, which can be provided by quantum gas microscopes [12], but are not adapted for 3D and/or homogeneous systems. On the other hand, extracting the temperature of a lattice gas from

$n(\vec{k})$ is uneasy, since there exists no analytical formula for the momentum distribution of the thermally depleted atoms. Furthermore, the lattice sinusoidal dispersion relation ($E_k \propto \sin(ka)$) tends to flatten the distribution with respect to the free particle case. This, in addition to the periodicity of $n(\vec{k})$, makes the thermal depletion very difficult to separate from the quantum depletion, which has a non-negligible fraction for strongly interacting systems.

Hence, in lattice experiments, the temperature is usually measured on the weakly interacting trapped BEC [133] before loading it in the optical lattice. Indeed, like we saw in chapter 3, the BEC is well described by the Bogoliubov approach, and the thermal depletion is well separated from the (very diluted) quantum depletion. If the temperature is not too low, the thermal distribution can be detected with optical probe, and fitted with a Bose function. The temperature inside the lattice is then deduced by assuming entropy conservation during the adiabatic transfer, which does not constitute a direct measurement.

New approaches

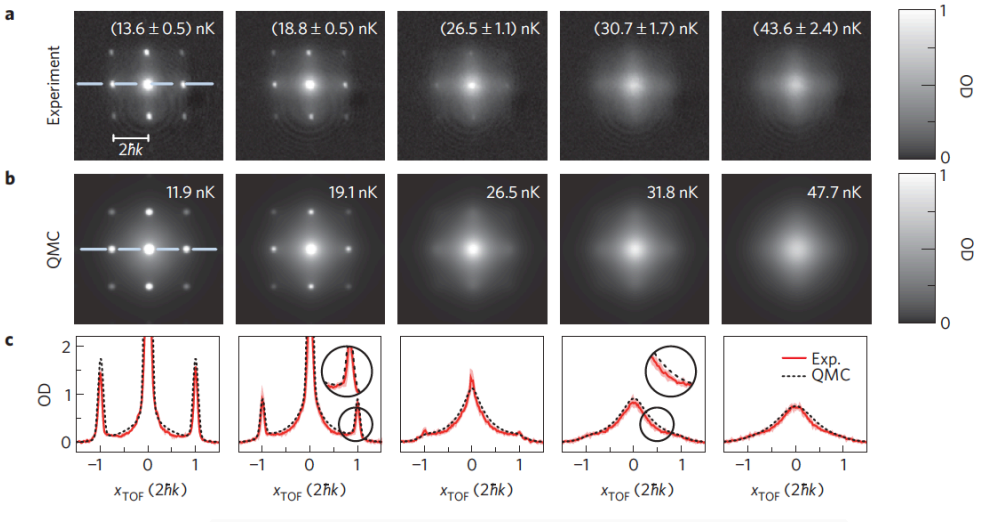

Figure 5.1: Extracted from [17]. Comparison between the distribution of an expanding lattice gas of ^{87}Rb, and QMC simulations based on the BH Hamiltonian. The distributions are probed by absorption imaging after a 15.5ms of ToF, and the simulations take into account both the finite expansion time, and the column integrated density.

Despite of those difficulties, various works have investigated alternative ways to provide precise thermometry methods for lattice systems in ToF experiments. An interesting idea is to use the band-mapping technique (see section 4.2.2), to probe the temperature through the quasi-momentum distribution [132]. However, this technique tends to fail as soon as $k_B T > J$, which is too restrictive to be used practically. In [134], the author has built a theoretical proposal based on the fluctuation-dissipation theorem. The idea is to extract T using the shot to shot momentum density fluctuations. The temperature is therefore not calculated from the average quantity $n(\vec{k})$, but from its fluctuations. This approach requires very stable working conditions, and a good Signal-to-Noise Ratio (SNR), and to our knowledge, it has not been experimentally demonstrated yet.

The authors of [17] developed a thermometry method, based on the comparison with ab-initio QMC calculations. Contrary to our approach (cf the results presented in the previous chapter), they do not calculate the momentum distribution of the gas, but rather the column integrated atomic distribution after a short expansion time, to simulate their ToF images taken by absorption. This work constituted the first direct comparison between the measurement of a lattice gas distribution, and a QMC simulation of the BH Hamiltonian (see figure 5.1). The calculations were conducted for various initial temperatures, allowing to perform a thermometry of the system by comparison with the experimental data. In particular, they demonstrated that the adiabatic loading approach works reasonably well to evaluate the temperature, and they were able to observe the decay of the critical temperature T_c when approaching the Mott transition.

We would like to implement a similar technique for our data, and extract the temperature of our system using the QMC calculations. In our case, the comparison is directly performed in the momentum space, without any spatial integration, so we expect the effects of the temperature to be much more stringent, and the thermometry very precise.

5.1.2 A density-ratio based thermometer

Principle

First of all, we want to define a simple quantity to perform the comparisons between the theory and the data. The QMC calculations were conducted for temperatures ranging from $(k_B)T = 1J$ to $10J$ by step of $0.5J$, and it would be laborious to compare those distributions over the full range of momenta to extract the temperature.

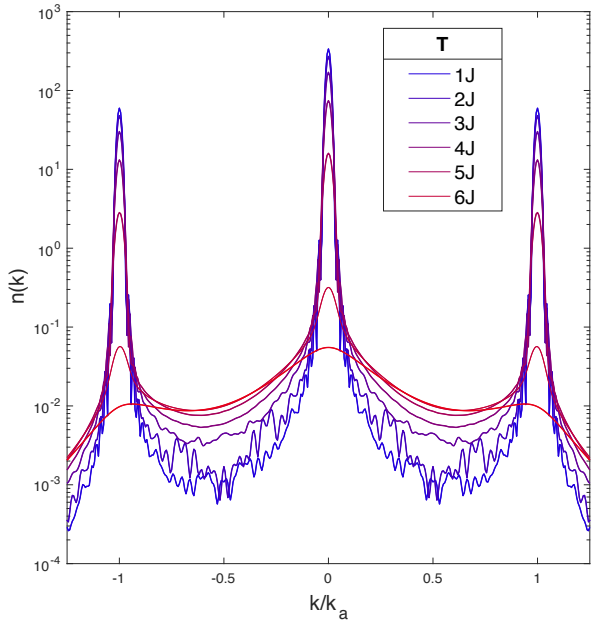

Figure 5.2: Theoretical momentum distribution of our lattice system, obtained by QMC calculation. The temperature is the only free parameter, and we have plotted the distribution for different T. The momentum regions the most affected by the temperature variations are the diffraction peaks ($k/k_a = -1, 0, +1$), and the edge of the Brillouin zone ($k/k_a = \pm 0.5$)

Below T_c, raising the temperature of the gas has two symmetrical consequences : decreasing the population of the lowest energy mode, and populating excited states. In terms of momentum

distribution, it implies a decay of the diffraction peaks' density, and a growth of the density outside the peaks [121]. In figure 5.2, we see that the edge of the Brillouin zone (momentum $k_a/2$) is the "low density" region which is the most affected by temperature variations. Thus, by defining the "thermometer" ratio between the density of the first-order diffraction peak and the density of the edge of the Brillouin zone :

$$r_T = n(k_a, 0, 0)/n(k_a/2, 0, 0), \tag{5.1}$$

we build a quantity which is very sensitive to temperature variations. Note that we use $n(k_a, 0, 0)$ rather than $n(0, 0, 0)$ to avoid saturation effects.

The thermometer curve

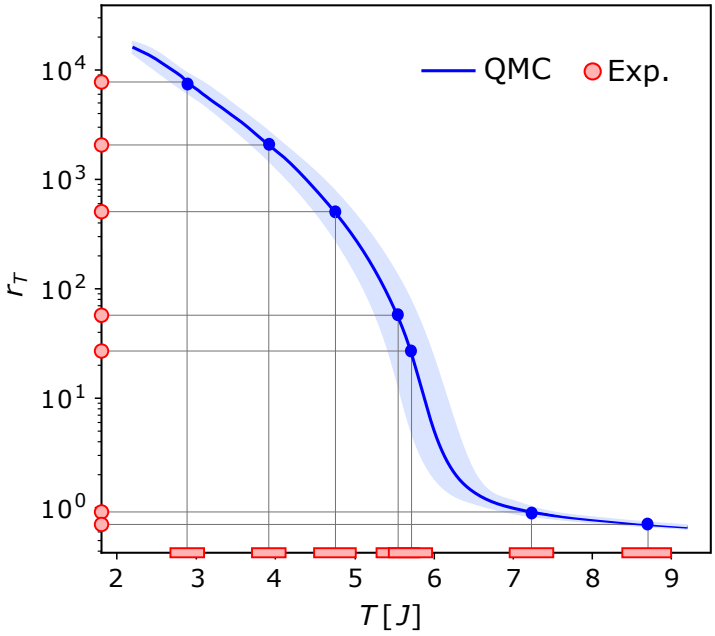

Figure 5.3: Thermometer curve (blue) obtained by interpolating the ratio r_T calculated from the different QMC distributions. The width of the curve (shaded blue area) stands for the atom-number uncertainty on the experiment. The red dots on the Y-axis are r_T ratios calculated from experimental data, and the red rectangles on the X-axis corresponds to the temperature extracted from the thermometer curve.

Figure 5.3 shows a "thermometer" curve obtained by interpolating the r_T values calculated for all the QMC distributions. As expected, this quantity decreases rapidly with temperature, decaying by 4 orders of magnitudes when the temperature varies from 2 J to 9 J. In the experiment, our main source of instability is the atom number, with a typical dispersion of 15% over the several hundreds of shots used to build a dataset. To take this fluctuations into account, we have also conducted QMC calculations for $N = 3.5 \times 10^5$atoms and $N = 4.5 \times 10^5$atoms, and calculated the corresponding r_T, resulting in a broadening of the thermometer curve (blue shaded area in figure 5.3). We have measured $n_\infty(\vec{k})$ with different heating sequences to vary the temperature (see section 4.2.1). The different r_T calculated for those heated clouds are indicated by red dots

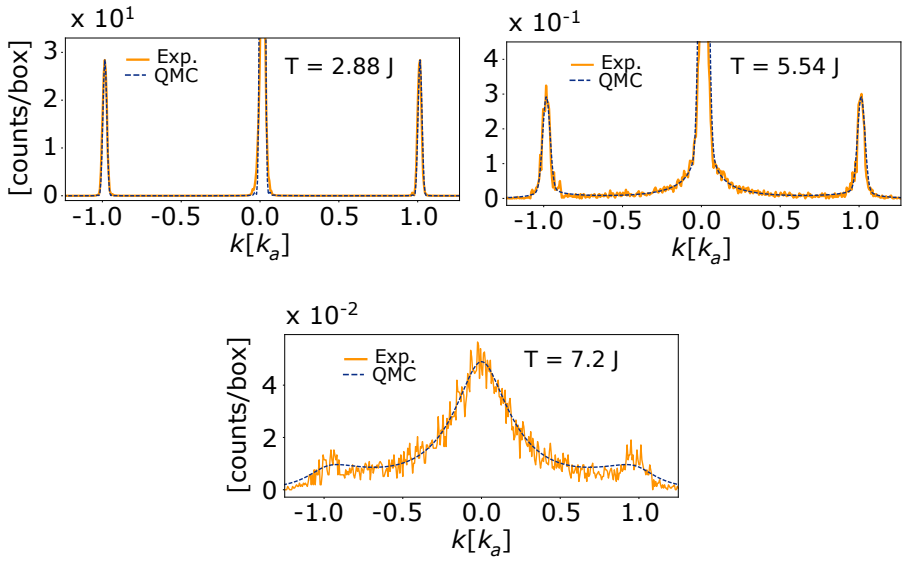

Figure 5.4: Comparison between QMC profiles and experimental 1D cut along $n(k, 0, 0)$. The different plots correspond to different T, which have been extracted from r_T.

along the y-axis of figure 5.3, and we project them on the thermometer curve to extract the temperature. In figure 5.4 we compare the 1D profiles extracted from the 3D distribution with the QMC profiles of the corresponding temperature, and find a very good agreement over the full range of momenta in all cases.

In conclusion, measuring the density at two different momenta $n(k_a, 0, 0)$ and $n(k_a/2, 0, 0)$ is sufficient to extract the temperature inside the lattice with a precision of 10% or better.

5.2 Measurement of the condensed fraction across the transition

Strictly speaking, a study of the BH phase-diagram should rely on the measurement of the superfluid fraction f_s, which is difficult to probe in a lattice gas [135]. On the other hand, the condensed fraction f_c possesses a clear signature in momentum space, and can be accessed with our setup. In the famous case of liquid helium, f_c is very low (of the order of the percent), even at zero temperature when $f_s = 1$, because the very strong interactions between the atoms keep the level of quantum depletion high. In the case of a lattice bosonic gas, f_c and f_s are almost equal for typical experimental parameters (see [121]). In particular, they both vanish similarly at T_c, making the condensed fraction a key quantity to investigate finite temperature phase diagrams.

5.2.1 Probing the condensed fraction in an expanding lattice cloud

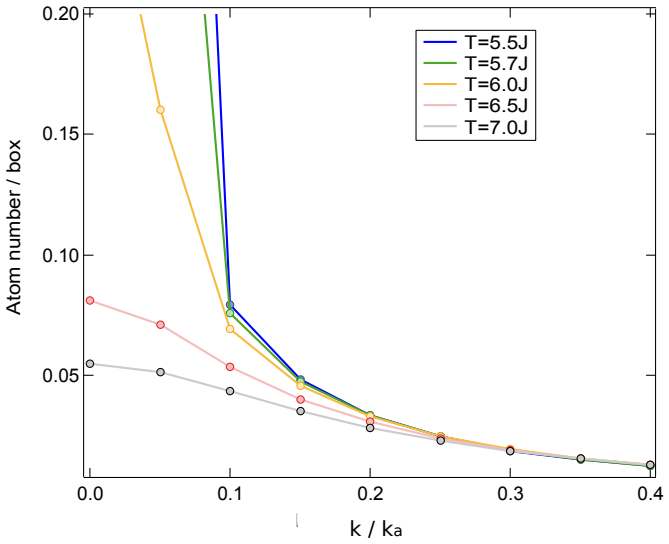

Figure 5.5: QMC calculations of $n(\vec{k})$, around the central peak region. The different plots represent different temperatures. For an equivalent homogeneous system, the critical temperature T_c is $\simeq 6.3J$ (see below). For $T < T_c$, we clearly see a change of slope around $k \simeq 0.1k_a$, indicating the frontier between the condensate and the rest of the distribution. The change of slope disappears at $T \geq T_c$, when the condensed fraction is zero.

Since the first realizations of Bose-Einstein condensates in atomic vapors, the condensed fraction of the gas is probed through ToF measurements [136, 9]. Indeed, the appearance of a narrow, dense structure on top of a broad, diluted distribution has always been considered as a proof of quantum degeneracy in diluted bosonic systems. Although this might be true for the Bose-Einstein condensation in an harmonic (or homogeneous) trap, it is more complicated in the lattice, where sharp structures in the momentum distribution can be observed, even above the critical temperature [121, 120]. Indeed, "sharp" is not very well defined, and it usually means "much narrower" than the distance d between the peaks. Hence, a thermal gas with a quasi-momentum distribution "much narrower" than the Brillouin zone will exhibit peaks in the FFR. Those peaks are not linked to the quantum degeneracy, and their width diminish when the temperature decreases. On the other hand, a clear and unambiguous signature of condensation is the appearance of ultra-narrow peaks of width $\simeq 2\pi/L$ on top of this already bimodal structure, indicating that the coherence have spread over the entire system. The emergence of those narrow peaks is characterized by a neat change of slope, close to $k \simeq 2\pi/L$, as shown in figure 5.5.

In previous experiments, the limitations due to finite resolution and finite expansion time were important obstacles to properly identify and measure the condensed fraction [23, 17]. Hence, other quantities were defined to try to pinpoint the emergence of coherence in the system. For instance, the authors of [17] use the variations of width and amplitude of the central peak to evaluate f_c across the SF-NG transition. Another example is the visibility, from which our thermometer curve is inspired. It is a measure of the contrast between $n_{\text{tof}}(k_a, 0, 0)$ and $n_{\text{tof}}\left(\frac{k_a}{\sqrt{2}}, \frac{k_a}{\sqrt{2}}, 0\right)$, and gives a relatively good estimation of T_c [120, 121, 137]. In [16], a fit of the central peak of an expanding 2D gas leads to a measure of f_c across the SF-MI transition compatible with QMC

calculations. However, a direct measurement of the condensed fraction in a 3D lattice gas was still lacking.

5.2.2 Measuring the condensed fraction from the 3D distribution

Identification of the lowest energy mode

The high-resolved 3D distributions offered by the MCP detector allows to observe the change of slope between the lowest energy mode and the rest of the distribution. In other words, we can identify the border k_0 of the diffraction peak corresponding to the condensate. We fit the central peak of the 1D profiles with a gaussian, and the depletion with a power law, and define k_0 as the intersection of the two curves (figure 5.6). Then, measuring f_c "simply" consists in counting the number of condensed atoms N_0 inside the central peak, and the number of non-condensed atoms N_{NC} in the rest of the first Brillouin zone. When no clear change of slope is visible, we consider that $f_c = 0$.

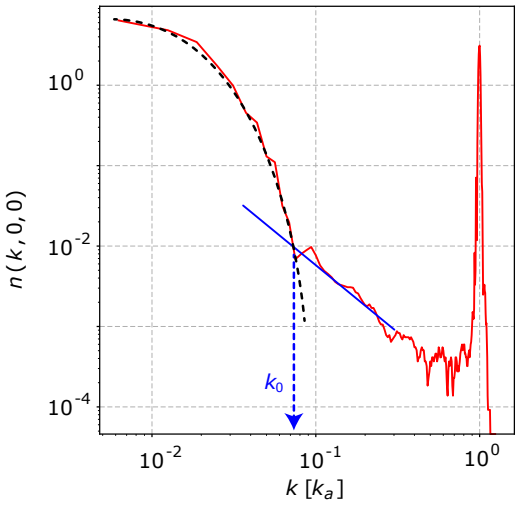

Figure 5.6: Extraction of the value k_0, which is the frontier between the momentum domains of the condensate and the depletion. k_0 is taken at the intersection between the gaussian fit of the condensate peak, and the power-law fit of the background depletion.

The effect of the central peak saturation

Counting N_0 and N_{NC} is not straightforward because of some technical limitations of the detector : on the one hand, the central peak is saturated, which makes it uneasy to evaluate N_0 from the first Brillouin zone, but on the other hand, the second Brillouin zones are not entirely covered by the 4cm radius of the MCP detector, so we can only evaluate N_{NC} from the first Brillouin zone. We therefore "correct" the saturation by multiplying the number of atoms inside the first peak by $\alpha = n(k_a, 0, 0)/[w(k_a) * n(0, 0, 0)]$. We then have :

$$f_c = \alpha N_0/(N_{\mathrm{NC}} + \alpha N_0). \tag{5.2}$$

The uncertainty in the estimation of f_c is typically around 20%, based on its standard deviation over ~ 1000 cycles. Such fluctuations in the shot-to-shot condensed fraction is not really surprising, because of the very low SNR outside of the peaks, and the fact that the saturation

effect in the central region is highly non-linear. Indeed, the typical 15% fluctuations in the total atom number can very well lead to higher fluctuations of the number of particles detected in the central peak, in a way which is difficult to evaluate.

5.2.3 Extracting the critical temperature

Condensation in a trapped system

One of the characteristics of most optical lattice experiments is the presence of an external confinement, which complicates a lot the comparison with theory, usually established for homogeneous system. The gaussian profile of the beams creates a spatial variation of the effective chemical potential, and leads to the coexistence of difference phases inside the trap [124]. One of the most striking example being the "wedding cake" structure at the Mott transition, experimentally observed in 2006 [138, 139]. In the SF to NG transition, for a unitary filling, the condensate is expected to appear first in the highest density regions, that is the center of the trap [17, 140]. The critical temperature for our trapped gas should thus be close to the one of an homogeneous system, whose density matches the density at the center of the trap.

Results

Figure 5.7 shows a plot of the measured f_c as a function of T. The characteristic decay of f_c indicates the vanishing of the condensed fraction at $T = T_c$. On the other hand, at $T = 0$, the condensed fraction is not expected to reach 1 because of the high quantum depletion induced by the lattice. We have used a site-decoupled approach based on the Gutzwiller ansatz [126] to estimate f_c at $T = 0$ and $U/J = 10$, and we find $f_c \simeq 85\%$. For lack of an analytical model, we use an empirical function [24] to fit the data, and obtain $T_c = 5.9(2)J$. As discussed above, it is tempting to compare this value to the critical temperature T_{c0} of an homogeneous system sharing the same microscopic properties, and whose chemical potential matches the one at the center of the trap. With a QMC approach based on the winding number estimator, we find $T_{c0} = 6.3(3)J$, indeed compatible with T_c.

In the future, it would be interesting to further address the question of the criticality in trapped system, and investigate the link with the homogeneous case. Within the framework of trap-size scaling theory, recent studies [141, 142, 143] have described the effect of the trap on critical parameters, leading to new theoretical proposals. For instance, the authors of [140] show that a precise measurement of $n(\vec{k})$ for a trapped system allows to identify the critical temperature of the homogeneous case, by monitoring the violation of the local density approximation at the phase transition.

5.3 Second-order correlations across the transition

5.3.1 The $g^{(2)}$ function in the lattice

By increasing the interactions between the atoms, the presence of the lattice increases the correlations of the system. In particular, it raises the quantum depletion by 2 orders of magnitude with respect to the weakly interacting BEC in an harmonic trap, and we can thus hope to observe some interaction-induced correlations between the depleted atoms.

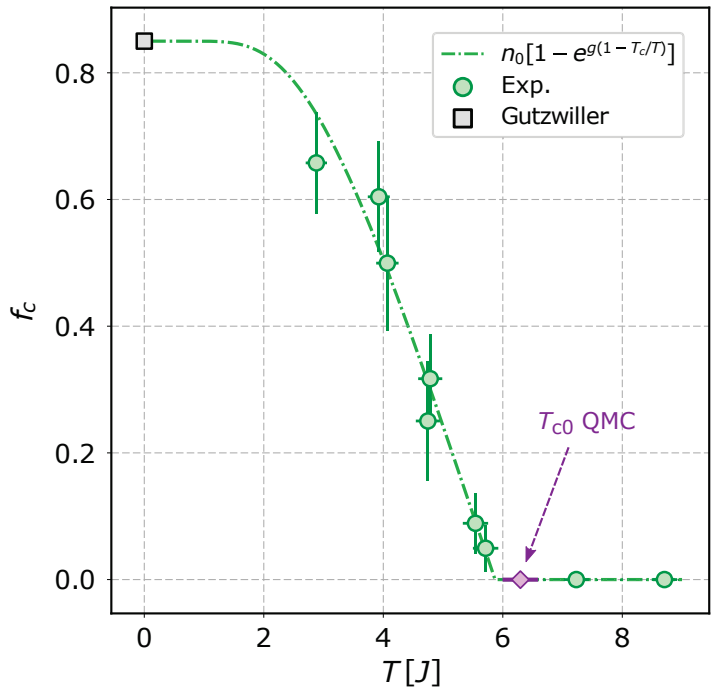

Figure 5.7: Condensed fraction plotted as a function of the temperature T. The green dots correspond to the experimental measurements, and the error bars are the standard deviation over ~ 1000 experimental cycles. The grey square correspond to the $T = 0$ prediction given by a mean-field, site-decoupled approach, and the violet diamond indicates the critical temperature for an homogeneous system with a chemical potential matching that at the trap center.

Correlations in the superfluid

As mentioned in chapters 2 and 3, in a BEC, where all the particles occupy the same $q = 0$ (quasi-)momentum state, the absence of interference between different bosonic modes lead to an absence second-order correlations, both in real and momentum space. With the second-quantization formalism presented in section 4.1, it is easy to write an analytical expression for the $g^{(2)}$ function of an homogeneous, ideal lattice BEC. Indeed, according to equation 4.23, the expression of the field operator in momentum space can be written :

$$\phi(k) = A(k) \sum_q b_q \frac{\sin\left(Ma(k-q)/2\right)}{\sin\left(a(k-q)/2\right)}. \tag{5.3}$$

The non-interacting, zero-temperature BEC quantum state is $|\Psi_0\rangle = \frac{1}{\sqrt{N!}}(b_0^\dagger)^N |0\rangle$, so only the terms $\langle b_0^\dagger b_0\rangle = N$ and $\langle b_0^\dagger b_0^\dagger b_0 b_0\rangle$ are non zero. We then have :

$$n(k) = \langle \phi(k)^\dagger \phi(k)\rangle = N|A(k)|^2 \left(\frac{\sin\left(Mak/2\right)}{\sin\left(ak/2\right)}\right)^2, \tag{5.4}$$

$$G^{(2)}(k,k') = \langle \phi(k')^\dagger \phi(k)^\dagger \phi(k)\phi(k')\rangle = n(k)n(k')\left(1 - \frac{1}{N}\right), \tag{5.5}$$

so that $g^{(2)}(k,k') = G^{(2)}(k,k')/n(k)n(k') \simeq 1$ when N is large, meaning that there is no correlation in the system. Note that this result is independent of the lattice depth V_0.

Like discussed in chapter 3, for a real system, interactions and temperature allow higher momentum modes to be populated, which carry richer correlation signals, like the bosonic bunching. However, it does not change the absence of correlation between the condensed atoms, and for large f_c, calculating the $g^{(2)}$ function over the entire cloud would wash out the correlations between depleted atoms, since the signal is dominated by the uncorrelated BEC. In our case, the ability to probe the 3D distribution with an atom-counting technique allows us to separate the condensate from the rest of the distribution, and to calculate the correlations between specific modes, without requiring an autocorrelation of the entire density profile [85, 84]. We thus have access to the $g^{(2)}$ function between the depleted atoms only, a technique we already used with the harmonically trapped BEC (see section 3.3.1).

At low temperature, when the quantum depletion dominates the excited population, both site-decoupled approximation and Bogoliubov approach (the latter is only valid for low lattice depth) predict bosonic bunching (diagonal (k,k) correlations) and pairing (anti-diagonal $(k,-k)$ correlations) [22]. This pairing has a simple physical interpretation in terms of momentum conservation : if an atom leaves the condensate and populates momentum k because of a two-body interaction, then the other atom of the pair have to populate momentum $-k$ to conserve the total momentum of the BEC. Let us add that both diagonal and anti-diagonal correlations have a k_a periodicity due to the lattice structure, so that detecting an atom at momentum k enhances the probability to detect another atom at momentum $k + nk_a$ and $-k + nk_a$, where $n \in \mathbb{N}$. Figure 5.8 shows a theoretical $g^{(2)}(k_1,k_2)$ of an homogeneous lattice gas, calculated with the Bogoliubov approach (see [22] for a detailed analytical expression). The aim of this plot is simply to illustrate the pairing and bunching correlations of the quantum depletion, not to provide a quantitative analysis, since the Bogoliubov approach is not expected to be valid at our lattice depth.

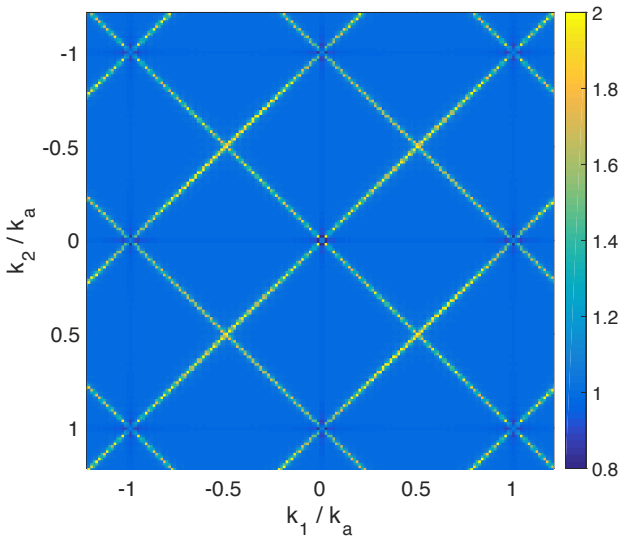

Figure 5.8: $g^{(2)}(k_1, k_2)$ of an homogeneous lattice gas at unity filling calculated with the Bogoliubov approach. The parameters of the calculation are : $U/J = 10$, $T = 0$, $L = 50a$.

Correlations above T_c

Above T_c, both the condensed fraction and the quantum depletion vanish, and the correlations become those of a thermal gas. We can calculate a theoretical $g^{(2)}$, by using the Bose statistics for the population of the modes (see again [22] for a detailed expression). Figure 5.9 shows a plot of $g^{(2)}(k_1, k_2)$ at $U/J = 10$ and $T = 8J$ for an homogeneous gas. It shows that the only remaining correlations in the system is the periodic bunching, that is the Hanburry-Brown and Twiss effect applied to a lattice. We can conclude that the sole qualitative difference in the $g^{(2)}$ signal between SF and NG is the presence of an anti-diagonal $(k, -k)$ pairing correlations.

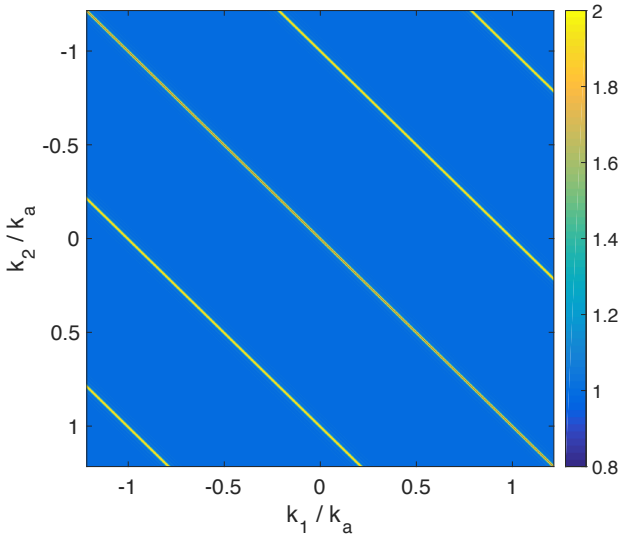

Figure 5.9: $g^{(2)}(k, k')$ of an homogeneous lattice gas at unity filling for an ideal thermal gas. The parameters of the calculation are : $U/J = 10$, $T = 8J$, $L = 50a$.

5.3.2 Measurement of second-order correlations

Correlations in the different momentum domains

With the algorithm presented in chapter 2, we calculate the functions $g_{\pm}^{(2)}(\delta k_z)$ for the lattice data. We chose to study the correlations along the z-axis (gravity) because, as we saw in chapter 1, the resolution σ_z is much less sensitive to variations of the detected particle's flux than $\sigma_{x,y}$. In figure 5.10, we have plotted the correlations obtained at $T = 2.88J$ (the coldest dataset), for two different momentum domains : inside and outside the diffraction peaks. In the first case, as expected, the signal is flat since there are no correlations between the condensed atoms. Outside the peaks, we recover the bunching, but we do not observe $(\vec{k}, -\vec{k})$ pairing signals, a result which is confirmed for all the temperatures.

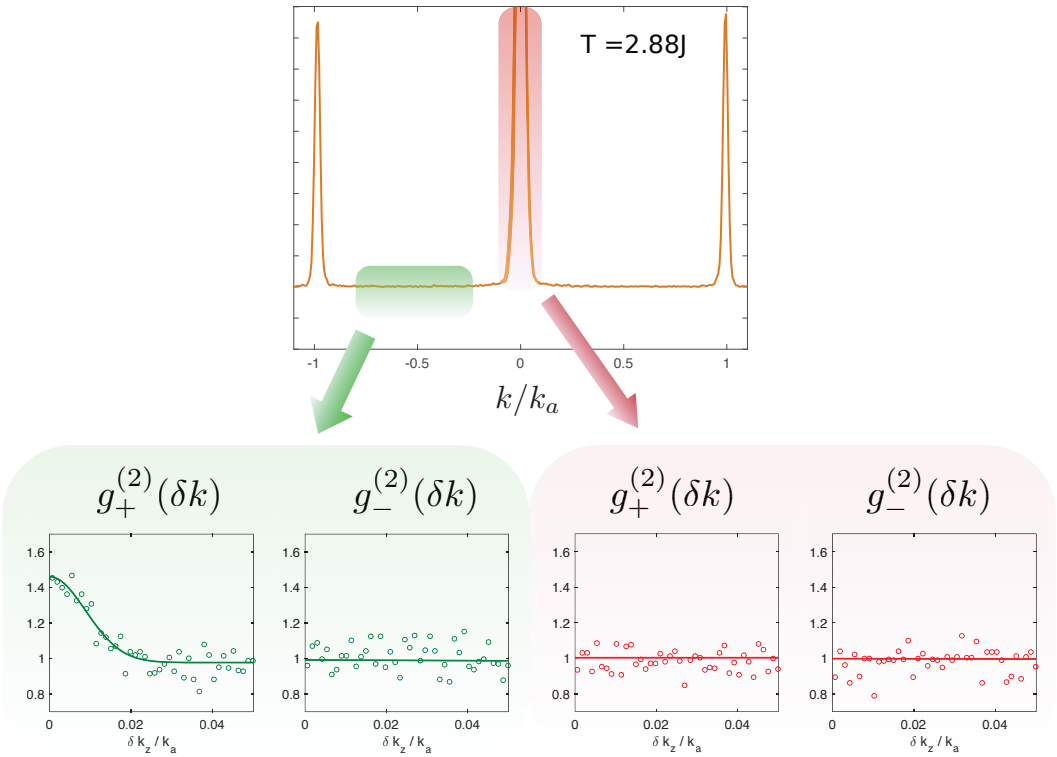

Figure 5.10: Correlation functions $g_+^{(2)}$ and $g_-^{(2)}$ for T=2.88J. The functions are calculated along the z-axis, inside and outside the condensate peak. We used $\Delta k_\perp = 0.012 k_a$ for the transverse integration.

The absence of pairing correlations might be related to the statistics : at low T, the very low density of the distribution between the peaks may not give a sufficiently high SNR to distinguish a clear correlation peak. At higher T the SNR is better, but only because more thermally excited atoms are added to the depletion, without "producing" any pairing correlations. An other explanation could come from the shot-to-shot fluctuation of the center of the cloud. Indeed, the ability to probe a $(\vec{k}, -\vec{k})$ signal strongly depends on the precision at which we can identify the Center-of-Mass (CoM) of the distribution. The very low SNR on the single-shot 3D distribution, and the saturation of the central peak makes it very difficult to precisely evaluate the shot-to-shot variations of the CoM. On the other hand, the good agreement between the measured width of the peaks and the QMC predictions suggests that the CoM does not fluctuate by more than

a fraction of the peak's width, which is of the same order than the expected correlation width ($\sim 1/L$). Finally, we can imagine that the $(\vec{k}, -\vec{k})$ pairs are destroyed by the interactions during the ToF dynamic, but since the average $n_\infty(\vec{k})$ distribution matches the expected $n(\vec{k})$ calculated by QMC, it requires a mechanism that preserves the expectation value of the momentum distribution, but disturb its fluctuations. To our knowledge, there exists no theoretical work investigating those questions.

Bosonic bunching across the transition

The ability to measure correlations outside of the condensate enables the possibility to investigate the bosonic bunching (see chapter 2) in a novel way. Up to now, experiments were restricted to a calculation of $g^{(2)}$ over the entire cloud [144, 83, 84, 93]. Averaging the correlation signal between the depletion and the condensate leads to a rapid flattening of $g^{(2)}(\delta k)$ below T_c, and hide the informations contained in the width of the bunching peak.

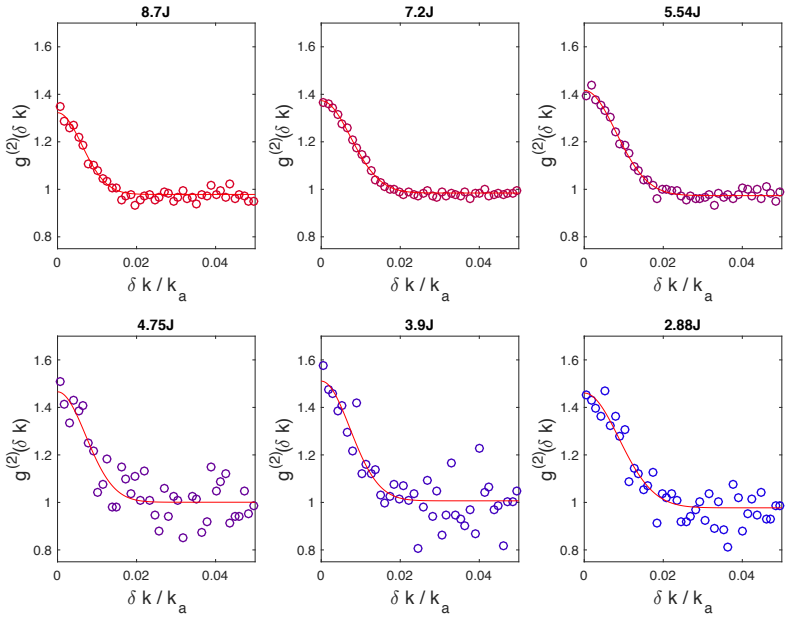

Figure 5.11: $g_+^{(2)}(\delta k_z)$ calculated over the first Brillouin zone for various temperatures. The calculation has been performed with $\Delta k_\perp = 0.012 k_a$, and only takes into account the atoms in the momentum region $\vec{k} > k_0$ to exclude the condensate. The solid line in each panel is a gaussian fit $b + a\exp(-\delta k^2/w^2)$ used to extract the effective correlation width w_z. The SNR increases with T, since more thermally depleted atoms contribute to the signal

Figure 5.11 presents a plot of the local correlation $g_+^{(2)}(\delta k_z)$ calculated outside of the condensate for various temperatures. The width w_z of the correlation peak can be extracted with a gaussian fit. To raise the SNR, we have computed the two-body correlations with a transverse integration $\Delta k_\perp = 12 \times 10^{-3}\, k_a$ (see section 2.2.2). As T raises, the correlation width diminishes, because of the evolution of the coherence properties of the thermal depletion (see below). On the other hand, the diminution of the bunching amplitude with T is not physical, and is a consequence of the reduction of the width, coupled to the finite resolution of the detector and the transverse integration $\Delta k_\perp$ (equation 2.22).

To extract the effective correlation width $w_z(T)$ in a more precise way, we repeat the procedure and calculate $g_+^{(2)}(\delta k_z)$ for various transverse integrations $\Delta k_\perp$. The value of $w_z(T)$ should not depend on $\Delta k_\perp$, but with this procedure, we multiply the number of fitted data, and therefore increases the precision on the measurement. We deduce the actual correlation length $l_{c_z}(T)$ from equation 2.20 : $l_{c_z} = \sqrt{w_z^2 - 4\sigma_z^2}$ where $\sigma_z = 2.5 \times 10^{-3}\, k_a$ is the resolution we have estimated in section 2.3.2. The results are presented in figure 5.12, and clearly show a diminution of l_{c_z} whith T, which is coherent with a diminution of the in-trap correlation length of the thermal fraction.

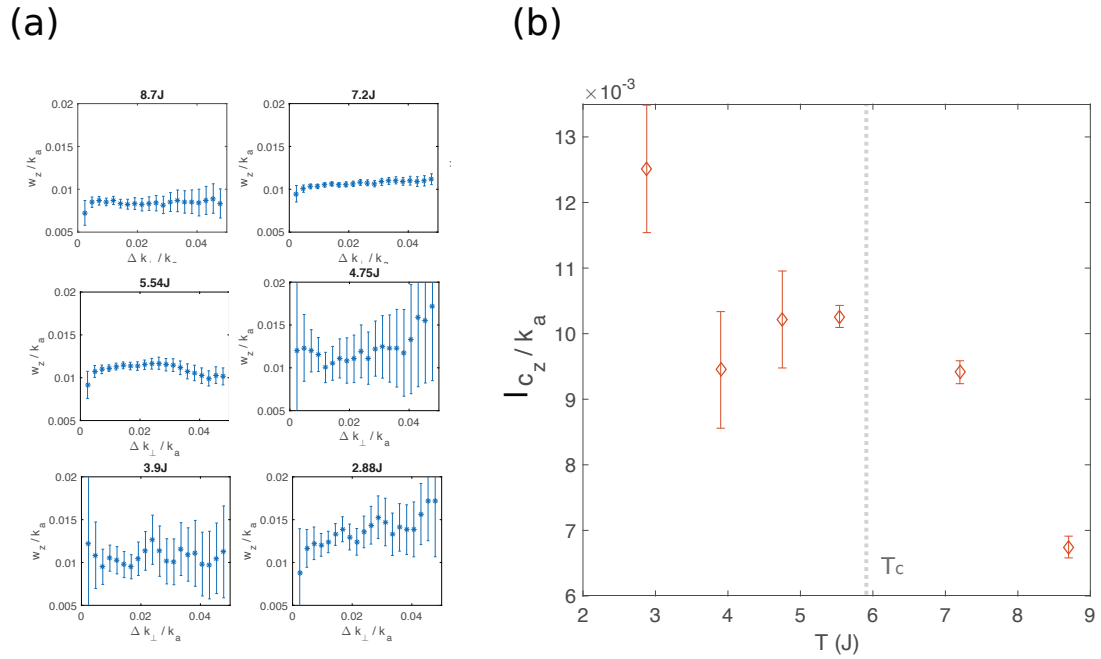

Figure 5.12: Variation of the correlation width across the transition. (a) Fitted effective width $w_z = \sqrt{l_{c_z}^2 + 4\sigma_z^2}$ as a function of the transverse integration $\Delta k_\perp$, for different temperatures. (b) $l_{c_z}(T)$ across the transition, the vertical grey line indicates T_c. We have used $\sigma_z = 0.0025\, k_a$ to calculate l_{c_z}.

Finally, it is interesting to compare $l_{c_z}(T)$ at high T with the Hanbury-Brown and Twiss (HBT) limit of a spatially incoherent gas of non-interacting particles in an harmonic trap, where the correlation width is equal to the inverse of the RMS size s of the trapped cloud (see chapter 2). We use the QMC curves $n(\vec{r})$ to extract the in-situ size s, and the comparison with $1/s$ is shown in figure 5.13. Surprisingly, the correlation width at $T > T_c$ does not match the HBT expectation. Note that all the temperatures involved here verify $T < U$, so the interactions might play a significant role in the size of $l_{c_z}(T)$. It would be interesting to perform similar measurements for different values of U/J.

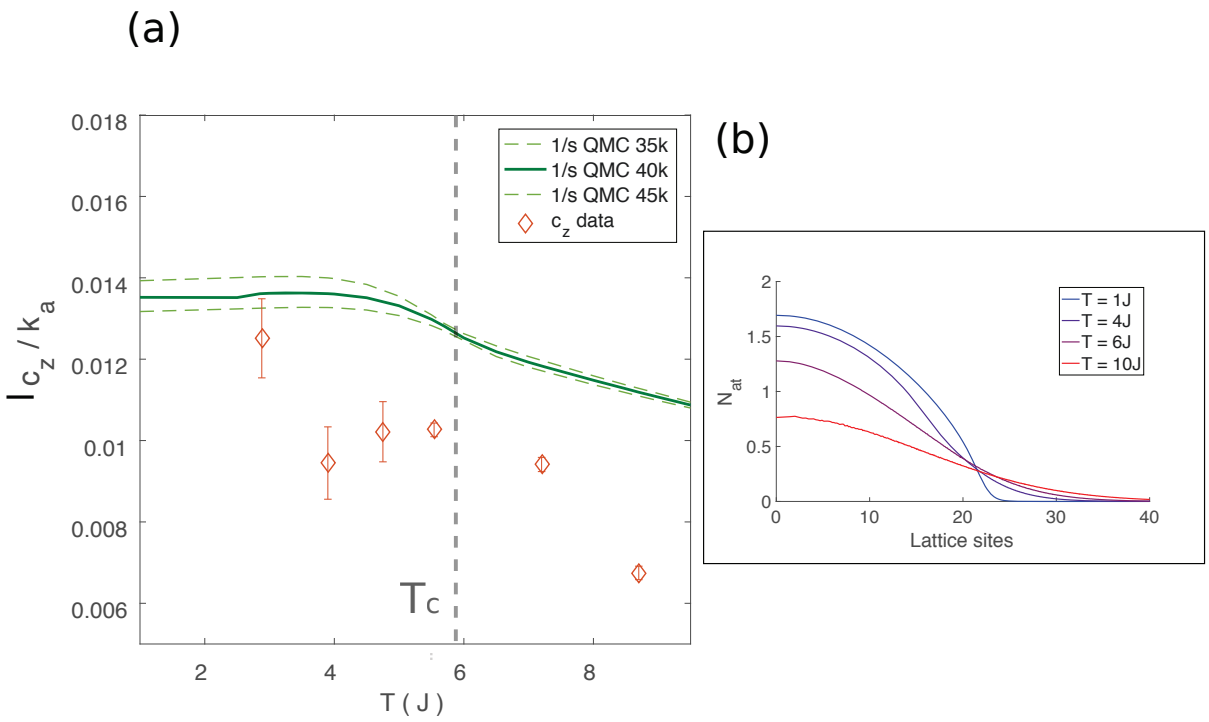

Figure 5.13: HBT limit. (a) Comparison between $s^{-1}(T)$ calculated from the QMC profiles $n(\vec{r})$, and $l_{c_z}(T)$ extracted from the $g^{(2)}$ data. (b) Plots of $n(\vec{r})$ simulation, for T = (1, 4, 6, 10) J.

Conclusion

Results

The main result of this work is the demonstration of a detection method capable of probing the momentum distribution of a 3D lattice gas at the single atom level [64]. This technique is based on the electronic detection of ultra-cold clouds of metastable Helium-4 (^{4}He*) by a Micro-Channel Plate (MCP) detector. The gas is detected after a time-of-flight of 325ms, long enough to enter the far-field regime of expansion, where the spatial distribution can be mapped to the asymptotic momentum distribution $n_\infty(\vec{k})$, through the ballistic relation $\hbar\vec{k} = m\vec{r}/t_{\text{tof}}$. If interactions do not play a significant role during the expansion, $n_\infty(\vec{k})$ coincides with the in-trap momentum distribution $n(\vec{k})$. For a sufficiently deep 3D lattice close to unity filling, it was suggested by previous works [23, 28] that the interactions between the particles can be neglected during the first instants of the ToF. Our comparison between $n_\infty(\vec{k})$ and the theoretical $n(\vec{k})$ calculated from the Bose-Hubbard (BH) hamiltonian with Quantum Monte Carlo (QMC) simulations validates this hypothesis, as we observe a match in density over more than 3 orders of magnitude, only limited by the saturation of the MCP detector in the high density regions.

Those results are the starting point of an exploration of the superfluid to normal gas transition, as the comparison with QMC allows us to perform a precise thermometry of our lattice gases. In particular, we perform the first 3D measurement of the condensed fraction across the transition, extracting a critical temperature compatible with the one of an homogeneous system, whose density matches the density at the center of our trap. We also investigate the momentum bunching of the thermal depletion across the transition, by calculating the $g^{(2)}$ function inside the excited modes only. We observe a decay of the momentum correlation width as the temperature is raised, coherent with a decay of the in-situ correlation length.

Another important part of this thesis is the study of the distribution $n_\infty(\vec{k})$ of a Bose-Einstein condensate (BEC) released from an harmonic trap [105]. Contrary to the lattice case, the initial expansion of the BEC is driven by the release of the mean-field energy, so that $n_\infty(\vec{k}) \neq n(\vec{k})$. The interesting aspect of this work is that the asymptotic momentum distribution itself becomes an object of study : what many-body dynamics govern the expansion? How is it linked to the in-trap momentum distribution? In this context, the observation of a k^{-4} tail in the distribution is a puzzling feature. Weakly interacting systems are well described by two-body contact interactions, which produce a polynomial k^{-4} decay in momentum. The amplitude of this decay, the celebrated Tan's contact C, is an intensive object of study in many-body systems. However, in the case of the interacting BEC in expansion, C is expected to decay in the timescale of the inverse trapping frequency ($\sim 300\mu$s), so observing such features in $n_\infty(\vec{k})$ is surprising. We recently discovered that our spin-polarized $m_J = +1$ BEC was "polluted" by an uncondensed $m_J = 0$ cloud, representing less than 1% of the trapped population. The distribution $n_\infty(\vec{k})$ of this cloud exhibits a k^{-4} decay, and might very well be the origin of the previous observations. We are currently investigating the interplay between this parasite cloud and the BEC, in the trap or during the expansion, in order to solve this mystery.

Outlook

Now it seems natural to pursue the exploration of the BH phase diagram, and study the Mott insulator phase. Very different from the normal gas transition presented in this work, the Mott transition occurs at zero-temperature, and is purely driven by the interactions. The correlations between the particles thus play a crucial role around the critical point, and it would be interesting to measure $g^{(2)}$ functions in this regime. We obtained the first ^{4}He* Mott insulator in April 2018, and we are currently investigating this new quantum state (see figure 5.14).

We are not done with the superfluid either, as we want to better understand the role of the interactions during the expansion of the lattice gas. In the work presented in chapters 4 and 5, no scattering halos were detectable between the diffraction peaks, while such features are commonly observed with lattice superfluids. We are currently monitoring the appearance of spherical scattering halos as we raise the atom number (filling factor > 1) and change the lattice depth.

In the meantime, we are interested in studying C in 1D systems, where it can be used to probe the fermionization transition [145]. C should be measurable with our setup, using an 1D gas engineered from the optical lattice : the strong interactions present in 1D systems increase C by orders of magnitude with respect to the 3D case, and the expansion dynamics, driven by the ground state energy of the transverse confinement ($\hbar\omega_\perp \gg \mu$) should preserve the in-situ velocity distribution along the longitudinal direction. Our first 1D gases were obtained during the redaction of this manuscript, and the analysis of its asymptotic momentum distributions is an ongoing work.

About the detector

The MCP detector has proven to be a very precise tool for the study of many-body physics, allowing to observe features in the momentum distribution with a level of detail and a density range never reached before. The ability to detect individual atoms is also very interesting to compute higher-order correlations in momentum space, as shown in this manuscript. Its saturation regime, however, is a real experimental limitation, making uneasy the detection of dense, narrow structures, like the diffraction peaks of the lattice superfluid. Hopefully strongly interacting systems, like 1D gases or Mott insulators, usually have a large momentum distribution because the interactions tend to populate many k-modes. Working with diluted distributions would further ease the data taking and analyzis, as no dense structure will disturb the detection process. This is also true for the upcoming system of study : fermionic lattice gases, as Helium-3 will be added to the experiment in a (hopefully) near future.

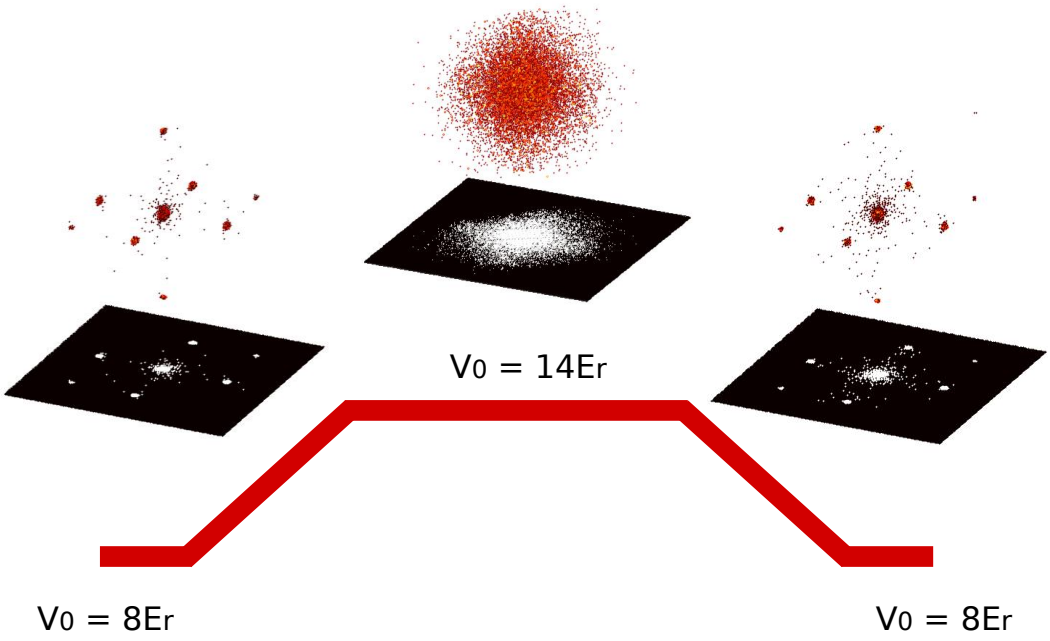

Figure 5.14: 3D asymptotic distribution $n_\infty(\vec{k})$ of the lattice gas as we raise the lattice depth. At $V_0 = 14\mathrm{E}_r$, the coherence is lost, as no diffraction peak is visible in the expanding cloud. This loss of coherence comes from the interactions, that tend to localize the atoms on the lattice sites (Mott insulator phase). If we now hold the gas and ramp down the lattice, the interactions become weaker, and we recover the coherence.

Appendix A

Constant fraction discriminator settings

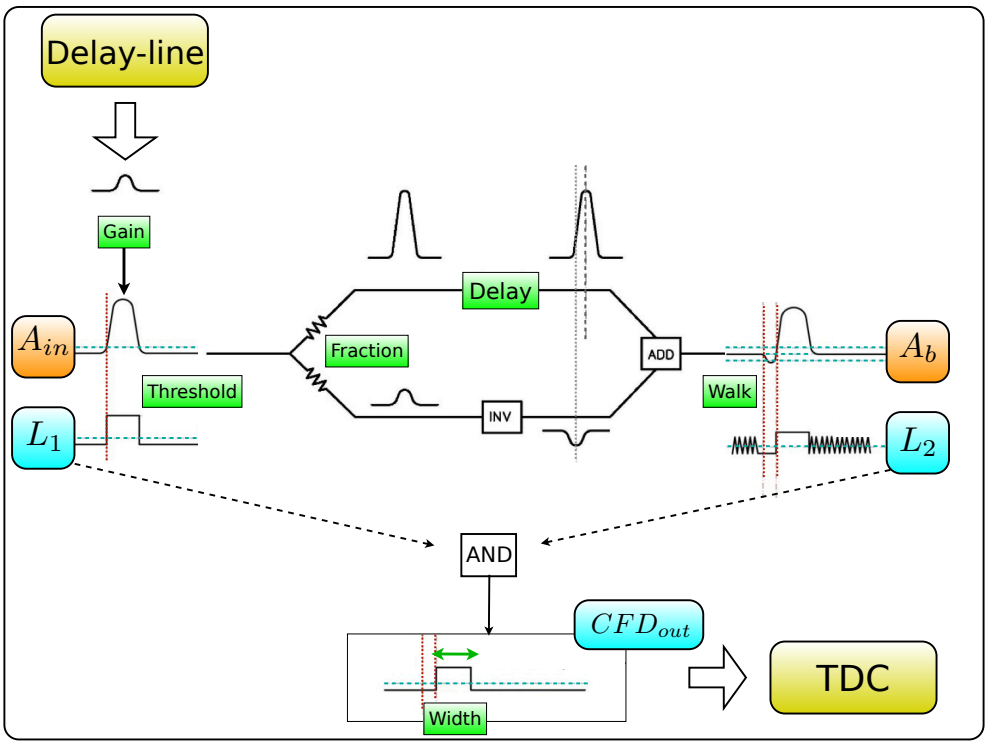

Figure A.1: Sketch of the Constant Fraction Discriminator functioning. The pulses coming from the delay lines are amplified (A_{in}), and turned into a bipolar signal (A_b). The output NIM signal (CFD_{out}) is triggered by the logical product of two square pulses, L_1 and L_2, which are generated by a leading-edge process working respectively on A_{in} and A_b.

This section gives a brief summary of how to properly set the Roentdek discriminator (the user guide manual is not always very clear). There are 6 parameters that the user can adjust for each CFD, they are indicated in **bold** throughout the paragraph. First, one can set the **gain** of the pre-amplification stage. The average pulse height at the output of the delay-lines strongly depends on the MCP polarization, and the gains have to be set in order to keep the signal amplitude in the operating range of the CFD (grossly between 30mV and 2V). One can also set the **fraction** and the **delay**, noted f_c and τ in equation 1.11. f_c is directly set manually by a potentiometer present in the front panel, while τ is set by the length of a LEMO cable that we

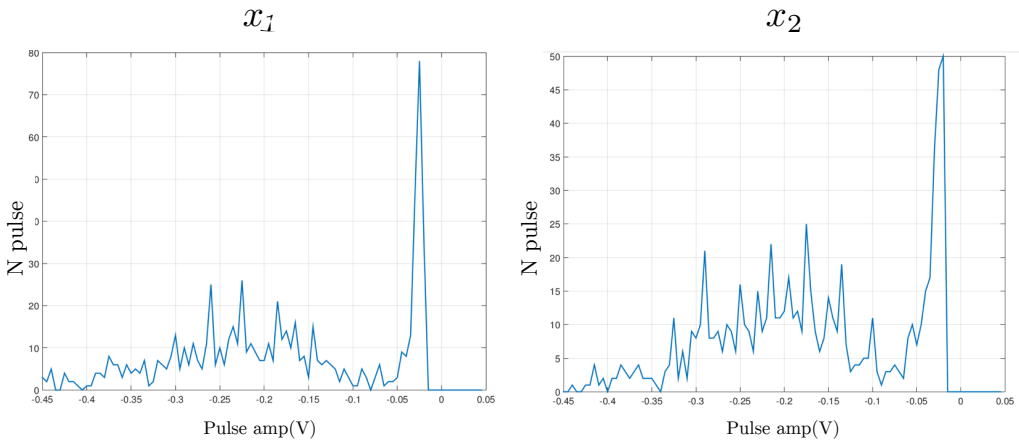

Figure A.2: Histograms of the A_{in} amplitude for channels x_1 and x_2. We see a typical double-structure : the signal (higher voltage values) is well separated from the noise (lower voltage values). The thresholds have to be set in between those 2 distributions (between 50mV and 100mV in this case).

plug in dedicated sockets. The three last parameters are directly related to the generation of the NIM signals. To understand them, we need to detail a bit more how the detection of the zero-point crossing is done.

The NIM signal at the output of the CFD is actually a product (logical AND) of two other logic signals, that we will call L_1 and L_2. L_1's value is 1 if the input signal A_{in} is above a certain **threshold**, and 0 otherwise. This threshold value can be set via a potentiometer (labelled Th in the front panel), and has to be slightly higher than the noise. To properly choose the value, one can plot the histogram of the input signal amplitude (after amplification) to observe the characteristic double structure of figure A.2, and set the threshold at the position where the noise and the signal separates.

The second logical pulse L_2 works on the bipolar pulse A_b. It takes the value of 1 when the value of A_b is above a certain **walk level**, and 0 otherwise. This walk level (noted Z in the front panel) has to be adjusted to the baseline (the noise level) so it mainly takes the value of 1, except when the signal becomes lower than zero, which happens only when a bipolar pulse is generated. In that case, L_2 will take a 0 value during the first half of the bipolar pulse (the negative part), and will go back to 1 as soon as the pulse become positive again. Figure A.3 shows how to properly adjust the walk level by looking at the trace of the oscilloscope. A poor choice of the walk level would lead to a timing offset in the output NIM pulse, and thus to an in-plane translation of the reconstruction map. At the end, the product of L_1 and L_2 will always take the value of 0, except at the zero-point crossing of a bipolar pulse A_b, and only if its corresponding analog input A_{in} is higher than the threshold. So it accomplishes the desired operation, because the resulting NIM signal has its rising edge centered on the zero of the bipolar signal, which does not depend on the amplitude of the input pulse. Finally, one can set the **width** of this output NIM signal, in order to match the working condition of the CFD : a signal too short might be missed by the TDC, while a signal too long will diminish the maximum rate of detection.

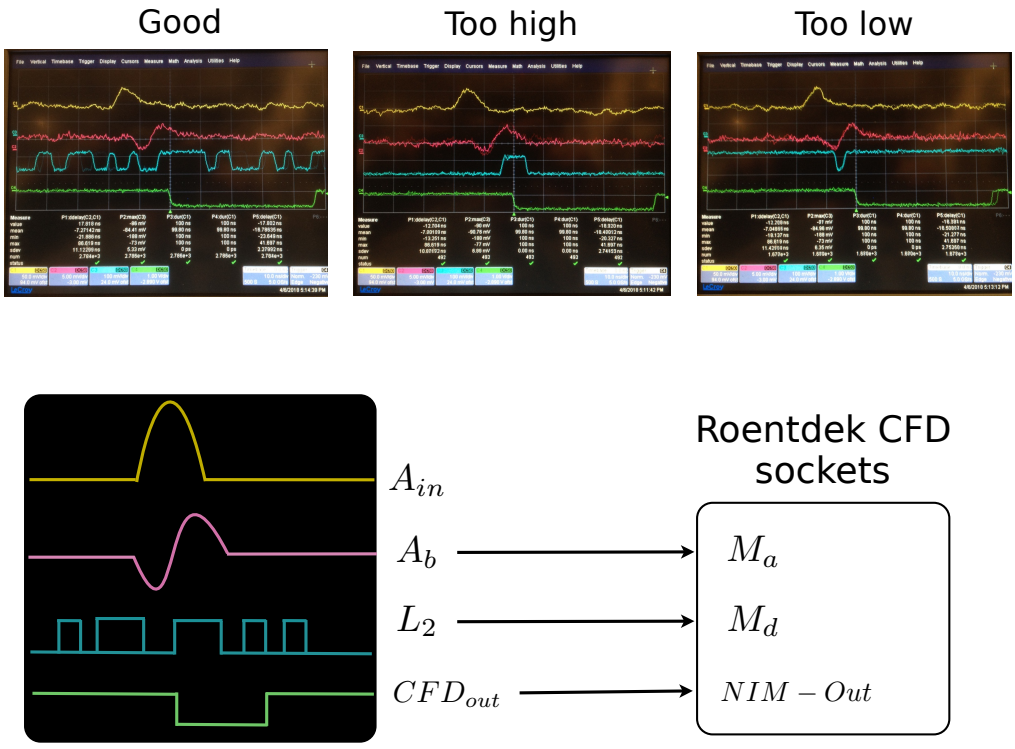

Figure A.3: Oscilloscope traces of A_{in}, A_b, L_2 and CFD_{out}. We show 3 different settings of the walk-level (the Z), which trigger the L_2 signal. When the level is well set, L_2 is "high" almost all the time, goes to zero when A_b becomes negative, and raises up again as soon as A_b crosses the zero-level. If the level is set too high, L_2 is "down" all the time, and raise up only when A_b is high enough, so that the raising edge of L_2 is slightly above the zero-level. On the opposite, when the walk level is set too low, the raising edge of L_2 is slightly below the zero-level.

Appendix B

The MCP Graphical User Interface

This section is a small user guide for the Graphical User Interface (GUI) developed during this thesis, and installed on the Pasquano computer. The interface can be used to reconstruct, organize and analyze the 3D distribution obtained with the MCP detector.

B.1 General architecture

B.1.1 The code

All the code used to compile the GUI is located in the folder : **/home/david/MCP_data/Code**. The code can be compiled through the Linux terminal : after opening a ROOT session (command : **root**), just enter the command **.x Gui_MCP.C**. The file **Gui_MCP.C** creates an instance of the class *MyMainFrame* which handles all the graphical display of the GUI's main window. The definition of the class *MyMainFrame* can be found in the header file **MainFrame_class.h**. The member functions of *MyMainFrame* use five other classes to operate, which are defined in the corresponding header files.

- *ReconstFolder_class* and *Reconstr_class* handles all the reconstruction process, using the algorithm described in 2.1, which turns a .TDC file into a list of (x, y, t) coordinates. The distribution can then be saved in a .txt format, and/or in a .root format to be imported and analyzed with the GUI.
- *DisplayAtoms_class* displays the reconstructed distributions inside 1D, 2D or 3D histograms. This class also contains member functions to export the histograms in .txt format, and to fit 1D plots.
- *Correlation_class* calculates second order correlations inside the reconstructed distribution, using the algorithm described in 2.2.2.
- *Map_class* reconstructs and records the Gain map and the D map of the MCP detector (see section 1.2.4).

Finally, the code includes a last header file called **Constants.h**, which defines the fundamental constant of the GUI, like the pixel size of the detector, the time of flight of the atomic distribution, the coding step of the TDC, and the different path used by the program.

If the GUI happens to crash, whatever the reason, you will not be able to re-compile it in the same ROOT session, where the header files have already been loaded. To avoid multiple definitions issues, you have to quit the current ROOT session (command : **.q**), and re-open a new one (command : **root**) before compiling the code again.

B.1.2 Main window

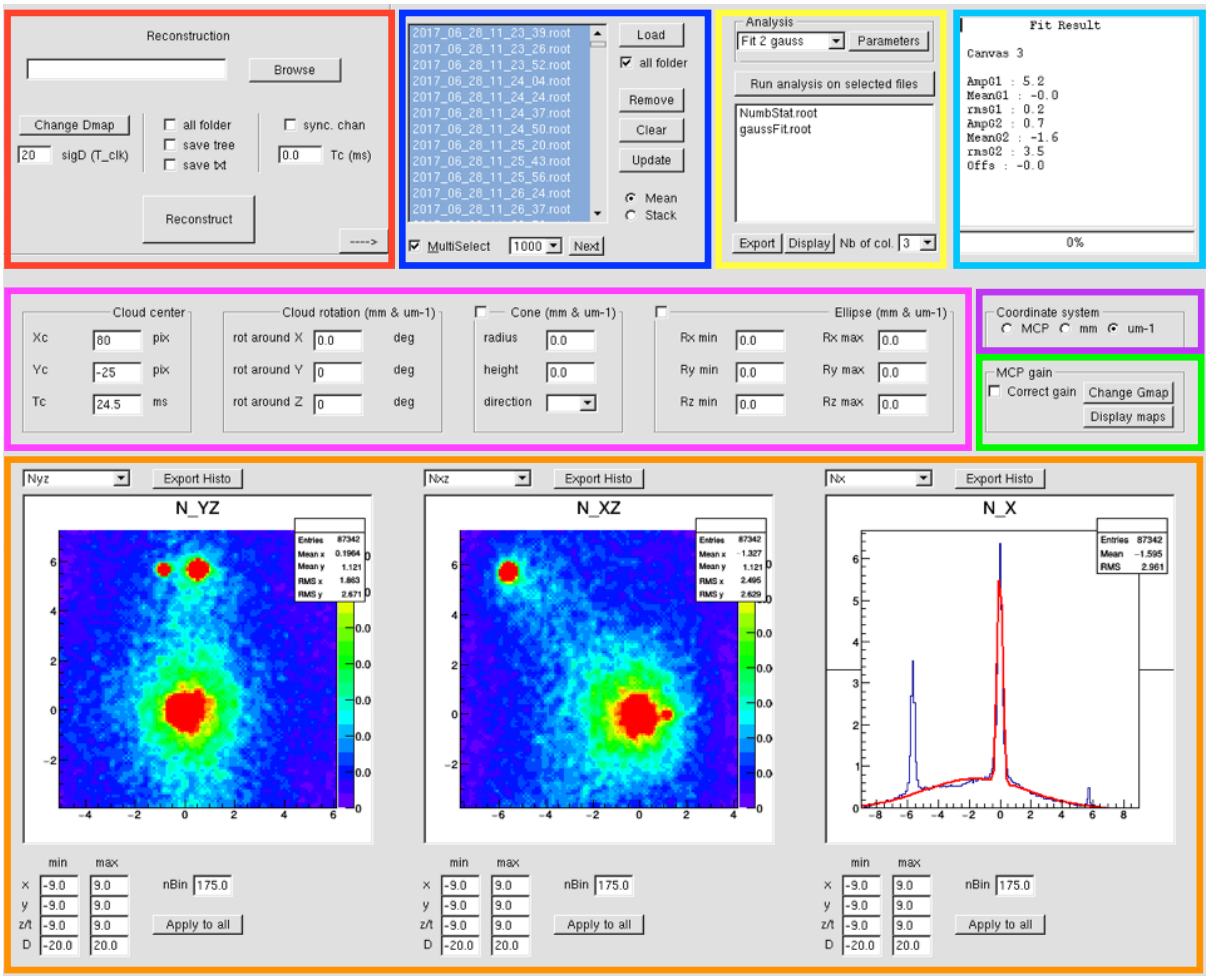

Figure B.1: Main frame of the GUI. The different blocs are highlighted with colored frame. From left to right, from top to bottom. **Red :** reconstruction bloc. **Blue :** file list bloc. **Yellow :** analysis bloc. **Cyan :** info window & progress bar. **Magenta :** geometry bloc (cloud center, rotation, conical and ellipsoidal cut). **Violet :** coordinate system bloc. **Green :** gain map bloc. **Orange :** canvases.

B.2 Reconstructing and displaying the 3D distribution

B.2.1 Reconstruction

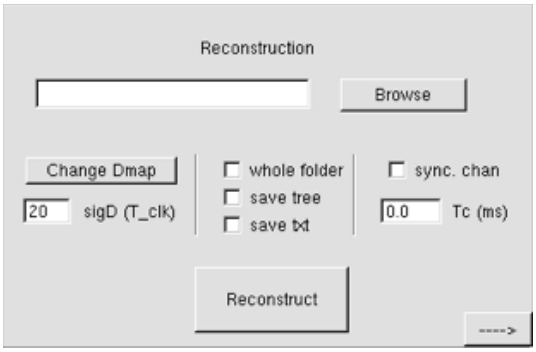

Figure B.2: Reconstruction bloc.

The reconstruction bloc allows to retrieve the (x, y, t) coordinates of a detected particle from its quadruplet of arrival times $\mathcal{Q}$ stored in a TDC file (see section 2.1). Start by pressing the **Browse** button and select a TDC file to reconstruct. To select the whole folder, select one file from this folder and tick the **whole folder** box. Press the **Reconstruct** button to launch the reconstruction. The resulting distribution can be stored in .txt files (tick the **save txt** box) and/or .root files (tick the **save tree** box). Those .root files can then be loaded and analyzed in the GUI (see below). In both cases (.txt and .root) the program creates a folder corresponding to the dataset's date, located in **/home/david/MCP_data/reconstructed_data_tree** (resp. **reconstructed_data_txt**). Once the reconstruction is over, if the **save tree** option was selected, press the **arrow** button (bottom right) to load directly the reconstructed dataset in the list of reconstructed files.

The D map used during the reconstruction can be chosen with the **Change Dmap** button (by default, the program loads the map indicated in the header file **Constants.h**). The entry **sigD** sets a maximum for the difference between the value $D_{\mathcal{Q}}$ of the quadruplets and the value $\langle D(x, y)\rangle$ of the Dmap at position (x, y). In other word, a quadruplet $\mathcal{Q}$, corresponding to the coordinates (x, y, t), and such that $|D_{\mathcal{Q}} - \langle D(x, y)\rangle| >$ sigD will be excluded from the reconstruction. In the .txt files, the informations are written in the following way : each reconstructed particles correspond to a line, which display the coordinates in this order : x (in TDC step) $\rightarrow y$ (in TDC step) $\rightarrow t$ (in ms) $\rightarrow D_{\mathcal{Q}}$ (in TDC step) $\rightarrow \langle D(x, y)\rangle$ (in TDC step).

When very diluted clouds are detected on the MCP (detection rate around 100s^{-1}), it is frequent that a bad counting of the 27^{th} bit's flips (see section 1.2.3) leads to a shift between the distributions of arrival times in the 4 channels. To avoid this issue, one can enter the expected arrival time of the cloud's center of mass in **Tc**, and tick the **sync. chan** box.

B.2.2 Display

The file list

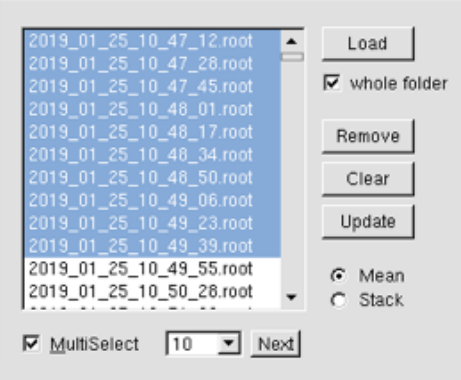

Figure B.3: The file list bloc, with many rec-files loaded in the list.

The rec-files, i.e the reconstructed files saved in .root format, contain two trees, titled "Atom" and "MCP". A tree is an instance of a ROOT class called TTree, which can store lists of data with different c++ types. The "Atom" tree stores, for each reconstructed particles, the x, y, t coordinates and the value $D = D_{\mathcal{Q}} - \langle D(x,y) \rangle$, where $\mathcal{Q}$ is the quadruplet of arrival times corresponding to the reconstructed particle. The "MCP" tree stores the distribution of arrival times on the 4 channels of the TDC.

The rec-files can be imported in the file list to be displayed and analyzed. Press the **Load** button and select the recfile you wish to import. In order to import the whole folder, tick the **whole folder** box. Once the rec-files have been loaded into the file list, you can select them to display the atomic distributions inside the 3 canvases (see below). Tick the **MultiSelect** box to allow multiple selections. You can also press the **Next** button to select the first n rec-files, with $n = 1, 10, 100, 500$ or 1000 (chosen from the combo-box, on the left). Pressing the **Next** button one more time will unselect the first n rec-files, and select the next n rec-files, etc.

You can also remove the selected rec-files from the list, by pressing the **Remove** button (this action will not delete the corresponding .root files from the computer). To remove all the rec-files in the list, just press the **Clear** button.

Canvases and histograms

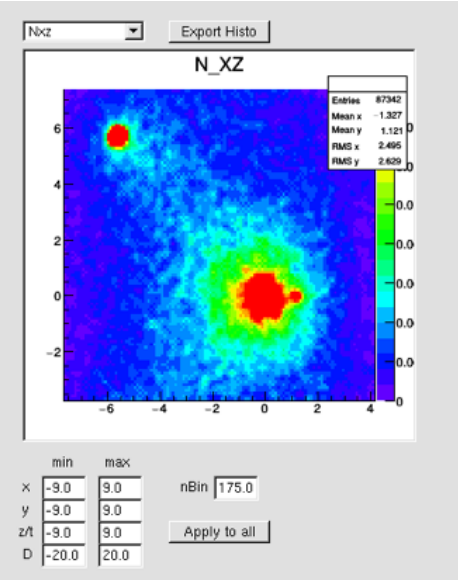

Figure B.4: A canvas displaying a Nxz (2D) histogram.

The atomic distribution of the selected rec-files are displayed in the 3 canvases. If the **Mean** radio-button (in the file list bloc) is selected, the canvas display an average of the selected rec-files. On the other hand, if the **Stack** radio-button is selected, the canvas display a sum of the rec-files. Each canvas can display a different histogram, which is chosen from the histogram combo-box, in the top left of the canvas. The histogram parameters ($x_{\min}, x_{\max}, y_{\min}, y_{\max}, z_{\min}, z_{\max}, D_{\min}, D_{\max}$ and n_{Bin}) can be adjusted for each canvas with the entries located below, and a specific set of parameter can be applied to all canvases by pressing the button **Apply to all**. The different histograms available are the following :

- Nx : a 1D plot of the atomic distribution along the x-axis. The histogram is composed of n_{Bin} bins between $x_{\min}$ and $x_{\max}$. The bin corresponding to the coordinate x_b is filled by counting the number of atoms inside the box centered on $(x_b, 0, 0)$, and of size (x_s, $y_{\max} - y_{\min}$, $z_{\max} - z_{\min}$), where $x_s = (x_{\max} - x_{\min})/n_{\text{Bin}}$ is the size of the bins.

- Ny : a 1D plot of the atomic distribution along the y-axis. The histogram is composed of n_{Bin} bins between $y_{\min}$ and $y_{\max}$. etc.

- Nz : a 1D plot of the atomic distribution along the z-axis. The histogram is composed of n_{Bin} bins between $z_{\min}$ and $z_{\max}$. etc.

- Nxy : a 2D plot of the atomic distribution along the x-axis and the y-axis. The histogram is composed of $n_{\text{Bin}} \times n_{\text{Bin}}$ bins between $x_{\min}$ and $x_{\max}$;, and between $y_{\min}$ and $y_{\max}$. The bin corresponding to the coordinate (x_b, y_b) is filled by counting the number of atoms inside the box centered on $(x_b, y_b, 0)$, and of size (x_s, y_s, $z_{\max} - z_{\min}$), where $x_s = (x_{\max} - x_{\min})/n_{\text{Bin}}$ and $y_s = (y_{\max} - y_{\min})/n_{\text{Bin}}$.

- Nxz : a 2D plot of the atomic distribution along the x-axis and the z-axis. The histogram is composed of $n_{\text{Bin}} \times n_{\text{Bin}}$ bins between $x_{\min}$ and $x_{\max}$ and between $z_{\min}$ and $z_{\max}$. etc.

- Nyz : a 2D plot of the atomic distribution along the y-axis and z-axis. The histogram is composed of $n_{\text{Bin}} \times n_{\text{Bin}}$ bins between $y_{\min}$ and $y_{\max}$, and between $z_{\min}$ and $z_{\max}$ along the z-axis. etc.
- Nr (only for mm and μm^{-1} units, see next section) : a 1D plot of the radial atomic distribution $r = \sqrt{x^2 + y^2 + z^2}$. The histogram is composed of n_{Bin} bins between 0 and $\text{Max}(x_{\max}, y_{\max}, z_{\max})$. The bin corresponding to the radius r_b is filled with the value $\frac{N_b}{4\pi r_b^2}$, or $\frac{N_b}{2\pi r_b^2(1-\cos(\theta_{\text{cone}}))}$ if the cone option is selected (see the geometry bloc), where N_b is the number of atoms of radius $r = r_b$.
- HistoD : A 1D plot of the distribution of $D = D_{\mathcal{Q}} - \langle D(x,y) \rangle$ of all the quadruplets $\mathcal{Q}$ associated to a reconstructed particle. The histogram is composed of n_{Bin} bins between $D_{\min}$ and $D_{\max}$.
- Nxyz : a 3D plot of the atomic distribution. The histogram is composed of $n_{\text{Bin}} \times n_{\text{Bin}} \times n_{\text{Bin}}$ bins between $x_{\min}$ and $x_{\max}$, $y_{\min}$ and $y_{\max}$ and between $z_{\min}$ and $z_{\max}$.
- chX1 (chX2, chY1, chY2) : A 1D plot of the distribution of arrival times in channel X1 (X2, Y1, Y2). The histogram is composed of n_{Bin} bins between $z_{\min}$ and $z_{\max}$.

At any moment, the displayed histogram can be exported in .txt format, by pressing the **Export Histo** button. The file can then be found in the folder **Export** of the current dataset (in the **reconstructed_data_tree** directory).

Coordinate system and gain map

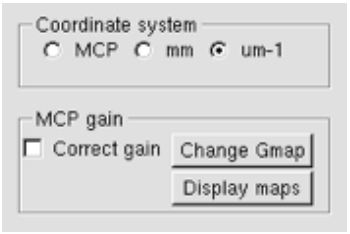

Figure B.5: The coordinate system bloc (top), and the gain map bloc (bottom).

The atomic distribution can be displayed using 3 coordinate systems. The "MCP" coordinate system is based on the raw reconstructed coordinates (x, y, t) given by the coding step of the TDC. Their units are in MCP pixel (for the in plane coordinate x and y) and ms (for t). Due to the difference of unit between the 3 axis, many analysis and display options are not available with the "MCP" units. It is for instance not possible to perform rotations, or conical cuts. The "mm" coordinate system express the three directions (x, y, z) in mm unit. To convert the t coordinate into the z coordinate, we make the approximation that all the atoms hit the MCP surface with the vertical velocity of the center of mass. Finally, the "um-1" option correspond to the momentum coordinate system (k_x, k_y, k_z), expressed in μm^{-1}. Note that for this coordinate system to be well defined, one need to identify precisely the (x, y, t) coordinates of the center of mass (see geometry bloc). Every-time the coordinate system is changed, the canvases parameters $x_{\min}, x_{\max}, y_{\min}, y_{\max}, z_{\min}$, and $z_{\max}$ automatically adjust to keep the same dimensions for the displayed histograms.

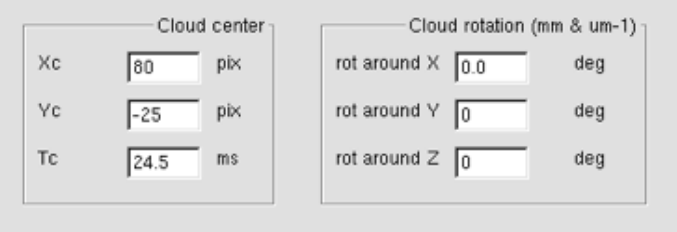

Figure B.6: The Cloud center bloc and the Cloud rotation bloc.

Figure B.7: The Cone bloc and the Ellipse bloc.

The distributions can be corrected by a gain map, if the **Correct gain** box is ticked. By default, the program loads the map indicated in the header file **Constants.h**, but it can be changed with the **Change Gmap** button. At any moment, you can display the current gain map and D map in canvases 1 and 2, by pressing the **Display maps** button.

The geometry bloc

The geometry bloc itself is composed of 4 blocs (Cloud center, Cloud rotation, Cone and Ellipse) that can be used to manipulate the geometry of the atomic distribution.

- The Cloud center bloc is used to define a new center of the (x, y, t) coordinate system. When the "um-1" unit is selected (Coordinate system bloc), the momentum distribution is calculated with this new center.

- The Cloud rotation bloc allows to perform 3D rotations of the distribution around the center defined by the Cloud center bloc. The rotations are executed in the following order : rotation around $z \rightarrow$ rotation around $y \rightarrow$ rotation around x. This option is not available for the "MCP" units.

- The Cone bloc contains the parameters **radius** and **height** defining a conical cut inside the 3D distribution (mm and μm^{-1} only). More precisely, the cut is a double spherical sector, defined by the cone of radius **radius**, bounding the sphere of radius **height**, with the two apexes touching at the center of the coordinate system. The direction of the revolution axis can be x, y or z (chosen from the combo-box located at the bottom of the bloc). If the cone option is enabled (top left box ticked), all the particles outside of the double spherical sector will be excluded from the distribution. Also, as long as the cone option is enabled, the normalization of the histogram Nr becomes $\frac{1}{2\pi r_b^2(1-\cos(\theta_{\text{cone}}))}$, with $\theta_{\text{cone}} = \text{Asin}(\text{radius}/\text{height})$ (see the **Canvases and histograms** section).

- Finally, the Ellipse bloc works similarly, by removing all the particles which are inside an ellipsoid "min" (parameters **Rx min**, **Ry min**, **Rz min**) and/or outside an ellipsoid "max" (parameters **Rx max**, **Ry max**, **Rz max**).

Some useful built-in ROOT methods

It is helpful to know some of ROOT's graphical classes to handle the histograms in canvases. A right click on any canvas will open a context menue, with several options. Among them, **Drawclass** is very convenient, since it gives access to a menu-bar, where most of the plot options can be set in **Edit**→ **Style** (for instance, changing any axis from lin to log). If the histogram is 3D, go in **View**→ **View with** → $\mathbf{X_{3D}}$ to open a new window handling the 3D distribution very smoothly. A right click on a 2D histogram will enable the options **SetShowProjectionX** and **SetShowProjectionY**, which creates 1D plot from integrating the distribution over a slice of variable size. Finally the **FitPanel** option (right quick on a 1D or 2D histogram) provide an efficient built-in fit program.

B.3 Analysis

B.3.1 The analysis list

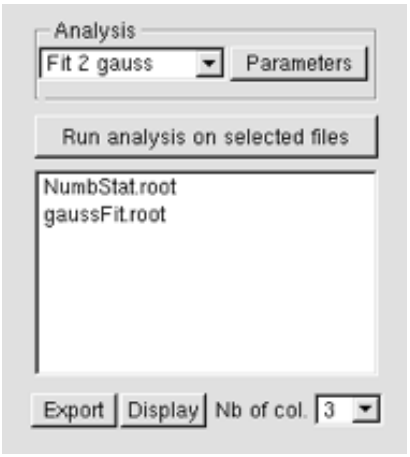

Figure B.8: The analysis bloc. The double gaussian fit (Fit 2 gauss) is currently selected in the combo-box. Two analysis files are in the list.

Several analysis can be conducted on the rec-files. Start by selecting the rec-files you want to analyse, then choose the type of analysis to perform with the combo-box (top left of the analysis bloc). For most of them, parameters can be set by pressing the **Parameters** button. Then launch the analysis with **Run analysis ...**. The results are displayed using histograms, stored inside .root files called the a-files. Those a-files can be found in the folder **Analysis** of the corresponding dataset (in the **reconstructed_data_tree** directory). They are automatically loaded in the file list of the analysis bloc, and the histograms they contain can be displayed inside a pop-up canvas (the number of columns of this pop-up window can be set using the small combo-box in the bottom right), or exported in .txt format (in the **Export** folder) by pressing the corresponding buttons.

B.3.2 Count and remove

Among the analysis options, two of them can be used to count the number of entries of the histograms displayed in each canvas. Running the **View** analysis on a set of rec-files calculates the distribution of entries over all the files, and for each canvas. The **Remove** analysis does the same, but also removes the rec-files for which one of the displayed histogram has a number of entries such that : $N_{\text{min}} > N_{\text{entries}}$ or $N_{\text{max}} < N_{\text{entries}}$, where N_{min} and N_{max} can be set in **Parameters**. It can for instance be used to remove all the empty rec-files from the list.

B.3.3 Fit

Three 1D fit options are available : a gaussian fit, a parabolic fit (Thomas-Fermi profile), and two bi-modal fits (gauss + gauss and TF + gauss). In all cases, the initial guesses can be tuned in **Parameters**, or can be set to auto-guess. If one a the fit option is selected, even without clicking on the **Run analysis ...** button, the program will fit the 1D histograms currently displayed in the canvases. This way, you can fit the distribution obtained from a multiple rec-files selection. On the other hand, if you press the **Run analysis ...** button, all the rec-files of the selection will be treated one by one, and the fit will be performed on each single file. At the output, the program generate the distribution of the fit results over all the files and for each canvas.

B.3.4 Correlations

The analysis **g2** allows to calculate the second-order correlation functions $g_{+}^{(2)}$ and $g_{-}^{(2)}$ (see chapter 2) over the selected rec-files, applying the algorithm described in 2.2.2. Note that this option is not supported for the "MCP" unit. In **Parameters**, one can set the transverse integration $\Delta k_{\perp}$, and the direction(s) along which the correlations are calculated (x, y and/or z).

B.3.5 Maps

With **Maps**, you can generate a D map and a gain map from the selected rec-files. The maps will be saved in the folder **/home/david/MCP_data/code**, and can be used in the GUI. In **Parameters**, you can select the binning of both maps, as well as the time window of the MCP acquisition used to calculate the maps. Indeed, if the number of particles detected per unit of time changes, the flux on the plate is not constant, and one might want to use a uniform flux to calculate the maps. Hence, you just need to select a time window over which the flux is more or less constant. This can be used to investigate the evolution of the gain map as a function fo the flux of particles.

Bibliography

[1] L. de Broglie. *Recherches sur la théorie des Quanta*. PhD thesis, 1924. 7

[2] C. J. Davisson and L. H. Germer. Reflection of electrons by a crystal of nickel. *Proceedings of the National Academy of Sciences of the United States of America*, 14:317–322, April 1928. 7

[3] F. Bloch. Ube die quantenmechanik der elektronen in kristalgittern. *Zeitschrift fur Physik*, 52:555–600, 1929. 7, 86

[4] N. W. Ashcroft and N. D. Mermin. *Solid State Physics*. HRW international editions. Holt, Rinehart and Winston, 1976. 7

[5] J. F. Allen and A. D. Misener. Flow of liquid helium ii. *Nature*, 141:75 EP –, 01 1938. 7, 61

[6] B. Gordon, C. Pethick, and D. Pines. Superfluidity in neutron stars. *Nature*, 224:673, 1969. 7

[7] A. Gezerlis, G. F. Bertsch, and Y. L. Luo. Mixed-spin pairing condensates in heavy nuclei. *Phys. Rev. Lett.*, 106:252502, Jun 2011. 7

[8] J. Dalibard. Une brève histoire des atomes froids. *Collège de France*, 2015. 8, 15, 18

[9] M. H. Anderson, J. R. Ensher, M. R. Matthews, C. E. Wieman, and E. A. Cornell. Observation of bose-einstein condensation in a dilute atomic vapor. *Science*, 269:198–201, 1995. 8, 61, 112

[10] I. Bloch. Ultracold quantum gases in optical lattices. *Nature Physics*, 1:23–30, 2005. 8, 24, 85

[11] P. Courteille, R. S. Freeland, D. J. Heinzen, F. A. van Abeelen, and B. J. Verhaar. Observation of a feshbach resonance in cold atom scattering. *Phys Rev Lett*, 81:69, 1998. 8

[12] W. S. Bakr, J. I. Gillen, A. Peng, S. Fölling, and M. Greiner. A quantum gas microscope for detecting single atoms in a hubbard-regime optical lattice. *Nature*, 462(7269):74–77, Nov 2009. 8, 41, 107

[13] R. Bücker, A. Perrin, S. Manz, T. Betz, C. Koller, T. Plisson, J. Rottmann, T. Schumm, and Jörg Schmiedmayer. Single-particle-sensitive imaging of freely propagating ultracold atoms. *New J. Phys.*, 11(10):103039, 2009. 8

[14] Y. Ohashi. Bcs-bec crossover in a gas of fermi atoms with a p-wave feshbach resonance. *Phys Rev Lett*, 94:050403, 2005. 8

[15] J. Simon, W. S. Bakr, R. Ma, M. E. Tai, P. M. Preiss, and M. Greiner. Quantum simulation of antiferromagnetic spin chains in an optical lattice. *Nature*, 472(7343):307–312, Jan 2011. 8

[16] I. B Spielman, W. D Phillips, and J. V Porto. Condensate fraction in a 2d bose gas measured across the mott-insulator transition. *Phys. Rev. Lett.*, 100(12):1–4, Mar 2008. 8, 9, 85, 112

[17] S. Trotzky, L. Pollet, F. Gerbier, U. Schnorrberger, I. Bloch, N. V. Prokof'ev, B. Svistunov, and M. Troyer. Suppression of the critical temperature for superfluidity near the mott transition. *Nat Phys*, 6(12):998–1004, Jan 2010. 8, 9, 85, 108, 109, 112, 114

[18] P. D. Lett, R. N. Watts, C. I. Westbrook, W. D. Phillips, P. L. Gould, and H. Metcalf. Observation of atoms laser cooled below the doppler limit. *Phys. Rev. Lett.*, 61:169, 1988. 8, 19

[19] Y. Sagi, T. E. Drake, R. Paudel, and D. S. Jin. Measurement of the homogeneous contact of a unitary fermi gas. *Phys Rev Lett*, 109:220402, 2012. 8, 74

[20] R. Ozeri, N. Katz, J. Steinhauer, and N. Davidson. Colloquium: Bulk bogoliubov excitations in a bose-einstein condensate. *Rev. Mod. Phys.*, 77(1):187–205, Jan 2005. 8

[21] J. Bardeen, L. N. Cooper, and J. R. Schrieffer. Theory of superconductivity. *Phys. Rev.*, 108:1175–1204, Dec 1957. 8

[22] E. Toth, A. Maria Rey, and P. Blair Blakie. Theory of correlations between ultracold bosons released from an optical lattice. *Phys. Rev. A*, 78(1):013627, Jan 2008. 8, 9, 57, 85, 93, 116, 117

[23] F. Gerbier, S. Trotzky, S. Foelling, U. Schnorrberger, J. D. Thompson, A. Widera, I. Bloch, L. Pollet, M. Troyer, B. Capogrosso-Sansone, N. V. Prokof'ev, and B. V. Svistunov. Expansion of a quantum gas released from an optical lattice. *Phys. Rev. Lett.*, 101(15):155303, Jan 2008. 8, 9, 85, 93, 94, 95, 112, 123

[24] U. Ray and D. M. Ceperley. Revealing the condensate and noncondensate distributions in the inhomogeneous bose-hubbard model. *Phys. Rev. A*, 87:051603, May 2013. 8, 9, 85, 114

[25] M. Greiner, O. Mandel, T. Esslinger, T. W. Hansch, and I. Bloch. Quantum phase transition from a superfluid to a mott insulator in a gas of ultracold atoms. *Nature*, 415(6867):39–44, Jan 2002. 9, 85

[26] M. Greiner, C. A. Regal, J. T. Stewart, and D. S. Jin. Probing pair-correlated fermionic atoms through correlations in atom shot noise. *Phys Rev Lett*, 94:110401, 2005. 9, 41, 85

[27] K. Xu, Y. Liu, D. Miller, J. Chin, W. Setiawan, and W. Ketterle. Observation of strong quantum depletion in a gaseous bose-einstein condensate. *Phys. Rev. Lett.*, 96(18):180405, May 2006. 9, 85

[28] J. Kupferschmidt and E. Mueller. Role of interactions in time-of-flight expansion of atomic clouds from optical lattices. *Phys. Rev. A*, 82(2):023618, Aug 2010. 9, 95, 123

[29] L. Hoendervanger. *A New Metastable Helium Machine : An Investigation into the Attributes of Trapping, Cooling and Detecting Metastable Helium.* PhD thesis, Institut d'Optique Graduate School, 2015. 11

[30] Q. Bouton. *Étude microscopique de la distribution en impulsion des condensats de Bose-Einstein d'Hélium métastable*. PhD thesis, Université Paris Saclay, 2016. 11, 22, 61, 67, 73

[31] S. S. Hodgman, R. G. Dall, L. J. Byron, K. G. H. Baldwin, S. J. Buckman, and A. G. Truscott. Metastable helium: A new determination of the longest atomic excited-state lifetime. *Phys. Rev. Lett.*, 103:053002, Jul 2009. 13

[32] A. Robert, O. Sirjean, A. Browaeys, J. Poupard, S. Nowak, D. Boiron, C. I. Westbrook, and A. Aspect. A bose-einstein condensate of metastable atoms. *Science*, 292:461–464, 2001. 13, 20

[33] F. Pereira Dos Santos, J. Leonard, J. Wang, C. J. Barrelet, F. Perales, E. Rasel, C. S. Unnikrishnan, M. Leduc, and C. Cohen-Tannoudji. Bose-einstein condensation of metastable helium. *Phys Rev Lett*, 86:3459, 2001. 13

[34] J. M. McNamara, T. Jeltes, A. S. Tychkov, W. Hogervorst, and W. Vassen. Degenerate bose-fermi mixture of metastable atoms. *Phys Rev Lett*, 97:080404, 2006. 13

[35] F. Pereira Dos Santos, F. Perales, J. Leonard, A. Sinatra, Junmin Wang, F. Saverio Pavone, E. Rasel, C.S. Unnikrishnan, and M. Leduc. Penning collisions of laser-cooled metastable helium atoms. *Eur. Phys. J. D*, 14:15–22, 2001. 13, 18

[36] F. Bardou, O. Emile, J.-M. Courty, C. I. Westbrook, and A. Aspect. Magneto-optical trapping of metastable helium: Collisions in the presence of resonant light. *Europhys. Lett.*, 20:681, 1992. 13, 18

[37] P. O. Fedichev, M. W. Reynolds, and U. M. Rahmanovand G. V. Shlyapnikov. Inelastic decay processes in a gas of spin-polarized triplet helium. *Phys Rev A*, 53:1447, 1996. 13, 24, 78

[38] A. S. Tychkov, T. Jeltes, J. M. Mcnamara, P. J. J. Tol, N Herschbach, W. Hogervorst, and W. Vassen. Metastable helium bose-einstein condensate with a large number of atoms. *Phys. Rev. A*, 73(3):031603, Jan 2006. 13, 20

[39] R. G. Dall and A. G. Truscott. Bose-einstein condensation of metastable helium in a bi-planar quadrupole ioffe configuration trap. *Opt Commun*, 270(2):255–261, Jan 2007. 13, 20

[40] M. Keller, M. Kotyrba, F. Leupold, M. Singh, M. Ebner, and A. Zeilinger. Bose-einstein condensate of metastable helium for quantum correlation experiments. *Phys Rev A*, 90:063607, 2014. 13, 20

[41] Q. Bouton, R. Chang, L. Hoendervanger, F. Nogrette, A. Aspect, C. I. Westbrook, and D. Clément. Fast production of bose-einstein condensates of metastable helium. *Phys Rev A*, 91:061402(R), 2015. 13, 23

[42] M. J. Verheijen, H. C. W. Beijerinck, L. Vonmoll, J. Driessen, and N. F. Verster. A discharge excited supersonic source of metastable rare-gas atoms. *J Phys E Sci Instrum*, 17(10):904–910, Jan 1984. 13

[43] F. Moron, A. L. Hoendervanger, M. Bonneau, Q. Bouton, A. Aspect, D. Boiron, D. Clément, and Christoph Westbrook. An oscillator circuit to produce a radio-frequency discharge and application to metastable helium saturated absorption spectroscopy. *Rev. Sci. Instrum.*, 83(4):044705, Apr 2012. 17

[44] W. D. Phillips and H. Metcalf. Laser deceleration of an atomic beam. *Phys. Rev. Lett.*, 48:596–599, Mar 1982. 17

[45] A. L. Migdall, J. V. Prodan, W. D. Phillips, T. H. Bergeman, and H. J. Metcalf. First observation of magnetically trapped neutral atoms. *Phys Rev Lett*, 54:2596, 1985. 17

[46] S. Chu, J. E. Bjorkholm, A. Ashkin, and A. Cable. Experimental observation of optically trapped atoms. *Phys. Rev. Lett.*, 57:314–317, Jul 1986. 17

[47] E. L. Raab, M. Prentiss, A. Cable, S. Chu, and D. E. Pritchard. Trapping of neutral sodium atoms with radiation pressure. *Phys. Rev. Lett.*, 59:2631–2634, Dec 1987. 17

[48] S. Chu, L. Hollberg, J. E. Bjorkholm, A. Cable, and A. Ashkin. Three-dimensional viscous confinement and cooling of atoms by resonance radiation pressure. *Phys. Rev. Lett.*, 55:48, 1985. 18

[49] R. Chang, L. Hoendervanger, Q. Bouton, Y. Fang, T. Klafka, K. Audo, A. Aspect, C. I. Westbrook, and D. Clément. Three-dimensional laser cooling at the doppler limit. *Phys Rev A*, 90:063407, 2014. 19

[50] P. D. Lett, W. D. Phillips, S.L. Rolston, C. E. Tanner, R. N. Watts, and C. I. Westbrook. Optical molasses. *J Opt Soc Am B*, 6:2084, 1989. 19

[51] C. Cohen-Tannoudji. Atomic motion in laser light. In *Fundamental Systems in Quantum Optics*, 1992. 19

[52] C. Valentin, M.-C. Gagné, J. Yu, and P. Pillet. One-dimension sub-doppler molasses in the presence of static magnetic field. *Europhys. Lett.*, 17:133, 1992. 19

[53] D. Boiron, C. Triche, D. R. Meacher, P. Verkerk, and G. Grynberg. Three-dimensional cooling of cesium atoms in four-beam gray optical molasses. *Phys. Rev. A*, 52:R3425, 1995. 19

[54] D. Boiron, A. Michaud, P. Lemonde, Y. Castin, C. Salomon, S. Weyers, K. Szymaniec, L. Cognet, and A. Clairon. Laser cooling of cesium atoms in gray optical molasses down to 1.1 microk. *Phys. Rev. A*, 53:R3734, 1996. 19

[55] D. Rio Fernandes, F. Sievers, N. Kretzschmar, S. Wu, C. Salomon, and F. Chevy. Sub-doppler laser cooling of fermionic 40k atoms in three-dimensional gray optical molasses. *Europhysics letters*, 2012. 19

[56] F. Sievers, S. Wu, N. Kretzschmar, D. Rio Fernandes, D. Suchet, M. Rabinovic C. V. Parker, L. Khaykovich, C. Salomon, and F. Chevy. Simultaneous sub-doppler laser cooling of fermionic 6li and 40k on the d1 line: Theory and experiment. *Phys Rev A*, 91:023426, 2015. 19

[57] A. Burchianti, G. Valtolina, J. A. Seman, E. Pace, M. De Pas, M. Inguscio, M. Zaccanti, and G. Roati. Efficient all-optical production of large 6li quantum gases using d1 gray-molasses cooling. *Phys Rev A*, 90:043408, 2014. 19

[58] Y. J. Lin, A. R Perry, R. L Compton, I. B Spielman, and J. V Porto. Rapid production of rb-87 bose-einstein condensates in a combined magnetic and optical potential. *Phys. Rev. A*, 79(6):063631, Jan 2009. 20

[59] E. Majorana. Atomi orientati in campo magnetico variabile. *Il Nuovo Cimento*, 9:43, 1932. 20, 22, 78

[60] G. V. Shlyapnikov, J.T.M. Walraven, U. M. Rahmanov, and M. W. Reynolds. Decay kinetics and bose condensation in a gas of spin-polarized triplet helium. *Phys Rev Lett*, 73:3247, 1994. 22

[61] G. Reinaudi, T. Lahaye, Z. Wang, and D. Guery-Odelin. Strong saturation absorption imaging of dense clouds of ultracold atoms. *Opt Lett*, 32(21):3143–3145, Jan 2007. 23

[62] L. Pitaevskii and S. Stringari. *Bose-Einstein Condensation*. Oxford University Press, 2003. 23

[63] J. Söding, D. Guéry-Odelin, P. Desbiolles, F. Chevy, H. Inamori, and J. Dalibard. Three-body decay of a rubidium bose–einstein condensate. *Appl Phys B*, 69, 257-261 1999. 24

[64] H. Cayla, C. Carcy, Q. Bouton, R. Chang, G. Carleo, M. Mancini, and D. Clément. Single-atom-resolved probing of lattice gases in momentum space. *Phys. Rev. A*, 97:061609, Jun 2018. 24, 123

[65] W. H. Smith. Triggering at lhc experiments. *Nuclear Instruments and Methods in Physics Research Section A: Accelerators, Spectrometers, Detectors and Associated Equipment*, 478(1):62 – 67, 2002. Proceedings of the ninth Int.Conf. on Instrumentation. 26

[66] A. William. Microchannel plate for surface-induced dissociation in mass spectrometry. *Analytical Chemistry*, 62:609–611, Dec 1990. 26

[67] L. von der Wense, B. Seiferle, M. Laatiaoui, J. B. Neumayr, H. J. Maier, H. F. Wirth, C. Mokry, J. Runke, K. Eberhardt, C. E. Düllmann, N. G. Trautmann, and P. G. Thirolf. Direct detection of the 229th nuclear clock transition. *Nature*, 553:47–, Dec 2016. 26

[68] G. W. Fraser, M. T. Pain, J. E. Lees, and J.F. Pearson. The operation of microchannel plate at high count rates. *Nuclear Instruments and Methods in Physics Research*, 306, 1991. 26, 38

[69] G. W. Fraser, M. T. Pain, and J. E. Lees. Microchannel plate operation at high count rates - further-studies. *Nucl Instrum Meth A*, 327(2-3):328–336, Jan 1993. 26, 38

[70] M. L. Edgar, J. S. Lapington, and A. Smith. The spatial extent of gain depression for mcp based photon detectors. *Review of Scientific Instruments*, 63, 1992. 26, 38

[71] O.H.W. Siegmund. Preconditioning of micro channel plate stacks. *SPIE*, 1072, 1989. 28

[72] Roentdek. Mcp delay line detector manual v 11.0.1803.1, 2013. 30, 34

[73] F. Nogrette, D. Heurteau, R. Chang, Q. Bouton, C. I. Westbrook, R. Sellem, and D. Clément. Characterization of a detector chain using a fpga-based time-to-digital converter to reconstruct the three-dimensional coordinates of single particles at high flux. *Review of Scientific Instruments*, 86:113105, 2015. 31, 36

[74] P. J. J. Tol, N. Herschbach, E. A. Hessels, W. Hogervorst, and W. Vassen. Large numbers of cold metastable helium atoms in a magneto-optical trap. *Phys. Rev. A*, 60:761, 1999. 32

[75] O. Sirjean. *Collisions ionisantes: un nouveau diagnostic pour les condensats de Bose-Einstein d'hélium métastable*. PhD thesis, Jul 2003. 32

[76] W. Vassen, R. P. M. J. W. Notermans, R. J. Rengelink, and R. F. H. J. van der Beek. *Ultracold Metastable Helium: Ramsey Fringes and Atom Interferometry*, pages 597–616. Springer International Publishing, Cham, 2018. 32

[77] M. Ebner. *Development of a metastable helium BEC as a platform for experiments with EPR-entangled matter waves.* PhD thesis, 2012. 38

[78] M. Schellekens. *L'effet Hanbury Brown et Twiss pour les atoms froids.* PhD thesis, Jul 2007. 39, 53

[79] W. S. Bakr, A. Peng, M.E. Tai, R. Ma J. Simon, J.I. Gillen, S. Foelling, L. Pollet, and M. Greiner. Probing the superfluid-to-mott insulator transition at the single atom level. *Science*, 329:547–550, 2010. 41

[80] M. Boll, T. A. Hilker, G. Salomon, A. Omran, J. Nespolo, L. Pollet, I. Bloch, and C. Gross. Spin- and density-resolved microscopy of antiferromagnetic correlations in fermi-hubbard chains. *Science*, 353:1257, 2016. 41

[81] T. Schweigler, V. Kasper, S. Erne, I. Mazets, B. Rauer, F. Cataldini, T. Langen, T. Gasenzer, J. Berges, and J. Schmiedmayer. Experimental characterization of a quantum many-body system via higher-order correlations. *Nature*, 545:323, 2017. 41

[82] T. A. Hilker, G. Salomon, F. Grusdt, A. Omran, M. Boll, E. Demler, I. Bloch, and C. Gross. Revealing hidden antiferromagnetic correlations in doped hubbard chains via string correlators. *Arxiv preprint*, page 1702.00642, 2017. 41

[83] M. Schellekens, R. Hoppeler, A. Perrin, J. Viana Gomes, D. Boiron, A. Aspect, and C. I. Westbrook. Hanbury brown twiss effect for ultracold quantum gases. *Science*, 310(5748):648–651, 2005. 41, 46, 50, 51, 76, 119

[84] A. Perrin, R. Bücker, S. Manz, T. Betz, C. Koller, T. Plisson, T. Schumm, and J. Schmiedmayer. Hanbury brown and twiss correlations across the bose-einstein condensation threshold. *Nature Physics*, 8:195–98, Jan 2012. 41, 50, 52, 116, 119

[85] S. Fölling, F. Gerbier, A. Widera, O. Mandel, T. Gericke, and I. Bloch. Spatial quantum noise interferometry in expanding ultracold atom clouds. *Nature*, 434(7032):481–484, Mar 2005. 41, 52, 116

[86] T Jeltes, J. M Mcnamara, W Hogervorst, W Vassen, V Krachmalnicoff, M Schellekens, A Perrin, H Chang, Denis Boiron, Alain Aspect, and Christoph I Westbrook. Comparison of the hanbury brown–twiss effect for bosons and fermions. *Nature*, 445(7126):402–405, Jan 2007. 41

[87] R. Hanbury-Brown and R. Q. Twiss. Correlations between photons in two coherent beams of light. *Nature*, 177:27–29, 1956. 50

[88] R. Hanbury-Brown and R. Q. Twiss. A test of a new type of interferometer on sirius. *Nature*, 178:1046–1048, 1956. 50, 51

[89] R. J. Glauber. The quantum theory of optical coherence. *Phys. Rev.*, 130:2529–2539, Jun 1963. 50, 51

[90] R. G. Dall, S. S. Hodgman, A. G. Manning, M. T. Johnsson, K. G. H. Baldwin, and A. G. Truscott. Observation of atomic speckle and hanbury brown–twiss correlations in guided matter waves. *Nature Communications*, 2:291–5, Apr 2011. 50

[91] J. W. Goodman. *Speckle phenomena in optics: theory and applications*. 2006. 50, 51

[92] M. Yasuda and F. Shimizu. Observation of two-atom correlation of an ultracold neon atomic beam. *Phys. Rev. Lett.*, 77:3090–3093, Oct 1996. 51

[93] A. Öttl, S. Ritter, M. Köhl, and T. Esslinger. Correlations and counting statistics of an atom laser. *Phys. Rev. Lett.*, 95:090404, Aug 2005. 51, 119

[94] J. Viana Gomes, A. Perrin, M. Schellekens, D. Boiron, C. I. Westbrook, and M. Belsley. Theory for a hanbury brown twiss experiment with a ballistically expanding cloud of cold atoms. *Phys Rev A*, 74:053607, 2006. 51, 52, 53, 58

[95] P. Kapitza. Viscosity of liquid helium below the $\lambda - point. Nature, 141 : 74, 1938.$ 61

[96] F. London. On the bose-einstein condensation. *Phys. Rev.*, 54:547, 1938. 61

[97] K. B. Davis, M. O. Mewes, M. R. Andrews, N. J. van Druten, D. S. Durfee, D. M. Kurn, and W. Ketterle. Bose-einstein condensation in a gas of sodium atoms. *Phys. Rev. Lett.*, 75:3969–3973, 1995. 61

[98] F. Dalfovo, S. Giorgini, M. Guilleumas, L. Pitaevskii, and S. Stringari. Collective and single-particle excitations of a trapped bose gas. *Phys Rev A*, 56:3840, 1997. 61

[99] S. B Papp, J. M Pino, R. J Wild, S Ronen, C. E Wieman, D. S Jin, and E. A Cornell. Bragg spectroscopy of a strongly interacting rb-85 bose-einstein condensate. *Phys. Rev. Lett.*, 101(13):135301, Jan 2008. 61

[100] R. J. Fletcher, R. Lopes, J. Man, N. Navon, R. P. Smith, M. W. Zwierlein, and Z. Hadzibabic. Two- and three-body contacts in the unitary bose gas. *Science*, 355:377, 2017. 61

[101] R. J. Wild, P. Makotyn, J. M. Pino, E. A. Cornell, and D. S. Jin. Measurements of tan's contact in an atomic bose-einstein condensate. *Phys Rev Lett*, 108:145305, 2012. 61

[102] C. Tozzo and F. Dalfovo. Phonon evaporation in freely expanding bose-einstein condensates. *Phys. Rev. A*, 69(5):053606, May 2004. 61

[103] C. Qu, L. P. Pitaevskii, and S.Stringari. Expansion of harmonically trapped interacting particles and time dependence of the contact. *Phys Rev A*, 94:063635, 2016. 61, 76

[104] Y. Castin and R. Dum. Bose-einstein condensates in time dependent traps. *Phys. Rev. Lett.*, 77(27):5315–5319, Jan 1996. 61, 65

[105] R. Chang, Q. Bouton, H. Cayla, C. Qu, A. Aspect, C. I. Westbrook, and D. Clément. Momentum-resolved observation of thermal and quantum depletion in an interacting bose gas. *Phys Rev Lett*, 117:235303, 2016. 61, 67, 74, 123

[106] A. Einstein. Concerning an heuristic point of view toward the emission and transformation of light. *American Journal of Physics*, 33(5)(1-16), 1905. 62

[107] S. N. Bose. Planck's law and light quantum hypothesis. *Zeitschrift fur Physik*, 26(178), 1924. 62

[108] A. Einstein. Quantum theory of the monoatomic ideal gas. *Sitzungsberichte I*, 1925. 62

[109] C. Cohen-Tannoudji, B. Diu, and F. Laloe. *Mecanique quantique vol.1*. Hermann, 2nd edition, 1997. 62

[110] C. J. Pethick and H. Smith. *Bose-Einstein Condensation in Dilute Gases*. Cambridge University Press, 2nd edition, 2008. 63, 64, 65

[111] L. P. Pitaevskii. Vortex lines in an imperfect bose gas. *Sov. Phys. JETP*, 13(2):451–454, 1925. 63

[112] E. P. Gross. Structure of a quantized vortex in boson systems. *Il Nuovo Cimento*, 20(3):454–457, 1925. 63

[113] N. Bogoliubov. On the theory of superfluidity. *Physical Review*, 11:23–32, 1947. 65

[114] F. Dalfovo, S. Giorgini, L. P. Pitaevskii, and S. Stringari. Theory of bose-einstein condensation in trapped gases, Jan 1999. 70

[115] A. Minguzzi, Vignolo P., and M. Tosi. High-momentum tail in the tonks gas under harmonic confinement. *Phys. Lett. A.*, 294(3-4):222–226, 2002. 74

[116] J. T. Stewart, J. P. Gaebler, T. E. Drake, and D. S. Jin. Verification of universal relations in a strongly interacting fermi gas. *Phys Rev Lett*, 104:235301, 2010. 74

[117] S. Tan. Energetics of a strongly correlated fermi gas. *Annals of Physics*, 323:2952–2970, 2008. 74

[118] S. Tan. Large momentum part of a strongly correlated fermi gas. *Annals of Physics*, 323:2971–2986, 2008. 74

[119] G. B Partridge, J.-C Jaskula, M. Bonneau, D. Boiron, and C. I. Westbrook. Bose-einstein condensation and spin mixtures of optically trapped metastable helium. *Phys. Rev. A*, 81(5):053631, May 2010. 79

[120] R. B. Diener, Q. Zhou, H. Zhai, and T.-L. Ho. Criterion for bosonic superfluidity in an optical lattice. *Phys Rev Lett*, 98:180404, 2007. 85, 112

[121] Y. Kato, Q. Zhou, N. Kawashima, and N. Trivedi. Sharp peaks in the momentum distribution of bosons in optical lattices in the normal state. *Nat Phys*, 4(8):617–621, Jan 2008. 85, 110, 111, 112

[122] J. Dalibard. Des cages de lumière pour les atomes : la physique des pièges et des réseaux optiques. *Collège de France*, 2013. 85

[123] G. H. Wannier. The structure of electronic excitation levels in insulating crystals. *Phys. Rev.*, 52:191–197, 1937. 86

[124] D. Van Oosten, P. Van Der Straten, and H. Stoof. Quantum phases in an optical lattice. *Phys. Rev. A*, 63(5):053601, Apr 2001. 90, 114

[125] B. G. Wild, P. B. Blakie, and D. A. W. Hutchinson. Finite-temperature treatment of ultracold atoms in a one-dimensional optical lattice. *Phys Rev A*, 73:023604, 2006. 90

[126] D. S. Rokhsar and B. G. Kotliar. Gutzwiller projection for bosons. *Zeitschrift fur Physik*, 44:10328, 1991. 90, 95, 114

[127] S. Fang, R. K. Lee, and D. W. Wang. Quantum fluctuations and condensate fraction during time-of-flight expansion. *Phys. Rev. A*, 82:031601, Sep 2010. 94

[128] J. H. Denschlag, J. E. Simsarian, H. Haffner, C. McKenzie, A. Browaeys, D. Cho, K. Helmerson, S.L. Rolston, and W.D. Phillips. A bose-einstein condensate in an optical lattice. *J Phys B-At Mol Opt*, 35(14):3095–3110, Jan 2002. 97

[129] M. Greiner, I. Bloch, O. Mandel, T. W. Hansch, and T. Esslinger. Exploring phase coherence in a 2d lattice of bose-einstein condensates. *Phys. Rev. Lett.*, 87(16):160405, Jan 2001. 99

[130] Q. Zhou and T. Ho. Universal thermometry for quantum simulation. *Phys Rev Lett*, 106:255301, 2011. 107

[131] J. F. Sherson, C. Weitenberg, M. Endres, M. Cheneau, I. Bloch, and S. Kuhr. Single-atom-resolved fluorescence imaging of an atomic mott insulator. *Nature*, 467(7311):68–72, Sep 2010. 107

[132] D. Mckay, M. White, and B. Demarco. Lattice thermodynamics for ultracold atoms. *Phys. Rev. A*, 79(6):063605, Jun 2009. 107, 108

[133] L. Pollet, C. Kollath, K. Van Houcke, and M. Troyer. Temperature changes when adiabatically ramping up an optical lattice. *New Journal of Physics*, 10(6):065001, 2008. 108

[134] T. Roscilde. Thermometry of cold atoms in optical lattices via artificial gauge fields. *Phys Rev Lett*, 112:110403, 2014. 108

[135] N. R. Cooper and Zoran H. Measuring the superfluid fraction of an ultracold atomic gas. *Phys. Rev. Lett.*, 104:030401, Jan 2010. 111

[136] M. O. Mewes, M. R. Andrews, N. J. van Druten, D. M. Kurn, D. S. Durfee, and W. Ketterle. Bose-einstein condensation in a tightly confining dc magnetic trap. *Phys Rev Lett*, 77:416, 1996. 112

[137] F. Gerbier, A. Widera, S. Foelling, O. Mandel, T. Gericke, and I. Bloch. Interference pattern and visibility of a mott insulator. *Phys. Rev. A*, 72(5):053606, Jan 2005. 112

[138] S. Fölling, A. Widera, T. Müller, F. Gerbier, and I. Bloch. Formation of spatial shell structure in the superfluid to mott insulator transition. *Phys. Rev. Lett.*, 97(6):1–4, Aug 2006. 114

[139] G. K. Campbell, J. Mun, M. Boyd, P. Medley, A. E. Leanhardt, L. G. Marcassa, D. E. Pritchard, and W. Ketterle. Imaging the mott insulator shells by using atomic clock shifts. *Science*, 313(5787):649–652, Aug 2006. 114

[140] L. Pollet, N. V. Prokofiev, and B. V. Svistunov. Criticality in trapped atomic systems. *Phys Rev Lett*, 104(24):245705, 2010. 114

[141] M. Campostrini and E. Vicari. Critical behavior and scaling in trapped systems. *Phys Rev Lett*, 102:240601, 2009. 114

[142] M. Campostrini and E. Vicari. Quantum critical behavior and trap-size scaling of trapped bosons in a one-dimensional optical lattice. *Phys Rev A*, 81:063614, 2010. 114

[143] M. Campostrini, A. Pelissetto, and E. Vicari. Finite-size scaling at quantum transitions. *Phys Rev B*, 89:094516, 2014. 114

[144] J. Schmitt, T. Damm, D. Dung, F. Vewinger, J. Klaers, and M. Weitz. Observation of grand-canonical number statistics in a photon bose-einstein condensate. *Phys. Rev. Lett.*, 112:030401, Jan 2014. 119

[145] H. Yao, D. Clément, A. Minguzzi, P. Vignolo, and L. Sanchez-Palencia. Tan's Contact for Trapped Lieb-Liniger Bosons at Finite Temperature. *ArXiv e-prints*, April 2018. 124

Titre : Mesure sensible à l'atome unique de la distribution d'impulsion d'un gaz sur réseau

Mots clés : Gaz sur réseau, Espace des impulsions, Atome unique, Helium métastable, Corrélations

Résumé : Ce travail de thèse démontre une technique de détection capable de mesurer, avec une sensibilité à l'atome unique, l'espace des impulsions d'un gaz ultrafroid chargé dans un réseau optique 3D. Nous avons développé un détecteur basé sur des galettes de micro-canaux, capable de sonder électroniquement des nuages d'Hélium-4 métastable. Le gaz est détecté après un temps de vol de 325ms, suffisamment long pour atteindre l'expansion de champ lointain, où la distribution spatiale du gaz coïncide avec la distribution d'impulsion asymptotique. En se plaçant dans un régime proche du remplissage unitaire du réseau, les effets de collisions entre atomes aux premiers instants de l'expansion deviennent négligeables, et donc la distribution d'impulsion asymptotique est égale à la distribution d'impulsion in situ. Nous démontrons expérimentalement cette égalité en comparant nos mesures en champ lointain avec la distribution d'impulsion calculée à partir de l'Hamiltonien de Bose-Hubbard, grâce à des simulations Monte Carlo Quantique. Nous observons un bon accord avec la théorie sur plus de 3 ordres de grandeur en densité. Ces simulations sont calculées à partir de nos paramètres expérimentaux, la température étant la seule variable ajustable. Nous utilisons ensuite cette comparaison pour réaliser une thermométrie précise du gaz sur réseau, permettant une exploration de la transition superfluide-gaz normal à travers la mesure directe de différentes quantités, comme la fraction condensée ou la fonction de corrélation à deux particules.

Title : Measuring the momentum distribution of a lattice gas at the single-atom level

Keywords : Lattice gas, Momentum space, Single atom, Metastable Helium, Correlations

Abstract : In this thesis, we report the demonstration of a detection technique able to probe, with a single-atom sensitivity, the momentum distribution of an ultracold gas loaded inside a 3D optical lattice. We have developed a micro-channel plate detector, able to electronically probe clouds of metastable Helium-4. The gas is detected after a time-of-flight of 325ms, long enough to reach the far-field expansion, where the spatial distribution of the cloud can be mapped to the asymptotic momentum distribution. By putting ourselves in a regime where the lattice filling is close to unity, the atomic collisions in the first instants of the expansion become negligible, so the asymptotic momentum distribution is equal to the in situ momentum distribution. We experimentally demonstrate this equality, by comparing our far-field measurements with the momentum distribution calculated from the Bose-Hubbard Hamiltonian, thanks to ab initio quantum Monte Carlo simulations. We show a good agreement with the theory over more than 3 orders of magnitude in density. Those simulations are calculated with our experimental parameters, the temperature being the only adjustable variable. We then use this comparison to perform a precise thermometry of the lattice gas, allowing us to explore the superfluid-normal gas transition through a direct measurement of different quantities, like the condensed fraction or the two-particles correlation function.

Université Paris-Saclay
Espace Technologique / Immeuble Discovery
Route de l'Orme aux Merisiers RD 128 / 91190 Saint-Aubin, France